AKADEMIA GÓRNICZO-HUTNICZA
IM. STANISŁAWA STASZICA W KRAKOWIE

TECHNISCHE
UNIVERSITÄT
WIEN
Vienna University of Technology

UCZELNIA
BADAWCZA
INICJATYWA DOSKONAŁOŚCI

DOCTORAL DISSERTATION

Mateusz Aleksander Gala

FIELD: **Natural Sciences**
DISCIPLINE: **Physical Sciences**

Modification of quantum states in strongly correlated systems by applying uniaxial pressure

Supervisor, AGH: **dr hab. inż. Wojciech Tabiś, prof. AGH**
Supervisor, TUW: **Prof. Dr. Neven Barišić**

Kraków, 2025

Statement by the author of the Dissertation

Aware of the criminal liability for certifying untruths, I declare that I have prepared this Doctoral Dissertation personally and independently and that I have not used any sources other than those indicated in the manuscript.

date, signature

Statement by the Supervisor

This Dissertation is ready for evaluation by reviewers.

date, signature

Streszczenie

Głównym celem niniejszej rozprawy doktorskiej, zatytułowanej *„Modyfikacja stanów kwantowych w silnie skorelowanych układach poprzez zastosowanie cisnienia jednoosiowego”*, było zbadanie, w jaki sposób naprężenie jednoosiowe, stosowane jako kontrolowane zaburzenie symetrii sieci krystalicznej, wpływa na właściwości strukturalne, magnetyczne i ładunkowe materiałów wykazujących silne korelacje elektronowe. Ciśnienie jednoosiowe stanowi obecnie potężne narzędzie eksperymentalne, uzupełniające ciśnienie hydrostatyczne, pole elektryczne oraz pole magnetyczne, umożliwiające w sposób kontrolowany kierunkowo-selektywną deformację sieci krystalicznej bez zmiany składu chemicznego. Podczas gdy ciśnienie hydrostatyczne systematycznie skraca wszystkie odległości międzyatomowe, naprężenie jednoosiowe modyfikuje jedynie wybrane kierunki krystalograficzne, co pozwala badać i kontrolować anizotropową równowagę pomiędzy konkurującymi oddziaływaniami, takimi jak sprzężenia elektron–elektron, elektron–fonon oraz oddziaływania magnetyczne. Podejście to jest szczególnie istotne w przypadku układów skorelowanych, w których domieszkowanie lub podstawienia atomowe, jak np. domieszkowanie ładunku w tlenkach, nieuchronnie wprowadzają nieuporządkowanie, zaburzając tym samym obserwację efektów wynikających z wewnętrznych korelacji.

Jednym z głównych wyzwań technologicznych w badaniach układów (skorelowanych) poddanych naprężeniu jednoosiowemu jest osiągnięcie wysokiej precyzji mechanicznej oraz wiarygodnej, ilościowej kalibracji przyłożonego ciśnienia. Nieliczne dotychczas przeprowadzone eksperymenty często charakteryzowały się brakiem dokładnego określenia wartości przyłożonego ciśnienia. Dlatego, kluczowymi elementemami niniejszej rozprawy były zaprojektowanie, budowa oraz kalibracja kompaktowej komórki do przykładania naprężenia jednoosiowego (SOL), umożliwiającej ilościowe, powtarzalne i kierunkowo selektywne ściskanie. Opracowana komórka działa na zasadzie imadła napędzanego śrubą i jest kompatybilna z wieloma technikami pomiarowymi, w tym z dyfrakcją rentgenowską (*ang.* X-ray diffraction; XRD), pomiarami rezystywności elektrycznej, zmiennoprądową podatnością magnetyczną oraz rentgenowską spektroskopią absorpcyjną (*ang.* X-ray absorption spectroscopy; XAS).

Spośród szerokiej grupy materiałów wykazujących silne korelacje elektronowe jako układ modelowy wybrano magnetyt stechiometryczny (Fe_3O_4), ponieważ łączy on długozasięgowy porządek ferrimagnetyczny z przemianą Verweya zachodzącą w temperaturze około $T_V \approx 123$ K, będącą sprzężoną przemianą ładunkową, orbitalną i strukturalną, w której symetria sieci krystalicznej zmienia się z kubicznej $Fd\bar{3}m$ na jednoskośną Cc. Modyfikacje stechiometrii, domieszkowanie lub zastosowanie ciśnienia hydrostatycznego są znane z tego, że obniżają temperaturę przemiany Verweya (T_V), natomiast przewidywania teoretyczne oraz ograniczone dane

eksperymentalne sugerują, iż ściskanie jednoosiowe może ją podwyższać. Magnetyt stanowi zatem idealną platformę do badania, w jaki sposób łamanie symetrii sieci krystalicznej wpływa na stany elektronowe w układach silnie skorelowanych.

Serię eksperymentów dyfrakcji rentgenowskiej przy użyciu promieniowania synchrotronowego przeprowadzono na linii pomiarowej ID11 w Europejskim Ośrodku Promieniowania Synchrotronowego (*ang.* European Synchrotron Radiation Facility; ESRF), stosując ściskanie jednoosiowe w kierunkach $\langle 100 \rangle$ oraz $\langle 110 \rangle$. Dane dyfrakcyjne ujawniły anizotropową odpowiedź sprężystą: ściskanie wzdłuż $\langle 100 \rangle$ powodowało zniekształcenie tetragonalne, natomiast wzdłuż $\langle 110 \rangle$ prowadziło do deformacji ortorombowej. Porównując ewolucję parametrów sieci krystalicznej mierzoną przy użyciu komórki SOL z danymi odniesienia uzyskanymi z kalibrowanej prasy mechanicznej ADMET, ustanowiono ilościową zależność pomiędzy obrotem śruby a przyłożonym naprężeniem w SOL.

Mikrostrukturę dwóch typów wysokiej jakości monokryształów magnetytu, z których jeden został otrzymany metodą topienia strefowego w piecu odbiciowym (*ang.* traveling solvent floating zone; TSFZ), a drugi przy użyciu techniki topienia indukcyjnego w zimnym tyglu (*ang.* skull-melter), zbadano w pierwszej kolejności za pomocą mikroskopii rentgenowskiej w ciemnym polu (*ang.* dark-field X-ray diffraction microscopy; DFXM) na linii pomiarowej ID03 w ESRF. Stwierdzono, że metoda syntezy pozostawia wyraźny odcisk strukturalny. Kryształy uzyskane techniką skull-melter charakteryzowały się niewielkim średnim odkształceniem, lecz wykazywały wyraźną teksturę mozaikową wynikającą z szybkiego schłodzenia na ostatnim etapie syntezy, podczas gdy kryształy wytworzone metodą TSFZ cechowały się większym odkształceniem osiowym, ale mniejszą liczbą rozległych defektów strukturalnych. Ponieważ takie cechy mikrostrukturalne mogą znacząco wpływać na odpowiedź materiału na naprężenia zewnętrzne, do dalszych eksperymentów ze ściskaniem jednoosiowym wybrano kryształy otrzymane metodą TSFZ.

Ponieważ jednoosiowe ciśnienie indukuje kierunkowe zniekształcenia sieci krystalicznej, odkształcenia resztkowe utrzymujące się po dekompresji zostały również zbadane metodą mikroskopii rentgenowskiej w ciemnym polu (DFXM). Obrazowanie ujawniło, że naprężenia przekraczające około 150 MPa tworzą stabilne, liniowe sieci dyslokacyjne o rozmiarach rzędu 10 mikrometrów, wykazujące preferencyjne uporządkowanie względem płaszczyzn poślizgu $\{111\}$. Pomimo obecności tych rozległych dyslokacji oraz pól odkształceń resztkowych, pomiary magnetycznej podatności zmiennoprądowej wykazały, że temperatura przemiany Verweya pozostaje niezmieniona nawet w próbkach poddanych naprężeniom przekraczającym 300 MPa. Obserwacja ta wskazuje, że rozległe sieci dyslokacyjne nie wpływają na kooperatywne uporządkowania ładunkowe i orbitalne związane z przemianą Verweya.

Skalibrowana komórka SOL została następnie wykorzystana do badania *in situ* ewolucji oporu elektrycznego oraz podatności magnetycznej pod wpływem ściskania jednoosiowego wzdłuż kierunków $\langle 100 \rangle$ i $\langle 110 \rangle$. W obu orientacjach temperatura przemiany Verweya wzrastała liniowo wraz z przyłożonym naprężeniem, co wskazuje na stabilizację jednoskośnej fazy

niskotemperaturowej. Efekt ten był silnie anizotropowy: wzrost T_V pod wpływem ściskania wzdłuż ⟨110⟩ był niemal rząd wielkości większy niż w przypadku kierunku ⟨100⟩. Różnica ta odzwierciedla odmienne symetrie odkształceń indukowanych przez ściskanie; ortorombową dla ⟨110⟩ i tetragonalną dla ⟨100⟩, oraz silniejsze sprzężenie tej pierwszej z mechanizmami uporządkowania ładunkowego i orbitalnego odpowiedzialnymi za przemianę Verweya. W temperaturze pokojowej opór malał liniowo wraz ze wzrostem jednoosiowego ciśnienia, co jest zgodne ze wzrostem ruchliwości nośników w warunkach naprężenia; również w tym przypadku efekt był około trzykrotnie silniejszy wzdłuż ⟨110⟩ niż wzdłuż ⟨100⟩.

Pomiary rentgenowskiej spektroskopii absorpcyjnej (*ang.* X-ray absorption spectroscopy; XAS) przy krawędzi K żelaza przeprowadzono w temperaturze pokojowej w celu zbadania ewentualnych zmian w lokalnym otoczeniu jonów żelaza wywołanych naprężenieniami. Analiza obszaru przedkrawędziowego (7105–7120 eV), wrażliwego na hybrydyzację orbitali $3d$–$2p$ oraz na zaburzenia symetrii inwersyjnej, nie wykazała mierzalnych zmian położenia, szerokości ani intensywności pików do wartości naprężenia około 200 MPa. Ta niezmienność dowodzi, że naprężenie jednoosiowe wzdłuż kierunków ⟨100⟩ i ⟨110⟩ indukuje odpowiednio tetragonalne i ortorombowe zniekształcenia sieci kubicznej, nie naruszając lokalnej symetrii inwersyjnej oktaedrów FeO_6. W konsekwencji, lokalna koordynacja wiązań Fe–O pozostaje niezmieniona, natomiast właściwości makroskopowe, takie jak temperatura przemiany Verweya (T_V), ulegają przesunięciu w wyniku kolektywnych, zachowujących symetrię zniekształceń strukturalnych.

Wyniki przedstawione w niniejszej Rozprawie tworzą zatem spójny i całościowy obraz sprzężenia pomiędzy odkształceniem sieci krystalicznej, korelacjami elektronowymi oraz przemianą fazową Verweya w magnetycie. Umiarkowane naprężenie jednoosiowe modyfikuje globalną symetrię kryształu i wpływa na kolektywne uporządkowanie ładunkowo-orbitalne, nie zmieniając jednak lokalnej konfiguracji elektronowej. Opracowanie, skonstruowanie i skalibrowanie komórki jednoosiowego ciśnienia SOL dostarczyło platformę eksperymentalną do badania innych silnie skorelowanych układów, takich jak nadprzewodniki wysokotemperaturowe, materiały z falami gęstości ładunku czy układy ciężkofermionowe, w których kontrolowane łamanie symetrii może stanowić skuteczną metodę kształtowania nowych stanów kwantowych.

Słowa kluczowe: magnetyt, ciśnienie jednoosiowe, układy silnie skorelowane, promieniowanie synchrotronowe, mikroskopia rentgenowska ciemnego pola (DFXM), transport ładunkowy, podatność magnetyczna zmiennoprądowa

Abstract

The general objective of this Doctoral Dissertation, entitled *"Modification of quantum states in strongly correlated systems by applying uniaxial pressure"*, was to investigate how uniaxial stress, applied as a controlled symmetry-breaking perturbation of the crystal lattice, affects the structural, magnetic, and electronic properties of materials exhibiting strong electronic correlations. Uniaxial pressure has recently emerged as a powerful experimental tool that complements hydrostatic pressure, electric fields, and magnetic fields by enabling direction-selective tuning of lattice distortions without altering the chemical composition. While hydrostatic pressure uniformly shortens all interatomic distances, uniaxial pressure modifies only selected crystallographic directions, allowing one to probe and control the anisotropic balance between competing interactions such as electron–electron, electron–phonon, and magnetic couplings. This approach is particularly valuable in correlated systems where doping or substitution, such as carrier doping in oxides, inevitably introduces disorder, thereby obscuring intrinsic correlation effects.

A major technological challenge in studying (correlated) systems under uniaxial stress lies in achieving high mechanical precision and reliable quantitative calibration of the applied load. The few experiments performed so far have often lacked accurate pressure determination. Therefore, a key component of this Dissertation was the design, construction, and calibration of a compact uniaxial pressure cell (SOL), enabling quantitative, reproducible, and direction-selective compression. The developed cell operates as a screw-driven vise and is compatible with multiple measurement techniques, including X-ray diffraction (XRD), electrical resistivity, alternating current (AC) magnetic susceptibility, and X-ray absorption spectroscopy (XAS).

From the broad family of strongly correlated materials, stoichiometric magnetite (Fe_3O_4) was chosen as the model system because it combines long-range ferrimagnetic order with the Verwey transition at approximately $T_V \approx 123$ K, a coupled charge, orbital, and structural transition from cubic $Fd\bar{3}m$ to monoclinic Cc symmetry. Modifications of stoichiometry, substitutional doping, or hydrostatic pressure are known to suppress the Verwey temperature (T_V), whereas theoretical predictions and limited experimental data suggest that uniaxial compression can increase it. Thus, magnetite represents an ideal platform for studying how lattice symmetry breaking affects correlated electron states.

A series of synchrotron XRD experiments was performed at the ID11 beamline of the ESRF, with uniaxial compression applied along the $\langle 100 \rangle$ and $\langle 110 \rangle$ directions. The diffraction data revealed an anisotropic elastic response: compression along $\langle 100 \rangle$ induced a tetragonal distortion, while compression along $\langle 110 \rangle$ resulted in an orthorhombic deformation. By comparing the evolution of lattice parameters measured in the SOL cell with reference data obtained from a calibrated ADMET mechanical press, a quantitative calibration was established between screw rotation and applied stress.

The microstructure of two types of high-quality magnetite single crystals, one grown by the traveling-solvent floating-zone (TSFZ) method and the other using the skull-melter technique, was first examined using Dark-Field X-ray Microscopy (DFXM) at the ID03 beamline of the ESRF. The synthesis method was found to leave a distinct structural fingerprint. Crystals produced by the skull-melter method exhibited low average strain but pronounced mosaic textures originating from rapid quenching, whereas TSFZ-grown crystals showed higher axial strain yet fewer extended defects. Since such microstructural characteristics can significantly influence the material's response to external stress, the TSFZ-grown crystals were selected for the subsequent uniaxial compression experiments.

Because uniaxial stress induces directional lattice distortions, the remanent strain fields persisting after decompression were also investigated using DFXM. The imaging revealed that stresses exceeding approximately 150 MPa generate stable, line-like dislocation networks on the order of 10 micrometers in size, preferentially aligned with the {111} slip planes. Despite the presence of these extended dislocations and residual strain fields, AC magnetic susceptibility measurements showed that the Verwey transition temperature remained unchanged even in samples subjected to stresses above 300 MPa. This observation indicates that extended dislocation networks do not affect the cooperative charge and orbital ordering associated with the Verwey transition.

The calibrated SOL cell was then used to study *in situ* the evolution of electrical resistivity and magnetic susceptibility under uniaxial compression along ⟨100⟩ and ⟨110⟩. In both orientations, the Verwey temperature increased linearly with applied stress, indicating the stabilization of the low-temperature monoclinic phase. The effect was strongly anisotropic: the enhancement of T_V under ⟨110⟩ compression was nearly an order of magnitude larger than under ⟨100⟩. This difference reflects the distinct strain symmetries induced by compression, orthorhombic for ⟨110⟩ and tetragonal for ⟨100⟩, and the stronger coupling of the former to the charge and orbital ordering mechanisms driving the Verwey transition. At room temperature, resistivity decreased linearly with compression, consistent with strain-enhanced carrier mobility, again showing a threefold stronger effect along ⟨110⟩ than along ⟨100⟩.

Complementary Fe K-edge X-ray absorption spectroscopy (XAS) measurements at room temperature were carried out to probe possible stress-induced modifications of the local electronic and structural environment. Analysis of the pre-edge region (7105–7120 eV), sensitive to $3d$–$2p$ hybridization and inversion-symmetry breaking, revealed no measurable variations in peak position, width, or intensity up to about 200 MPa. This invariance demonstrates that uniaxial stress along ⟨100⟩ and ⟨110⟩ induces tetragonal and orthorhombic distortions of the cubic lattice without breaking the local inversion symmetry of the FeO_6 octahedra. Consequently, the local Fe–O coordination remains unaffected, while macroscopic properties such as T_V are shifted due to collective, symmetry-preserving distortions.

Taken together, the results presented in this Dissertation establish a comprehensive and self-consistent picture of the coupling between lattice strain, electronic correlations, and phase transitions in magnetite. Moderate uniaxial stress modifies the global symmetry of the crystal and tunes the collective charge-orbital order without altering the local electronic configuration. The successful design and calibration of the SOL uniaxial cell provides a quantitative experimental platform for probing other correlated electron systems, such as high-temperature superconductors, charge-density-wave materials, or heavy-fermion compounds, where controlled symmetry breaking may serve as a route to tailor emergent quantum states.

Keywords: magnetite, uniaxial stress, correlated systems, synchrotron radiation, dark-field X-ray microscopy, electronic transport, magnetic susceptibility

Zusammenfassung

Der allgemeine Zweck dieser Doktordissertation mit dem Titel *"Modifikation der Quantenzustände in stark korrelierten Systemen durch Anwendung von einachsigem Druck"* bestand darin zu untersuchen, wie einachsiger Druck, angewendet als kontrollierte Symmetriebrechung im Kristallgitter, die strukturellen, magnetischen und elektronischen Eigenschaften von Materialien mit starken Ladungskorrelationen beeinflusst. Einachsiger Druck hat sich in letzter Zeit als ein mächtiges Werkzeug erwiesen, das den hydrostatischen Druck sowie elektrische und magnetische Felder durch richtungsselektive Gitterstörungen ergänzt, ohne die chemische Zusammensetzung zu verändern. Während hydrostatischer Druck die interatomaren Abstände gleichmäßig verkürzt, modifiziert einachsiger Druck nur ausgewählte kristallographische Richtungen. Dadurch kann man das anisotrope Gleichgewicht zwischen Elektron–Elektron-, Elektron–Phonon- und magnetischen Kopplungen, die miteinander im Wettbewerb stehen, testen und kontrollieren. Dieser Ansatz ist insbesondere wertvoll für das Studium stark korrelierter Systeme, bei denen Dotier- oder Substitutionsatome, zum Beispiel bei der Ladungsträgerdotierung in Oxiden, unvermeidlich Unordnung einführen und spontane Korrelationseffekte stören.

Eine große ingenieurtechnische Herausforderung beim experimentellen Testen von (korrelierten) Systemen besteht darin, eine hohe mechanische Präzision sowie eine zuverlässige quantitative Kalibrierung der kompressiven Kraft zu erreichen. Einige bisher durchgeführte Experimente litten unter einer unzureichenden Kalibrierung des angewandten Drucks. Daher waren Konstruktion, mechanischer Aufbau und Kalibrierung einer kompakten einachsigen Druckkammer (SOL) die zentrale Leistung dieser Dissertation. Die SOL-Kammer ermöglicht eine quantitative, reproduzierbare und richtungsselektive Kompression. SOL arbeitet nach dem Schraubstockprinzip und ist mit einer Reihe von Festkörpermessmethoden kompatibel, darunter Röntgendiffraktion (XRD), elektrischer Widerstand, magnetische Wechselstromsuszeptibilität und Röntgenabsorptionsspektroskopie (XAS).

Unter mehreren korrelierten Materialien wurde stöchiometrischer Magnetit Fe_3O_4 aufgrund seiner ausgeprägten ferrimagnetischen Ordnung sowie der Verwey-Verwandlung bei $T_V \approx 123$ K als Modellsystem ausgewählt. Die Verwey-Verwandlung koppelt die Ladungs-, Orbital- und strukturelle Transformation von der kubischen $Fd\overline{3}m$ in die monokline Cc Symmetrie. Änderungen der Stöchiometrie, die Einführung externer Atome oder die Anwendung von hydrostatischem Druck sind bekannte Faktoren, die die Verwey-Temperatur (T_V) absenken. Gleichzeitig legen theoretische Vorhersagen und die begrenzten experimentellen Ergebnisse nahe, dass einachsiger Druck T_V erhöhen kann. In diesem Sinne stellt Magnetit eine ideale Plattform dar, um zu untersuchen, wie derartige Gitter-Symmetriebrüche die korrelierten Elektronenzustände beeinflussen.

Ein Teil der Synchrotron-Diffraktionsexperimente wurde an der Strahlführung ID11 des Europäischen Synchrotronstrahlungszentrums (ESRF) durchgeführt. Während dieser Experimente

wurde der einachsige Druck entlang der ⟨100⟩- und ⟨110⟩-Richtungen angelegt. Die Röntgendiffraktionsmessungen zeigten eine anisotrope elastische Reaktion. Wie es sich herausstellt, regte die Kompression in der ⟨100⟩-Richtung eine tetragonale Verzerrung an, wohingegen die Kompression entlang ⟨110⟩ eine orthorhombische Deformation hervorrief. Durch den Vergleich der in der SOL-Kammer gemessenen Entwicklung der Gitterparameter mit den Daten, die mithilfe einer kommerziellen mechanischen ADMET-Presse gewonnen wurden, konnte eine quantitative Kalibrierung zwischen der Drehung des Schraubenkopfs und dem erzeugten Druck hergestellt werden.

Die Mikrostruktur zweier Arten von Magnetit-Einkristallen hoher Qualität wurde mittels Röntgen-Dunkelfeldmikroskopie (DFXM) an der ID03-Strahlführung des ESRF untersucht. Ein Kristall wurde mithilfe des Kalttiegelverfahrens (Schädelschmelzverfahren) hergestellt, der andere mittels zonenrandstabilisierter Schmelzzüchtung (TSFZ). Es wurde nachgewiesen, dass die Synthesemethode einen deutlichen Einfluss auf die resultierende Struktur hat. Die im Kalttiegelverfahren gezüchteten Kristalle wiesen eine geringere durchschnittliche einachsige Verformung, jedoch eine stärkere mosaikartige Textur infolge der spontanen Abkühlung auf. Hingegen zeichneten sich die mittels Zonenschmelze gezüchteten Kristalle durch höhere einachsige Verformung und einzelne ausgeprägte Defekte aus. Da solche mikrostrukturellen Eigenschaften die materielle Reaktion auf externen Druck wesentlich beeinflussen können, wurden die zonengeschmolzenen Kristalle für die nachfolgenden Kompressionsexperimente ausgewählt.

Da einachsiger Druck gerichtete Gitterstörungen hervorruft, wurden die nach der Dekompression verbleibenden Deformationsfelder ebenfalls mit DFXM untersucht. Die DFXM-Aufnahmen zeigten, dass Kompressionswerte über 150 MPa stabile Liniendislokationen erzeugen. Dieses Dislokationsfeld ist durch eine Ausdehnung von etwa 10 μm sowie eine bevorzugte Orientierung entlang der 111-Gleitebenen gekennzeichnet. Trotz der Anwesenheit dieser ausgedehnten Versetzungen und verbleibenden Deformationen bestätigten Messungen der magnetischen Wechselstromsuszeptibilität, dass die Verwey-Temperatur intakt blieb, selbst in Proben, die mit Drücken über 300 MPa belastet wurden. Diese Beobachtung zeigt, dass die ausgedehnten Versetzungsfelder die Kopplung zwischen Ladungs- und Orbitalordnungen, die eng mit der Verwey-Umwandlung verbunden sind, nicht beeinträchtigen.

Die kalibrierte SOL-Kammer wurde anschließend verwendet, um die *in situ*-Abhängigkeit des elektrischen Widerstands und der magnetischen Suszeptibilität von der einachsigen Kompression entlang ⟨100⟩ und ⟨110⟩ zu untersuchen. Für beide Orientierungen verhielt sich die bestimmte Verwey-Temperatur linear zum angelegten Druck. Dieses Verhalten deutete darauf hin, dass die einachsige Kompression die niedertemperaturige monokline Phase stabilisierte. Dieser Effekt war stark anisotrop: die Erhöhung von T_V unter Kompression entlang ⟨110⟩ war nahezu eine Größenordnung stärker als unter ⟨100⟩. Dieser Unterschied spiegelt die unterschiedlichen Verformungssymmetrien wider, orthorhombisch für ⟨110⟩ (stärker mit den Mechanismen verknüpft, die die Verwey-Umwandlung steuern) und tetragonal für ⟨100⟩, die durch die Kompression in-

duziert wurden. Bei Raumtemperatur verringerte sich der elektrische Widerstand linear mit zunehmender Kompression. Diese Beobachtung ist konsistent mit einer druckinduzierten Erhöhung der Ladungsträgermobilität. Wiederum wurde der etwa dreifach stärkere Effekt der Kompression entlang ⟨110⟩ im Vergleich zu ⟨100⟩ bestätigt.

Komplementäre Eisen-*K-Linie*-Röntgenabsorptionsspektroskopie-Messungen (XAS) wurden bei Raumtemperatur durchgeführt, um potenzielle druckgetriebene Modifikationen der lokalen elektronischen und strukturellen Umgebung zu untersuchen. Die Analyse der Vorlinienregion (7105–7120 eV), die empfindlich auf die $3d$–$2p$-Hybridisierung und auf Inversionssymmetriebrüche reagiert, zeigte bis zu einer Kompression von 200 MPa keine wesentlichen Änderungen in der Position, Breite oder Intensität der K_α Spitze. Diese Unveränderlichkeit zeigt, dass einachsiger Druck entlang ⟨100⟩ und ⟨110⟩ tetragonale bzw. orthorhombische Verzerrungen im kubischen Gitter verursacht, ohne die lokale Inversionssymmetrie in den FeO_6-Oktaedern zu brechen. Folglich bleiben die lokalen Fe–O-Koordinationsumgebungen erhalten, während makroskopische Eigenschaften wie T_V durch kollektive, symmetrieerhaltende Verzerrungen verschoben werden.

Insgesamt fordern die in dieser Dissertation präsentierten Ergebnisse das bisherige, umfassende und selbstkonsistente Bild der Kopplung zwischen Gitterverformungen, elektronischen Korrelationen und dem Verwey-Phasenübergang in Magnetit heraus. Moderater einachsiger Druck modifiziert die globale Symmetrie des Kristalls und stellt die kollektive Ladungs-Orbital-Ordnung ein, ohne die lokale Elektronenkonfiguration zu verändern. Der erfolgreiche Entwurf und die Kalibrierung der einachsigen SOL-Kammer liefern eine quantitative experimentelle Plattform für das Studium weiterer Elektronensysteme, wie Hochtemperatursupraleiter, Ladungsdichtewellenmaterialien oder Schwermetall-Fermion-Verbindungen, bei denen kontrollierter Symmetriebruch als Werkzeug zur Untersuchung emergenter Quantenzustände dienen kann.

Schlüsselwörter: Magnetit, einachsiger Druck, korrelierte Systeme, Synchrotronstrahlung, Röntgen Dunkelfeldmikroskopie, elektrischer Transport, magnetische Suszeptibilität

Acknowledgments

The work was supported by the National Science Centre, Poland, Grant No. OPUS: UMO-2021/41/B/ST3/03454, the Polish National Agency for Academic Exchange under "Polish Returns 2019" Programme: PPN/PPO/2019/1/00014, and the subsidy of the Ministry of Science and Higher Education of Poland.

The work at the TU Wien was supported by FWF Project P 35945-N.

This research was also partly supported by the program "Excellence Initiative–Research University" (Projects No. 2773, No. 7887, and No. 6387) for the AGH University of Krakow.

Contents

Chapter 1.

Introduction

This Chapter is devoted to establishing the theoretical framework necessary to understand the basics of strongly correlated systems studied in this project and to justify the use of uniaxial stress as a precise and symmetry-breaking tool for fine-tuning the interplay between electronic, magnetic, and structural degrees of freedom in magnetite.

Section 1.1 outlines the theoretical framework of strongly correlated electron systems, focusing on the Hubbard model and the role of electron-electron interactions as the key mechanism driving correlated behavior. It highlights how the balance between kinetic energy and on-site Coulomb repulsion determines whether a system is metallic or insulating, and how this balance can be tuned by temperature, doping, or external stress. Among transition-metal oxides, *magnetite* (Fe_3O_4) stands out as one of the most extensively studied correlated materials. Its characteristic Verwey transition, a coupled charge, orbital, and structural transformation, illustrates the intimate interplay between electronic and lattice degrees of freedom. Section 1.2 discusses in detail the structure and electronic properties of magnetite, the mechanism of the Verwey transition, and the effects of stoichiometry, chemical substitution, hydrostatic pressure, and uniaxial stress.

The research presented in this Dissertation had two main objectives: (*i*) to design and construct a custom uniaxial pressure apparatus capable of applying controlled, quantifiable stress to single crystals during complementary measurements such as resistivity, magnetization, and X-ray diffraction; and (*ii*) to experimentally investigate how uniaxial stress influences the strong electronic correlations in magnetite, with particular emphasis on how symmetry breaking and lattice anisotropy modify the Verwey transition and the associated magnetic and transport properties. The detailed aims of the project are outlined in Section 1.3, while the overall structure of the Dissertation is summarized in Section 1.4.

1.1. Strongly correlated systems

The band theory of solids, developed nearly a century ago [1], provides a fundamental framework for describing the electronic and transport properties of crystalline materials. It assumes that electrons move almost independently through a periodic potential formed by the regularly arranged atomic cores. In this approximation, the overlap of atomic orbitals gives rise to continuous energy bands separated by forbidden gaps. Depending on whether the electronic bands are completely or partially filled, the material exhibits insulating or metallic behavior, respectively. Within this independent-electron picture, often referred to as the one-electron or mean-field approximation, the essential features of electrical conductivity can be captured without explicitly accounting for electron–electron interactions.

Electrons in solids are indistinguishable fermions that obey the Pauli exclusion principle, and their individual kinetic energies collectively define the Fermi energy, E_F. At the same time, they experience mutual Coulomb repulsion, giving rise to an interaction energy that can be comparable in magnitude to their kinetic energy. In a weakly interacting system, this Coulomb term does not destroy the overall band picture but instead renormalizes the electronic states into long-lived quasiparticles; excitations described within the framework of Fermi liquid theory. These quasiparticles retain the quantum numbers of free electrons but have an effective mass and lifetime determined by many-body interactions. Within this approximation, the motion of electrons through a periodic lattice potential remains well described by Bloch's theorem, where each quasiparticle state in a given energy band is characterized by a crystal momentum $\mathbf{k}$.

The reciprocal space, which encompasses all possible wave vectors $\mathbf{k}$, together with the corresponding energy dispersion relation $E(\mathbf{k})$, fully characterizes the allowed electronic states and their dynamics in a crystalline solid. This formalism, based on the independent-electron approximation, successfully describes a wide range of materials, including those with recently discovered topological electronic states. However, the one-electron picture fails when electron–electron interactions become comparable to or exceed the kinetic energy scale set by the Fermi energy, E_F. In such cases, correlations between electrons qualitatively alter the ground state of the system. For instance, nickel oxide (NiO), which according to band theory should be metallic due to its partially filled $3d$ band, is experimentally found to be a robust insulator [2]. Similarly, chromium-doped vanadium oxide ($V_2{-}xCr_xO_3$) exhibits a re-entrant metal–insulator transition (MIT) that cannot be explained without accounting for strong Coulomb interactions [3]. These examples demonstrate that to correctly describe the physics of such systems, the electron–electron interaction energy must be treated on an equal footing with the kinetic term.

The simplest model that explicitly incorporates electron–electron correlations is the Hubbard model. Its Hamiltonian, expressed in the language of second quantization, takes the form

$$\hat{H} = -t \sum_{i,\sigma} \left(\hat{c}^{\dagger}_{i,\sigma} \hat{c}_{i+1,\sigma} + \hat{c}^{\dagger}_{i+1,\sigma} \hat{c}_{i,\sigma} \right) + U \sum_{i} \hat{n}_{i,\uparrow} \hat{n}_{i,\downarrow}, \tag{1.1.1}$$

where:

- $\hat{c}^{\dagger}_{i,\sigma}$ and $\hat{c}_{i,\sigma}$ are the creation and annihilation operators, respectively, for an electron with spin σ at site i;
- $\hat{n}_{i,\sigma} = \hat{c}^{\dagger}_{i,\sigma} \hat{c}_{i,\sigma}$ is the number operator that counts the occupation of site i by an electron of spin σ;
- t is the hopping integral describing the kinetic energy associated with the motion of an electron between neighboring sites;
- U denotes the on-site Coulomb repulsion energy between two electrons of opposite spin occupying the same atomic site.

The Hubbard Hamiltonian captures the fundamental competition between the kinetic energy that favors electron delocalization and the Coulomb repulsion that promotes localization. The first term in Eq. 1.1.1, proportional to t, represents the hopping of electrons between neighboring lattice sites and therefore tends to form extended Bloch states characteristic of metallic behavior. In contrast, the second term, proportional to U, penalizes the simultaneous occupation of the same site by two electrons, leading to charge localization and insulating behavior when U dominates. The ratio U/t thus determines the electronic ground state of the system: for $U \ll t$, electrons are itinerant and the material behaves as a conventional metal, while for $U \gg t$, the system becomes a Mott insulator with one localized electron per site. The transition between these two regimes, known as the Mott–Hubbard transition, is one of the central problems in correlated electron physics.

As schematically illustrated in Fig. 1.1, only double occupancy of a lattice site incurs an interaction energy U, while electrons on different sites do not interact. In the limit of vanishing interaction ($U = 0$), the hopping integral t dominates, producing a half-filled d-band in which renormalized electrons move freely through the lattice, as shown on the left in Fig. 1.1b. However, when the Coulomb interaction becomes comparable to or larger than the kinetic energy, double occupancy of a single site is suppressed. This leads to a splitting of the metallic band into the lower and upper Hubbard subbands, depicted on the right of Fig. 1.1b. The emergence of this correlation-induced energy gap marks the crossover from metallic to insulating behavior.

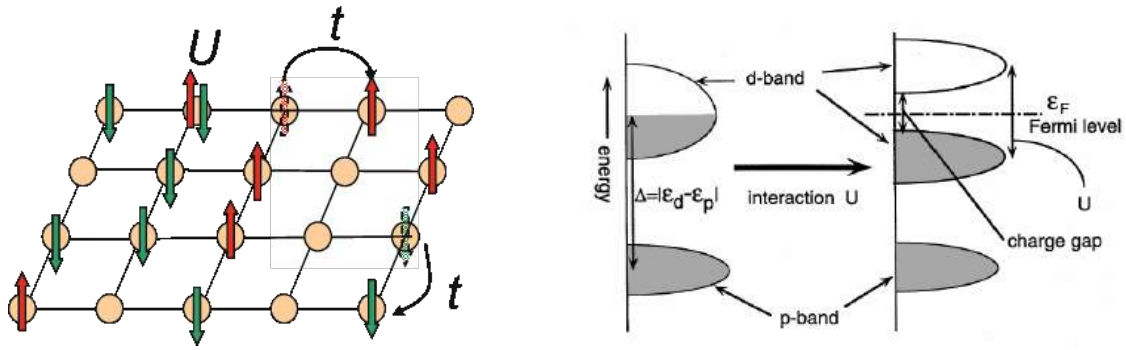

(a) (b)

Fig. 1.1. (a) Schematic representation of the on-site Coulomb repulsion U and electron hopping parameter t in a two-dimensional lattice, as described by Eq. 1.1.1 [4]. **(b)** When $U = 0$, one electron per site results in a half-filled metallic band (left). As the electron–electron interaction U becomes comparable to or larger than the hopping integral t, charge localization occurs, the band splits into two subbands, and a charge gap opens—driving the system into an insulating state (right) [5].

Strongly correlated materials are governed by the delicate balance between several competing interactions; most notably electron–electron, electron–phonon, and magnetic couplings. These interactions often act on comparable energy scales, giving rise to emergent phases such as unconventional superconductivity, charge and orbital ordering, or metal-insulator transitions (MITs). Understanding how these interactions compete and cooperate is essential for describing the complex behavior of systems such as high-T_c cuprates, strontium ruthenates, and transition-metal oxides (TMOs) like magnetite, which serve as canonical examples of correlated electron systems. Each of these materials exhibits characteristic phase transitions that can be tuned by external stimuli, including temperature, chemical doping, and, most relevant to this work, mechanical stress.

The response of a correlated-electron system to external pressure, whether hydrostatic or uniaxial, directly reflects the strength and anisotropy of the underlying electronic interactions. Pressure modifies interatomic distances and orbital overlap, thereby altering the effective hopping integral t, the exchange coupling, and the balance between kinetic and potential energies that governs the electronic ground state. In the Hubbard model, discussed above, pressure effectively tunes the ratio U/t. In this sense, stress acts as a powerful tuning parameter that can either enhance or suppress electronic correlations, depending on the symmetry and direction of the applied deformation. Because electronic ordering in correlated oxides is strongly coupled to the lattice, even modest strains can drive dramatic changes in physical properties ranging from superconducting critical temperatures to metal–insulator transition points.

Historically, the role of the lattice in correlated phenomena was debated, even by Sir Nevill Mott, who questioned whether structural changes were a cause or consequence of electronic localization. Modern experimental and theoretical studies, however, have established that the lattice degrees

of freedom are deeply intertwined with charge and spin correlations. This coupling becomes especially pronounced near critical points, such as the onset of superconductivity or the spin- and/or orbital-ordering transitions, where even small perturbations can shift the balance between competing electronic phases [6].

Among correlated systems, magnetite (Fe_3O_4) offers a particularly insightful platform for exploring how symmetry-breaking mechanical stimuli affect collective electronic order. Its Verwey transition si a coupled charge, orbital, and structural transformation which provides a sensitive probe of the interplay between lattice strain and electronic correlations. As will be discussed in the following Sections, while the effects of hydrostatic pressure on this transition have been extensively studied, the influence of uniaxial stress remains largely unexplored. Addressing this gap forms the central motivation of this Dissertation, which aims to elucidate how direction-dependent lattice distortions modify the electronic, magnetic, and structural properties of stoichiometric magnetite.

1.2. Magnetite: general information

Magnetite (Fe_3O_4) is the oldest known magnetic mineral, discovered nearly 4000 years ago in the region of present-day Türkiye by a shepherd named Magnes. In nature, high-purity magnetite occurs in association with igneous and metamorphic rocks, typically forming octahedral or cubic crystals with a characteristic metallic gray to black luster.

Since a magnetized needle aligns with the Earth's magnetic field, magnetite was used in the earliest compasses and played a pivotal role in enabling global navigation and exploration. Remarkably, magnetite crystals have also been identified in the beaks and brains of migratory birds, providing physical evidence for their internal magnetic navigation systems, which allow for precise long-distance orientation [7].

Beyond its geological and historical significance, magnetite has become a material of technological and scientific importance. Owing to its spin-polarized charge transport, it is considered a promising candidate for spintronic applications [8]. Moreover, it can act as an ultra-fast electronic switch: laser excitation can drive magnetite within femtoseconds from its low-temperature insulating phase ($T < T_V = 124$ K) to a high-temperature semi-metallic phase [9]. This remarkable transformation, known as the Verwey transition, is named after Evert Verwey (1905–1981), the Dutch physicist and chemist who first described it and devoted much of his career to understanding its microscopic origin.

Accordingly, a substantial portion of this theoretical introduction is devoted to a detailed discussion of the Verwey transition (VT), including its physical nature and the ways in which it is influenced by chemical composition and external pressure.

Because magnetite is abundant in nature, it was initially studied primarily by geologists interested in understanding how extreme conditions, such as those prevailing deep within the Earth's interior, affect rock formation and mineral stability. However, it soon became evident that magnetite also possesses remarkable physical properties that extend far beyond geology.

The first quantitative study of magnetic susceptibility in magnetite, performed using liquefied air as a coolant, was carried out in 1913 at ETH Zürich by Karl Renger, a doctoral student of Pierre Weiss and Albert Einstein [10]. A decade later, in 1924, the first magnetostriction measurements were reported on magnetite samples of geological origin, although their precise stoichiometry was not yet recognized [11].

Systematic investigations of the electrical and magnetic behavior of natural magnetite began in the late 1930s, culminating in Verwey's pioneering studies between 1939 and 1950, which established the foundation for understanding its phase transition and transport properties [12, 13].

In the following decades, particularly throughout the 1960s and 1970s, significant research efforts focused on exploring the effects of high hydrostatic pressure, comparable to those in the Earth's core, on various iron oxides and magnetic ores, including magnetite [14, 15, 16]. At that time, however, the crucial role of stoichiometry in determining the magnetic and transport properties of magnetite was not yet fully appreciated, largely because reliable methods for growing single crystals with controlled composition were still under development.

The following Sections of this Chapter provide a comprehensive discussion of the fundamental properties of magnetite, beginning with its crystal structure, magnetic behavior, and charge transport characteristics. Particular emphasis is placed on the Verwey phase transition, which has been the subject of intensive investigation for more than a century. Despite this extensive research, its microscopic mechanism remains an open question. Finally, the Chapter outlines the current understanding of how hydrostatic and uniaxial pressure influence the Verwey transition in magnetite, forming the conceptual foundation for the experimental studies presented in this Dissertation.

1.2.1. Crystallographic structure

Under ambient conditions, magnetite is a ferrimagnetic material with an inverse spinel structure, belonging to the cubic space group $Fd\bar{3}m$. In ferrimagnets, the magnetic moments of the two magnetic sublattices are aligned antiparallel but have unequal magnitudes, resulting in a nonzero net magnetization that is smaller than that of a typical ferromagnet. The crystal structure of magnetite corresponds to a face-centered cubic (fcc) lattice with equal lattice parameters $a_C = b_C = c_C \equiv a$, typically ranging between 8.39 and 8.41 Å (see Fig. 1.2a) [17, 18, 19].

As depicted in Fig. 1.2b, two types of oxygen coordination sites are distinguished in the face-centered cubic lattice of magnetite: tetrahedral (A) and octahedral (B) sites. The interstitial A sites are occupied exclusively by Fe^{3+} cations, each surrounded by four O^{2-} anions. In contrast, the B sites are equally populated by Fe^{2+} and Fe^{3+} cations, each coordinated by six O^{2-} anions. Accordingly, the ideal spinel structure of magnetite can be expressed by the chemical formula $[Fe^{3+}]_{(A)}[Fe^{2+}Fe^{3+}]_{(B)}O_4$.

This atomic arrangement can be understood in terms of the Crystal Field Stabilization Energy (CFSE) [18, 20]. The CFSE, determined by the electronic configuration of a given ion, is higher for the Fe^{2+} cation in the high-spin $3d^6$ state than for the Fe^{3+} cation in the high-spin $3d^5$ configuration, for which CFSE $= 0$. Consequently, the Fe^{3+} cations preferentially occupy the energetically more favorable tetrahedral (A) sites, each coordinated by four O^{2-} anions. In contrast, the remaining Fe^{3+} and Fe^{2+} cations compete for the energetically less favorable octahedral (B) sites, where each iron ion is surrounded by six O^{2-} anions.

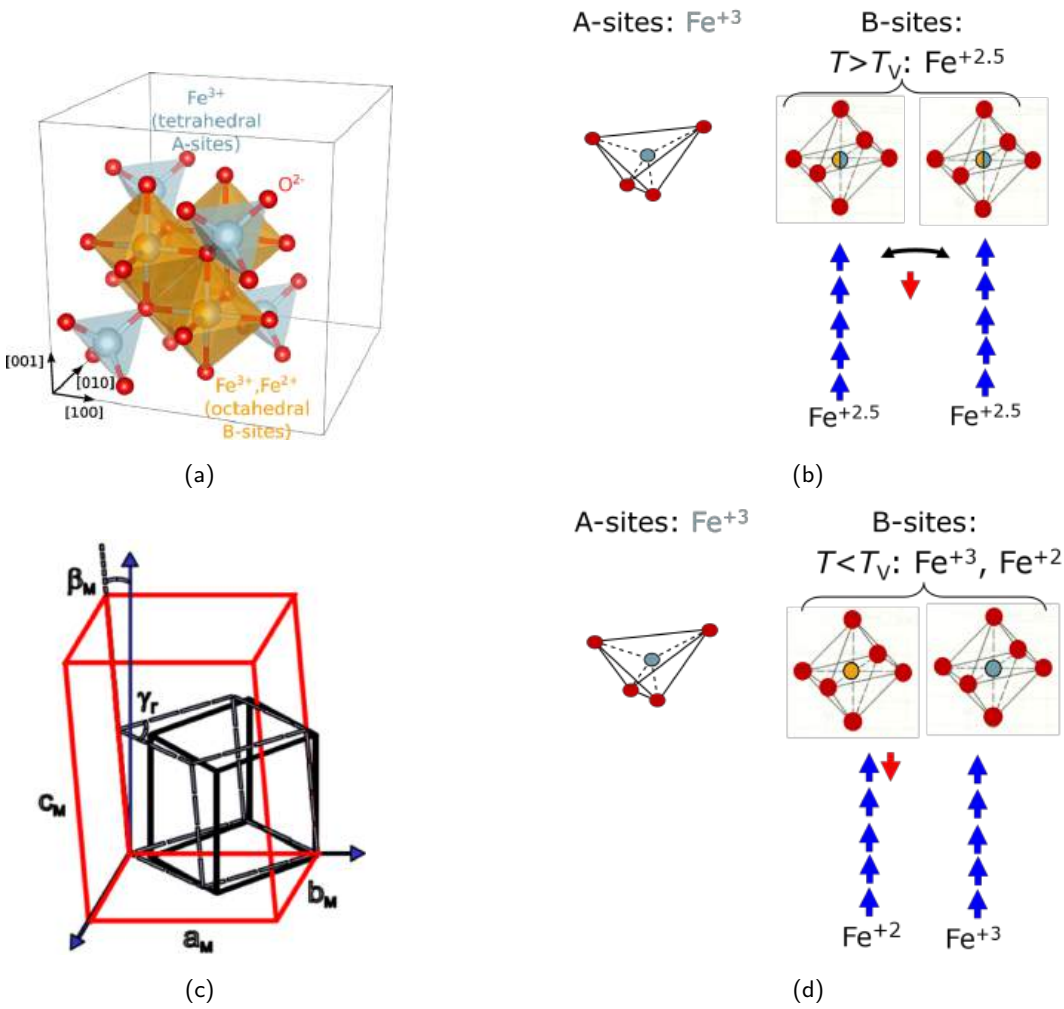

Fig. 1.2. Schematic representation of the Verwey model describing the interplay between crystal symmetry, charge order, and electron dynamics across T_V. **(a)** Crystal structure of magnetite in the high-temperature cubic phase with $Fd\bar{3}m$ symmetry. Oxygen coordination sites are marked in **gray** for tetrahedral A sites and in **orange** for octahedral B sites, respectively. The A and B sites form a face-centered cubic (fcc) lattice. The schematic of the unit cell is adapted from [21]. **(b)** Schematic representation of electron hopping between adjacent octahedral B sites above T_V. At $T > T_V$, the A sites are occupied by trivalent Fe^{3+} cations, while the B sites host Fe cations with an average valence of $+2.5$, resulting from rapid electron hopping between Fe^{2+} and Fe^{3+} states. **(c)** Magnetite crystal structure in the low-temperature monoclinic phase (Cc symmetry), superimposed on the high-temperature cubic cell. The **black** and **gray** frameworks correspond to the cubic $Fd\bar{3}m$ symmetry, while the **red** framework represents the monoclinic Cc phase. a_M, b_M, and c_M denote the monoclinic lattice constants, with $\beta_M \approx 0.2°$ describing the deviation of c_M from the vertical c axis in cubic notation. **(d)** Below the Verwey transition ($T < T_V$), electron hopping ceases, and charge ordering occurs on the B sites, leading to the formation of distinct Fe^{2+} and Fe^{3+} cations.

X-ray diffraction studies have revealed that, at low temperatures, the crystal structure of magnetite adopts a monoclinic symmetry described by the space group Cc. This structural transition involves small relative atomic displacements on the order of 0.1 Å with respect to the high-temperature cubic lattice [17]. In addition, the temperature-induced reorganization of atoms within the magnetite lattice gives rise to a rhombohedral distortion occurring in the $\{\bar{1}\,1\,\bar{1}\}$ plane of the monoclinic unit cell. This distortion causes the c_M axis to tilt by approximately $\beta_M \approx 0.2^\circ$ from the vertical direction, toward the $-a_M$ axis [22]. As a result, the monoclinic basis vectors a_M, b_M, and c_M are nearly aligned with the [1$\bar{1}$0], [110], and [001] directions of the cubic setting, as illustrated in Fig. 1.2.

Cubic, $Fd\bar{3}m \rightarrow$	$\rightarrow$ **Monoclinic,** Cc
a_C, b_C, c_C	a_M, b_M, c_M
[1 0 0]	[1 1 0]
[0 1 0]	[1 $\bar{1}$ 0]
[0 0 1]	[0 0 2]

Tab. 1.1. Transformation of crystallographic directions between the cubic ($Fd\bar{3}m$) and monoclinic (Cc) unit cells of magnetite. The lattice constants in the cubic setting are denoted as a_C, b_C, and c_C, while those in the monoclinic setting are represented by a_M, b_M, and c_M, respectively.

Denoting the axis length of the cubic unit cell as a, the corresponding monoclinic unit cell can be expressed with dimensions $\sqrt{2}a \times \sqrt{2}a \times 2a$, as illustrated in Fig. 1.2c. The precise correspondence between the crystallographic directions in the cubic and monoclinic symmetries is summarized in Table 1.1.

1.2.2. Verwey phase transition

As discussed in the previous Section, magnetite undergoes a structural phase transition at $T_V = 124$ K, transforming from the high-temperature cubic phase with $Fd\bar{3}m$ symmetry to the low-temperature monoclinic phase with Cc symmetry. This reduction in lattice symmetry is accompanied by pronounced anomalies in both the magnetic and electrical properties of magnetite at $T = T_V$, as illustrated in Fig. 1.3.

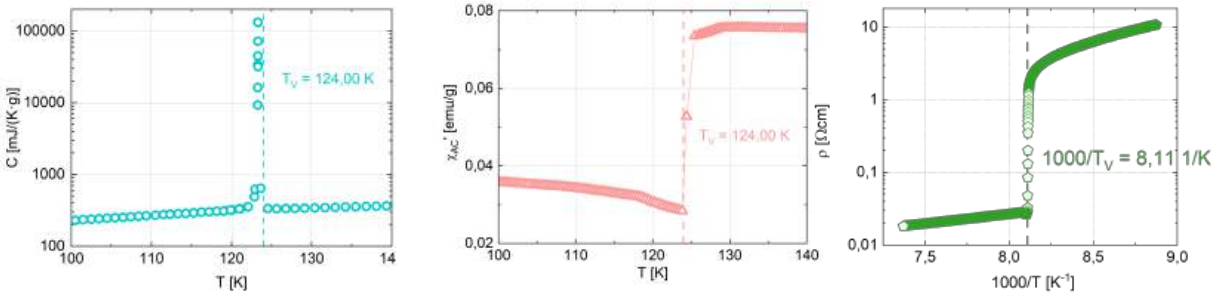

(a) (b) (c)

Fig. 1.3. Experimental signatures of the Verwey transition (VT) in stoichiometric magnetite. In each panel, the transition temperature T_V is indicated by a vertical dashed line. **(a)** Temperature dependence of the specific heat $C(T)$. The sharp discontinuity in $C(T)$ demonstrates the release of latent heat associated with the structural and electronic reorganization of the lattice, confirming the first-order nature of the transition. **(b)** Temperature dependence of the AC magnetic susceptibility $\chi_{\mathrm{AC}}(T)$. The abrupt change in χ_{AC} at $T = T_V$ reflects the magnetic response to the Verwey transition. **(c)** Electrical resistivity ρ plotted as a function of inverse temperature, $\log\{\rho(1000/T)\}$. At $T = T_V$, ρ increases abruptly by nearly two orders of magnitude, marking the transition from a semi-metallic to an insulating state.

The temperature dependence of the specific heat shown in Fig. 1.3a exhibits a sharp discontinuity at $T = T_V$, corresponding to the release of latent heat. The singular character of $C(T)$ provides clear evidence that the Verwey transition is a first-order phase transformation. The release of latent heat is accompanied by a change in the motion of magnetic domain walls, which accounts for the step-like feature observed in the alternating current (AC) magnetic susceptibility $\chi_{\mathrm{AC}}(T)$ presented in Fig. 1.3b [23].

Figure 1.3c displays the temperature dependence of the electrical resistivity $\rho(T)$, which increases abruptly by nearly two orders of magnitude at $T = T_V$. As discussed in the previous Section, the high-temperature phase of magnetite can be regarded as a disordered electron system composed of trivalent Fe^{3+} ion cores and highly correlated charges resonating between adjacent octahedral (B) sites, effectively corresponding to mixed-valence Fe^{2+}/Fe^{3+} states. Consequently, magnetite exhibits relatively low electrical resistivity at room temperature, $\rho \approx 5 \times 10^{-3}\ \Omega\mathrm{cm}$. Upon cooling to T_V and below, these mobile electrons localize on specific octahedral (B) sites, resulting in a reduction of carrier mobility and the onset of insulating behavior characteristic of the low-temperature phase [24].

As originally proposed by Verwey and later supported by the "Anderson criterion" [25], strong electron–electron Coulomb interactions constitute the fundamental mechanism underlying the phase transitions in magnetite and related spinel compounds. Similar behavior has been observed, for example, in the pressure-induced transition of $NiFe_2O_4$ [26]. Owing to its conceptual simplicity and its ability to explain many key properties of magnetite, the Verwey model remained widely accepted for decades. One notable success of this ionic framework was the correct prediction of the total magnetic moment per formula unit of Fe_3O_4, $M = 4.06\ \mu_B$ [27]. Nevertheless, to achieve a more complete understanding of magnetite across the full temperature range, the original Verwey model had to be extended to include the coupling between electronic charge and the crystal lattice, as revealed by subsequent theoretical and experimental studies.

The crucial role of electron–phonon coupling in the mechanism of the Verwey transition was first indicated by neutron scattering experiments [28, 29]. These studies revealed critical quasi-elastic scattering above T_V at reciprocal lattice vectors Q corresponding to the Bragg reflections observed below the transition temperature. In addition, intense diffuse scattering was detected for Q vectors incommensurate with the low-temperature structure, persisting up to approximately 80 K above T_V (see Fig. 1.4a).

Subsequent density functional theory (DFT) calculations by Piekarz and co-workers demonstrated that electron–phonon coupling contributes to the Verwey transition with a significance comparable to that of electron–electron interactions [30, 31, 32, 33]. As shown in Fig. 1.4b, these theoretical studies predicted a pronounced hardening of selected phonon modes throughout the Brillouin zone as the system enters the low-temperature phase.

This lattice stiffening predicted by theory was later confirmed experimentally. Acoustic spectroscopy measurements revealed a clear increase in the elastic shear modulus c_{44} across the Verwey transition, both in stoichiometric magnetite under hydrostatic pressure and in Zn-doped single crystals (see Fig. 1.4c) [34]. These observations collectively confirm that the Verwey transition arises from a cooperative interplay between strong electronic correlations and pronounced electron–phonon coupling.

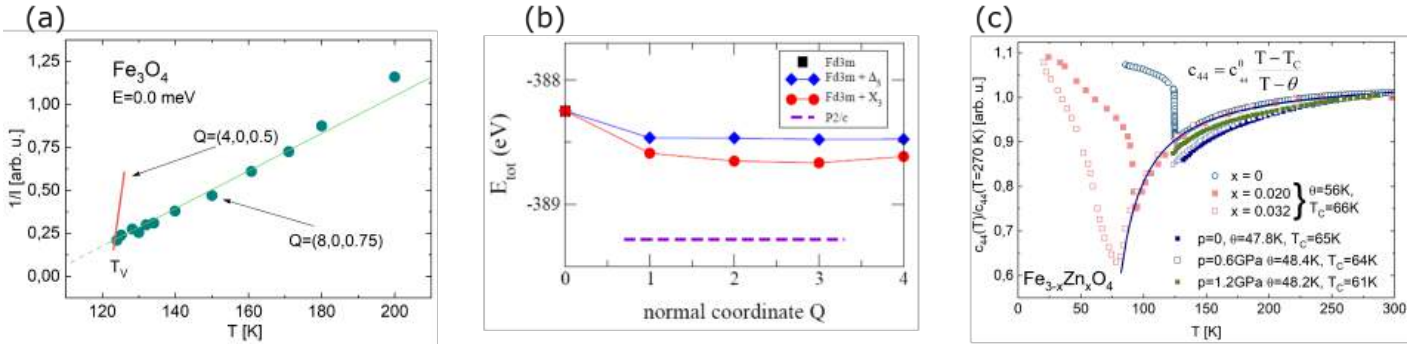

Fig. 1.4. Experimental and theoretical evidence for the involvement of electron–phonon coupling in the Verwey transition of magnetite. **(a)** Temperature dependence of the inverse intensity of the critical diffuse scattering in Fe_3O_4 for two representative reciprocal lattice vectors Q, corresponding to the quasi-elastic component ($E = 0$ meV). The divergence of the diffuse scattering intensity near T_V indicates the onset of a structural instability driven by phonon softening [29]. **(b)** DFT-calculated total energy as a function of the normal coordinate Q for the X_3 and Δ_5 phonon modes, showing an energy gain associated with their condensation below T_V [30]. **(c)** Temperature dependence of the elastic shear modulus c_{44} in stoichiometric magnetite at ambient pressure [35, 36] and in $Fe_{3-x}Zn_xO_4$ single crystals under hydrostatic pressures up to 1.2 GPa [34]. The deviation of $c_{44}(T)$ from its high-temperature value reflects lattice stiffening across the Verwey transition, consistent with enhanced electron–phonon coupling.

Experimental studies combining neutron scattering [28, 29], measurements of elastic constants [34, 35], and diffuse X-ray scattering [37] have established that strong electron–phonon coupling plays a central role in the Verwey transition. These results collectively suggest the coexistence of at least two coupled mechanisms driving the transition. The first of them is active already at room temperature and plausibly extends up to the Néel temperature, T_N, indicating that short-range lattice and charge fluctuations persist far above T_V [38, 39]. The second mechanism appears to be triggered only a few kelvins above T_V, manifesting as the condensation of specific phonon modes and the onset of charge and orbital ordering.

The mutual interplay between these two instabilities has recently been discussed as a key ingredient in the onset of the Verwey transition: one associated with dynamic electron-phonon correlations and the other with a symmetry-lowering lattice distortion [40]. Understanding this interplay requires detailed insight into the octahedral (B) sublattice of magnetite, where mixed-valence Fe^{2+} and Fe^{3+} ions reside. The low-temperature symmetry of magnetite was first identified as monoclinic (Cc) by Iizumi *et al.* using neutron diffraction in 1982 [41]. However, the precise charge and orbital ordering pattern within the B-sublattice was only resolved three decades later by Senn, Wright, and co-workers using high-resolution X-ray diffraction under an applied magnetic field [17].

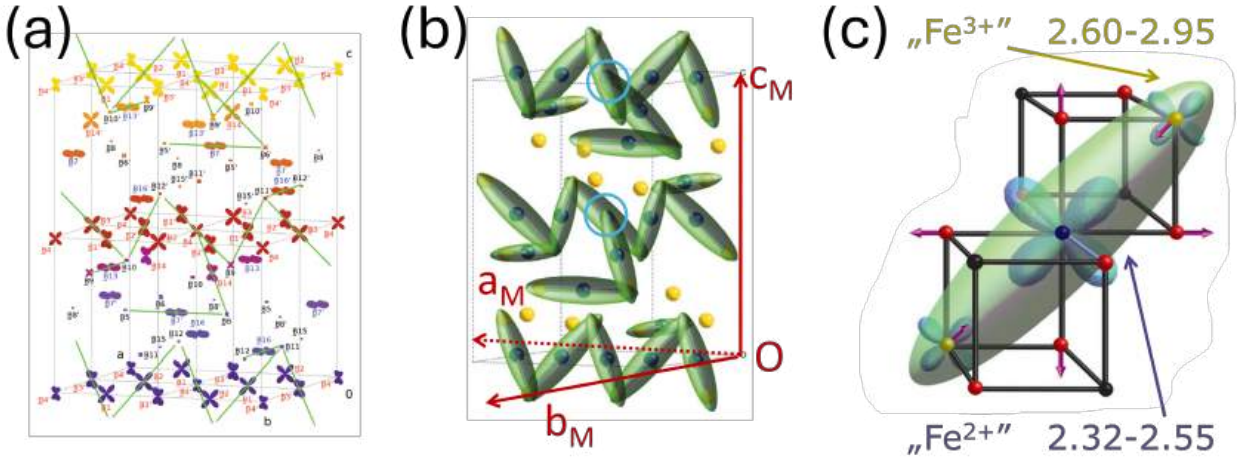

Fig. 1.5. Low-temperature charge and orbital ordering pattern in magnetite proposed by Senn and Wright *et al.* (2012) [17]. **(a)** Refined atomic structure of magnetite in the monoclinic Cc phase below T_V, showing the minority-spin t_{2g} electron density associated with the octahedral (B) Fe cations. The charge ordering forms characteristic linear triatomic units, so-called *trimerons*, each marked with green lines [42]. **(b)** Collective arrangement of trimerons within the monoclinic Cc unit cell. The trimerons align cooperatively along selected crystallographic directions, forming a complex pattern of orbital order. The origin of the monoclinic coordinate system is denoted by O, and the respective lattice vectors by a_M, b_M, and c_M. **(c)** Schematic representation of a single trimeron. The central Fe^{2+} ion (blue) exhibits an elongated charge density along the Fe-Fe bond, partially overlapping with the neighboring Fe^{3+} sites (yellow). The effective valence of the Fe cations varies between approximately $+2.32$ – $+2.55$ for Fe^{2+}-like sites and $+2.60$ – $+2.95$ for Fe^{3+}-like sites, reflecting partial charge delocalization rather than discrete integer oxidation states. The longitudinal olive-green envelope represents the spatial extent of this delocalized minority-spin electron, which couples charge ordering with orbital polarization along the trimeron axis.

Senn's and Wright's study revealed that below the Verwey transition temperature, $T < T_V$, the iron atoms within the octahedral (B) sublattice of magnetite self-organize into three-atomic polarons, termed *trimerons*. The local electronic density associated with each trimeron adopts the form of an elongated, cigar-shaped ellipsoid extending along the Fe–Fe–Fe chain. As illustrated in Fig. 1.5, the iron cations forming a single trimeron possess fractional effective valences within the range $[2, 3]$, in contrast to the discrete integer oxidation states (Fe^{2+} and Fe^{3+}) postulated in the original Verwey model. Although most trimerons intersect only peripherally, the blue circles in Fig. 1.5b indicate two exceptional Fe cations that simultaneously serve as the end of one trimeron and the center of another.

This discovery demonstrated that charge ordering in magnetite is not purely ionic but instead partially delocalized, governed by strong electron–lattice interactions. In this framework, the temper-

ature dependence of the electrical resistivity can be more accurately described in terms of interacting small polarons coupled to lattice vibrations, rather than by static charge localization alone. Trimerons are thus interpreted as quasiparticles representing localized yet correlated charge and orbital states immersed in a dynamically fluctuating phonon background.

Experimental diffuse-scattering studies indicate that these correlations persist even above T_V, suggesting the existence of a dynamically disordered or "trimeron liquid" phase [38]. The trimeronic ground state identified by Senn and Wright has since been successfully reproduced in density functional theory (DFT) calculations by Řezníček *et al.* [42], confirming its energetic stability and electronic character. Together, these theoretical and experimental advances extend and refine Verwey's original concept, offering a more complete description of the interplay between charge, orbital, and lattice degrees of freedom in magnetite.

1.2.3. Magnetism and correspondence of the Verwey and Néel temperatures

As discussed in Section 1.2, magnetite is a ferrimagnetic material with a Néel temperature of $T_N = 850$ K. Figure 1.6a illustrates the temperature dependence of the sublattice magnetization components associated with the tetrahedral (A) and octahedral (B) sites, which together determine the total magnetization M. Near the Verwey transition temperature, T_V, the magnetic moments residing on the Fe cations are coupled through a combination of *superexchange* and *double exchange* interactions mediated by oxygen anions, as schematically shown in Fig. 1.6b [43].

Within each sublattice, the exchange interactions are ferromagnetic, giving rise to magnetic moments of approximately $5\,\mu_B$ for the (A) sites and $9\,\mu_B$ for the (B) sites. In contrast, the coupling between the two sublattices is antiferromagnetic, resulting in a net ferrimagnetic alignment in which the magnetic moments of the (A) and (B) sublattices partially compensate each other, as depicted in Fig. 1.6a. Because the intersublattice exchange coupling constant J_{AB} dominates over the intrasublattice terms, the resultant magnetic moment per formula unit equals approximately $4\,\mu_B$, consistent with the experimentally determined value of $4.06\,\mu_B$ [44].

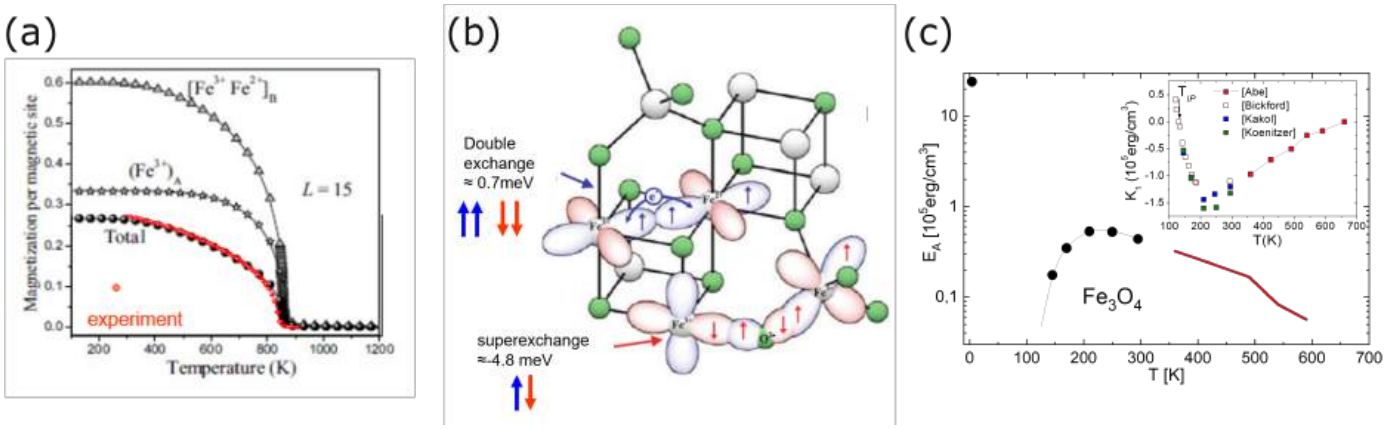

Fig. 1.6. Magnetic interactions and anisotropy in magnetite. **(a)** Temperature dependence of the magnetization per magnetic site. The red circles represent experimental data, while the ★ and △ symbols denote the contributions from the tetrahedral $Fe^{3+}{}_A$ and octahedral $(Fe^{3+}, Fe^{2+})_B$ sublattices, respectively [45]. The total magnetization $M(T)$ results from the vector sum of these antiparallel sublattice contributions, consistent with the ferrimagnetic ordering of magnetite. **(b)** Schematic representation of the dominant exchange interactions: ferromagnetic *double exchange* (∼0.7 meV) between neighboring Fe^{2+} and Fe^{3+} ions within the (B) sublattice, and antiferromagnetic *superexchange* (∼4.8 meV) between Fe cations located on (A) and (B) sites mediated by O^{2-} anions [43]. **(c)** Temperature dependence of the magnetic anisotropy energy $E_A(T)$ for Fe_3O_4. The inset shows the variation of the first anisotropy constant $K_1(T)$ compiled from different experimental reports [46, 47]. The observed evolution of E_A and K_1 reflects the temperature-dependent reorientation of the easy magnetization axis, which becomes particularly pronounced near the Verwey transition.

In stoichiometric magnetite, the magnetocrystalline anisotropy in the high-temperature cubic phase is characterized by its easy, intermediate, and hard magnetization axes oriented along the $\langle 111 \rangle$, $\langle 110 \rangle$, and $\langle 001 \rangle$ directions, respectively. The anisotropy energy, E_A, exhibits a pronounced decrease at the isotropy point $T_{\mathrm{IP}} \approx 130$ K, as shown in Fig. 1.6c. At this temperature, the energy barriers separating equivalent magnetization directions effectively vanish. Below T_{IP}, the easy axis of magnetization switches to the $\langle 100 \rangle$ direction, which remains stable in the low-temperature phase [48, 49].

This reorientation of the easy axis coincides closely with the Verwey transition, reflecting the intimate coupling between the crystal lattice and the spin system. Since the same $3d$ electrons of the Fe cations occupying the octahedral (B) sites are responsible both for mediating magnetic exchange interactions and for participating in the charge ordering process, a pronounced modification of the magnetic anisotropy and overall magnetization is expected in the vicinity of T_V.

Surprisingly, the absolute change in magnetization observed at the Verwey transition does not exceed 0.1% [50, 51]. In stark contrast, the magnetic anisotropy energy E_A decreases by nearly two

orders of magnitude at the same temperature. This pronounced loss of anisotropy occurs slightly above the Verwey transition, at the isotropy point $T_{\mathrm{IP}} > T_V$ [47, 52, 48, 51, 44].

The concurrence of these effects, together with the experimentally established correlation between the Verwey temperature T_V and the Néel temperature T_N [48, 51, 39], provides strong evidence for the essential role of magnetic degrees of freedom in the mechanism driving the Verwey transition. Although this coupling is not directly manifested in the magnetization magnitude, it becomes apparent through its impact on the charge and orbital ordering. Therefore, to better understand the contribution of magnetism to the Verwey transition, it is necessary to re-examine the problem from the perspective of charge localization and electron–lattice coupling in magnetite.

The trimeronic order that governs magnetite below the Verwey transition temperature ($T < T_V$) appears to persist, in a modified or dynamic form, up to the Néel temperature T_N. Furthermore, even at $T \gg T_V$, local probes reveal deviations from the global cubic $Fd\overline{3}m$ symmetry. Within the scale of a single unit cell, regions exhibiting short-range monoclinic distortions have been detected, whose evolution follows the temperature dependence of the magnetization [38]. This observation suggests that the cubic symmetry observed above T_V represents an average, dynamically fluctuating state rather than a truly stable structural phase.

Consequently, both the residual trimeronic correlations and the magnetic interactions dominating in the range $T_V < T < T_N$ likely coexist in a dynamic equilibrium. Such an interplay gives rise to the high-temperature phase of magnetite, in which structural, electronic, and magnetic degrees of freedom remain strongly coupled. These findings indicate that the Verwey transition is not a purely static structural transformation but rather the culmination of temperature-dependent electronic and lattice fluctuations stabilized by magnetically mediated interactions [38].

Over the decades, numerous attempts have been made to interpret the Verwey transition in terms of magnetic phenomena. Most of these models proposed that the nonzero net magnetization of magnetite stabilizes the long-range charge and orbital ordering below T_V [53]. However, this hypothesis has proven difficult to justify experimentally. For instance, the step-like decrease in the magnetic susceptibility $\chi_{\mathrm{AC}}(T)$ observed below T_V does not signify a disruption of the intrinsic magnetic order. Instead, it primarily reflects the dynamics of magnetic domain walls associated with the underlying structural transformation [23].

More recently, a complementary interpretation has emerged from combined core-level X-ray spectroscopy, electrical transport measurements, and theoretical modeling. These studies revealed a temperature-dependent redistribution of charge among the (B)-site Fe cations, often referred to as "self-doping", which sets in already at room temperature, shows little direct dependence on magnetic order, and gradually increases across the Néel temperature T_N [54]. This finding indicates that the primary driving force of the Verwey transition lies in the coupling between charge and lattice degrees of freedom, while magnetism plays a secondary, cooperative role. Consequently, the long-standing assumption of magnetization-driven stabilization of the low-temperature phase has been largely revised in favor of an electronically driven mechanism.

Until recently, there had been no direct experimental evidence linking the low-temperature Verwey transition with the high-temperature magnetic ordering in magnetite. However, recent studies have demonstrated a quantitative relationship between these two transitions, revealing that the Verwey temperature ($T_V \approx 125$ K) scales positively with the Néel temperature ($T_N \approx 858$ K). This correlation was established through a systematic series of electrical conductivity, alternating current (AC) susceptibility, and magnetization measurements performed on single crystals with varying stoichiometry and controlled levels of chemical doping [39].

These results provide compelling evidence that the mechanisms responsible for charge and orbital ordering at T_V are intrinsically connected to those governing magnetic order at T_N. In other words, the structural–electronic reorganization occurring at low temperatures appears to share a common microscopic origin with the high-temperature magnetic exchange interactions. This discovery establishes a unified framework linking magnetite's electronic and magnetic degrees of freedom across a remarkably broad temperature range.

After establishing the current understanding of the charge, orbital, and magnetic correlations underlying the Verwey transition in magnetite, the following three Subsections of this Chapter will examine how these electronic states can be modified experimentally. The discussion will begin with the influence of non-stoichiometry and atomic substitutions. For example, doping the magnetite lattice with nonmagnetic elements can disrupt the established charge order and reveal those electronic states that are most sensitive to local symmetry breaking. Such effects can be subsequently probed through electrical transport or magnetic measurements.

In addition to compositional tuning, the following Subsections will address the influence of external pressure, both hydrostatic and uniaxial. These two types of pressure act as symmetry-breaking perturbations and therefore have a direct impact on the quantum states of the system. While the effects of hydrostatic pressure on magnetite have been investigated for decades and are well documented in the literature, the influence of uniaxial pressure remains largely unexplored. Apart from two experimental studies published by the same research group in Japan [55, 56], no systematic investigation of this phenomenon has yet been reported. One of the main reasons for this gap is the technical difficulty of constructing and operating experimental setups capable of applying well-calibrated uniaxial stress while simultaneously enabling precise electrical and structural characterization of the sample.

1.2.4. Influence of nonstoichiometry and doping on the Verwey transition

In the face-centered cubic unit cell of magnetite, 32 oxygen atoms coordinate 8 iron atoms occupying the tetrahedral (A) sites and 16 iron atoms located at the octahedral (B) sites. Owing to this simple composition, Fe_3O_4, consisting solely of iron and oxygen, stands out among transition metal oxides as a chemically straightforward yet electronically complex material. Despite its apparent simplicity, the interplay of charge, orbital, and spin degrees of freedom gives rise to remarkably rich

physical behavior.

One of the most striking manifestations of this complexity is the pronounced sensitivity of the Verwey transition to atomic substitutions at the iron sites. Even minor deviations from stoichiometry or partial replacement of Fe ions can strongly modify the transition temperature and even its character. Such effects have been observed, for example, using nuclear magnetic resonance (NMR) spectroscopy, which revealed that changes in local coordination and charge ordering are readily detectable upon atomic substitution [57, 49]. These findings demonstrate that even small lattice perturbations, whether caused by chemical doping or intrinsic point defects, can significantly alter the microscopic interactions underlying the Verwey transition.

Variations in the iron-to-oxygen ratio in nonstoichiometric magnetite, expressed as $Fe_{3\cdot(1-\delta)}O_4$, leads to a progressive suppression and broadening of the Verwey transition as observed in electrical resistivity measurements. When the deviation from stoichiometry, quantified by $3 \cdot \delta$, exceeds approximately 0.0036, the transition is completely suppressed, as illustrated in Fig. 1.7a [58]. This behavior reflects the destabilization of the charge-ordered state caused by the introduction of cation or anion vacancies that disturb the delicate Fe^{2+}/Fe^{3+} balance within the octahedral sublattice.

Further insight into the influence of chemical substitution is provided by specific heat measurements of $Fe_{3-x}Zn_xO_4$, shown in Fig. 1.7b. The presence of zinc impurities alters the nature of the Verwey transition from discontinuous to continuous, indicating that Zn substitution not only affects the transition temperature but also changes the underlying thermodynamic character of the transformation.

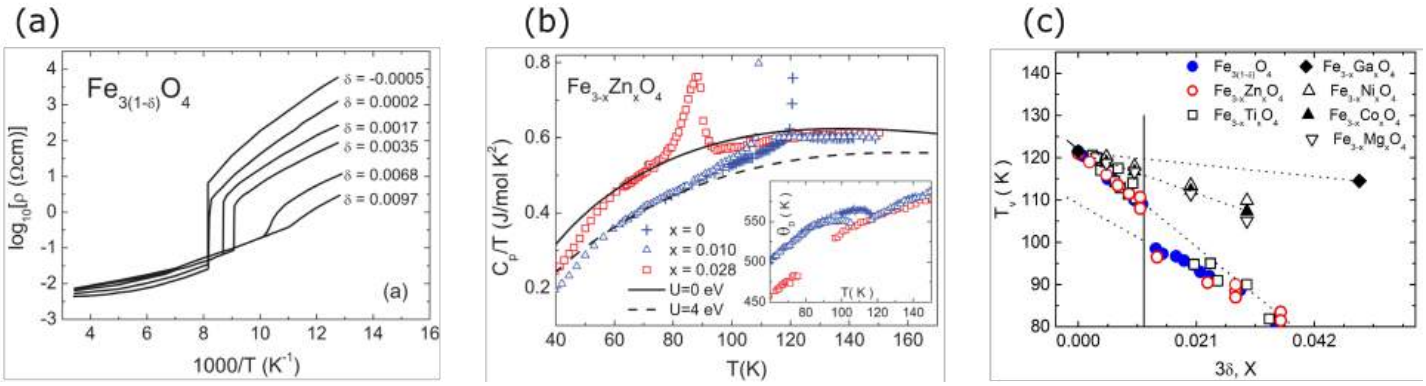

Fig. 1.7. (a) Dependence of the electrical resistivity, $\log_{10}\rho$ as a function of inverse temperature, $1000/T$ for single crystals of magnetite $Fe_{3\cdot(1-\delta)}O_4$ with varying non-stoichiometry parameter, δ [59, 60, 61]. **(b)** Temperature dependence of the reduced specific heat for zinc ferrite $Fe_{3-x}Zn_xO_4$. The sharp spike of the C_p/T response for $x = 0$ and $x = 0.1$ signifies the first order character of the phase transition, while the the diffuse shape for $x = 0.028$ marks the continuous phase transformation. The dotted and the continuous black lines are guide to the eye. The inset presents for each experimental curve collected the dependence of the Debye temperature, θ_D which indicates on the lattice stiffening below T_V. In the inset, peaks of the C_p were removed for clarity [36]. **(c)** Dependence of the Verwey temperature, T_V on doping, x in $Fe_{3-x}M_xO_4$, where M = Zn, Ti, Ga, Ni, Co, Mg and non-stoichiometry parameter, δ in $Fe_{3\cdot(1-\delta)}O_4$. Doping with especially Ti or nonmagnetic Zn and nonstoichiometry systematically diminish T_V and for x $(3\cdot\delta)$ exceeding 0.012 $(3\cdot 0.04 = 0.012)$, the character of the VT changes from discontinuous to continuous according to the universal relation of T_V vs. defect concentration $x = 3\cdot\delta$ [36, 62].

Any deviation from stoichiometry, quantified by $3\cdot\delta$, or the presence of substitutional dopants with concentration x, introduces excess charge carriers that modify the local electronic density within the magnetite unit cell and consequently affect the Verwey transition. More than two decades ago, it was demonstrated that the incorporation of zinc or titanium produces an equivalent and nearly universal effect on T_V. The transition temperature systematically decreases with increasing dopant concentration and is completely suppressed when the Zn or Ti content exceeds approximately $\frac{1}{3}\%$ of the total atomic fraction. A comparable suppression is observed for the effective nonstoichiometry parameter, $x \Leftrightarrow 3\cdot\delta$ [36, 62].

However, as shown in Fig. 1.7c, the linear attenuation of T_V as a function of $x = 3\cdot\delta$ does not hold as strictly for dopants such as Ga, Ni, Co, or Mg, which produce weaker or nonmonotonic effects. Nevertheless, the overall trend confirms that point defects and cation disorder play an essential role in destabilizing the charge-ordered state responsible for the Verwey transition. Recent theoretical analyses further suggest that this sensitivity arises from long-range Coulomb interactions between

next-nearest-neighbor Fe sites, which are particularly susceptible to perturbations induced by dopants or vacancies [63, 64].

1.2.5. Response of the Verwey transition to hydrostatic pressure

Hydrostatic pressure primarily shortens the interatomic distances, thereby enhancing the overlap of electronic wave functions between adjacent ions. This increased orbital overlap can modify the charge transport properties, for instance by inducing a more metallic character or even triggering structural transformations. The influence of hydrostatic pressure, p, on the Verwey transition has been extensively investigated since the late 1970s [65, 66, 67, 68, 69]. These studies consistently demonstrated that increasing p reduces the Verwey transition temperature, T_V, in both stoichiometric and non-stoichiometric magnetite. A similar pressure-induced suppression of T_V was also observed in zinc ferrite [67].

As shown in Fig. 1.8a, application of hydrostatic pressure up to 8 GPa results in a continuous reduction of T_V with increasing p, approaching a point at which the transition vanishes altogether. This behavior has been interpreted as evidence for the presence of a quantum critical point (QCP) near the critical pressure, separating the low-temperature insulating and high-temperature metallic phases of magnetite [70].

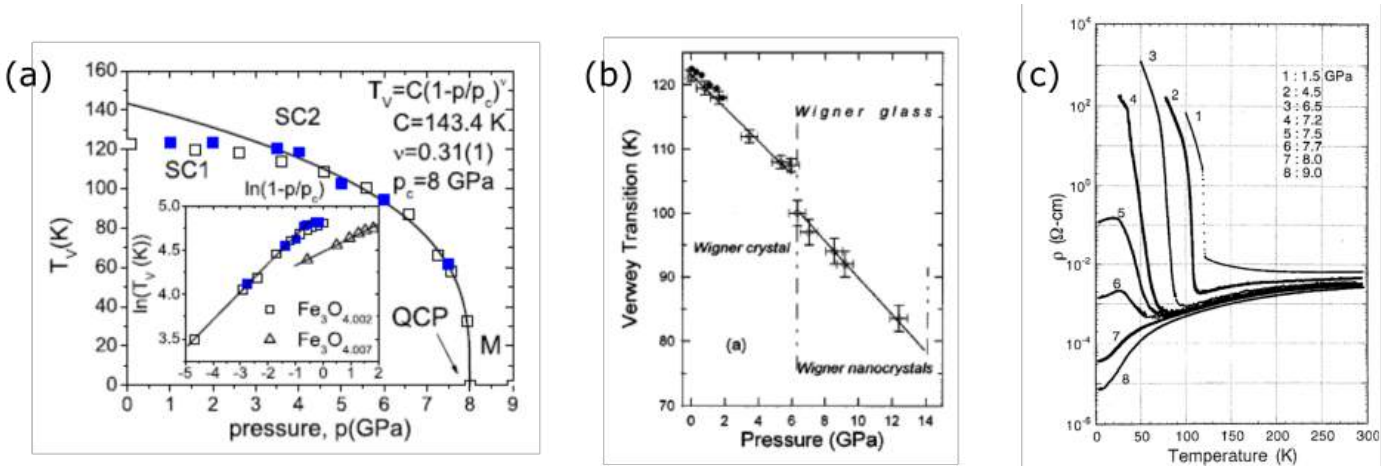

Fig. 1.8. Response of the Verwey transition to hydrostatic pressure. **(a)** Phase diagram of the Verwey temperature, T_V, as a function of hydrostatic pressure, p. The transition temperature decreases continuously with increasing p and vanishes above the critical pressure $p_c \approx 8$ GPa, where magnetite becomes metallic (M). The intermediate semiconducting regions, SC1 and SC2, are separated by the proposed quantum critical point (QCP) at $p = p_c$. Inset: logarithmic dependence of T_V on $\ln\left(1 - \frac{p}{p_c}\right)^{\nu}$, fitted with the critical exponent $\nu = 0.31(1)$ [70]. **(b)** Variation of T_V with hydrostatic pressure compared with the effects of doping and non-stoichiometry (cf. Fig. 1.7c). The character of the transition changes from discontinuous (first-order) to continuous (second-order) at approximately $p = 6$ GPa [67]. **(c)** Temperature dependence of the electrical resistivity, $\rho(T)$, under hydrostatic pressure ranging from 1.5 to 9 GPa [71]. The abrupt resistivity jump associated with the VT gradually diminishes with increasing p, and for $p > 8$ GPa, the low-temperature phase exhibits purely metallic behavior, consistent with the phase diagram in panel (a).

Figure 1.8b illustrates the pressure-induced evolution of the Verwey transition, which changes its character from discontinuous (first-order) to continuous (second-order) at a hydrostatic pressure of approximately 6 GPa, a behavior analogous to that observed for chemical doping and non-stoichiometry. As shown in Fig. 1.8c, increasing hydrostatic pressure p systematically lowers the transition temperature T_V, as evidenced by the progressive shift of the resistivity anomaly toward lower temperatures. At pressures exceeding the critical value $p_c = 8$ GPa, the Verwey transition is completely suppressed, and magnetite exhibits metallic conductivity throughout the entire temperature range [72].

In collaboration between AGH University of Krakow and Ludwig-Maximilians-Universität (LMU) München, it was demonstrated that a shock-induced hydrostatic stress of approximately 2 GPa caused a reversible freezing of the lattice disorder, which subsequently relaxed over time [45]. When

the applied hydrostatic pressure exceeded 2 GPa, T_V increased irreversibly and the transition became broader. For lower pressures, persistent changes of T_V were not observed, since no long-lived point defects were introduced into the crystal lattice.

At higher pressures, however, the formation of point defects significantly altered the transition behavior. Mössbauer spectroscopy (MS) measurements performed under hydrostatic pressures up to 18 GPa revealed that these defects progressively suppressed the Verwey transition, which eventually vanished at the critical pressure of $p_c \approx 7.5$ GPa [73]. The results suggest that the very presence of stress-induced point defects affects the Verwey transition more strongly than their absolute concentration. Such defects are believed to locally pin charge carriers and promote a partial charge ordering, consistent with previous estimates of entropy changes, ΔS, across the transition [74].

Recent X-ray Absorption Near Edge Structure (XANES) measurements performed on stoichiometric magnetite under hydrostatic compression at room temperature revealed that, at $p = 40$ GPa, the crystal structure transforms from the inverse spinel phase to an orthorhombic structure of the $CaTi_2O_4$-type with space group $Bbmm$ [75]. This symmetry change, previously postulated in earlier and somewhat controversial reports [76], was confirmed by a pronounced shift in the main absorption peak energy, E_β, and a distinct variation in the pre-edge intensity, I_α, as shown in Fig. 1.9a. Furthermore, the high-pressure (h-Fe_3O_4) phase exhibited metallic conductivity, consistent with the pressure-induced metallization reported in electrical resistivity studies (Figs. 1.8a,c).

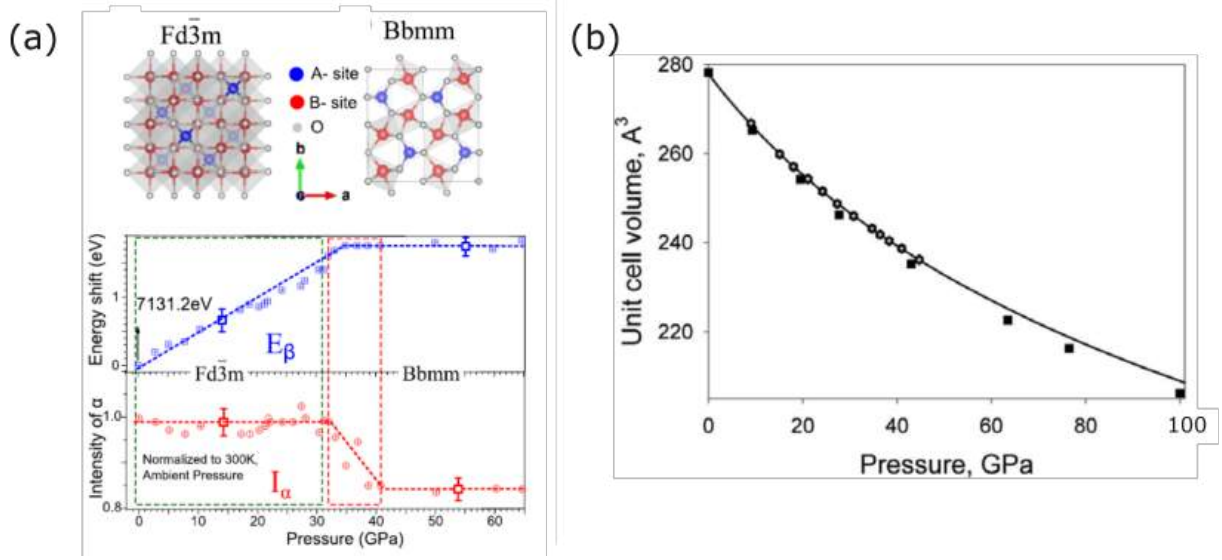

Fig. 1.9. (a) Room-temperature crystal structure of magnetite under increasing hydrostatic compression, showing the transition from the cubic inverse spinel symmetry $Fd\bar{3}m$ to the high-pressure h-Fe_3O_4 phase of the $CaTi_2O_4$-type with orthorhombic $Bbmm$ symmetry. The structural transformation initiates at $p \approx 30$ GPa [75] and is evidenced in the X-ray Absorption Near Edge Structure (XANES) spectra by a monotonic increase in the main peak energy, E_β, and a concurrent suppression of the pre-edge intensity, I_α. **(b)** Compression-induced decrease of the unit cell volume of magnetite up to $p = 100$ GPa [67]. The smooth reduction of the lattice volume reflects the progressive densification of the Fe–O framework preceding the structural transition.

The application of hydrostatic pressure and its subsequent release alters the atomic ground state within the crystal lattice, potentially redistributing pre-existing defects and transiently influencing the Verwey transition temperature, T_V [45]. However, since the decrease of T_V is consistently observed under hydrostatic compression and the accompanying modification of the electronic structure correlates with the systematic reduction of the unit cell volume (Fig. 1.9b), it is evident that changes in the charge correlations dominate over the influence of defect rearrangement. This suggests that the suppression of the Verwey transition under pressure is primarily an intrinsic electronic effect, arising from enhanced Fe–O orbital overlap and progressive delocalization of charge carriers, rather than from extrinsic defect formation.

The suppressive influence of hydrostatic pressure on the Verwey transition was further confirmed by complementary vibrating sample magnetometry (VSM) measurements carried out on a single crystal of stoichiometric magnetite synthesized using the optical floating-zone method. The experiment, presented in Fig. 1.10, was performed specifically for the purposes of this Dissertation at the Institute of Nuclear Physics, Polish Academy of Sciences, in Krakow. The studied crystal originated

from the same batch as those used in the uniaxial compression and diffraction experiments discussed in Chapters 3, 4, and 5, ensuring direct comparability between datasets.

The primary goal of this measurement was to determine how relatively low hydrostatic pressures, comparable in magnitude to those applied in uniaxial compression, affect the Verwey transition temperature, T_V. Previous studies predominantly focused on pressures in the gigapascal range, where the reported trends in T_V were sometimes contradictory (see Fig. 1.8 a). The present results unambiguously demonstrate that within the lower pressure regime, up to several hundred megapascals, hydrostatic compression consistently leads to a decrease in T_V. This finding provides a critical reference point for interpreting the uniaxial stress data presented later in this Dissertation.

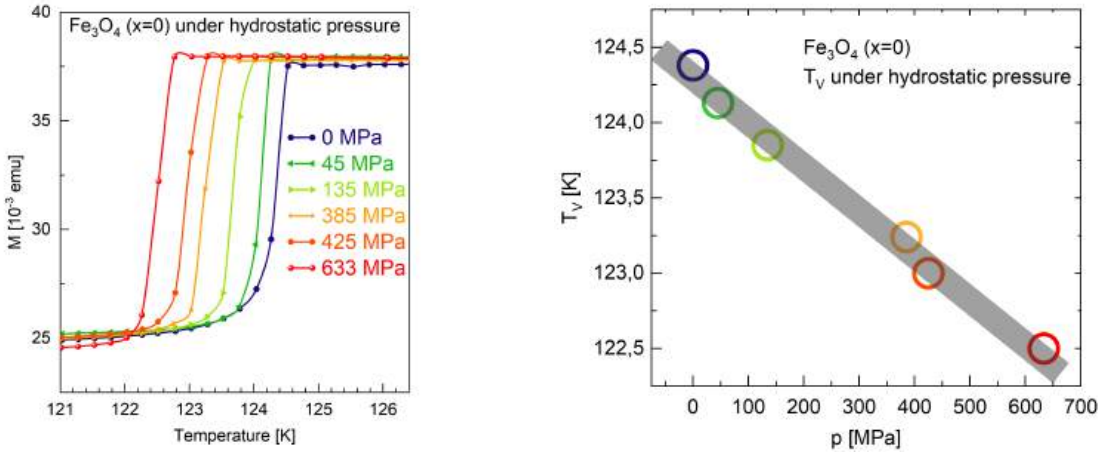

(a) (b)

Fig. 1.10. Influence of hydrostatic pressure on the Verwey transition in stoichiometric magnetite, determined using vibrating sample magnetometry (VSM). **(a)** Temperature dependence of the magnetization, $M(T)$, measured under progressively increasing hydrostatic pressures from 0 MPa to 633 MPa. The transition temperature systematically decreases with increasing pressure, indicating a pressure-induced destabilization of the low-temperature insulating phase. **(b)** Dependence of the Verwey transition temperature, T_V, determined as the inflection point of each $M(T)$ curve shown in panel (a), on the applied hydrostatic pressure, p. The fitted linear trend yields a slope of approximately -3 mK/MPa, demonstrating a clear negative correlation between T_V and p in the low-pressure regime. The measurement was performed by Dr. Naveen K. C. M. at the Institute of Nuclear Physics, Polish Academy of Sciences (Krakow).

In this experiment, magnetization, $M(T)$, was measured in the vicinity of the Verwey transition over the temperature range 121–126 K under hydrostatic pressures gradually increasing from 0 to

633 MPa, as shown in Fig. 1.10a. The transition temperature, T_V, was determined as the inflection point of each magnetization curve and is plotted as a function of pressure in Fig. 1.10b. The data reveal a clear linear dependence of T_V on hydrostatic pressure, characterized by a slope of approximately $-3\ \mathrm{mK/MPa}$. This result confirms that even relatively small isotropic compressions, comparable in magnitude to those applied in the uniaxial stress experiments discussed later, systematically suppress the Verwey transition temperature in stoichiometric magnetite.

The magnetic behavior observed near the Verwey transition at low temperatures can be related to the high-temperature evolution of magnetization under pressure. Schult *et al.* [77] demonstrated that the Néel temperature, T_N, increases with hydrostatic pressure, indicating an enhancement of the superexchange interaction between the octahedral (B) and tetrahedral (A) sublattices. This observation is particularly relevant in the context of the proposed magnetic contribution to the Verwey transition mechanism [38, 39].

In contrast, high-pressure neutron diffraction combined with *ab initio* calculations revealed a gradual reduction of the magnetic moments at both (A) and (B) sites in magnetite with increasing pressure [78]. The apparent discrepancy between the magnetization and diffraction results was further examined through studies of the pressure dependence of the elastic moduli c_{11}, c_{12}, and c_{44}. Measurements of these constants under both moderate (up to 1.2 GPa [34, 79]) and high (up to 20 GPa [80]) hydrostatic pressures indicate that the coupling between the order parameter and the applied strain progressively weakens as p increases. Consequently, the overall response of the charge and magnetic correlations in magnetite to hydrostatic compression remains complex and non-linear, making the detailed prediction of $T_V(p)$ behavior inherently challenging.

The discussion above demonstrates that hydrostatic pressure acts isotropically on the magnetite lattice, simultaneously modifying interatomic distances and electronic interactions along all crystallographic directions. As a result, the individual directional contributions to the electronic, magnetic, and structural responses cannot be disentangled under such isotropic compression. In contrast, applying uniaxial stress provides a controlled means of breaking the cubic symmetry in a specific crystallographic direction, thereby allowing one to probe the anisotropy of the electronic and magnetic correlations that underpin the Verwey transition.

Despite the extensive research effort devoted to the effects of hydrostatic pressure on magnetite, remarkably little attention has been given to the influence of uniaxial stress. Only a few experimental reports, mostly limited in scope and conducted under challenging technical conditions, have addressed how directional compression affects the Verwey transition or the underlying electronic and magnetic correlations. This scarcity of data leaves fundamental questions unanswered regarding the anisotropic response of magnetite to symmetry-breaking strain.

The following Section therefore introduces the limited theoretical and experimental work that has so far been carried out on magnetite under uniaxial compression. These pioneering efforts form the essential foundation for the present project, which aims to systematically investigate how controlled

uniaxial stress along (100) and (011) modifies the electronic, magnetic, and structural properties of stoichiometric magnetite.

1.2.6. Influence of the uniaxial pressure on the Verwey phase transition

As discussed in the previous Section, hydrostatic compression acts isotropically, simultaneously shortening interatomic distances and distorting bond angles along all crystallographic directions while reducing the overall crystal volume. In contrast, uniaxial pressure represents a distinct, symmetry-breaking perturbation: when applied along a specific axis, it selectively enhances the overlap of electronic orbitals in that direction and thereby modifies only a subset of the available lattice degrees of freedom.

Such directional stress can induce anisotropic responses not only in the crystal lattice but also in the magnetic interactions, particularly in transition-metal oxides like magnetite, where oxygen-mediated double-exchange and super-exchange mechanisms dominate. Consequently, uniaxial compression can destabilize the delicate balance between competing electronic and magnetic phases or selectively modify one of the principal correlation channels, such as electron–electron or electron–phonon coupling.

Importantly, unlike hydrostatic compression, uniaxial stress produces minimal changes in the unit-cell volume and does not alter the global defect concentration. This makes it an exceptionally sensitive probe of the intrinsic anisotropic degrees of freedom. The following Sections will illustrate how this directional strain manifests in measurable changes to the electronic transport and magnetic properties of stoichiometric magnetite.

The first attempts to explore the influence of uniaxial stress on magnetic oxides date back nearly sixty years. In these pioneering studies, Nagata and co-workers investigated the magnetization, M, of titanium ferrite ($FeTiO_3$) as a function of uniaxial compression applied along the $\langle 111 \rangle$ direction [81, 16]. These early experiments were primarily motivated by geophysical interests, aiming to understand how mechanical stress within the Earth's crust could affect the magnetic properties of natural minerals. Although technically limited by the available instrumentation, this work laid the conceptual groundwork for studying stress-induced magnetic anisotropy in ferrites and related oxides.

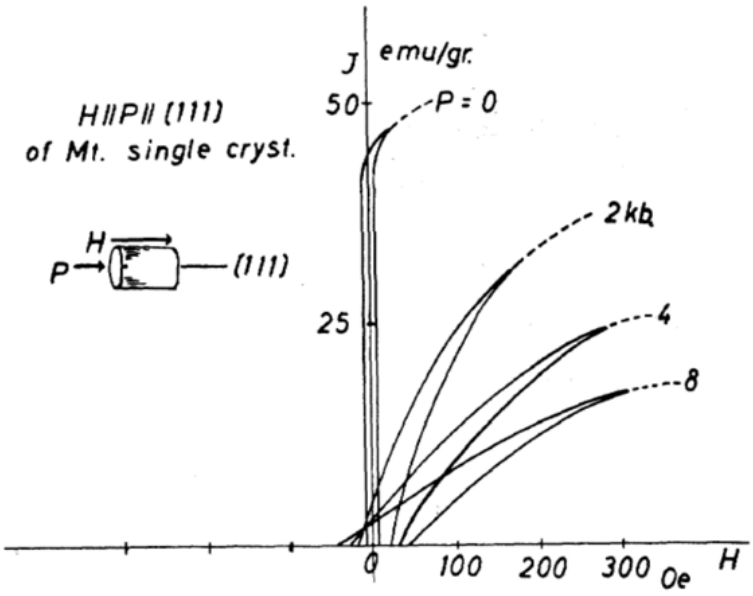

Fig. 1.11. Effect of uniaxial compression on the magnetization of titanium ferrite single crystals at room temperature. Magnetization J (in emu/g) was measured as a function of magnetic field H under various uniaxial pressures up to 8 kbar ($\approx$ 800 MPa) applied along the $\langle 111 \rangle$ crystallographic direction. Increasing compression systematically reduced the saturation magnetization and broadened the hysteresis loops, indicating stress-induced damping of magnetic alignment. These measurements, performed on both natural and synthetic titanium ferrites, represent one of the earliest demonstrations of magnetoelastic coupling under uniaxial stress [81].

As shown in Fig. 1.11, applying uniaxial compression of several hundred megapascals along the $\langle 111 \rangle$ direction systematically reduced the total magnetization and narrowed the hysteresis loops, demonstrating a clear damping of magnetic alignment under stress. However, a major limitation of the study by Nagata *et al.* was the insufficient description of the experimental setup used to generate uniaxial stress and the absence of any reported calibration procedure for determining the applied pressure. This lack of methodological detail makes it difficult to quantitatively compare their results with subsequent investigations or to assess the precise magnitude of the magnetoelastic coupling observed.

The work of Nagata and co-workers demonstrated that uniaxial compression can significantly influence the magnetic properties of ferrites, highlighting the potential of directional stress as a probe of magnetoelastic coupling. This observation is particularly relevant for magnetite, where the Verwey transition represents a structural transformation involving a symmetry change from cubic ($Fd\overline{3}m$) to monoclinic (Cc) at the characteristic temperature T_V. The nature of this transformation may be compared to the crystallization of water into ice; both processes proceed through nucleation and cooperative ordering once a critical thermodynamic condition is reached. Consequently, any

modification of the unit-cell shape or volume implies that the phase boundary between the cubic and monoclinic phases should be sensitive to both hydrostatic and uniaxial stresses.

A comprehensive thermodynamic analysis of the Verwey transition under external stress was developed by Coe *et al.* [82]. Their model extended the conventional hydrostatic treatment, which accounts only for isotropic volume and entropy changes, by incorporating the full stress tensor and the anisotropic strain accompanying the cubic-to-monoclinic transformation. Within this framework, the rate of change of the transition temperature with an applied uniaxial stress along a specific crystallographic direction, $\sigma_{\langle hkl\rangle}$, is expressed as

$$M_{\langle hkl\rangle} = \frac{\partial T_V}{\partial \sigma_{\langle hkl\rangle}} = v_0 \frac{\Delta \varepsilon_{\langle hkl\rangle}}{\Delta s},$$

where v_0 is the molar volume of cubic magnetite at $T = T_V$, $\Delta\varepsilon_{\langle hkl\rangle}$ is the strain component generated along the chosen crystallographic direction during the transformation, and Δs is the molar entropy change.

Using experimentally determined parameters ($v_0 = 4.45 \times 10^{-5}\ \mathrm{m^3\,mol^{-1}}$, $\Delta s = -5.91\,\mathrm{J\,mol^{-1}\,K^{-1}}$), Coe *et al.* obtained the hydrostatic pressure coefficient $dT_V/dP = -3.7\ \mathrm{K/GPa}$, confirming that isotropic compression suppresses the transition temperature. When uniaxial stress is considered, however, the response becomes highly anisotropic. In terms of the three principal strain axes of the cubic-to-monoclinic transformation, the corresponding uniaxial coefficients are:

$$M_1 = -23.3\ \mathrm{K/GPa}, \qquad M_2 = +8.8\ \mathrm{K/GPa}, \qquad M_3 = +10.8\ \mathrm{K/GPa},$$

where M_1 corresponds to the direction of maximum lattice expansion (approximately the cubic $\langle 111\rangle$ axis), and M_2 and M_3 correspond to the two orthogonal contraction axes that roughly align with the $\langle 110\rangle$-type directions. Thus, compression or tension applied along $[111]$ produces the strongest *negative* shift in the transition temperature, with $\frac{dT_V}{d\sigma_{[111]}} \approx -23.3\ \mathrm{K/GPa}$, while stress applied along $[110]$ or $[1\bar{1}0]$ leads to pronounced *positive* shifts of $+8.8$ and $+10.8\ \mathrm{K/GPa}$, respectively. These are 2.4 to 6.3 times larger in absolute magnitude than the hydrostatic slope.

The theoretical predictions by Coe *et al.* regarding the anisotropic response of T_V to uniaxial stress have, so far, not been experimentally verified. To date, only a single dedicated study by Nagasawa *et al.* [83] has reported measurements of the Verwey transition under uniaxial compression. In that work, the applied stress was oriented exclusively along the cubic $\langle 110\rangle$ direction, and the evolution of T_V was monitored using vibrating magnetometry. The experiments were performed under a magnetic field of 2 T in the field-cooling (FC) mode, while the uniaxial stress was systematically increased from 0 to 1.5 kbar (150 MPa).

As shown in Fig. 1.12, the magnetization curves exhibited a systematic shift of the transition temperature toward higher values with increasing compressive stress. The resulting linear dependence of T_V on σ yielded a slope coefficient of approximately $+13\ \mathrm{mK/MPa}$, in excellent agreement with the theoretical predictions of $+8.8$ to $+10.8\ \mathrm{K/GPa}$ for compression along the $\langle 110 \rangle$ and $\langle 1\bar{1}0 \rangle$ directions, respectively [82]. Although this result provides partial confirmation of Coe's model, the study was limited to a single crystallographic orientation and therefore could not test the full anisotropic behavior of T_V predicted under uniaxial stress.

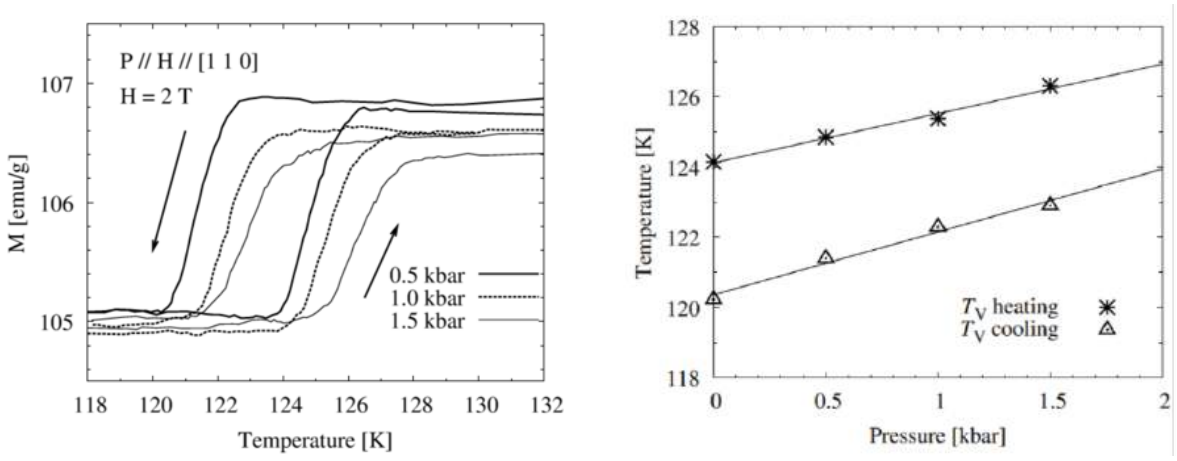

(a) (b)

Fig. 1.12. Influence of uniaxial stress applied along the cubic [110] direction on the Verwey transition in stoichiometric magnetite, measured using vibrating sample magnetometry (VSM). **(a)** Temperature dependence of the magnetization, $M(T)$, recorded during heating and cooling under uniaxial compressive stresses of 0.5, 1.0, and 1.5 kbar (corresponding to 50, 100, and 150 MPa, respectively) in a magnetic field of $2\ \mathrm{T}$ applied parallel to the stress axis ($P \parallel H \parallel [110]$). The Verwey transition shifts systematically toward higher temperatures with increasing applied stress. **(b)** Dependence of the transition temperature, T_V, determined from the inflection points of the $M(T)$ curves in panel (a), on the applied uniaxial stress. Separate linear fits were applied to data obtained during heating and cooling cycles, yielding slope coefficients of approximately $+13\ \mathrm{mK/MPa}$ ($+13\ \mathrm{K/GPa}$). This positive rate of change of T_V with stress is consistent with the theoretical predictions of Coe *et al.* [82] for compression along the $\langle 110 \rangle$ direction. Reproduced from Nagasawa *et al.* [84].

Complementary insight into the effect of uniaxial compression on the Verwey transition was provided by the electrical transport measurements of Nagasawa *et al.* [85]. As shown in Fig. 1.13, the resistivity of stoichiometric magnetite was measured under uniaxial stress applied along the cubic $\langle 110 \rangle$ direction in the same pressure range used for the magnetization study (up to $1.5\ \mathrm{kbar}$). The

results demonstrated that resistivity below the transition increased systematically with applied stress, whereas above T_V it decreased, producing opposite pressure coefficients in the insulating and metallic phases.

This contrasting behavior reflects changes in the Fe–O bond length and the corresponding overlap between the Fe $3d$ and O $2p$ orbitals. Below T_V, compression along $\langle 110 \rangle$ reduces the hopping integral between neighboring B-site Fe cations, enhancing charge localization and widening the insulating gap ΔE. Above T_V, however, the same strain promotes orbital overlap within the itinerant cubic phase, leading to improved carrier delocalization and a moderate reduction in resistivity. The observed trends confirm that uniaxial stress couples strongly and anisotropically to the charge and lattice degrees of freedom, consistent with the magnetometric evidence of a positive $\partial T_V/\partial\sigma$ and in agreement with the theoretical framework proposed by Coe *et al.* [82].

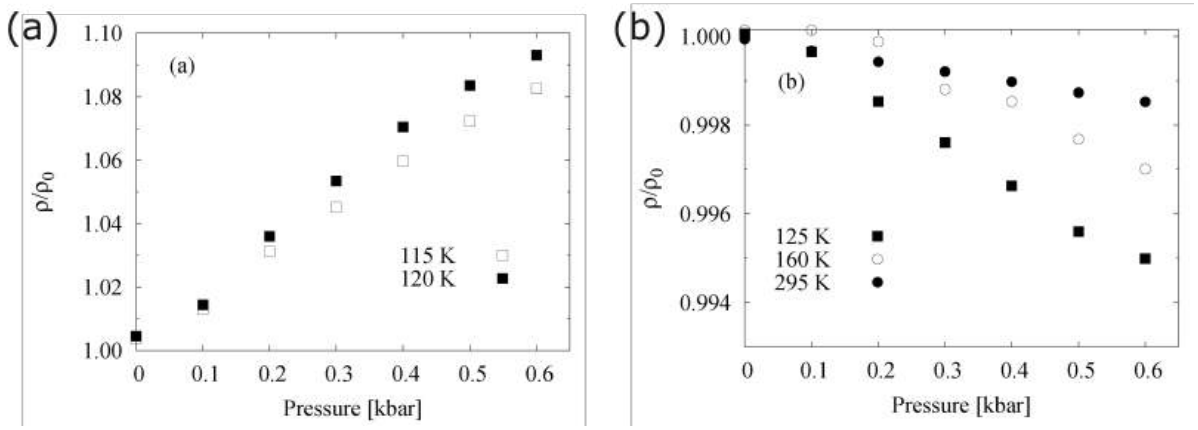

Fig. 1.13. Influence of uniaxial compression along the cubic [110] direction on the electrical resistivity of stoichiometric magnetite, as reported by Nagasawa *et al.* [55]. **(a)** Relative change in resistivity, ρ/ρ_0, measured below the Verwey transition ($T = 115$ and 120 K). The resistivity increases systematically with applied uniaxial pressure, indicating enhanced charge localization in the monoclinic insulating phase. **(b)** Relative change in ρ/ρ_0 measured above T_V ($T = 125$, 160, and 295 K). In contrast to the low-temperature regime, the resistivity decreases slightly with increasing stress, reflecting improved carrier delocalization in the cubic metallic phase. Both behaviors demonstrate that uniaxial stress couples anisotropically to the Fe–O bonding geometry, modifying the Fe $3d$–O $2p$ hybridization and the electronic transport across the Verwey transition.

In recent years, attention has shifted from bulk magnetite to thin-film systems, where strain can be tuned more precisely using epitaxial or piezoelectric substrates. In particular, Liu *et al.* [86] demonstrated that the Verwey transition in magnetite can be modulated by electric-field–induced strain in magnetite bilayers grown on 71%$Pb(Mg_{1/3}Nb_{2/3})O_3$–29%$PbTiO_3$ (PMN–PT) substrates. The polarization of PMN–PT via the inverse piezoelectric effect generated an in-plane lattice strain, which altered the resistive properties of the attached Fe_3O_4/PMN–PT heterostructure even at room

temperature. Upon cooling, this elastic coupling allowed direct control of the Verwey transition in the magnetite film through the strain state of the underlying piezoelectric substrate.

Building on this concept, subsequent studies explored epitaxial Fe_3O_4 thin films of various thicknesses (40–200 nm) grown on spinel-type substrates, including Co_2TiO_4, Mn_2TiO_4, Mg_2TiO_4, and Fe_2TiO_4 [87, 88]. As shown in Fig. 1.14, these investigations revealed that both the magnitude and sign of epitaxial strain imposed by the substrate significantly influence the Verwey transition temperature and resistivity behavior. Such findings highlight that even subtle lattice mismatch–induced distortions in magnetite thin films can emulate the effects of uniaxial stress, thereby reinforcing the pivotal role of strain in tuning the electronic and structural properties of magnetite.

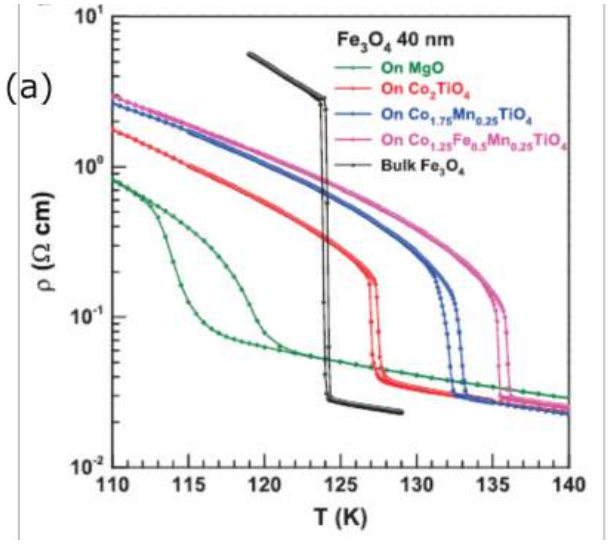

(b)

Table 1. Lattice constants

	Substrate a	*40 nm Fe_3O_4 c*	*80 nm Fe_3O_4 c*	*200 nm Fe_3O_4 c*
Co_2TiO_4	8.4528 Å	8.3332 Å	8.3330 Å	8.3316 Å
$Co_{1.75}Mn_{0.25}TiO_4$	8.4797 Å	8.3042 Å	8.3048 Å	8.3054 Å
$Co_{1.25}Fe_{0.5}Mn_{0.25}TiO_4$	8.4898 Å	8.2800 Å	8.2806 Å	8.2855 Å

Lattice constants of 40, 80 and 200 nm Fe_3O_4 thin films on Co_2TiO_4, $Co_{1.75}Mn_{0.25}TiO_4$ and $Co_{1.25}Fe_{0.5}Mn_{0.25}TiO_4$.

Fig. 1.14. Electronic transport properties of 40 nm single-crystalline Fe_3O_4 films grown epitaxially on different spinel and rock salt substrates, after Liu *et al.* [87]. **(a)** Temperature dependence of the electrical resistivity, $\rho(T)$, for magnetite films on MgO, Co_2TiO_4, $Co_{1.75}Mn_{0.25}TiO_4$, and $Co_{1.25}Fe_{0.5}Mn_{0.25}TiO_4$ substrates, compared to bulk Fe_3O_4. Films grown on MgO experience in-plane tensile strain due to lattice mismatch, which suppresses and broadens the Verwey transition, T_V, similarly to the effect of hydrostatic pressure. In contrast, films grown on spinel-type tetratitanate substrates experience in-plane compressive strain, which sharpens the transition and increases T_V, analogous to uniaxial compression effects observed in bulk crystals. **(b)** Lattice constants of Fe_3O_4 thin films of different thicknesses (40, 80, and 200 nm) grown on the respective spinel substrates. The bulk lattice constant of magnetite is $a_0 = 8.397$ Å. Films exhibiting a smaller (larger) in-plane lattice constant than a_0 are under compressive (tensile) strain, corresponding to an increase (decrease) in T_V.

The results reported by Liu *et al.* [87, 88] revealed that increasing the lattice constant of the substrate systematically shortened the out-of-plane c axis of the epitaxial Fe_3O_4 films. This strain-induced lattice distortion was accompanied by a significant increase in the Verwey temperature, T_V, consistent with the trend previously observed by Nagasawa [56] under uniaxial compression along the

$\langle 110 \rangle$ direction. In these strained thin films, the in-plane tensile strain imposed by lattice mismatch was balanced by a compensating compressive strain along the c axis. Consequently, the resistivity decreased below T_V and increased above it, inverting the trend observed for bulk magnetite under uniaxial stress by Nagasawa *et al.* [55] (see Fig. 1.13).

This apparent discrepancy can be attributed to the complex strain state in epitaxial films, where in-plane tension coexists with out-of-plane compression, as well as to possible magnetic interactions originating from the substrate. Some of the spinel substrates used by Liu *et al.* contained magnetic cations such as Co^{2+} or paramagnetic Mn^{2+}, which could influence the magnetite layer via magnetic exchange across the interface. To isolate the effect of strain from that of magnetic coupling, Liu *et al.* also examined Fe_3O_4 films grown on non-magnetic substrates. In all cases, the epitaxial magnetite films exhibited distinct magnetic behavior near T_V, reflecting the sensitivity of exchange interactions to the Fe–O–Fe bond geometry. Since uniaxial strain modifies both super exchange and double exchange pathways, it can alter magnetic anisotropy and even shift the effective Néel temperature. Notably, it was later demonstrated that the simultaneous application of magnetic field and uniaxial stress can detwin magnetite films at the Verwey transition, further highlighting the strong coupling between lattice strain, charge ordering, and magnetism [88].

The results discussed above collectively demonstrate that external stress, whether hydrostatic, uniaxial, or epitaxial, profoundly influences the structural and electronic behavior of magnetite around the Verwey transition. Hydrostatic pressure uniformly shortens all interatomic distances, suppressing T_V and eventually destroying the transition at high pressures through isotropic lattice contraction. In contrast, uniaxial or epitaxial strain introduces direction-selective distortions that couple directly to the order parameter of the cubic-to-monoclinic transformation. Theoretical analyses by Coe *et al.* [82] established that the Verwey transition is significantly more sensitive to uniaxial than to hydrostatic stress, with the response depending strongly on the crystallographic orientation of the applied load. Specifically, compression along the cubic $\langle 100 \rangle$ and $\langle 110 \rangle$ directions is predicted to increase T_V by up to $+10$ K/GPa, while compression along $\langle 111 \rangle$ should produce the opposite effect, reducing T_V by approximately -23 K/GPa.

Although these predictions have been qualitatively supported by isolated studies on thin films [87, 88] and by the uniaxial compression experiments of Nagasawa *et al.* [56], no systematic experimental verification has yet been performed on bulk stoichiometric magnetite single crystals. Moreover, compression along the $\langle 111 \rangle$ direction is expected to suppress T_V, making it difficult to distinguish between the intrinsic electronic effect of stress and the extrinsic influence of defect formation, both of which can lower T_V similarly to chemical doping or non-stoichiometry. For this reason, the experimental work presented in this Dissertation focuses on uniaxial compression applied along the cubic $\langle 100 \rangle$ and $\langle 011 \rangle$ axes, directions predicted to yield the largest positive $\partial T_V / \partial \sigma$ values. These geometries offer the most promising conditions for disentangling the pure electronic and structural consequences of anisotropic stress, without interference from defect-driven effects.

The uniaxial stress, being a controlled symmetry-breaking perturbation, provides a unique means of tuning the coupling between lattice strain, charge ordering, and magnetic interactions in magnetite. By applying stress along specific crystallographic directions and monitoring the resulting changes in transport, magnetic, and structural properties, this work aims to experimentally validate the theoretical framework proposed by Coe *et al.*, clarify the role of strain anisotropy in the Verwey transition, and establish uniaxial compression as a new tool for studying correlated-electron behavior in magnetite. The following Sections outline the objectives, methodology, and results of this research in detail.

1.3. Objectives of the Dissertation

The theoretical and experimental background presented in the preceding Sections outlined the current understanding of how chemical composition, hydrostatic pressure, and uniaxial stress affect the physical properties of magnetite, with particular emphasis on its Verwey phase transition. The literature review has shown that, although the influence of hydrostatic pressure on magnetite has been extensively studied and well characterized, the effects of uniaxial stress remain only partially explored and experimentally underrepresented.

Therefore, the central objective of this Doctoral Dissertation was to investigate how uniaxial compression applied along the cubic $[100]$ and $[011]$ directions modifies the lattice symmetry of stoichiometric magnetite and how these structural distortions influence its electronic transport and magnetic response, both at room temperature and in the vicinity of the Verwey transition. These crystallographic orientations were selected based on thermodynamic predictions [82], which indicate that stress applied along them should produce the largest positive shifts in the Verwey transition temperature, T_V. Studying these specific strain geometries provides direct experimental insight into the anisotropic coupling between lattice distortion, charge-orbital ordering, and magnetism in this prototypical strongly correlated oxide.

Carrying out such an investigation presents a considerable experimental challenge. The study of physical properties under controlled uniaxial compression requires dedicated instrumentation capable of simultaneously applying a calibrated mechanical load while allowing *in-situ* measurements of electrical resistivity, magnetic response, and structural parameters. Commercial solutions for such combined measurements are very limited, and only a few research groups worldwide have achieved stable and reproducible operation of standard techniques, such as magnetometry, diffraction, or transport, in parallel with uniaxial stress.

Consequently, a major part of this work involved the design, construction, and calibration of a custom-built uniaxial pressure cell, specifically developed to perform the measurements presented in this dissertation. This instrument was engineered to ensure precise control of the applied stress and compatibility with multiple measurement geometries, enabling the first systematic

study of the Verwey transition in bulk stoichiometric magnetite under well-defined uniaxial compression.

1.4. Outline

The structure of this Dissertation is organized as follows. Chapter 1 provides an introduction to the topic and theoretical framework of this work. It briefly outlines the nature of electronic interactions in strongly correlated systems, governed by competing electronic and lattice interactions. The Chapter then presents a comprehensive discussion of magnetite, its characteristic Verwey phase transition, and the related charge, orbital, and structural orders. Furthermore, it reviews the influence of stoichiometry, chemical doping, hydrostatic pressure, and uniaxial stress on the Verwey transition. In particular, the motivation for studying magnetite under uniaxial deformation is developed, leading to the formulation of the main research hypothesis.

Chapter 2 introduces the experimental methods and instruments used throughout this Dissertation. It begins with a review of the most effective techniques for the quantitative application of uniaxial stress and then provides a detailed description of the design, construction, and operation of a custom-built, screw-driven uniaxial pressure device developed specifically for this project. The applied compression values were verified through engineering calculations, finite-element modeling, and single-crystal X-ray diffraction calibration. This Chapter also describes the synthesis of high-quality stoichiometric magnetite single crystals and their characterization using alternating current (AC) resistivity and susceptibility measurements.

Chapter 3 presents X-ray diffraction (XRD) measurements performed under uniaxial compression on single crystals of stoichiometric magnetite. The response of the magnetite unit cell to stress applied along the [100] and [011] directions was analyzed through refinement of the diffraction patterns, allowing determination of the evolution of lattice parameters with increasing stress. From these data, the elastic components of the stress tensor were reconstructed, confirming that the measured response agrees with theoretical predictions. In addition, this Chapter includes the calibration procedure for the uniaxial pressure cell based on diffraction data.

Chapter 4 discusses synchrotron experiments conducted using the Dark-Field X-ray Microscopy (DFXM) technique. DFXM was employed to characterize the microstructure, defect density, and crystalline quality of magnetite samples obtained via two different synthesis methods. The technique provided spatially resolved information on lattice curvature and strain, enabling a direct comparison between crystals subjected to varying levels of uniaxial compression. These measurements allowed evaluation of how local defects evolve under applied stress.

Having established and validated the system for quantitative application of uniaxial compression, Chapter 5 examines the macroscopic physical properties of magnetite under load. This Chapter presents the influence of uniaxial stress applied along the [100] and [011] directions on electrical resistivity and AC magnetic susceptibility, both at room temperature and in the vicinity of the Verwey

transition. The results reveal a systematic, anisotropic increase in T_V with applied stress, approximately three times greater for compression along the [011] direction than for [100]. Furthermore, this Chapter includes X-ray absorption spectroscopy (XAS) measurements at the Fe K-edge, performed at room temperature, which probe possible changes in the local electronic environment under compression and demonstrate the feasibility of such *in-situ* studies.
Chapter 6 summarizes the results obtained throughout this work and presents the general conclusions.

Bibliography

[1] J. Clark and S. Blair. "Band Theory of Metals and Insulators". URL: *https://chem.libretexts.org/Bookshelves/Inorganic_Chemistry/Map%3A_Inorganic_Chemistry_(Housecroft)/06%3A_Structures_and_Energetics_of_Metallic_and_Ionic_solids/6.08%3A_Bonding_in_Metals_and_Semicondoctors/6.8B%3A_Band_Theory_of_Metals_and_Insulators#:~:text=Band%20Theory%20was%20developed%20with,not%20much%20difference%20in%20energy.* (visited on 07/21/2025).

[2] A. G. Gavriliuk, I. A. Trojan, and V. V. Struzhkin. "Insulator-Metal Transition in Highly Compressed NiO". *Physical Review Letters* **109** (2012), pp. 086402. DOI: 10.1103/PhysRevLett.109.086402.

[3] M.-H. Lee et al. "Controlling Metal–Insulator Transitions in Vanadium Oxide Thin Films by Modifying Oxygen Stoichiometry". *ACS Applied Materials & Interfaces* **13** (2020). DOI: 10.1021/acsami.0c18327.

[4] S. Yamada, T. Imamura, and M. Machida. "High Performance LOBPCG Method for Solving Multiple Eigenvalues of Hubbard Model: Efficiency of Communication Avoiding Neumann Expansion Preconditioner". *Supercomputing Frontiers*. Vol. 10533. Lecture Notes in Computer Science. Springer, 2018, pp. 243–256. DOI: 10.1007/978-3-319-69953-0_14.

[5] B. K. Nikolić. "Quick and Dirty Introduction to Mott Insulators. PHYS 624: Introduction to Solid State Physics, University of Delaware". URL: *http://www.physics.udel.edu/~bnikolic/teaching/phys624/phys624.html* (visited on 07/21/2025).

[6] S. Riccò et al. "In situ strain tuning of the metal-insulator-transition of Ca_2RuO_4 in angle-resolved photoemission experiments". *Nat. Commun.* **9** (2018), pp. 4535. DOI: 10.1038/s41467-018-06945-0.

[7] J. Baumgartner et al. "Magnetotactic bacteria form magnetite from a phosphate-rich ferric hydroxide via nanometric ferric (oxyhydr)oxide intermediates". *Proc. Nat. Acad. Sci. U.S.A.* **110** (2013), pp. 14883–14888. DOI: 10.1073/pnas.1307119110.

[8] A. Gupta and J. Z. Sun. "Spin-polarized transport and magnetoresistance in magnetic oxides". *J. Magn. Magn. Mater.* **200** (1999), pp. 24–43. DOI: 10.1016/S0304-8853(99)00373-X.

[9] S. de Jong et al. "Speed limit of the insulator–metal transition in magnetite". *Nat. Mater.* **12** (2013), pp. 882–886. DOI: 10.1038/nmat3718.

[10] K. Renger. "Die anfängliche Suszeptibilität von Eisen und Magnetit in Abhängigkeit von der Temperatur". PhD thesis. Eidgenössische Technische Hochschule Zürich, 1913. DOI: 10.3929/ethz-a-000091771.

[11] C. W. Heaps. "The Magnetostriction of a Magnetite Crystal". *Phys. Rev.* **24** (1924), pp. 60. DOI: 10.1103/PhysRev.24.60.

[12] E. Verwey. "Electronic Conduction of Magnetite (Fe_3O_4) and its Transition Point at Low Temperatures". *Nature* **144** (1939), pp. 327–328. DOI: 10.1038/144327b0.

[13] C. A. Domenicali. "Magnetic and Electric Properties of Natural and Synthetic Single Crystals of Magnetite". *Phys. Rev.* **78** (1950), pp. 458. DOI: 10.1103/PhysRev.78.458.

[14] J. M. Hall and R. N. Neale. "Stress Effects on Thermoremanent Magnetization". *Nature* **188** (1960), pp. 805–806. DOI: 10.1038/188805a0.

[15] R. S. Carmichael. "Hydrostatic Pressurization of Magnetite". *Geophysics* **34** (1969), pp. 775–779. DOI: 10.1190/1.1440048.

[16] T. Nagata. "Effects of a uniaxial compression on remanent magnetizations of igneous rocks". *Pure and Applied Geophysics (PAGEOPH)* **78** (1970), pp. 100–109. DOI: 10.1007/BF00874778.

[17] M. S. Senn, J. P. Wright, and J. P. Attfield. "Charge order and three-site distortions in the Verwey structure of magnetite". *Nature* **481** (2012), pp. 173–176. DOI: 10.1038/nature10704.

[18] A. '. Chemistry'. "SPINELS (Normal or Inverse)". URL: *http://www.chemohollic.com/2016/07/spinels-normal-or-inverse.html* (visited on 07/16/2025).

[19] W. H. Bragg. "XXX. The Structure of the Spinel Group of Crystals". *The London, Edinburgh and Dublin Philosophical Magazine and Journal of Science* **30** (1915), pp. 305–315. DOI: 10.1080/14786440808635400.

[20] T. Kołodziej et al. "Magnetic field induced structural changes in magnetite observed by resonant x-ray diffraction and Mössbauer spectroscopy". *Physical Review B* **102** (2020), pp. 075126. DOI: 10.1103/PhysRevB.102.075126.

[21] R. Gröger. "Mechanism of magnetization reversal in bulk and nanoparticles of magnetite". *Physical Review B* **111** (2025), pp. 134439. DOI: 10.1103/PhysRevB.111.134439.

[22] A. K. Lindquist et al. "The effects of dislocations on crystallographic twins and domain wall motion in magnetite at the Verwey transition". *Earth, Planets and Space* **71** (2019), pp. 5. DOI: 10.1186/s40623-018-0981-7.

[23] M. Bałanda et al. "Magnetic AC susceptibility of stoichiometric and low zinc doped magnetite single crystals". *Eur. Phys. J. B* **43** (2005), pp. 201–212. DOI: 10.1140/epjb/e2005-00043-5.

[24] E. J. W. Verwey and P. W. Haayman. "Electronic conductivity and transition point of magnetite ("Fe3O4")". *Physica* **8** (9, 1941), pp. 979–987.

[25] P. W. Anderson. "Ordering and Antiferromagnetism in Ferrites". *Phys. Rev.* **102** (1956), pp. 1008. DOI: 10.1103/PhysRev.102.1008.

[26] T. E. Whall, K. K. Yeung, and M. R. B. Jones. "An electronic phase transition in NiFe2O4?" *Journal of Magnetism and Magnetic Materials* **15–18** (1980), pp. 899–900. DOI: 10.1016/0304-8853(80)90814-8.

[27] Z. Kąkol, R. N. Pribble, and J. M. Honig. "Magnetocrystalline anisotropy of $Fe_{3\cdot(1-\delta)}O_4$, $0 \leq \delta < 0.01$". *Solid State Communications* **69** (1989), pp. 793–796. DOI: 10.1016/0038-1098(89)90833-8.

[28] Y. Fujii, G. Shirane, and Y. Yamada. "Study of the 123-K phase transition of magnetite by critical neutron scattering". *Physical Review B* **11** (1975), pp. 2036–2049. DOI: 10.1103/PhysRevB.11.2036.

[29] S. M. Shapiro, M. Iizumi, and G. Shirane. "Neutron scattering study of the diffuse critical scattering associated with the Verwey transition in magnetite (Fe_3O_4)". *Physical Review B* **14** (1976), pp. 200. DOI: 10.1103/PhysRevB.14.200.

[30] P. Piekarz, K. Parlinski, and A. M. Oleś. "Origin of the Verwey transition in magnetite: Group theory, electronic structure, and lattice dynamics study". *Phys. Rev. B* **76** (2007), pp. 165124. DOI: 10.1103/PhysRevB.76.165124.

[31] P. Piekarz et al. "Trimeron-phonon coupling in magnetite". *Phys. Rev. B* **103** (2021), pp. 104303. DOI: 10.1103/PhysRevB.103.104303.

[32] L. V. Gasparov et al. "Infrared and Raman studies of the Verwey transition in magnetite". *Phys. Rev. B* **62** (2000), pp. 7939. DOI: 10.1103/PhysRevB.62.7939.

[33] D. Ihle and B. Lorenz. "Small-polaron conduction and short-range order in Fe3O4". *Journal of Physics C: Solid State Physics* **19** (1986), pp. 5239. DOI: 10.1088/0022-3719/19/26/020.

[34] S. Isida et al. "Pressure effect on the elastic constants of magnetite". *Physica B: Condensed Matter* **219–220** (1996), pp. 638–640. DOI: 10.1016/0921-4526(95)00837-3.

[35] H. Schwenk et al. "Charge ordering and elastic constants in $Fe_{3-x}Zn_xO_4$". *European Physical Journal B* **13** (2000), pp. 491–494. DOI: 10.1007/s100510050060.

[36] Z. Kąkol and A. Kozłowski. "Possible influence of electron-lattice interactions on the Verwey transition in magnetite". *Solid State Sciences* **2** (2000), pp. 737–746. DOI: 10.1016/S1293-2558(00)01083-9.

[37] A. Bosak et al. "Short-Range Correlations in Magnetite above the Verwey Temperature". *Physical Review X* **4** (2014), pp. 011040. DOI: 10.1103/PhysRevX.4.011040.

[38] G. Perversi et al. "Co-emergence of magnetic order and structural fluctuations in magnetite". *Nat. Commun.* **10** (2019), pp. 2857. DOI: 10.1038/s41467-019-10949-9.

[39] K. Podgórska et al. "Correlation between magnetism and the Verwey transition in magnetite". *Phys. Rev. B* **111** (2025), pp. 245161. DOI: 10.1103/yn1s-3hv3.

[40] M. A. Carpenter et al. "A linear/quadratic order parameter coupling description of the Verwey transition in magnetite, Fe_3O_4". *Acta Crystallographica Section B: Structural Science, Crystal Engineering and Materials* **81** (2025), pp. 427–436. DOI: 10.1107/S2052520625004779.

[41] M. Iizumi et al. "Structure of magnetite (Fe_3O_4) below the Verwey transition temperature". *Acta Crystallographica Section B: Structural Crystallography and Crystal Chemistry* **38** (1982), pp. 2121–2133. DOI: 10.1107/S0567740882008176.

[42] R. Řezníček et al. "Hyperfine field and electronic structure of magnetite below the Verwey transition". *Physical Review B* **91** (2015), pp. 125134. DOI: 10.1103/PhysRevB.91.125134.

[43] J. A. Cuenca et al. "Study of the magnetite to maghemite transition using microwave permittivity and permeability measurements". *Journal of Physics: Condensed Matter* **28** (2016), pp. 106002. DOI: 10.1088/0953-8984/28/10/106002.

[44] Z. Kąkol and J. M. Honig. "Influence of deviations from ideal stoichiometry on the anisotropy parameters of magnetite $Fe_3(1-\delta)O_4$". *Phys. Rev. B* **40** (1989), pp. 9090. DOI: 10.1103/PhysRevB.40.9090.

[45] I. Biało et al. "The influence of strain on the Verwey transition as a function of dopant concentration: towards a geobarometer for magnetite-bearing rocks". *Geophysical Journal International* **219** (2019), pp. 148–158. DOI: 10.1093/gji/ggz274.

[46] K. Abe, Y. Miyamoto, and S. Chikazumi. "Magnetocrystalline Anisotropy of Low Temperature Phase of Magnetite". *Journal of the Physical Society of Japan* **41** (1976), pp. 1894–1902. DOI: 10.1143/JPSJ.41.1894.

[47] J. W. Koenitzer. "PhD Thesis". PhD thesis. Purdue University, 1992.

[48] R. Aragón. "Cubic magnetic anisotropy of nonstoichiometric magnetite". *Physical Review B* **46** (1992), pp. 5334. DOI: 10.1103/PhysRevB.46.5334.

[49] P. Novák et al. "NMR in magnetite below and around the Verwey transition". *Physical Review B* **61** (2000), pp. 1256. DOI: 10.1103/PhysRevB.61.1256.

[50] S. Chicazumi. "Magnetism Conference Contribution". *AIP Conference Proceedings*. Vol. 29. 1975, p. 382.

[51] R. Aragón. "Magnetization and exchange in nonstoichiometric magnetite". *Physical Review B* **46** (1992), pp. 5328. DOI: 10.1103/PhysRevB.46.5328.

[52] Z. Kąkol, J. Sabol, and J. M. Honig. "Cation distribution and magnetic properties of titanomagnetites $Fe_{3-x}Ti_xO_4$ $(0 \leq x < 1)$". *Phys. Rev. B* **43** (1991), pp. 649. DOI: 10.1103/PhysRevB.43.649.

[53] F. Walz. "The Verwey transition — a topical review". *J. Phys.: Condens. Matter* **14** (2002), pp. R285–R340. DOI: 10.1088/0953-8984/14/12/203.

[54] H. Elnaggar et al. "Temperature-Driven Self-Doping in Magnetite". *Phys. Rev. Lett.* **127** (2021), pp. 186402. DOI: 10.1103/PhysRevLett.127.186402.

[55] Y. Nagasawa, R. Hara, T. Seino, et al. "Uniaxial Strain Effect on T_V and Electrical Resistivity in Magnetite (Fe3O4)". *Japanese Journal of Applied Physics* (2006). DOI: 10.1063/1.2355167.

[56] Y. Nagasawa et al. "Effect of Uniaxial Strain on Verwey Transition in Magnetite". *J. Phys. Soc. Jpn.* **76** (2007), pp. 110–111. DOI: 10.1143/JPSJS.76SA.110.

[57] M. Mizoguchi. "Structure of Fe_3O_4 in the low temperature phase as deduced from advanced analysis of the NMR study". *Journal of the Physical Society of Japan* **54** (1985), pp. 2168–2183. DOI: 10.1143/JPSJ.54.2168.

[58] J. Żukrowski et al. "AC magnetic susceptibility under pressure and Mössbauer effect studies of the isotropy point TIP in magnetite". *Journal of Alloys and Compounds* **442** (2007), pp. 219–221. DOI: 10.1016/j.jallcom.2006.06.113.

[59] R. Aragón and R. H. McCallister. "Phase and point defect equilibria in the titanomagnetite solid solution". *Phys. Chem. Miner.* **8** (1982), pp. 112–120. DOI: 10.1007/BF00311281.

[60] R. Aragón et al. "Skull melter single crystal growth of magnetite (Fe_3O_4) – ulvospinel (Fe_2TiO_4) solid solution members". *J. Cryst. Growth* **61** (1983), pp. 221–228. DOI: 10.1016/0022-0248(83)90358-5.

[61] R. Aragón et al. "Effect of stoichiometry changes on electrical properties of magnetite". *Journal of Magnetism and Magnetic Materials* **54–57** (1986), pp. 1335–1336. DOI: 10.1016/0304-8853(86)90844-9.

[62] M. J. Jackson and B. Moskowitz. "On the distribution of Verwey transition temperatures in natural magnetites". *Geophys. J. Int.* **224** (2021), pp. 1314–1325. DOI: 10.1093/gji/ggaa516.

[63] R. Prozorov et al. "Response of the Verwey transition in magnetite to controlled point-like disorder induced by 2.5 MeV electron irradiation". *Materials Research Bulletin* **167** (2023), pp. 112442. DOI: 10.1016/j.materresbull.2023.112442.

[64] K. Yuan et al. "Oxidation induced strain and defects in magnetite crystals". *Nature Communications* **10** (2019), pp. 703. DOI: 10.1038/s41467-019-08470-0.

[65] S. S. Aplesnin and G. I. Barinov. "Pressure-induced orbital ordering in magnetite above the Verwey temperature". *Physics of the Solid State* **49** (2007), pp. 1949–1952. DOI: 10.1134/S1063783407100228.

[66] N. Môri et al. "Metallization of magnetite at high pressures". *Physica B* **312–313** (2002), pp. 686–690. DOI: 10.1016/S0921-4526(01)01525-3.

[67] G. K. Rozenberg et al. "Nature of the Verwey transition in magnetite (Fe3O4) to pressures of 16 GPa". *Physical Review B* **53** (1996), pp. 6482. DOI: 10.1103/PhysRevB.53.6482.

[68] Y. Kakudate, N. Mori, and Y. Kino. "Pressure effect on the anomalous electrical conductivity of magnetite". *Journal of Magnetism and Magnetic Materials* **12** (1979), pp. 22–25. DOI: 10.1016/0304-8853(79)90329-9.

[69] S. K. Ramasesha et al. "High-pressure study of Fe_3O_4 through the Verwey transition". *Physical Review B* **50** (1994), pp. 13789–13792. DOI: 10.1103/PhysRevB.50.13789.

[70] J. Spałek et al. "Verwey transition in Fe_3O_4 at high pressure: Quantum critical point at the onset of metallization". *Phys. Rev. B* **78** (2008), pp. 100401(R). DOI: 10.1103/PhysRevB.78.100401.

[71] N. Môri, S. Todo, N. Takeshita, et al. "Metallization of magnetite at high pressures". *Physica B: Condensed Matter* **312–313** (2002), pp. 686–690. DOI: 10.1016/S0921-4526(01)01525-3.

[72] S. Todo et al. "Metallization of magnetite under high pressure". *Journal of Applied Physics* **89** (2001), pp. 7347–7349. DOI: 10.1063/1.1359460.

[73] H. Kobayashi et al. "Structural properties of magnetite under high pressure studied by Mössbauer spectroscopy". *Physical Review B* **73** (2006), pp. 104110. DOI: 10.1103/PhysRevB.73.104110.

[74] Z. Tarnawski et al. "Studies of the Verwey Transition in Magnetite". *Acta Phys. Pol. A* **106** (2004), pp. 771–774. DOI: 10.12693/APhysPolA.106.771.

[75] K. Chen et al. "Revisiting the Phase Transition of Magnetite under Pressure". *J. Phys. Chem. C* **123** (2019), pp. 21114–21119. DOI: 10.1021/acs.jpcc.9b04140.

[76] L. S. Dubrovinsky et al. "The structure of the metallic high-pressure Fe_3O_4 polymorph: experimental and theoretical study". *J. Phys.: Condens. Matter* **15** (2003), pp. 7697–7706. DOI: 10.1088/0953-8984/15/44/003.

[77] A. Schult. "Effect of pressure on the Curie temperature of titanomagnetites $[(1-x)\cdot \mathrm{Fe_3O_4} - x\cdot \mathrm{TiFe_2O_4}]$". *Earth and Planetary Science Letters* **10** (1970), pp. 304–308. DOI: 10.1016/0012-821X(70)90067-1.

[78] S. Klotz et al. "Magnetism and the Verwey transition in Fe_3O_4 under pressure". *Phys. Rev. B* **77** (2008), pp. 012411. DOI: 10.1103/PhysRevB.77.012411.

[79] S. Isida et al. "Ultrasonic Study of the High Temperature Phase of Fe_3O_4". *Journal of the Physical Society of Japan* **67** (1998), pp. 3125–3129. DOI: 10.1143/JPSJ.67.3125.

[80] J.-F. Lin et al. "Abnormal Elastic and Vibrational Behaviors of Magnetite at High Pressures". *Scientific Reports* **4** (2014), pp. 6282. DOI: 10.1038/srep06282.

[81] T. Nagata and H. Kinoshita. "Studies on piezo-magnetization (I): Magnetization of titaniferous magnetite under uniaxial compression". *J. Geomagnetism and Geoelectricity* **17** (1965), pp. 121–135. DOI: 10.5636/jgg.17.121.

[82] R. S. Coe et al. "The thermodynamic effect of nonhydrostatic stress on the Verwey transition". *Earth and Planetary Science Letters* **319–320** (2012), pp. 207–217. DOI: 10.1016/j.epsl.2011.11.021.

[83] Y. Nagasawa et al. "Effect of Uniaxial Strain on Verwey Transition in Magnetite". *J. Phys. Soc. Jpn.* **76** (2007), pp. 110–111. DOI: 10.1143/JPSJS.76SA.110.

[84] Y. Nagasawa et al. "Effect of Uniaxial Strain on Verwey Transition in Magnetite". *Journal of the Physical Society of Japan Supplement* **76** (2007), pp. 110–111. DOI: 10.1143/JPSJS.76SA.110.

[85] Y. Nagasawa et al. "Uniaxial Strain Effect on T_V and Electrical Resistivity in Magnetite (Fe_3O_4)". *AIP Conf. Proc.* Vol. 850. 2006, pp. 1267–1268. DOI: 10.1063/1.2355167.

[86] M. Liu et al. "Non-volatile ferroelastic switching of the Verwey transition and resistivity of epitaxial Fe_3O_4/PMN-PT (011)". *Sci. Rep.* **3** (2013), pp. 1876. DOI: 10.1038/srep01876.

[87] X. Liu et al. "Fe_3O_4 thin films: controlling and manipulating an elusive quantum material". *npj Quantum Mater.* **1** (2016), pp. 16027. DOI: 10.1038/npjquantmats.2016.27.

[88] X. H. Liu, W. Liu, and Z. D. Zhang. "Evolution of magnetic properties in the vicinity of the Verwey transition in Fe_3O_4 thin films". *Phys. Rev. B* **96** (2017), pp. 094405. DOI: 10.1103/PhysRevB.96.094405.

Chapter 2.

Uniaxial pressure application and sample preparation

The purpose of this Chapter is to present and discuss the experimental work carried out within the scope of this Dissertation. Section 2.1 begins with a review of uniaxial stress setups previously reported in the literature, providing the context for the experimental design adopted in this study.

Section 2.1.2 then describes the custom uniaxial stress cell developed specifically for this project and employed in all subsequent experiments. The apparatus is a screw-driven, vise-like system in which a titanium alloy spring transfers the applied load to the sample. To determine the force acting on the specimen, the setup was analyzed using three complementary approaches: analytical modeling based on the Euler–Bernoulli formalism (Section 2.1.4), finite element simulations (Section 2.1.5), and experimental calibration by single-crystal X-ray diffraction (Section 2.1.6).

Section 2.2 describes the synthesis of stoichiometric magnetite single crystals using two complementary methods: the Traveling Solvent Floating Zone and the Skull Melter techniques. The subsequent Section 2.3 presents the procedures used for crystal characterization and for measuring their response to applied stress, including four-probe electrical resistivity (Section 2.3.1) and AC magnetic susceptibility (Section 2.3.2). Finally, Section 2.3.3 details the design and testing of the custom AC susceptibility setup adapted for operation under controlled uniaxial stress.

2.1. Uniaxial pressure devices

During the last century, geophysicists have studied mineral materials under extreme conditions, such as high and low temperatures, high magnetic fields, and high pressures reaching hundreds of gigapascals (GPa). For specimens of geological origin, such high hydrostatic pressures mimic the conditions prevailing in the Earth's interior. In physics and materials science, hydrostatic pressure has been applied to systems that exhibit novel electronic properties, providing insights into how electronic states respond to increased band overlap and uncovering potential lattice instabilities arising from reduced interatomic distances.

High hydrostatic pressures on the order of GPa are typically generated using diamond anvil cells (DACs). A DAC consists of two opposing diamonds with flattened culets and a metallic gasket placed between them. At the center of this gasket, there is a small chamber that contains both the sample and a pressure indicator, usually a ruby crystal; see Fig. 2.1a [1].

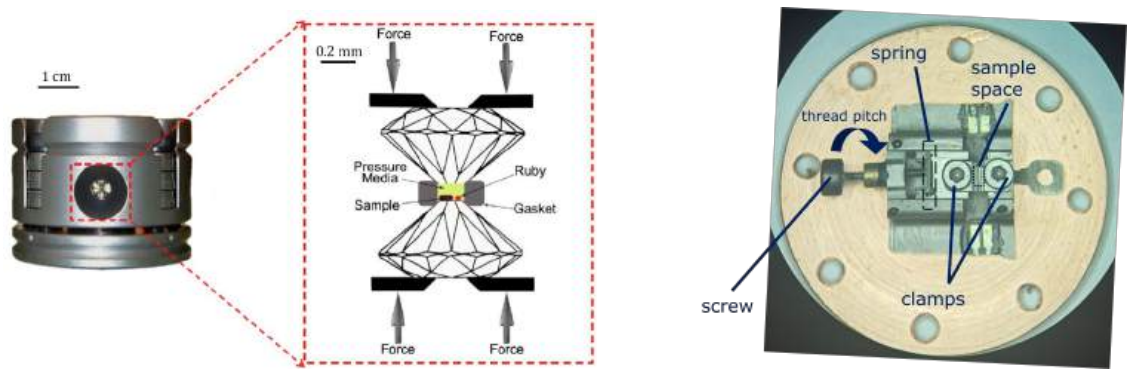

(a) (b)

Fig. 2.1. Representations of a typical hydrostatic and uniaxial pressure device. **(a)** Schematic of a diamond anvil cell (DAC). **Zoom in:** Enlarged frontal cross-section of the DAC. The diamonds are compressed by normal forces applied from the top and bottom of the setup. The sample and pressure-transmitting fluid are enclosed within a gasket, together with a ruby crystal used as a pressure reference [1]. **(b)** Prototype of a screw-driven uniaxial pressure application system, developed in collaboration between AGH and TU Wien. The active component of this device is a flat, deformable spring that compresses the sample positioned between the mounting clamps.

In parallel with the development of hydrostatic techniques, the last two decades have seen rapid progress in the design and use of setups that generate uniaxial pressure. The experimental advantage of uniaxial stress lies in its ability to break rotational symmetry and potentially induce new effects, particularly in systems that are anisotropic in their equilibrium state or undergo phase transitions that result in asymmetric ordering.

This behavior has, for example, been observed in cuprate superconductors, which feature a layered structure with a tetragonal CuO_2 plaquette as their fundamental unit. Application of uniaxial stress

breaks the C_4 symmetry, distorting the copper oxide planes and thereby influencing superconductivity [2, 3, 4].

In another fundamentally important strongly correlated system, magnetite, the high-temperature structure is regular *Fd-3m*, but it transforms into a monoclinic *Cc* structure below T_V, as discussed in Chapter 1. Here, the application of uniaxial stress deforms the structure both above and below T_V, influencing the Verwey transition [5, 6].

In both systems, the need to explore their properties has driven the development of experimental techniques involving uniaxial stress. The next section presents and discusses several methods for the quantitative generation and control of uniaxial stress. Following that, the setup used in this work is described in detail.

2.1.1. Overview of the pressure application techniques

Most uniaxial pressure cells described in the literature operate on a vise-like principle, as illustrated in Fig. 2.1b. The generated force is applied to the clamps, which then transfer it to the mounted sample. Several methods for generating uniaxial stress have been reported, with the most commonly used including:

- differential thermal contraction between the cell components;
- application of voltage to a piezoelectric material;
- expansion of a known volume of compressed gas;
- mechanical displacement of jaws.

The first setup, a strain rig operating on the principle of differential thermal contraction between titanium and aluminum, was discussed in detail in [7]. As the temperature changes, titanium contracts at a different rate than aluminum, leading to the compression of the sample platform. A detailed schematic of this instrument is shown in Fig. 2.2.

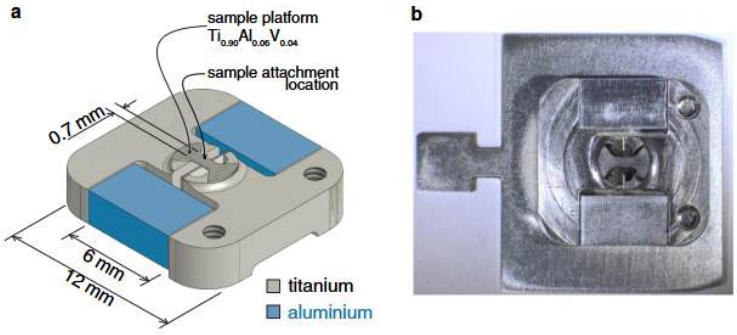

Fig. 2.2. Uniaxial pressure cell designed on an Omicron holder, operating based on thermal contraction. **(a):** Illustration of the strain rig. The sample is mounted at the center of the rig. The passive part is made of **titanium**, while the active bottom part is made of **aluminum**. Upon cooling, the differing contraction of these components generates stress, which is transferred to the sample. **(b):** Photograph of the strain rig mounted on a standard flag-style sample plate. Adapted from [7].

The stress device that operates based on the piezoelectric effect is shown in the left panel of Fig. 2.3. The piezoelectric actuators are connected to a power supply and contract/expand depending on the applied voltage. By selecting the polarity of the power supply, either tensile or compressive stress can be applied. The use of this type of cell, combined with magnetic susceptometry (as shown in the middle panel of Fig. 2.3), led in 2017 to the observation of a pronounced peak in the temperature dependence of susceptibility at the critical temperature of the magnetic phase transition in strontium ruthenate, Sr_2RuO_4 [2]. Piezoelectric uniaxial cells, like the one depicted in Fig. 2.3, are now commercially available.

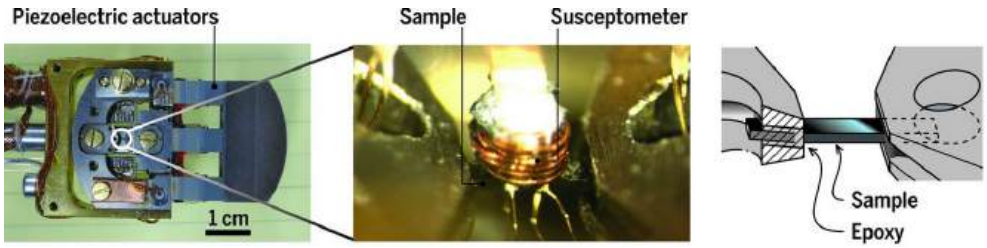

Fig. 2.3. Experimental setup used for measuring AC susceptibility under uniaxial stress. **Left:** Sample cartridge with the zoomed area highlighted. **Middle:** Enlarged view of the sample with attached susceptibility coils. **Right:** Schematic illustration of sample mounting using epoxy glue. Adapted from [2].

In recent years, a prototype pressure probe driven by compressed helium gas was developed in collaboration between AGH and Technische Universität Wien (TUW); see Fig. 2.4. The device comprises two gas pistons, one fixed and the other movable. Injection of helium gas into the system at a chosen pressure actuates the pistons with high precision, allowing accurate control of the applied uniaxial strain.

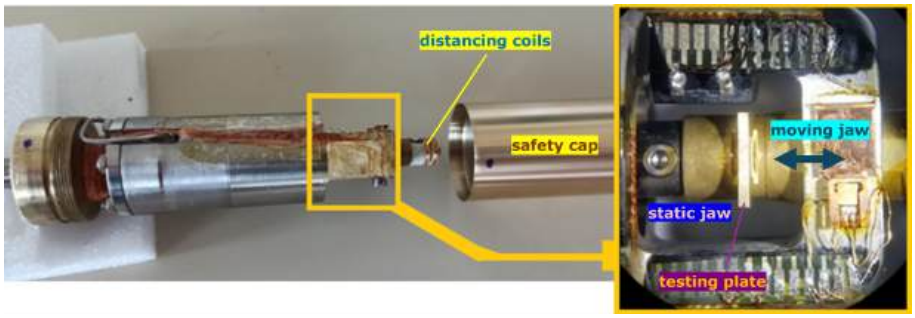

Fig. 2.4. Side view of the uniaxial pressure probe driven by compressed helium, with a safety cylinder mounted on the probe's stem. The head of the probe features an inductive displacement measurement system comprising two coils wound onto movable ceramic holders. **Inset:** Top view of the pressure clamps holding a brass test plate of millimeter thickness. The left jaw is fixed to the cartridge and remains stationary, while the right jaw shifts in response to helium gas flow. The relative displacement between the jaws is measured via the self-induction voltage generated by the displacement coils. Proprietary photograph.

Two ceramic disks are attached to the lower end of the probe, each containing a tightly wound coil of 0.1 mm copper wire. These coils are used for inductive measurement of the distance between the mounting jaws. The maximum separation between the jaws is 3 mm, which sets the upper limit for the length of the crystal under investigation. This probe can be switched between two working modes by reversing the direction of the gas flow. The pressure jaws then either compress or apply tension. The operational temperature range is between 6 K and 300 K.

A screw-driven mechanical chamber, shown in Fig. 2.5, was recently used to investigate the effects of uniaxial pressure on NdFeB magnets [8]. This type of cell was also employed in all experiments conducted within the framework of this Dissertation. Its operating principle is relatively simple, which offers practical advantages, for example, when working inside a high-vacuum chamber. However, under such conditions, it can be challenging to precisely manipulate the screw and, consequently, to control the applied pressure indirectly.

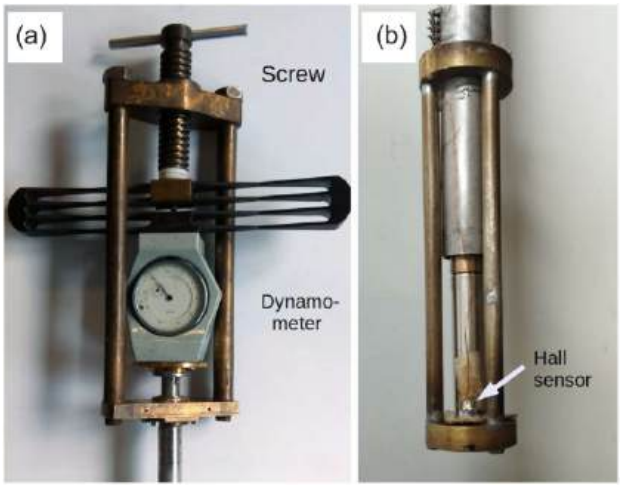

Fig. 2.5. (a): Screw-driven mechanical chamber with a compression indicator. The pressure application mechanism is based on a 3D-printed cartridge, which transfers the force onto the magnet specimen and enables reading the applied pressure from the dynamometer. **(b):** A Hall sensor attached to the magnet measures the magnetic induction, $\mathbf{B}$.

This brief overview of current uniaxial pressure techniques highlights only the most representative approaches. The following section presents the development, characterization, and testing of uniaxial pressure devices, which constitute one of the key achievements of this dissertation.

2.1.2. Construction of the uniaxial SOL systems

All the results presented in this dissertation were obtained using a mechanical uniaxial pressure cell developed in collaboration between AGH University and TU Wien. The system was specifically adapted for use with Omicron flag-type holders to enable operation at the end stations of the National Center for Synchrotron Radiation SOLARIS, Jagiellonian University in Krakow. Consequently, each generation of these cells was referred to as "SOL" for short. A schematic of the SOL uniaxial pressure cell and a photograph of an actual device are shown in Figs. 2.6a and 2.6b, respectively.

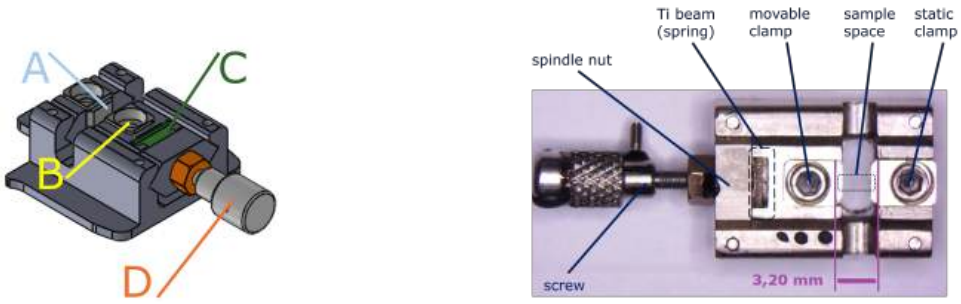

(a) (b)

Fig. 2.6. (a): Schematic of the SOL system. Labels A through D indicate the main components of the setup: A – sample mounting spot, B – compressing clamp, C – a flat plate spring, D – spindle with an M1.6 screw. **(b):** Photograph of the SOL3 cell. The maximum sample length is 3 mm. The spring is a flat plaquette made from a Ti-6Al-4V alloy, deformed by the M1.6 screw during the stress application. The system was tested over a temperature range from 10 K to 330 K.

The SOL cells employ a vise-like mechanism with a detachable base plate and are compatible with both synchrotron and laboratory-based experimental setups. Each SOL apparatus can accommodate a crystal in the shape of a parallelepiped, up to 3 mm in length. The pressure application system consists of two components: a flat-plate spring and a screw. The spring is made from a Ti-6Al-4V alloy, composed of 90% titanium, 6% aluminum, and 4% vanadium, with a Young's modulus of $E = 112.0$ GPa at room temperature. The dimensions of the spring are $5 \times 3 \times 0.5$ mm^3, with rounded fillets at the edges. It is mounted so that its effective length is 3.8 mm. Rotating the screw bends the spring, which in turn applies force to the mounting clamps. The sample placed between these clamps is thereby subjected to uniaxial compression.

The force exerted on the clamp, resulting from a known deformation of the screw, was first estimated analytically, as detailed in Section 2.1.4. Additionally, it was simulated numerically using the finite element method (FEM), as discussed in Section 2.1.5, and directly measured through single-crystal diffraction experiments (Section 2.1.6).

2.1.3. Calibration of pressure cells

An accurate estimation of the force exerted on the sample upon rotation of the screw to a specified angle is fundamental to the operation of the developed cells. This estimation was initially obtained using an analytical approach and subsequently compared with calculations performed in the ABAQUS engineering environment. Finally, the estimated force was validated through a diffraction experiment, in which the deformation measured in the SOL cells was compared to that observed using a calibrated ADMET press.

2.1.4. Analytical estimation of the applied stress

The active element of the SOL cell is a flat spring made of a titanium alloy, further referred to as the "beam". The known deformation of this beam generates the force $\underline{\mathbf{F}}$, which acts indirectly on the sample. The magnitude of this force, F, was estimated based on the depth to which the screw was driven, using the simplified Euler-Bernoulli equation for the bending of a one-dimensional beam.

The configuration of the beam that pushes the clamp holding the sample is illustrated in Fig. 2.7. The absolute dimensions of the undeformed beam along the x, y, and z directions are denoted by L_b, B_b, and T_b, respectively. The flat surface lies in the xy-plane, while the thickness is measured along the z-axis. When the beam, fixed at both ends, is bent, the clamp is displaced by the combined effect of the reaction forces $\underline{\mathbf{F}} = \underline{\mathbf{F_A}} + \underline{\mathbf{F_C}}$.

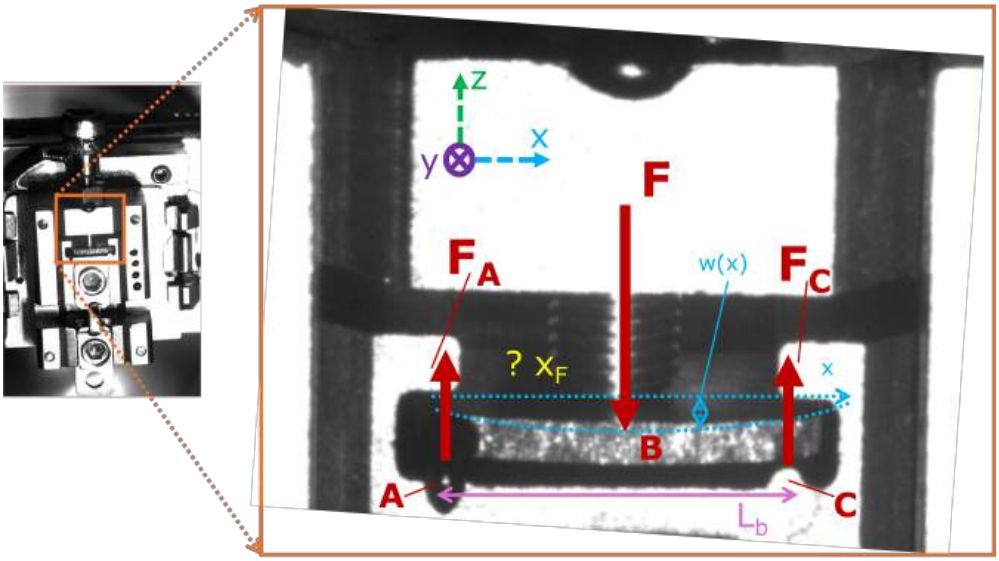

Fig. 2.7. SOL4 cell in the ultra high vacuum chamber of the PIRX beamline at SOLARIS. Zoom: The screw is turned to the extent that the deformation profile of the beam $w(x)$ can be clearly noticed. Points A and C denote the fixed edges of the beam spaced by L_b. The central force $\underline{\mathbf{F}}$ in point B is compensated by the resultant of the reaction forces, $\underline{\mathbf{F_A}}$ and $\underline{\mathbf{F_C}}$.

Since the central force $\underline{\mathbf{F}}$ applied at position x_F, as well as the corresponding reaction forces $\underline{\mathbf{F_A}}$ and $\underline{\mathbf{F_C}}$ on the clamp blades, act vertically along the $-z$-axis, they generate opposing torques. For mechanical equilibrium, the sum of all torques produced by these forces must cancel out, which implies:

$$F_A = F \cdot \frac{L_b - x_F}{L_b}, \tag{2.1.1}$$

$$F_C = F \cdot \frac{x_F}{L_b}. \tag{2.1.2}$$

The external deforming forces determine the elastic response of the beam, which, in turn, generates internal forces distributed along its length. These internal forces cause local deformations of the beam and are described by the bending moment. In the reference frame adopted here, the bending moment is oriented solely along the y-axis:

$$\underline{\mathbf{M_{xy}}} = -\left[\int_y dy \left[\int_0^{T_b} dz \quad (\sigma_{xx} \cdot z)\right] \underset{\sim}{\mathbf{e_y}}\right], \tag{2.1.3}$$

where σ_{xx} is a normal component of the stress tensor and $\underset{\sim}{\mathbf{e_y}}$ is the versor of y. Respecting Eq. 2.1.1, the bending moment, M_{AB} acting on the point x with the arm to the left of the applied force F, is given by:

$$M_{AB}(x) = F_A \cdot x, \tag{2.1.4}$$

and from Eq. 2.1.2, the bending moment at point x, with the lever arm extending to the right of the force F, is given by:

$$M_{BC}(x) = F_C \cdot (L_b - x). \tag{2.1.5}$$

These moments bend the beam, and its deflection profile, $w(x)$, can be described using the simplified Euler–Bernoulli beam equation:

$$\frac{\partial^2 (w(x))}{\partial x^2} = -\frac{M(x)}{E \cdot I_y}, \tag{2.1.6}$$

where $M(x)$ represents the bending moment at position x, defined as $M(x) \equiv M_{AB}(x)$ for the left segment and $M(x) \equiv M_{BC}(x)$ for the right segment of the beam, respectively. E denotes the Young's modulus of the beam material, while I_y is the second moment of area (also known as the area moment of inertia) about the y-axis, characterizing the distribution of internal stresses and strains resulting from the applied bending moment M:

$$I_y = \int_{-\frac{B_b}{2}}^{\frac{B_b}{2}} dy \left(\int_{-\frac{T_b}{2}}^{\frac{T_b}{2}} dz \quad z^2\right) = \frac{B_b \cdot T_b^3}{12}. \tag{2.1.7}$$

The maximum deformation of the beam, w_{max}, is derived from Eq. 2.1.6. The shape functions for the left and right segments of the beam, w_{AB} and w_{BC}, along with their first derivatives, are continuous and equal at the point of applied force, $x = x_F$. By solving Eqs. 2.1.1, 2.1.2, and 2.1.3 independently and applying the boundary conditions at $x = 0$ and $x = L_b$, the beam deflection w_{max} is obtained at $x = x_F = \frac{L_b}{2}$:

$$w\left(\frac{L_b}{2}\right) \equiv w_{\mathsf{max}} = \frac{F \cdot L_b^3}{4 \cdot E \cdot B_b \cdot T_b^3}, \tag{2.1.8}$$

and, therefore, the force dependent on the maximal deformation of the beam is given by:

$$F = w_{\mathsf{max}} \cdot \frac{4 \cdot E \cdot B_b \cdot T_b^3}{L_b^3}. \tag{2.1.9}$$

Since w_{max} is determined by the screw pitch, the force F acting on the sample scales linearly with the rotation of the thread. This force is ultimately converted into the uniaxial stress applied to the sample according to the relation $\sigma = \frac{F}{w \cdot t}$, where w and t represent the width and thickness of the sample, respectively.

The detailed derivation of Eq. 2.1.9 is broader discussed in the Appendix D.

2.1.5. Simulation of the spring deformation using Finite Element Method

Engineering problems such as heat dissipation, mechanical impacts, or fluid dynamics must be addressed using mathematical formalism and numerical methods. Models developed with these tools aim to reproduce real-world behavior as accurately as possible. The specific model discussed in this section consists of two elements: a flat beam and a long rod. The beam, shaped into a rounded plate, is supported at its edges on the rear side, as in the case of the SOL cell. The end of the rod, acting as the tip of the screw, is in contact with the front face of the beam.

The movement of the rod, quantified as the elastic deformation of the beam, is described by a differential equation (DE) for the entire system. However, due to the non-trivial geometry of the setup, deriving and solving the equation of motion directly from first principles becomes cumbersome. Therefore, the Finite Element Method (FEM) was chosen to address this problem. In the FEM procedure, called meshing, the analyzed object is divided into many smaller parts known as elements. These elements are connected at specific points called nodes. While differential equations describe the behavior of each individual element, for the entire model, equations governing the interactions at the element boundaries are formulated. These discontinuities within the domain are referred to as boundary conditions (BCs).

The exact solutions of the differential equations (DEs) are approximated within the individual elements through a procedure that involves the following steps:

1. In each finite element (FE), a shape function (SF) is defined. The SF should approximate the physical behavior of the system while remaining simple enough for efficient computation. Typically, linear functions or low-degree polynomials are used. These functions are then used to construct approximations of the general solutions to the partial differential equations (PDEs).

2. The shape functions defined in the individual elements are then combined ("glued") at the nodes to form basis functions that span the entire computational domain, which consists of the sum of all FEs.

3. Next, the original PDEs are reformulated into an integral form that incorporates the predefined boundary conditions (BCs).

4. The approximate solution produced by FEM is expressed as a linear combination of the basis functions. The input for the FEM solver is a large system of linear algebraic equations. Solving this system yields the coefficients (weights) of the basis functions that together represent the desired solution.

Calculations are repeated or adjusted if the obtained results deviate significantly from realistic behavior predicted by experiments. The most common sources of error include inaccurately defined model geometry, material constants or interactions, and imprecise boundary conditions (BCs). Additionally, insufficient accuracy in the representation of floating-point numbers can lead to poor approximations. The basics of the ABAQUS/CAE software used in this study, along with a simple example of solving the equation $y = x^2$ using FEM, are provided in Appendix C. ABAQUS does not use a native unit system, placing the responsibility for all necessary unit conversions on the user. The FEM analysis of the beam deformation was performed in the following stages:

- sketching the parts and meshing the geometry;
- applying the loads and boundary conditions;
- submitting the job for analysis;
- visualization and postprocessing.

The beam was made of an alloy composed of 90% Ti, 6% Al, and 4% V (Ti-6Al-4V). The mechanical properties assigned to this alloy in the simulation are listed in Table 2.8. The screw tip, an M1.6 thread with a pitch of 0.20 mm used to bend the beam, was assumed to be made of ST4 construction steel ($E = 200000\,\mathrm{MPa},\ \nu = 0.28$).

PARAMETER	Ti-6Al-4V
E [MPa]	112‘000
ν [1]	0.342

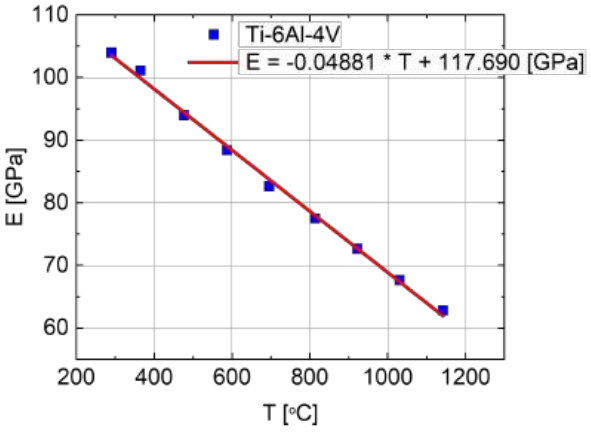

Fig. 2.8. Left: Mechanical properties of the Ti-6Al-4V alloy at room temperature as defined in the Abaqus environment. The values of the Young's modulus, E, and the Poisson's ratio, ν, were extrapolated from the graph shown on the right. **Right:** Temperature dependence of the Young's modulus for the Ti-6Al-4V alloy in the range of 250–1200°C. Adapted from [9].

The simulation began with the definition of the geometry of the elements used for mechanical analysis, as shown in Fig. 2.9. The computational mesh was generated using a semi-automated algorithm and consisted of approximately 11‘000 polyhedral elements.

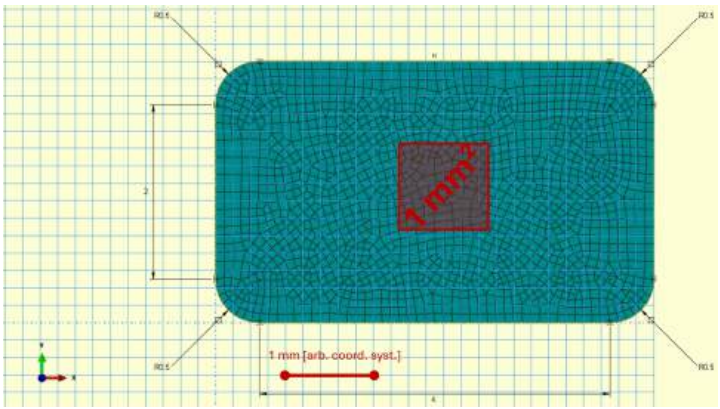

Fig. 2.9. Geometry definition for the FEM simulation. The plate was meshed using a combination of cubic and polyhedral elements. The mesh dimensions are indicated in the figure. The central red square marks the region impacted by the cell screw and is used for stress recalculations.

The front geometry of the simulation and the applied contact load are shown in Fig. 2.10a, while the fixed section of the beam in contact with the clamp blades is depicted in Fig. 2.10b. It was assumed that one-tenth of a full screw rotation displaced its tip by 0.02 mm, corresponding to a 0.20 mm displacement for a complete turn.

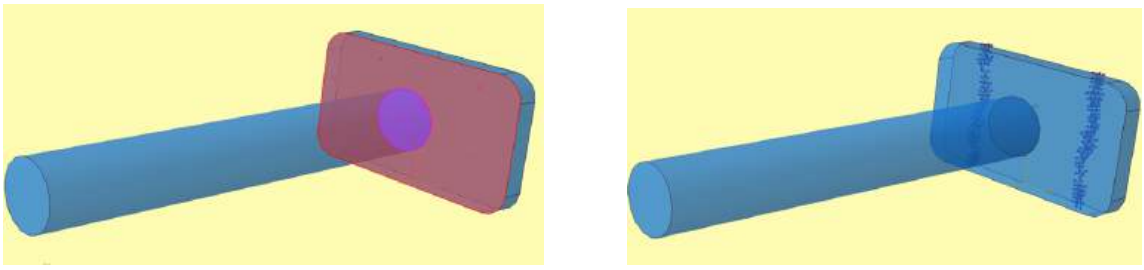

(a) (b)

Fig. 2.10. Definition of the contact interaction and boundary conditions (BCs). **(a):** Front view of the bolt and plate used for mechanical analysis. The violet circle indicates the master surface initiating the contact, while the orange-red envelope marks the slave surface receiving it. **(b):** View of the model with constrained BCs. The dark blue symbols represent nodes with restricted translation and rotation, corresponding to the rear section of the clamp in contact with the plate via two vertical blades.

The results of the completed calculations are shown in Fig. 2.11. The color scale indicates the magnitude of the reaction force (RF) accumulated in the individual elements of the model. The total force, obtained by summing the RF at each node of the mesh, was 14.50 N per 1° of screw rotation. Assuming a linear relationship between the applied force and the beam deformation, the estimated force corresponding to a full screw rotation was 5220 N. The obtained value was several times higher than that estimated analytically or experimentally assessed from the crystal lattice parameters measured using X-ray diffraction. This experimental approach is briefly presented in Section 2.1.6, with more details and quantitative analysis provided in Chapter 3.

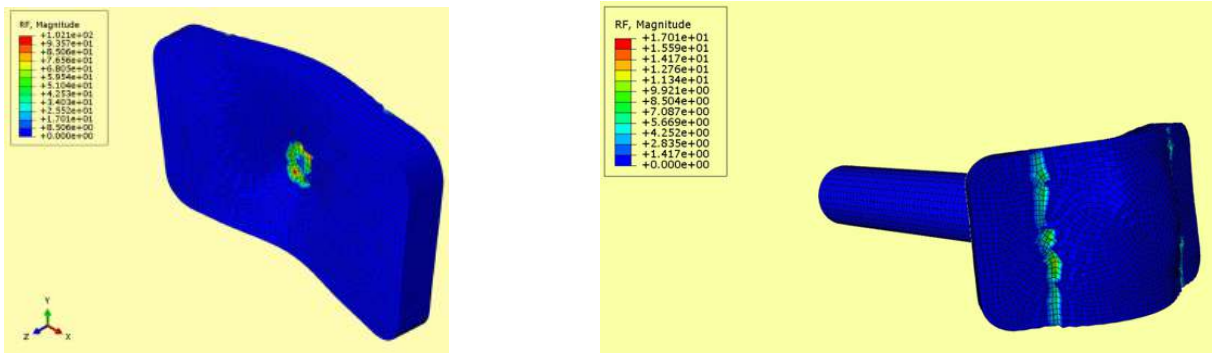

(a) (b)

Fig. 2.11. Distribution of the reaction force (RF) obtained from the FEM calculations. Green indicates RF values between 30 and 70 N, while yellow and red correspond to values ranging from 70 to 100 N. **(a):** Front view of the mesh. The largest deflection and accumulated force are observed in the elements in direct contact with the screw tip. **(b):** Rear view of the deformed mesh. The highest RF values are concentrated in the immobilized nodes, which simulate the spring pressing against the clamp blades.

2.1.6. Experimental calibration of the developed SOL devices

The calibration of each SOL cell was carried out using single-crystal X-ray diffraction at the ID11 beamline of the ESRF. At this stage, the procedure is presented solely from a methodological perspective, while the full quantitative analysis of the calibration results is provided in Chapter 3. This separation ensures that Chapter 2 focuses on the experimental setup and methodological aspects of the calibration, while Chapter 3 provides a comprehensive quantitative evaluation based on the diffraction results.

During the experiment, X-ray diffraction (XRD) patterns were collected at room temperature for single crystals of stoichiometric magnetite subjected to increasing uniaxial compression. Two samples, denoted as A and B, were investigated specifically to enable a direct comparison between different uniaxial loading systems. Sample A, with a cross-sectional area of 1.00 mm^2, was mounted in the commercial ADMET press, whereas Sample B, with a cross-sectional area of 0.36 mm^2, was mounted in the SOL2 cell. The conversion from applied force to stress was performed using the cross-sectional area S, according to the relation $\sigma = \frac{F}{S}$. Both samples were compressed along the [011] crystallographic direction, and at each pressure step their lattice constants and lattice angles were extracted from the analysis of the XRD patterns. Because the ADMET system is equipped with an integrated force sensor, the uniaxial stress calculated for sample A provided an absolute reference. This, in turn, enabled the calibration of the stress values obtained for sample B in the SOL2 cell, where the applied force was then converted into the screw rotation.

The raw data used for calibrating the SOL2 cell against the ADMET press are presented in Fig. 2.12. In panels (a) and (c), the lattice parameters and angles, respectively, are plotted as a function of stress for the sample mounted in the ADMET press, whereas in panels (b) and (d) the corresponding quantities are plotted as a function of screw rotation for the SOL2 cell. A direct comparison of the evolution of lattice constants and angles obtained for samples A and B enabled the determination of the calibration factor for the SOL2 cell. Assuming a linear dependence of the lattice parameters on the applied uniaxial stress, a change in the b and c axes from 8.397 to 8.934 Å was observed for sample A at a stress of $\sigma = 150$ MPa. This variation corresponded to approximately 164° of screw rotation for sample B, yielding a calibration factor of 1.09 ± 0.05 MPa/1°. Converting the stress back into force gave a corresponding value of 0.39 ± 0.02 N/1°.

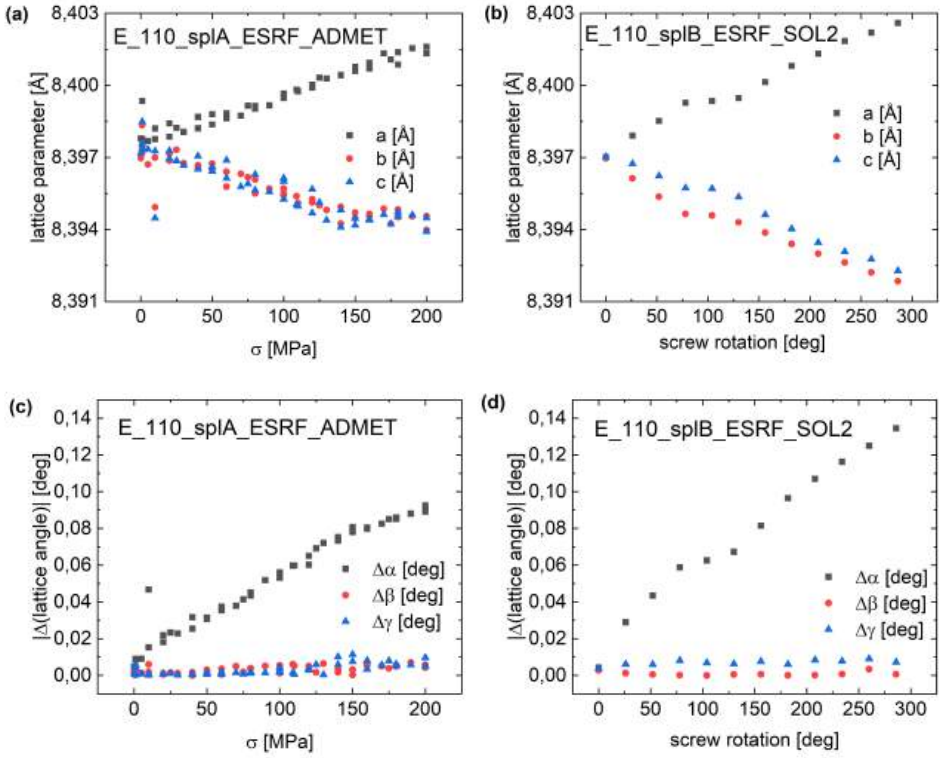

Fig. 2.12. Evolution of the lattice parameters **(a), (b)** and lattice angles **(c), (d)** of magnetite under uniaxial compression along the [011] direction, measured for reference sample A using the calibrated ADMET cell (left) and for sample B using the uncalibrated SOL2 cell (right). The direct comparison of lattice constants and angles between both datasets enabled the calibration of the SOL2 cell, yielding a conversion factor of approximately 1 MPa per 1° of screw rotation.

An analogous procedure was performed for the samples labeled G and F, which were compressed along the [100] crystallographic direction. Sample G was mounted in the ADMET press, while sample F was installed in the SOL3 cell. Both samples had identical cross-sectional areas of 0.40 mm^2. In this case, the comparison between ADMET and SOL3 was based exclusively on the evolution of the lattice parameters, since the lattice angles exhibited negligible variation with pressure, consistent with the expected tetragonal distortion of the cubic lattice under [100] compression. As shown in Fig. 2.13, the c lattice parameter of sample G reached 8.391 Å at an applied uniaxial stress of $\sigma = 87$ MPa. This matched the deformation observed in sample F after 150° of screw rotation, corresponding to a calibration factor of 0.58 MPa/1° (0.23 N/1°).

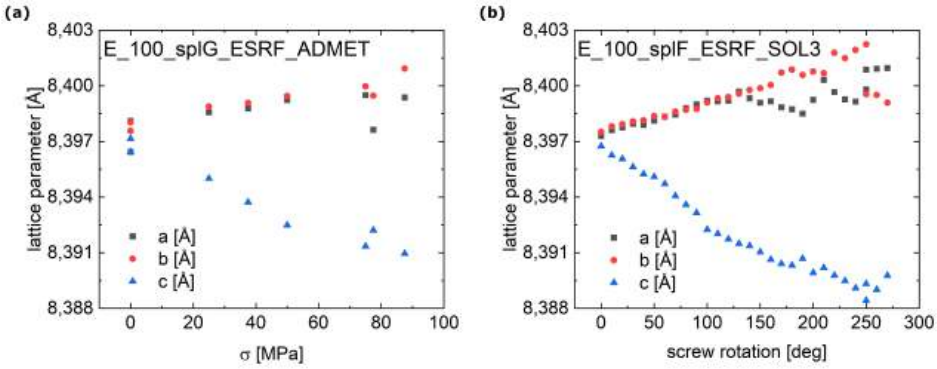

Fig. 2.13. Evolution of the lattice parameters under uniaxial stress applied along the [100] direction. **(a):** Sample G was mounted in the ADMET press and served as the reference frame. **(b):** Sample F was installed in the SOL3 cell, and the applied compression was estimated based on the screw rotation. Comparison of matching lattice constants between samples G and F yielded a calibration factor for SOL3 of approximately 0.6 MPa/1°.

The calibration factors extracted for the [100] and [011] directions differed by approximately 53%. In principle, the Ti-alloy beam in the SOL cell undergoes the same deformation for each 1° screw rotation, and the resulting force should be independent of the crystal orientation. However, if the screw rotation also induces axial translation, a portion of the thread pitch may not be fully converted into applied force, which could partly account for the observed discrepancy. In addition, the proper mounting of the sample in the SOL cell was found to have a significant influence on the magnitude of the generated uniaxial force. It should also be emphasized that the calibration was performed in terms of force rather than pressure. This distinction is the fundamental reason why the calibration factors obtained for the SOL cells differed between the [100] and [011] orientations, as further discussed in Chapter 3.

The complete quantitative analysis of all samples measured at ID11, including the three SOL cells and the reference measurements performed with the ADMET press, is presented in Chapter 3. All samples originated from the same batch grown by the floating-zone technique and were cut into nearly identical dimensions. The reproducibility observed for samples A, B, G, and F is therefore representative of the entire batch. Consequently, the calibration procedure described here can be reliably generalized to the samples investigated with other experimental techniques, as reported in Chapters 4 and 5.

A summary of all the techniques used to calibrate the force in this Chapter is provided in Table 2.1. Among the available approaches, X-ray diffraction (XRD) offered the most direct and accurate estimation of the uniaxial force exerted by the SOL systems. Nevertheless, alternative methods, analytical modeling, and numerical simulations were also explored, as they remain widely used for force estimation and can provide valuable insight during early-stage design and implementation, even if they lack absolute accuracy.

The initial estimates of the force using a simplified Euler–Bernoulli model describing the bending of a flat titanium alloy beam offered a straightforward analytical framework and served as a practical starting point for understanding the mechanical response of the system. However, the model relies on idealized assumptions, including uniform material properties, small deformations, and well-defined boundary conditions, which are often not fully met in real-world setups. To improve upon these limitations, the mechanical system was further analyzed using the Finite Element Method (FEM), implemented in the ABAQUS simulation environment. This method accounted for the realistic geometry of the SOL system and more complex boundary constraints. However, the FEM simulations significantly overestimated the force applied for a given screw rotation, with values far exceeding both analytical predictions and experimental calibration.

This overestimation can be attributed to several factors. First, the FEM model likely overconstrained the deformation region, relying on idealized assumptions about contact mechanics between the screw tip and the spring plate. In reality, the geometry of the screw is more complex: the model treated it as a smooth, flat cylinder, whereas the actual screw is threaded and has a cone-shaped tip. These simplifications may have led to unrealistic stress localization. Second, the computations neglected friction effects, both between the spindle and the screw thread and within the moving clamp assembly of the SOL cell. Such interactions, though difficult to model, significantly influence the effective transmission of force. While these limitations could be addressed through more sophisticated meshing and by incorporating additional elements of the SOL cell into the model, this would greatly increase the complexity of the simulation, which was not the main objective of this dissertation. Third, although the material properties for the Ti-6Al-4V alloy were extrapolated from literature, subtle variations introduced by machining, cold work, or surface finish may have modified the actual mechanical response. Fourth, ABAQUS requires the user to define a consistent unit system, and inaccuracies in dimensional scaling or material parameters can strongly distort the final output. Finally, the real system exhibits further mechanical transmission losses, such as backlash and elastic dissipation at interfaces, which are not captured in the simplified numerical model.

Despite these limitations, both the analytical and numerical methods remain valuable tools for preliminary modeling and qualitative understanding. However, only the X-ray diffraction approach, described in detail in Chapter 3, enabled precise *in- situ* calibration of the uniaxial stress, based on the evolution of lattice parameters under controlled compression. This method inherently accounts for all mechanical imperfections and material-specific behaviors, making it the reference standard throughout this dissertation. Therefore, all reported pressure values are derived from XRD-based calibration, and the other methods are presented here primarily for completeness and cross-validation.

F [N/1°]	F [N/1 rotation]	Method
0.4	145	single-crystal XRD
2.0	720	theory of elasticity
14.5	5220	FEM simulation

Tab. 2.1. Comparison of the calibration factors obtained for the SOL2 cell using X-ray diffraction, the simplified Euler–Bernoulli formula, and FEM simulation. The left column shows the force value normalized to a 1° rotation of the screw, while the middle column provides the value for a full turn. The calibration method used is indicated in the right column.

2.2. Synthesis of magnetite single crystals

Although the synthesis of the samples was not part of the work carried out within the scope of this dissertation, this section provides an overview of two methods used for the synthesis of high-purity, stoichiometric magnetite single crystals. These are the Traveling Solvent Floating Zone (TSFZ) method and the skull melting technique. Crystals produced by both methods were measured and further characterized for internal defects, which will be discussed in detail later in the dissertation.

One of the crystals was obtained using the skull melting method in the laboratory of Prof. J. Honig at Purdue University (West Lafayette, IN). This single crystal, grown in the 446^{th} batch, was labeled SM446. The texture and disorder in sample SM446 were investigated using diffraction microscopy, as presented in Chapter 4. The same sample was also used to test the AC susceptibility coils under uniaxial pressure, which is described in this chapter and further detailed in Appendix B.

The second crystal was obtained using the TSFZ technique. All samples studied as a function of uniaxial pressure originated from this single synthesis batch. The batch was kindly provided through a collaboration with Dr. Emilio Lorenzo from the Institut Néel CNRS and Dr. Christophe Marin from the Université Grenoble Alpes, France. As a result, these samples were typically labeled with a capital letter “E” at the beginning.

2.2.1. Synthesis with the Traveling Solvent Floating Zone method

The synthesis using the Traveling Solvent Floating Zone (TSFZ) method is carried out in a reflective optical furnace, schematically illustrated in Fig. 2.14a. The key components of this furnace include two halogen lamps, two concave mirrors, and a rotatable sample holder. This holder accommodates a pelletized rod made from powdered polycrystalline material. The halogen lamps, positioned on either side of the furnace, emit electromagnetic radiation with peak intensity in the infrared range. The ellipsoidal mirrors located behind the lamps focus the thermal energy onto a central region known as the “hot zone” [10]. A small piece of the desired compound, known as the

seed crystal, is required to initiate and sustain the crystal growth. The seed can be obtained either by locally heating the rod to form a nucleation point or by inserting a pre-grown crystal produced by an alternative method [11, 12].

The samples investigated in this dissertation were synthesized using a Crystal Systems, Inc. FZ-T-10000-H-VI-P-G optical furnace. The crystal growth process begins with the preparation of two rods from powdered, polycrystalline material. The Fe_3O_4 feed and seed rods were fabricated using high-purity powder (Alfa Aesar, 99.997%) that was compressed into cylindrical shapes under a pressure of 1200 bar using an isostatic press [13]. To ensure high density, the compacted rods underwent a two-step annealing process: first, they were annealed for 12 hours at 850 °C in air, followed by an additional 12-hour annealing at 1350 °C under a pure argon atmosphere.

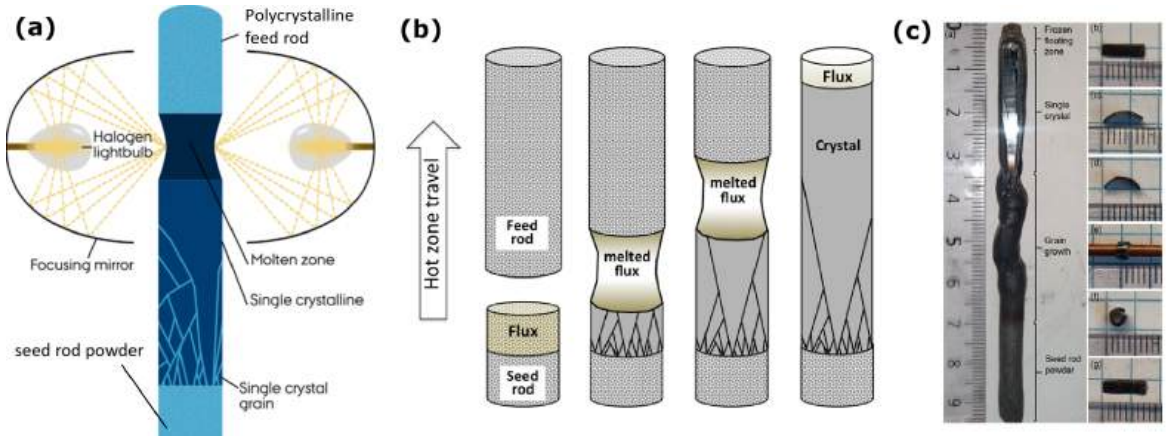

Fig. 2.14. (a): Schematic of a traveling solvent floating zone furnace. The seed crystal that initiates the growth is typically obtained from a previous batch or produced by maintaining the hot zone at a fixed position for an extended period. The polycrystalline material melts within the hot zone, as the light generated by halogen lamps is concentrated using ellipsoidal mirrors [11]. **(b):** The molten zone is suspended between the polycrystalline feed rod and the growing crystal. By gradually shifting the hot zone upward, the single crystal is formed as material recrystallizes onto the seed rod [14, 15]. **(c):** A few centimeters long growth of InSe obtained with the TSFZ technique. Photograph adapted from [16].

Inside the furnace, the feed rod is hung with a thin platinum wire above the seed rod, so that they are spaced by a few milimeters. Applying the heat from the halogen lamps and focusing it by the set of elliptical mirrors melts the tips of the feed and seed rods. At that point, the upper feed rod is levered down to touch the seed rod and form a stable melt zone. Throughout the synthesis, both these rods are moved downwards, so that the molten zone, denoted in Fig. 2.14b as the flux, progresses up the length of the feed rod. The hot zone can reach temperature of 2400° C during the operation of the furnace, while the rest of the synthesis chamber remains mostly cool [15, 17, 18].

TSFZ is a crucible-less technique and relies on moving the hot zone that melts the substrates by aligning the infrared optics. The reaction conditions are typically controlled using a noble gas

mixed with oxygen. In this case, the crystal growth was stabilized under a continuous flow of argon at 1.013 bar. Argon was flushed at a rate of 0.5 l/min, corresponding to a partial pressure of O_2 equal to 2.026×10^{-5} bar. The growth rate was maintained at 5 mm/h, with the feed and seed rods rotating at 30 rpm. The resulting single crystal rod measured approximately 5 cm in length and 6 mm in diameter. Its high structural quality was confirmed by the presence of a sharp Verwey transition at $T_V = 121$ K.

2.2.2. Synthesis with the skull melter method

Another method for producing high-quality single crystals, particularly suitable for iron oxides, is the skull melter technique. This method relies on radio frequency (RF) induction heating of the feed material within a cold crucible formed by the unmelted portion of the same material. A simplified schematic of the induction melter, showing the RF coils and cooling fingers, is presented in Fig. 2.15.

The synthesis begins with powdered hematite, Fe_2O_3, of at least 99.995% purity. The powder serves as the "skull," isolating the melt from the water-cooled copper fingers and preventing external contamination [19, 20]. The molten powder is then subjected to subsolidus annealing in a CO/CO_2 gas mixture, which maintains the desired 3:4 stoichiometric ratio between iron and oxygen. The annealing time is calculated based on the vacancy diffusion constants in magnetite and typically amounts to approximately 3 days for 1 cm^3 crystals annealed at $T = 1200\,^{\circ}$C.

If the reaction temperature was stable and the partial pressures of CO and CO_2 were fixed by a constant flow ratio, the partial pressure of oxygen, pO_2, remained conserved. pO_2 was monitored using a ZrO_2/Y_2O_3 transfer chamber calibrated against Ni/NiO phase boundaries. This sensor consisted of two electrodes separated by a solid electrolyte, ZrO_2, functioning analogously to galvanic cells containing ions dissolved in a liquid. Pure oxygen served as the reference gas, and a difference in pO_2 between the electrodes generated an electromotive force (EMF), which enabled the control of $\log(pO_2)$ with an accuracy of 1%.

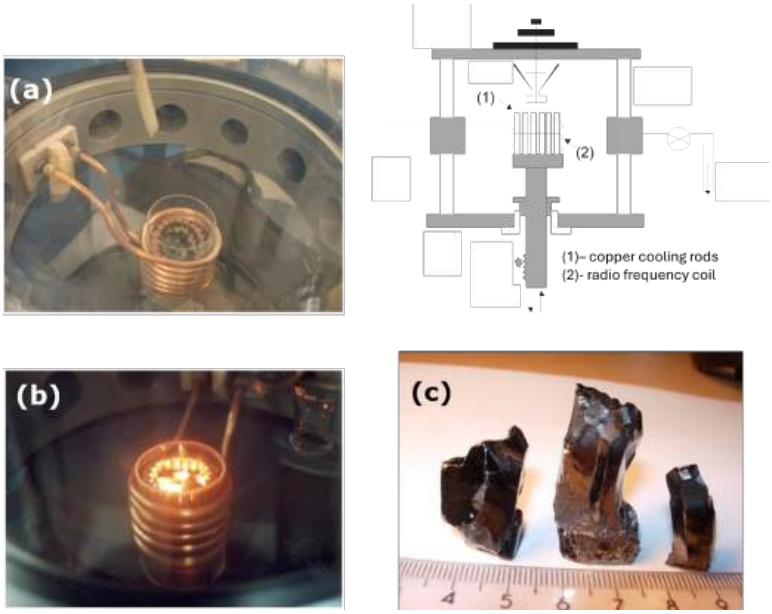

Fig. 2.15. Synthesis of magnetite single crystals using a skull melter. **(a):** The crucible equipped with cooling rods. In the schematic diagram shown on the right, the cooling rods and the RF coil are labeled as (1) and (2), respectively. **(b):** Photograph of an ongoing synthesis process. The emitted glow originates from the molten reagents. **(c):** Fragments of single crystals, each of approximately cm^3 volume, obtained from a single growth run.

This was sufficient to ensure that the stoichiometry parameter, δ, in $Fe_{3\cdot(1-\delta)}O_4$ was controlled with an accuracy of up to 10^{-4}. Following synthesis, the crystals were rapidly quenched to room temperature to halt further diffusion of O_2 into the structure. This procedure caused the partially oxidized surface layers to detach and chip off.

The principal disadvantage of the skull melter method is the large temperature gradients that occur within the boule. These gradients give rise to parasitic processes, such as segregation or intergrowth, which compromise the homogeneity of the synthesis. Additionally, the presence of thermal gradients combined with rapid quenching increases the strain field by generating high-temperature disorders and vacancies at the B site. These imperfections are readily detected using techniques such as the Magnetic After Effect [21]. The single crystals of magnetite grown by this method typically reach sizes of a few cm^3.

2.3. Characterization of magnetite single crystals

In the following Sections, 2.3.1 and 2.3.2, the characterization methods and the general procedure for preparing uniaxial pressure experiments are described. These procedures were followed throughout this work. The samples were investigated under uniaxial compression using two techniques:

temperature-dependent AC electrical resistivity (measured at 2000 Hz in the range 77–1000 K) and low-frequency AC magnetic susceptibility (measured in the range 77–300 K).

2.3.1. Electrical resistivity measured using the four-probe method

The first step in sample preparation was to orient the grown crystals along one of the $\langle 100 \rangle$ or $\langle 110 \rangle$ directions. The orientation was done using a Laue back-scattering instrument in the laboratories of the Institute of Solid-State Physics at TU Wien in Austria. An example of such a diffraction pattern, obtained for a single crystal of magnetite oriented along the $\langle 100 \rangle$ direction, is shown in Fig. 2.16a.

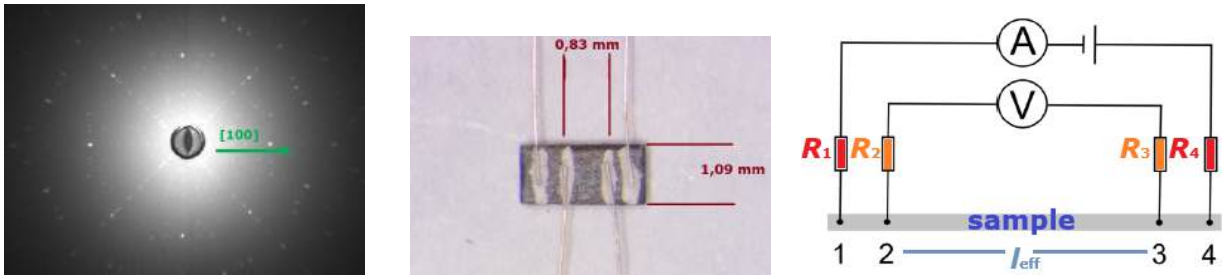

(a) (b) (c)

Fig. 2.16. Preparation of the sample for electronic transport measurements. **(a):** Orientation using the Laue technique. The diffraction pattern shows cubic symmetry, with the green arrow indicating the [100] direction along which the crystal was cut. **(b):** After cutting and polishing, the sample was electrically contacted using 50 μm gold wires and 6838 HT silver paint. The longest edge of the crystal is aligned with the [100] direction. The markers indicate the effective length between the voltage contacts, 0.83 mm, and the width of the crystal, 1.09 mm. **(c):** Schematic of the four-probe method. l_{eff} is the effective length of the sample. A and V are the ammeter and voltmeter, respectively. The red pair, R_1 and R_4, indicates the resistance of the current contacts, while the orange pair, R_2 and R_3, represents the resistance of the voltage contacts.

The oriented crystal was subsequently cut into slices and then into strips with typical dimensions of $l = 2.5$ mm, $w = 1.0$ mm, and $t = 0.5$ mm, aligned along the specified crystallographic directions. The final polishing was performed using P500 and P1000 grade water sandpapers. Considering the use of a high-precision cutting tool (Well Diamond Wire Saw, Inc.) and the size of the silver paste contacts, as shown in Fig. 2.16b, the uncertainty in the effective sample dimensions used for estimating the specific resistivity was approximately 0.1 mm.

The temperature dependence of the resistivity, $\rho(T)$, was measured using the four-probe method. The principle of this method is illustrated in Fig. 2.16c. It involves two current contacts, I, and two voltage contacts, U. The key advantage of the four-probe technique is that the measurement of the voltage drop across the sample is not influenced by the contact resistance at the sample-

electrode interface. Both the current and voltage contacts were prepared using silver paste, as shown in Fig. 2.16c. Further details on contact preparation are provided in Appendix A.

2.3.2. Characterization of magnetic susceptibility with alternating current method

The alternating current (AC) magnetic susceptibility, χ_{AC}, was employed as a complementary technique to electrical resistivity for characterizing the magnetite samples. A major experimental achievement of this dissertation was the design and implementation of a dedicated system for measuring χ_{AC} under uniaxial compression. Compact enough to fit within the mechanical and cryogenic constraints of the SOL pressure cells, the system is shown in Fig. 2.17 and described in detail in Section 2.3.3 and Appendix B. Its construction required careful experimental optimization of coil parameters, including wire thickness, number of turns, and geometry, while maintaining a miniature footprint compatible with the pressure setup. Signal quality was enhanced by fine-tuning the excitation conditions, such as the driving current amplitude and frequency, to maximize sensitivity and minimize noise. The final configuration allowed reliable detection of $\chi_{AC}(T)$ with sufficient resolution to track subtle features, including the Verwey transition under varying uniaxial loads, forming the basis of the results presented in Chapter 5.

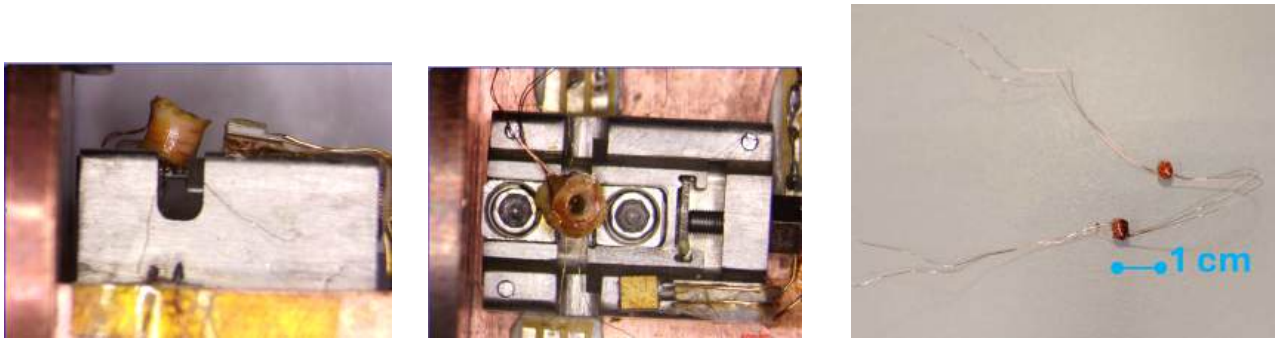

(a) (b) (c)

Fig. 2.17. Measurement of AC susceptibility under uniaxial pressure. **(a):** Side view of the pressure cell with signal coils attached to the sample. **(b):** Top view of the setup shown in panel 2.17a, where the reference coils are mounted at the base of the pressure cell. **(c):** Top view of the coils prepared for AC susceptibility measurements, prior to their attachment to the pressure cell. The light blue line serves as a scale reference.

The principle of the χ_{AC} technique is well established and relies on the generation of an alternating magnetic field by an emitter coil. This field is modified by the magnetic response of the sample, and, according to Faraday's law, induces an electromotive force (EMF) in the receiver coil. The magnitude of the induced EMF is proportional to the magnetic susceptibility, χ, of the sample.

2.3.3. Design of the AC susceptibility measurement system under uniaxial compression

The final coil configuration used for the measurements is shown in Fig. 2.17c. It consisted of a signal coil pair placed on top of the sample and a detection coil pair, as schematically illustrated in Fig. 2.18. The coils in the signal pair were wound together in a clockwise direction, denoted as $[\uparrow,\uparrow]$. In contrast, the detection pair consisted of one coil wound clockwise and the other counterclockwise, represented as $[\uparrow,\downarrow]$.

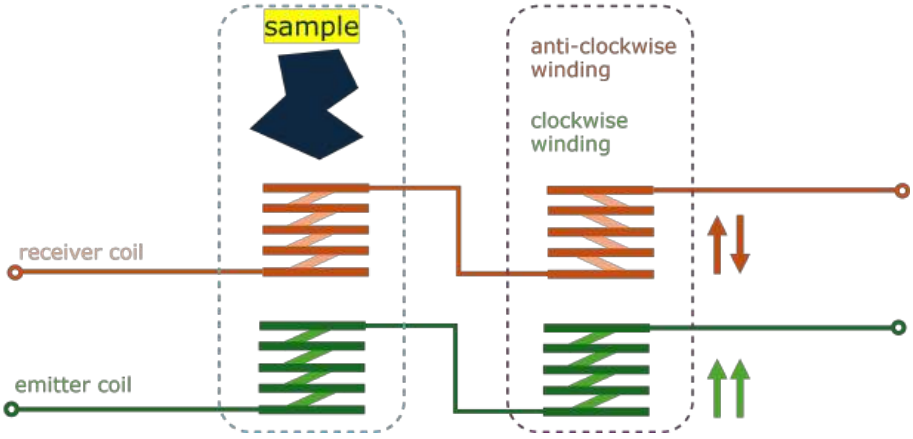

Fig. 2.18. Schematic of the custom-designed AC susceptibility setup. The emitter circuit is plotted in green, and the receiver circuit in orange. The input current generates a magnetic flux in the emitter coils, which is transferred to the receiver coils via mutual induction. The measured susceptibility is proportional to the voltage detected in the receiver coils. The coils attached to the sample and responsible for signal generation are enclosed in the cyan dashed frame, while the reference coils set is marked with the purple dashed frame.

The emitter coils are driven by a lock-in amplifier supplying an alternating current with frequency $f = \frac{\omega}{2\pi}$, which generates a time-dependent magnetic field of the form $H(t) = H_0 + H_1 \cdot \cos(\omega t)$. This field is nominally identical for both emitter coils. If the receiver coils are also identical, the electromotive forces (EMFs) induced in the receiver circuit nearly cancel each other out. However, when a sample is introduced, the symmetry is broken, and a net EMF is detected. When the magnetic field generated by the emitter coils oscillates in time, the sample responds with a phase-shifted magnetization:

$$M(t) = M_0 + M_1 \cdot \cos(\omega t - \varphi) = M_0 + M_1 \cdot \cos(\omega t) \cdot \cos(\varphi) + M_1 \cdot \sin(\omega t) \cdot \sin(\varphi), \qquad (2.3.10)$$

where the possibility of static magnetization, M_0 due to the static field, H_0 is taken into account. Finally:

$$M(t) = \chi_0 \cdot H_0 + \frac{M_1 \cdot \cos(\varphi)}{H_1} \cdot H_1 \cdot \cos(\omega t) + \frac{M_1 \cdot \sin(\varphi)}{H_1} \cdot H_1 \cdot \sin(\omega t) \tag{2.3.11}$$

$$M(t) = \chi_0 \cdot H_0 + \chi' \cdot H_1 \cdot \cos(\omega t) + \chi'' \cdot H_1 \cdot \sin(\omega t), \tag{2.3.12}$$

where:

$$\chi_0 = \frac{M_0}{H_0}, \quad \chi' = \frac{M_1 \cdot \cos(\varphi)}{H_1}, \quad \chi'' = \frac{M_1 \cdot \sin(\varphi)}{H_1}. \tag{2.3.13}$$

represent, respectively, the static susceptibility (χ_0), the dispersive (real) component of the dynamic susceptibility (χ'), and the absorptive (imaginary) component (χ''), which corresponds to the energy dissipated in the system. The sample magnetization $M(t)$ induces an alternating magnetic field $B_1(t)$ in the first receiver coil and $B_2(t)$ in the second:

$$B_1(t) = \mu_0 \cdot H_1 \cdot \cos(\omega t) + \mu_0 \cdot (\chi' \cdot H_1 \cdot \cos(\omega t) + \chi'' \cdot H_1 \cdot \sin(\omega t)), \tag{2.3.14}$$

$$B_1(t) = \mu_0 \cdot H_1 \cdot ((1 + \chi') \cdot \cos(\omega t) + \chi'' \cdot \sin(\omega t)), \tag{2.3.15}$$

$$B_2(t) = \mu_0 \cdot H_1 \cdot \cos(\omega t). \tag{2.3.16}$$

Therefore, the EMFs produced in both coils are as follows:

$$\mathcal{E}_1 = -A \cdot \frac{\partial B_1(t)}{\partial t} = A \cdot \mu_0 \cdot H_1 \cdot \omega \cdot (-(1 + \chi') \cdot \sin(\omega t) + \chi'' \cdot \cos(\omega t)), \tag{2.3.17}$$

$$\mathcal{E}_2 = -A \cdot \frac{\partial B_2(t)}{\partial t} = A \cdot \mu_0 \cdot H_1 \cdot \omega \cdot (-\sin(\omega t)), \tag{2.3.18}$$

where A denotes the effective area (geometry) of the coil. Thus, the EMF signal detected by the lock-in amplifier, $\cdot\mathcal{E}$, is given by:

$$\cdot\mathcal{E} = \mathcal{E}_1 - \mathcal{E}_2 = A \cdot \mu_0 \cdot H_1 \cdot \omega \cdot (-\chi' \cdot \sin(\omega t) + \chi'' \cdot \cos(\omega t)). \tag{2.3.19}$$

Both χ' and χ'' can be measured simultaneously, with each component detected at the appropriate phase shift relative to the driving current. For the presentation of the experimental results in Chapter 5, the component χ' was selected to study the Verwey transition using $\chi_{AC}(T)$ under uniaxial compression, as it exhibits a clear step at T_V.

2.4. Conclusions

This Chapter provided a comprehensive review of the most prominent techniques used for applying hydrostatic and uniaxial stress in condensed matter experiments. Particular attention was given to uniaxial pressure setups based on the miniaturized vise principle, owing to their mechanical simplicity

and adaptability to different experimental platforms. Within this framework, a novel class of screw-driven uniaxial pressure cells, collectively referred to as "SOL", was developed in collaboration between AGH University and TU Wien. These cells were specifically engineered to integrate with Omicron-style holders and operate reliably at the end stations of the SOLARIS synchrotron in Kraków. Their robust mechanical design, compact size, and adaptability for cryogenic and high-vacuum environments make them a practical and versatile tool for synchrotron-based studies of correlated electron systems.

The force exerted by the SOL uniaxial pressure systems was quantified using a comprehensive, multi-method approach. The initial estimates were derived analytically using the simplified Euler–Bernoulli formalism for bending a flat Ti-6Al-4V alloy spring. This model offered an accessible approximation of the mechanical response based on known geometric and material parameters. To account for more complex constraints and geometry, these results were further refined using numerical simulations based on the Finite Element Method (FEM) implemented in the ABAQUS environment. While FEM allowed for realistic modeling of contact interactions and stress distributions, it significantly overestimated the applied force compared to both the analytical predictions and experimental data.

The most accurate force calibration was achieved through synchrotron-based single-crystal X-ray diffraction. By comparing the lattice deformations of magnetite samples subjected to uniaxial stress in the SOL setup with those in a calibrated commercial ADMET press, precise force-to-rotation conversion factors were determined. This approach inherently accounted for real mechanical behavior, including contact losses and material-specific effects. Slight discrepancies were observed depending on the crystallographic orientation and quality of sample mounting, underscoring the importance of consistent experimental configuration. The full calibration methodology and its validation are discussed in detail in Chapter 3, which serves as the foundation for all pressure values reported in this dissertation.

This Chapter also outlined the methods employed for synthesizing high-quality single crystals of stoichiometric magnetite, using both the Traveling Solvent Floating Zone (TSFZ) technique and the skull melter method. The TSFZ technique, performed in a reflection furnace under carefully controlled atmospheres, yielded crystals of high structural integrity, used throughout this dissertation. In contrast, crystals produced via the skull melter exhibited increased internal strain due to rapid quenching and steep thermal gradients, as discussed in relation to magnetic aftereffect studies. Comprehensive characterization of the crystals was conducted through temperature-dependent AC electrical resistivity and AC magnetic susceptibility measurements. Notably, a custom-built miniature setup for AC susceptibility under uniaxial compression was developed, validated, and integrated into the SOL uniaxial pressure system. The design and operational details of this susceptibility rig are presented in Appendix B.

Bibliography

[1] Z. Dong and Y. Song. "Novel Pressure-Induced Structural Transformations of Inorganic Nanowires". *Nanowires - Fundamental Research*. Chapter published July 19, 2011. IntechOpen, 2011. DOI: 10.5772/17084.

[2] A. Steppke et al. "Strong peak in T_c of Sr_2RuO_4 under uniaxial pressure". *Science* **355** (2017), pp. eaaf9398. DOI: 10.1126/science.aaf9398.

[3] N. Barišić and D. K. Sunko. "High-T Cuprates: a Story of Two Electronic Subsystems". *Journal of Superconductivity and Novel Magnetism* **35** (2022), pp. 1781–1799. DOI: 10.1007/s10948-022-06183-y.

[4] E. Johansson et al. "The effect of strain and pressure on the electron-phonon coupling and superconductivity in MgB_2 — Benchmark of theoretical methodologies and outlook for nanostructure design". *Journal of Applied Physics* **131** (2022), pp. 063902. DOI: 10.1063/5.0078765.

[5] Y. Nagasawa et al. "Uniaxial Strain Effect on T_V and Electrical Resistivity in Magnetite (Fe_3O_4)". *AIP Conf. Proc.* Vol. 850. 2006, pp. 1267–1268. DOI: 10.1063/1.2355167.

[6] Y. Nagasawa et al. "Effect of Uniaxial Strain on Verwey Transition in Magnetite". *J. Phys. Soc. Jpn.* **76** (2007), pp. 110–111. DOI: 10.1143/JPSJS.76SA.110.

[7] V. Sunko et al. "Direct observation of a uniaxial stress-driven Lifshitz transition in Sr_2RuO_4". *npj Quantum Materials* **4** (2019), pp. 37. DOI: 10.1038/s41535-019-0185-9.

[8] V. Nizhankovskiy. "Influence of uniaxial compression on magnetization of NdFeB magnet". *Acta Physica Polonica A* **147** (2025), pp. 3. DOI: 10.12693/APhysPolA.147.3.

[9] R. Peraldi and J. C. Scully. "The effect of temperature on the stress corrosion cracking of a high strength steel in a CO2/H2S environment". *Materials Science and Engineering: A* **125** (1990), pp. 35–44. DOI: 10.1016/0921-5093(90)90097-M.

[10] S. M. Koohpayeh. "Single crystal growth by the traveling solvent technique: A review". *Progress in Crystal Growth and Characterization of Materials* **62** (2016), pp. 22–34. DOI: 10.1016/j.pcrysgrow.2016.03.001.

[11] National High Magnetic Field Laboratory. "Image Furnace". URL: *https://nationalmaglab.org/about/around-the-lab/what-the/image-furnace* (visited on 01/04/2025).

[12] Paul Scherrer Institut. "Materials Synthesis, Crystal Growth and Characterization". URL: *https://www.psi.ch/en/lmx-ssc/equipment* (visited on 03/17/2025).

[13] F. Delille et al. "Study of the electronic paraprocess and antiphase boundaries as sources of the demagnetisation phenomenon in magnetite". *Journal of Magnetism and Magnetic Materials* **294** (2005), pp. 27–39. DOI: 10.1016/j.jmmm.2004.12.018.

[14] N. Kase, N. Kimizuka, and N. Miyakawa. "Recent progress of the single crystal growth of homologous $(InGaO_3)_m(ZnO)_n$". *CrystEngComm* **24** (2022), pp. 4481–4495. DOI: 10.1039/D2CE00439A.

[15] Z. R. Group. "Single Crystal Growth". URL: *https://alexzevalkink.wordpress.com/research/* (visited on 08/01/2025).

[16] J. Svane et al. "Optical Floating-Zone Furnace Single-Crystal Synthesis of van der Waals Material InSe". *Cryst. Growth Des.* **24** (2024), pp. 6965–6971. DOI: 10.1021/acs.cgd.4c00520.

[17] Max Planck Institute For Chemical Physics of Solids. "Optical Floating Zone". URL: *https://www.cpfs.mpg.de/2651167/optical-floating-zone* (visited on 01/07/2025).

[18] K. Kuroda et al. "$NdBa_2Cu_3O_{7-\delta}$ Single Crystal Growth by the Traveling-Solvent Floating-Zone Method". *Advances in Superconductivity VIII*. Ed. by H. Hayakawa and Y. Enomoto. Tokyo: Springer, 1996. DOI: 10.1007/978-4-431-66871-8_71.

[19] H. R. Harrison and J. M. Honig. "Skull melting as a technique in the growth of single crystals". *Bulletin of Materials Science* **3** (1981), pp. 247–253. DOI: 10.1007/BF02747589.

[20] A. Wiecheć. "The role of magnetic interactions in Verwey's transformation based on studies of the magnetic properties of magnetite and zincoferrites $Fe_{3-x}Zn_xO_4$ ($x \leq 0.05$) - doctoral dissertation". 2008.

[21] F. Walz et al. "Magnetic After-Effects in Single- and Poly-Crystalline Magnetite". *physica status solidi (b)* **110** (1982), pp. K125–K129. DOI: 10.1002/pssb.2221100212.

Chapter 3.

Elastic and structural properties of magnetite under uniaxial compression

Chapter 3 presents single-crystal X-ray diffraction (XRD) measurements performed under uniaxial compression at the ID11 beamline of the European Synchrotron Radiation Facility (ESRF). The experiments pursued two main objectives. The first was to determine the crystallographic and elastic response of stoichiometric magnetite subjected to compression along the [100] and [011] directions. From the diffraction data, the evolution of lattice parameters and interaxial angles with applied stress was derived, allowing reconstruction of the corresponding stress tensor in both the laboratory and sample reference frames. The second objective was to quantitatively calibrate the custom-built uniaxial SOL cells, extending the methodology introduced in Chapter 2. This was achieved by comparing the lattice response measured with the SOL cells to reference data obtained using the calibrated ADMET press, thus establishing accurate conversion factors between screw rotation and applied stress.

This Chapter is organized as follows. Section 3.1 introduces basic concepts of elasticity, including Hooke's law and the stress tensor. Section 3.2 summarizes key principles of single-crystal XRD, such as Bragg's law and the Ewald sphere. Section 3.3 describes the experimental geometry of the ID11 beamline and sample preparation for uniaxial compression using the ADMET and SOL setups. Section 3.4 presents the evolution of lattice parameters and angles with applied load, followed by Section 3.5, which details the quantitative calibration of the SOL cells. Finally, Section 3.6 discusses the evolution of the stress tensor under compression along [100] and [011].

3.1. Elements of the theory of elasticity

As discussed in Chapters 1 and 2, the application of uniaxial pressure to strongly correlated systems such as magnetite can induce profound changes in material properties that originate directly from electronic interactions. Among the most immediate manifestations of these interactions are the mechanical properties, which characterize the response of the material to external stress and provide insights into the underlying electronic states and their correlations. In magnetite, the application of uniaxial stress lowers the intrinsic crystal symmetry, and the resulting distortions of the unit cell can therefore help disentangle the fundamental properties of this system. In the following, the relationship between crystallographic structure and uniaxial stress is examined for compression applied along the [100] direction and along the [011] direction, which has relatively small interatomic distances.

Unidirectional tension and compression are among the most fundamental tests for investigating the mechanical properties of materials. The deformation of a material can be described in terms of strain, which generates a corresponding stress field. Conversely, the application of stress produces a measurable strain field. The typical relationship between applied force and resulting displacement in a compressed material is illustrated in Fig. 3.1a, where the linear region corresponds to the elastic regime. In the simplest case, the response of a material under external compression is described by Hooke's law:

$$\sigma_{xx} = \frac{F_{xx}}{S_{xx}} = E \cdot \frac{\Delta l}{l} = E \cdot \varepsilon_{xx}, \tag{3.1.1}$$

where:

- σ_{xx} is the uniaxial stress, a component of a more general object, the stress tensor presented in Eq. 3.1.2 [MPa],
- F_{xx} - the force normal to the cross-section of the sample presented in Fig. 3.1a [N],
- S_{xx} - the sample cross-section [mm^2],
- E - Young modulus [MPa],
- and $\varepsilon_{xx} = \frac{\Delta l}{l}$ is the one-dimensional strain being a ratio of the absolute elongation divided by the length of the sample, respectively, [mm/mm=1].

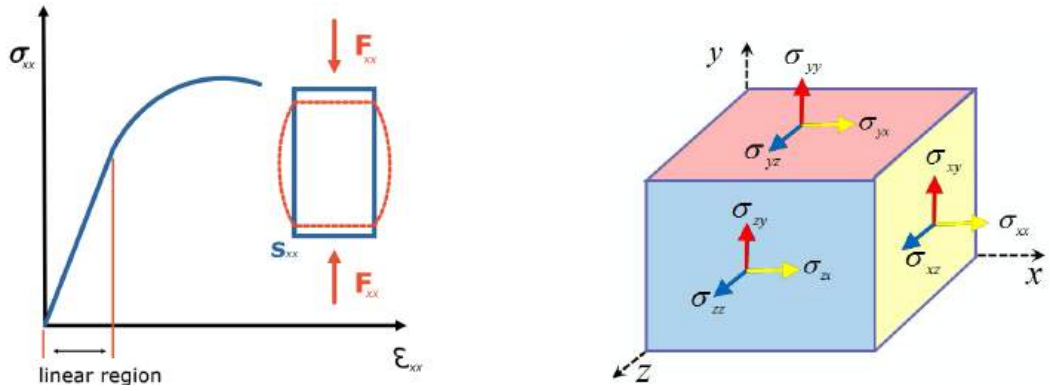

(a) (b)

Fig. 3.1. (a) Typical compression curve $\sigma_{xx} = f(\varepsilon_{xx}) = E \cdot \varepsilon_{xx}$ for a material under uniaxial load. The linear region, indicated by the red vertical lines, corresponds to the elastic regime described by Hooke's law, in which the material recovers its original shape once the stress is removed. At higher stresses, irreversible plastic deformation occurs, eventually leading to sample failure. The inset illustrates the geometry of the uniaxial compression test, where a force F_{xx} is applied along the x direction over the cross-sectional area S_{xx}. **(b)** Representation of the stress tensor in the unit volume of an isotropic material. Each tensor component is labeled with two indices: the first denotes the direction of the force, while the second indicates the orientation of the surface on which the force acts. Adapted from [1].

Figure 3.1 schematically illustrates a stress–strain relationship during a compression test. The mechanical durability of a material is commonly characterized by two fundamental quantities: the Young's modulus and the Poisson's ratio. The Young's modulus E corresponds to the slope of the linear region in the stress–strain curve, reflecting the material's stiffness. The Poisson's ratio ν quantifies the transverse deformation that accompanies a longitudinal strain. Based on these parameters, materials can be classified according to their mechanical response, for instance, as stiff or brittle. For comparison, steel is a stiff material with a Young's modulus of about 200 GPa and a Poisson's ratio of 0.30 at room temperature. Magnetite, in contrast, is anisotropic: depending on crystallographic direction, it can behave as either stiff or brittle. Reported values for its Young's modulus range from 60 to 190 GPa, while the Poisson's ratio lies between 0.26 and 0.33 [2]. This strong anisotropy makes magnetite particularly suitable for investigating direction-dependent effects under uniaxial stress, as explored in this Chapter.

In a three-dimensional space, the generalized relation between the applied force and the response of a body is expressed using tensor formalism. Fig. 3.1b presents an imaginary unit cube inside an isotropic material. Each element of the stress tensor, σ_{ij}, $i,j \in \{x,y,z\}$, is defined as the ratio of the force component F_i to the area S_j of the cube face over which this force acts.

The first index i denotes the direction of one of the three individual components of the deforming force, xj. Therefore, the stress that arises from F_x on the j-th face of the cube is described by the components σ_{xx}, σ_{xy}, and σ_{xz}, respectively.

At first glance, a complete description of the stress in this cube would seem to involve 18 quantities, corresponding to the three force components acting on each of the six faces. However, stresses on opposite faces are equal in magnitude and opposite in direction, so the number of independent quantities reduces to 9. These 9 values form the 3×3 stress tensor, a quadratic matrix that fully characterizes the local stress state of the material and can be transformed under a rotation of the reference frame.

$$\hat{\sigma}_{ij} = \begin{bmatrix} \sigma_{xx} & \sigma_{xy} & \sigma_{xz} \\ \sigma_{yx} & \sigma_{yy} & \sigma_{yz} \\ \sigma_{zx} & \sigma_{zy} & \sigma_{zz} \end{bmatrix} \tag{3.1.2}$$

In addition, the stress tensor (cf. Eq. 3.1.2) is symmetric, which means that its off-diagonal elements are pairwise equal and correspond to the shear stresses, $\sigma_{ij} = \sigma_{ji}$. By an appropriate choice of the reference frame, the stress tensor can always be expressed in diagonal form, as shown in Eq. 3.1.3, where all shear components vanish.

$$\hat{A}\hat{\sigma}_{ij} = \hat{\sigma_{ij}}' = \begin{bmatrix} \sigma'_{xx} & 0 & 0 \\ 0 & \sigma'_{yy} & 0 \\ 0 & 0 & \sigma'_{zz} \end{bmatrix}. \tag{3.1.3}$$

Similarly to stress, strain is also represented by a second-rank tensor. Both quantities are related through the constitutive equation $\underline{\sigma} = \hat{C}_{mn} \cdot \underline{\varepsilon}$, where $\hat{C}_{mn}$ is the fourth-rank elastic stiffness tensor. For practical purposes, a contracted index notation is often employed, for example $\{\ xx \to 1;\ yy \to 2;\ yz \to 4\}$, which reduces the index representation of C_{mn}. In the case of a cubic crystal such as magnetite, the symmetry of the lattice simplifies the stiffness tensor considerably, leaving only three independent elastic constants: C_{11}, C_{12}, and C_{44}. The corresponding form of the tensor is presented in Eq. 3.1.4.

$$\begin{bmatrix} \sigma_{xx} \\ \sigma_{yy} \\ \sigma_{zz} \\ \sigma_{yz} \\ \sigma_{zx} \\ \sigma_{xy} \end{bmatrix} = \begin{bmatrix} C_{11} & C_{12} & C_{12} & 0 & 0 & 0 \\ C_{12} & C_{11} & C_{12} & 0 & 0 & 0 \\ C_{12} & C_{12} & C_{11} & 0 & 0 & 0 \\ 0 & 0 & 0 & C_{44} & 0 & 0 \\ 0 & 0 & 0 & 0 & C_{44} & 0 \\ 0 & 0 & 0 & 0 & 0 & C_{44} \end{bmatrix} \cdot \begin{bmatrix} \varepsilon_{xx} \\ \varepsilon_{yy} \\ \varepsilon_{zz} \\ 2 \cdot \varepsilon_{yz} \\ 2 \cdot \varepsilon_{zx} \\ 2 \cdot \varepsilon_{xy} \end{bmatrix} \tag{3.1.4}$$

$C_{44} = \dfrac{C_{11} - C_{12}}{2} = \mu$ defines the shear modulus and reflects the degree of elastic anisotropy in the crystal. For example, doping magnetite with the non-magnetic element Zn has been shown to strongly influence the behavior of C_{44}, as measured by sound velocity in variable-temperature experiments [3].

In general, the elastic constants can be expressed in terms of the macroscopic mechanical parameters, namely the Young's modulus and the Poisson's ratio. A more detailed discussion of the theory of elasticity and its mathematical formulation is provided in Appendix D.

3.2. Single crystal diffraction

X-ray diffraction (XRD) is one of the most widely used characterization techniques for single crystals. The method requires three essential components: a monochromatic X-ray source, a single-crystalline sample, and a detector.

When the incident X-ray photons interact with the atoms in the crystal lattice, they are scattered. Constructive interference of these scattered waves occurs only when the Bragg condition,

$$n \cdot \lambda = 2 \cdot d \cdot \sin(\theta), \tag{3.2.5}$$

is satisfied. The symbols in Eq. 3.2.5 denote, respectively:

- n – the order of diffraction, an integer $\{1, 2, \dots\}$;
- λ – the X-ray wavelength [nm];
- d – the spacing between crystallographic planes [Å];
- θ – the Bragg angle, i.e., the angle between the incident beam and the lattice planes [°].

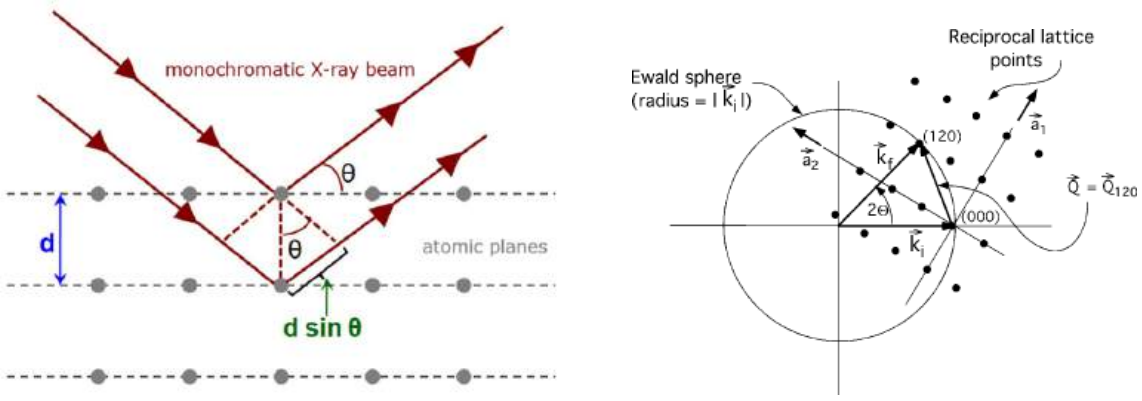

(a) (b)

Fig. 3.2. (a) Schematic illustration of Bragg's law. Constructive interference occurs when the path difference between X-rays diffracted from successive atomic planes is an integer multiple of the incident wavelength λ. The interplanar spacing is denoted by d, and θ represents the Bragg angle. **(b)** Diffraction expressed in reciprocal space using the Ewald sphere construction. The sphere has a radius equal to the magnitude of the incident wave vector $|\underline{\mathrm{k_i}}|$. A diffraction condition is satisfied when a reciprocal lattice point lies on the sphere, i.e., when the scattering vector $\underline{\mathrm{Q}} = \underline{\mathrm{k_f}} - \underline{\mathrm{k_i}}$ coincides with a reciprocal lattice vector $\mathbf{G}$. The figure is adapted from [4].

Alternatively, the diffraction condition can be formulated in reciprocal space. Constructive interference occurs when the difference between the incident and diffracted wave vectors corresponds to a reciprocal lattice vector of the crystal. This difference is defined as the scattering vector,

$$\underline{\mathrm{Q}} = \underline{\mathrm{k_f}} - \underline{\mathrm{k_i}},$$

where $\underline{\mathrm{k_i}}$ and $\underline{\mathrm{k_f}}$ denote the incident and diffracted wave vectors, respectively.

Since in XRD the incident and diffracted photons have the same energy, the magnitudes of $\underline{\mathrm{k_i}}$ and $\underline{\mathrm{k_f}}$ are equal. As a result, the reciprocal lattice must be rotated relative to the fixed incident beam in order to satisfy the condition $\underline{\mathrm{Q}} = \mathbf{G}$, where $\mathbf{G}$ is a reciprocal lattice vector. This construction is conveniently represented by the Ewald sphere, shown in Fig. 3.2b.

3.3. Experimental

The results of the single crystal XRD presented within this Chapter were obtained on the ID11 beamline of ESRF. This beamline offers high-energy diffraction and imaging techniques to study the physical, chemical, and mechanical properties of various systems of interest. The available spatial resolution is below 100 nm and the time resolution is around 1 ms. The 3DXRD instrument, which operates with a far-field diffraction, was used to conduct the uniaxial pressure experiments. The measurement relied on the observation of a pattern consisting of a set of individual spots recorded

as the sample rotated vertically. The lattice parameters and their dependence on the applied uniaxial stress were reconstructed from the collected pattern.

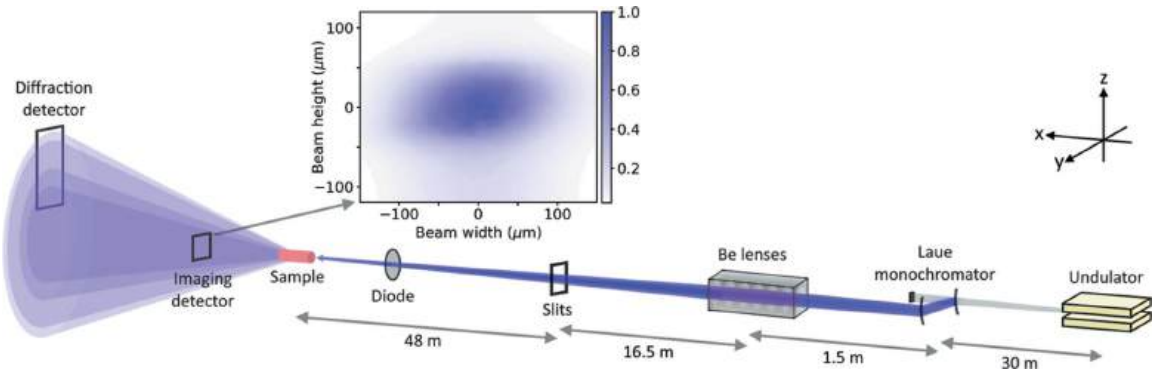

Fig. 3.3. Schematic of the experimental setup at the ID11 beamline of the ESRF. X-rays generated by the undulator are monochromatized with a Laue crystal, focused using Be lenses, and shaped by slits before reaching the sample. A diode monitors the transmitted intensity, while diffraction and imaging detectors record the scattered signal. The inset shows the measured cross-sectional intensity profile of the focused beam. Adapted from [5].

The experiment was carried out at a photon energy of 65.35 keV with a focused X-ray beam of cross-sectional dimensions 0.1×0.1 mm^2. Single crystals of stoichiometric magnetite were measured under uniaxial compression at room temperature using two types of pressure cells.

The first device was the ADMET mechanical press, a commercially available instrument that provides controlled and uniform compression with forces measured directly in Newtons. For its application at the ID11 beamline, a dedicated steel adapter was manufactured specifically to accommodate small single-crystalline samples, as shown in Fig. 3.4a. To guarantee the uniform transmission of uniaxial pressure, the sample was positioned between two ceramic cylinders within the adapter, as illustrated in Fig. 3.4b.

The second type of device was the SOL cell, described in detail in Chapter 2. Three similar cells (SOL2, SOL3, and SOL4) were used in the experiments. Each was mounted on an aluminum monstrance-shaped stand, which itself was fixed to the beamline goniometer. This supporting element is depicted in Figs. 3.4c and 3.4d.

During data acquisition, the samples were rotated around the vertical axis. In this configuration, certain structural elements of the pressure cells could partially obstruct the X-ray beam. To minimize absorption, hard X-rays with an energy of 66 keV were employed. At this energy, the transmission through a 0.8 mm thick iron plate (some of the elements of the ADMET press) is approximately 74%. Titanium and aluminum, which constitute parts of the SOL cells, absorb X-rays more weakly at this energy and therefore do not significantly attenuate the radiation [6]. The mounting configurations of the samples in both the ADMET and SOL cells are shown in Fig. 3.4.

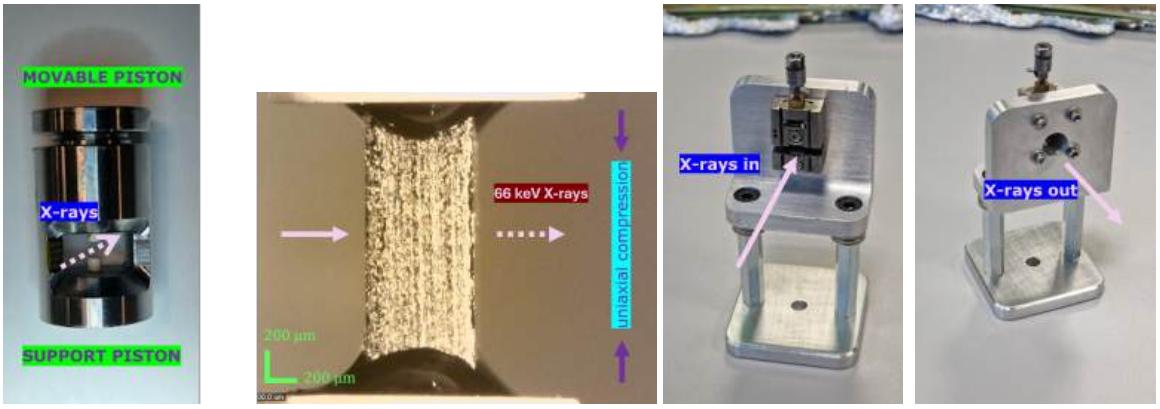

(a) (b) (c) (d)

Fig. 3.4. (a): ADMET insert with the ceramic cylinders holding the sample. **(b):** Sample mounted to the ADMET cell with the Loctite® Stycast 2850FT epoxy resin. **(c):** Front and **(d):** rear views on the SOL2 cell encased into a goniometer holder for ID11 beamline.

All samples investigated were single crystals of stoichiometric magnetite, cut from the same larger crystal grown by the zone-melting technique described in Chapter 2. The samples were oriented such that their faces contained crystallographic planes of type $\{100\}$ or $\{0\bar{1}1\}$. Accordingly, the longest edge of each bar was aligned along the $\langle 100\rangle$ or $\langle 011\rangle$ direction, respectively. The crystals were shaped into bars with lengths ranging from 2.00 to 3.00 mm and cross-sectional areas between 0.36 and 1.00 mm^2.

The samples were mounted such that uniaxial compression was applied along either the [100] or [011] crystallographic directions. For compression along [100], the sample was oriented so that the (100) plane was perpendicular to the incident X-ray beam. In the case of compression along [011], the incident wave vector was aligned normal to the $(0\bar{1}1)$ planes, as illustrated in Fig. 3.5.

The starting parameters used for processing the diffraction data were as follows: space group Fd$\bar{3}$m (227), lattice parameters $a = b = c = 8.394$ Å, and lattice angles $\alpha = \beta = \gamma = 90°$. A summary of the orientation of each sample and the compression device employed is provided in Table 3.1.

No. sample	Name	l [mm]	$w \cdot t$ [mm^2]	Axis of compression	Device
1.	**sample A**	3.00	1.00	**[011]**	**ADMET**
2.	sample B	3.00	0.36	[011]	SOL2
3.	sample 1 (after XAS)	2.50	0.82	[011]	SOL3
4.	sample C	2.50	0.40	[011]	SOL4
1.	**sample G**	2.00	0.40	**[100]**	**ADMET**
2.	sample F	2.00	0.40	[100]	SOL3

Tab. 3.1. Summary of the magnetite single-crystal samples studied at the ID11 beamline under uniaxial compression using the ADMET and SOL devices. The parameter l denotes the sample length (in mm), while the product of width and thickness, $w \cdot t$, gives the cross-sectional area (in mm^2). Samples A and G served as reference crystals for compression along the [011] and [100] directions, respectively, using the ADMET press. Samples B, 1 (after XAS), C, and F were studied with the SOL cells. The sample "sample 1 (after XAS)" acquired its name because it had previously been investigated by X-ray absorption spectroscopy (XAS) at the SOLARIS synchrotron in Kraków.

The principle of data acquisition, along with the definitions of the lattice parameters and angles, as well as the schematic representation of the sample positioning under uniaxial compression along the [011] and [100] directions, are illustrated in Fig. 3.5. The figure highlights the distinction between the laboratory frame and the crystal reference frame, the applied force geometry, and the rotation scheme used to record the diffraction patterns.

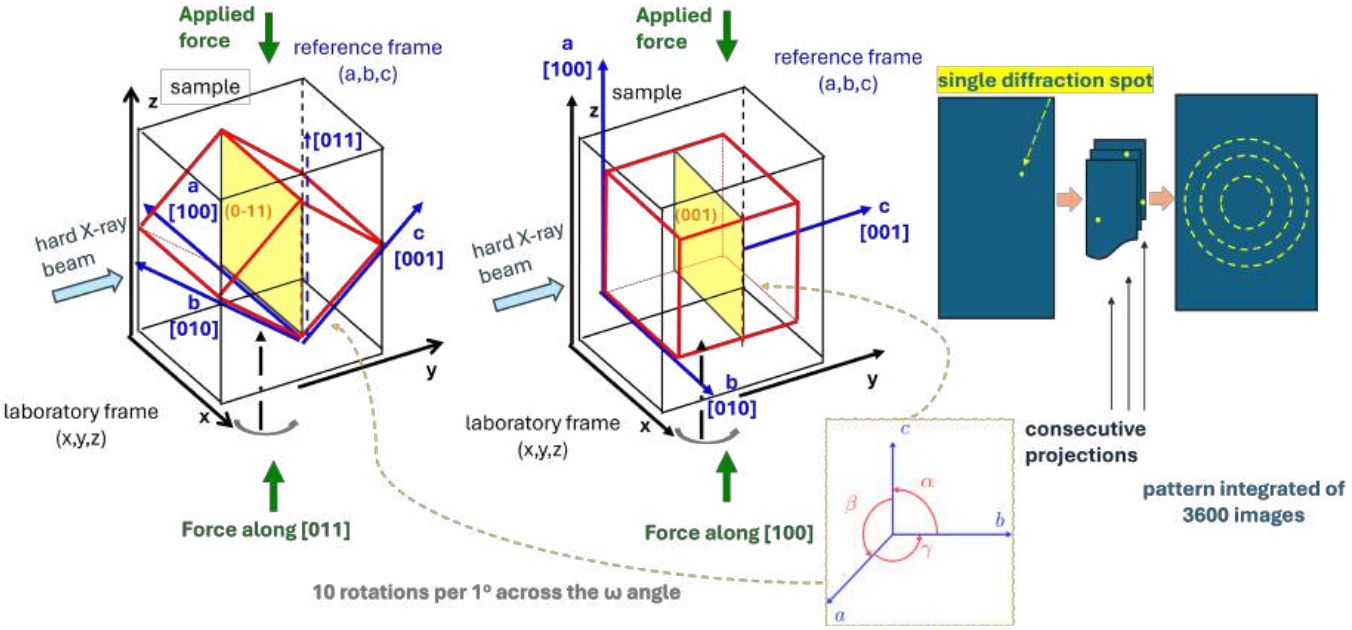

Fig. 3.5. Schematic of the experimental geometry at the ID11 beamline for XRD measurements under uniaxial compression applied along the [011] or [100] crystallographic directions. The laboratory frame (x, y, z) and the edges of the sample are indicated in black. The reference frame of the crystal (a, b, c) is shown in blue, while the cubic unit cell is represented by the **red grid**. The inset outlined with an orange dashed-dotted frame defines the crystallographic lattice angles α, β, and γ. Diffraction patterns were collected in an interlaced sequence: the sample was rotated around the z-axis (ω-angle) in ten consecutive runs, with steps of 0.1° per exposure. Each frame corresponded to a single irradiation of the sample. In total, 3600 single projections were acquired and subsequently integrated into one diffraction pattern. From these data, the dependence of the lattice parameters, lattice angles, and stress tensor components on the applied uniaxial pressure was determined using dedicated Python analysis codes.

3.4. Response of lattice parameters and angles to uniaxial stress applied along [001] and [011]

Under ambient conditions, magnetite adopts the cubic crystal structure with space group Fd$\bar{3}$m. In this experiment, the measured quantities were the lattice constants a, b, and c, together with the lattice angles α, β, and γ. These crystallographic parameters were systematically monitored as a function of externally applied uniaxial compression, recorded *in situ* for two experimental geometries: compression applied along the [100] and [011] crystallographic directions.

Since all the samples studied in this experiment were cut from the same larger crystal, it was assumed that their responses to uniaxial stress would be reproducible within the experimental un-

certainty. This uncertainty originated from two main sources. The first was related to the pressure devices themselves, for example, friction within the mechanical cells. The second source was associated with the samples, such as slight misalignment during mounting. In addition, the crystallographic orientation after cutting could deviate by up to 1° from the intended direction. These subtle effects may have contributed to the small variations observed in the results presented in this Section.

The compressive stress in the ADMET cell was determined directly from the applied force, read in Newtons from the pressure gauge, divided by the cross-sectional area of the sample. The applied force was increased in constant steps, corresponding to a stress increment of 10 MPa with respect to the cross sections of samples A and G. In contrast, for the SOL cells, the pressure was not measured directly but estimated from the rotation angle of the driving screw. Using Eq. 2.1.9 together with the cross-sectional areas of the mounted samples, the screw rotation step was chosen between 15° and 25°, such that the estimated stress reached approximately 100 MPa. Therefore, calibration of the SOL cells required direct comparison with the ADMET reference measurements, as described in detail in Section 3.5.

Let us first consider the data collected under uniaxial compression along the [011] crystallographic direction. The results obtained for the reference sample A, measured with the calibrated ADMET cell, are shown in Fig. 3.6. As illustrated schematically in Fig. 3.5, the lattice parameters b and c are expected to evolve identically under [011] compression, while the parameter a responds differently. This behavior reflects the reduction of the initial cubic symmetry to a monoclinic distortion: the b and c axes remain equivalent with respect to the applied stress, whereas the a axis becomes inequivalent. A corresponding symmetry breaking is observed in the lattice angles, where β and γ are expected to follow the same trend, while the α angle evolves independently. Together, these relationships provide a direct crystallographic fingerprint of the transition from cubic to monoclinic geometry induced by uniaxial stress along [011].

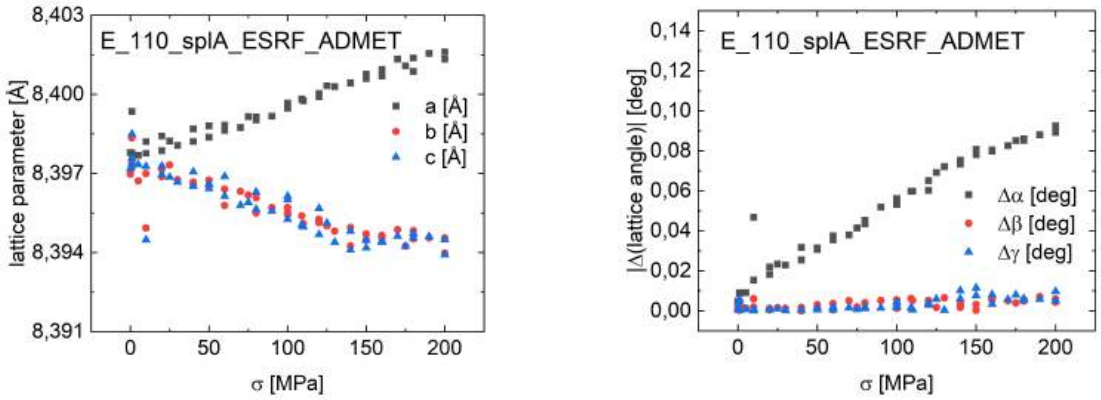

(a) (b)

Fig. 3.6. Evolution of the lattice parameters and lattice angles of magnetite under uniaxial compression along the [011] direction, measured for sample A using the calibrated ADMET press. **(a):** Lattice constants a, b, and c as a function of applied stress σ.**(b):** Corresponding changes in the lattice angles α, β, and γ as a function of applied stress. The internal figure label "E_110_splA_ESRF_ADMET" follows the notation used throughout this chapter: "E_110" denotes compression along the [011] crystallographic direction, "splA" identifies sample A, and "ADMET" indicates the pressure device employed. This dataset serves as the absolute stress reference for calibrating SOL-cell measurements.

As shown in Fig. 3.6a, compression along the [011] axis leads to an anisotropic lattice response. The lattice parameter along [100] increases with stress, while the parameters along [010] and [001] contract correspondingly. In parallel, the lattice angles exhibit distinct behavior (Fig. 3.6b): the α angle deviates from 90° by up to 0.09° at an applied stress of 200 MPa, whereas β and γ remain essentially unchanged within experimental uncertainty. The evolution of b, c, and α is quasilinear up to approximately 150 MPa, consistent with Hooke's law in the elastic regime. Above this stress level, however, the slope decreases, indicating a departure from the ideal elastic behavior and suggesting the onset of non-linear lattice response.

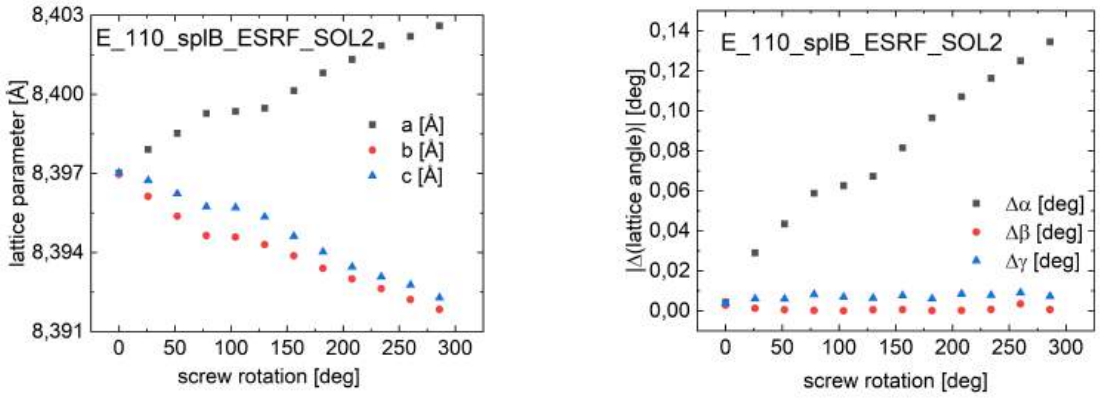

(a) (b)

Fig. 3.7. Evolution of the crystal lattice of magnetite under uniaxial compression applied along the [011] direction, measured for sample B using the SOL2 cell. **(a):** Dependence of the lattice constants a, b, and c on screw rotation. **(b):** Corresponding evolution of the lattice angles α, β, and γ. The internal figure label "E_110_splB_ESRF_SOL2" follows the previously introduced convention.

Sample B was compressed along the same [011] crystallographic direction as sample A, but using the SOL2 cell. The results for this sample, presented in Fig. 3.7, exhibited the same overall trend as those obtained for sample A, thereby confirming the reproducibility of the measurements across different pressure devices. A noticeable deviation from the expected linear (Hookean) response was observed in the range of 50–100° screw rotation. This effect is attributed to the mechanical characteristics of the SOL2 cell rather than to the intrinsic elastic response of magnetite. As will be discussed in Section 3.5, this range of screw angles corresponds to an estimated uniaxial compression of approximately 100 MPa.

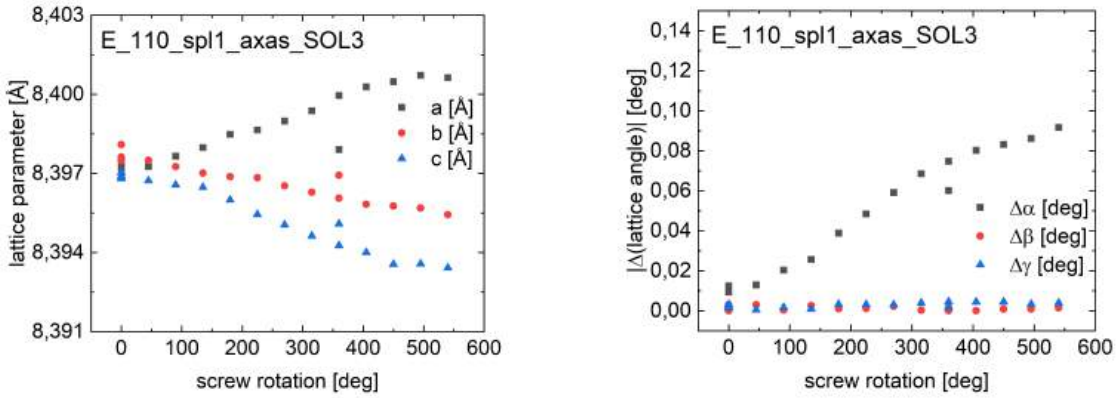

(a) (b)

Fig. 3.8. Evolution of the crystal lattice of magnetite under uniaxial compression along the [011] direction, measured for sample "1_axas" using the uncalibrated SOL3 cell. **(a):** Dependence of the lattice constants a, b, and c on screw rotation (in degrees). **(b):** Corresponding evolution of the lattice angles α, β, and γ as a function of screw rotation. "spl1_axas" identifies the sample, which previously was studied by XAS.

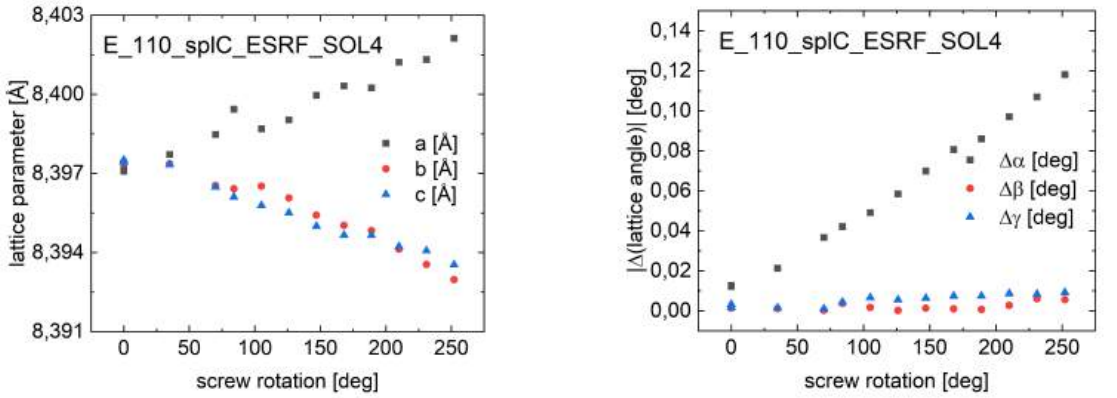

(a) (b)

Fig. 3.9. Evolution of the crystal lattice of magnetite under uniaxial compression along the [011] direction, measured for sample C using the uncalibrated SOL4 cell. **(a):** Lattice constants a, b, and c as a function of screw rotation (in degrees). **(b):** Corresponding evolution of the lattice angles α, β, and γ. Since SOL4 was uncalibrated, the data are presented relative to screw rotation rather than absolute stress.

Figure 3.8 shows the response of the crystal lattice for sample 1_axas compressed with the SOL3 cell. The observed non-linear evolution of both the lattice constants and the α angle can be attributed to the prior deformation history of this sample, as it had been previously subjected to XAS measurements. Residual plastic strains likely influenced its mechanical response. In addition, the lack of coincidence between the b and c lattice constants under increasing screw rotation suggests that the sample was not compressed uniformly, or that the applied force deviated slightly from the ideal [011] crystallographic direction.

In contrast, the response of sample C, measured with the SOL4 cell and shown in Fig. 3.9, exhibited a more regular elastic-like behavior. Here, the b and c axes evolved consistently, as expected for [011] compression. The a lattice constant displayed small irregularities (notably around 80°, 180°, and 210° screw rotation), while the α angle varied smoothly and monotonically with compression. Since samples B, 1_axas, and C were nominally equivalent and cut from the same batch, the differences in their responses are most plausibly linked to subtle mechanical factors specific to the SOL2, SOL3, and SOL4 devices, such as machining tolerances, alignment precision, or differences in the transmission of uniaxial force.

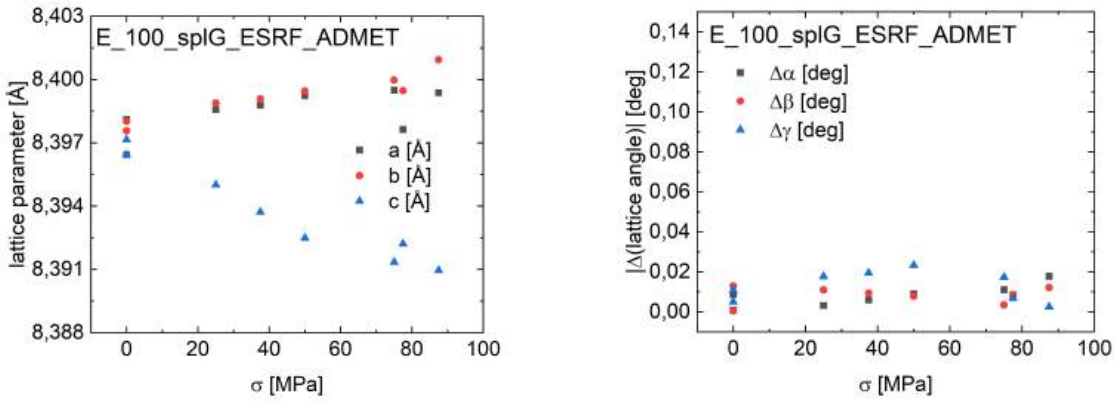

(a) (b)

Fig. 3.10. Evolution of the crystal lattice parameters of magnetite under uniaxial compression along the [100] direction, measured for sample G using the ADMET cell with force calibration. **(a):** Lattice constants a, b, and c as a function of applied uniaxial stress, σ. **(b):** Corresponding evolution of the lattice angles α, β, and γ.

Now, let us turn to the experiments performed with the uniaxial compression applied along the [100] crystallographic direction. The reference results obtained for sample G, measured with the calibrated ADMET cell, are presented in Fig. 3.10. As the applied stress increased, the lattice constants a and b remained degenerate, reflecting the preservation of their equivalence under [100] compression, while the c axis contracted proportionally. This anisotropic response is characteristic of a tetragonal distortion of the initially cubic lattice. In agreement with this expected symmetry, the lattice angles

α, β, and γ did not show any systematic changes within the investigated stress range, confirming that the deformation remained essentially tetragonal without additional shear contributions.

The corresponding measurements performed on sample F using the uncalibrated SOL3 cell are shown in Fig. 3.11. In this case, the evolution of the lattice constants a, b, and c as a function of screw rotation followed a nearly linear trend that closely matched the response observed in the calibrated ADMET experiment on sample G. This consistency enabled the use of lattice constants alone for the calibration of the SOL3 cell against the ADMET reference, as the lattice angles in sample F did not exhibit a clear systematic dependence as expected for tetragonal deformation. However, at the largest screw rotations, deviations in the lattice angles became apparent, suggesting that the elastic limit of the crystal may have been exceeded. This observation is supported by the simultaneous saturation of the lattice constants, indicating the onset of non-elastic behavior, likely associated with defect formation or the beginning of plastic deformation.

Overall, the comparison between samples G (ADMET) and F (SOL3) demonstrates a high level of consistency in the elastic regime. The quantitative match in the lattice constants confirms that the SOL3 cell can reliably reproduce the pressure-dependent structural response once properly calibrated, while the deviations observed at high stress highlight the limits of linear elasticity in magnetite under [100] compression.

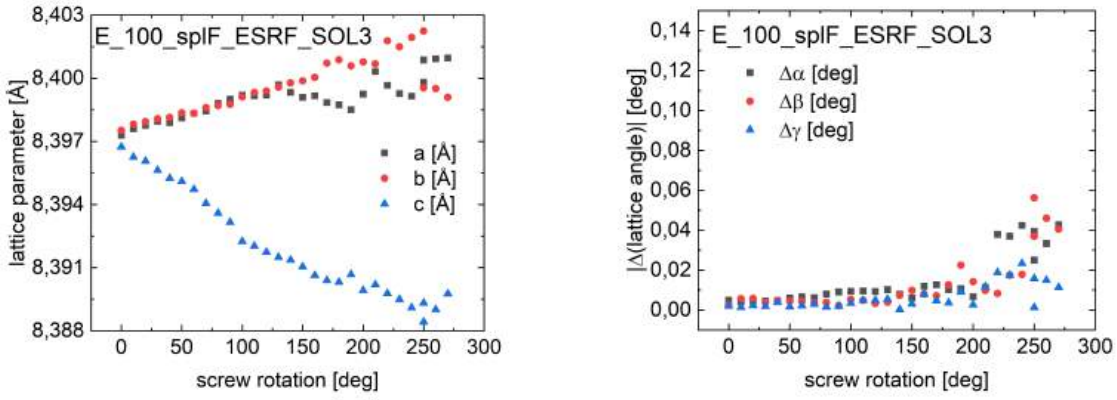

(a) (b)

Fig. 3.11. Evolution of the crystal lattice parameters of magnetite under uniaxial compression along the [100] direction, measured for sample F using the uncalibrated SOL3 cell. **(a):** Lattice constants a, b, and c as a function of screw rotation (in degrees). **(b):** Corresponding evolution of the lattice angles α, β, and γ.

3.5. Calibration of the developed SOL setups

The XRD measurements demonstrated a high degree of reproducibility across all investigated samples, thereby providing a solid foundation for calibration. This reproducibility allowed the uniaxial

pressure applied in the SOL cells to be quantitatively referenced against the absolute force calibration of the ADMET press. The calibration procedure, described in detail in the following Section, was conducted in a systematic manner and consisted of the following steps:

1. The variable of interest, denoted in general as Ψ, represented the crystallographic parameters that qualitatively and quantitatively evolved with the applied uniaxial stress σ.

2. For compression along the [011] direction, Ψ was chosen among the lattice constants a, b, c, or the lattice angle α. For compression along the [100] direction, Ψ referred exclusively to the lattice constants, since the angles were not affected by such deformation.

3. Each parameter identified in Step 2 was assumed to vary linearly with the applied stress. Accordingly, each dataset was fitted to the model

$$\Psi = \mathcal{A} \cdot \sigma + \mathcal{B},$$

where $\mathcal{A}$ and $\mathcal{B}$ denote the slope and intercept of the linear fit, respectively, determined using the least-squares method.

4. Since the lattice constants b and c exhibited nearly identical evolution in the [011] geometry, they were treated as equivalent. A virtual averaged parameter was therefore introduced,

$$d = \frac{b+c}{2}.$$

In the [100] geometry, the same procedure was applied to a and b, giving $d = \frac{a+b}{2}$. Linear fits were then performed with d as the variable.

5. The value of Ψ measured with the ADMET press at a given uniaxial stress σ was directly compared to the corresponding value of Ψ measured with a SOL cell at a known screw rotation angle δ.

6. It was assumed that this screw rotation angle δ produced the same uniaxial stress σ, proportional through a calibration factor C, such that

$$\sigma = C \cdot \delta.$$

7. Finally, the calibration factor C was determined from

$$C = \frac{\sigma}{\delta} = \frac{\frac{\Psi - \mathcal{B}}{\mathcal{A}}}{\delta}.$$

Sample A served as the reference standard for the calibration of the SOL2, SOL3, and SOL4 cells in the [011] geometry. For the [100] geometry, the only available reference was sample G. Accordingly, the results obtained for sample F were calibrated against those of sample G to determine the calibration factor for the SOL3 cell in the [100] configuration. The computed calibration constants differed among the SOL cells, most likely reflecting subtle variations in their fabrication and assembly tolerances.

The calibration algorithm is illustrated in detail using the example of the SOL3 cell. As shown in Fig. 3.10a, in the [100] geometry the lattice constants a and b increase slightly with applied pressure, whereas the constant c decreases. To account for their equivalent behavior under [100] compression, the constants a and b were averaged, and the resulting parameter was used for fitting. The corresponding linear fit equations were then obtained as follows:

- For the dependence of the averaged lattice parameter $d = \dfrac{a+b}{2}$ on the applied stress σ:

$$\mathcal{A} = (2.92 \pm 0.48) \times 10^{-5} \ \text{[Å/MPa]}, \qquad \mathcal{B} = 8.39770 \pm 0.00024 \ \text{[Å]}.$$

- For the dependence of the lattice constant c on the applied stress σ:

$$\mathcal{A} = (-7.01 \pm 0.54) \times 10^{-5} \ \text{[Å/MPa]}, \qquad \mathcal{B} = 8.3966 \pm 0.0003 \ \text{[Å]}.$$

Thus, the calibration factors for the SOL3 cell, obtained separately for each lattice parameter in the [100] geometry, were:

- $a(\sigma, \delta)$: $C_a = 0.35 \pm 0.11$ [MPa/°];
- $b(\sigma, \delta)$: $C_b = 0.47 \pm 0.11$ [MPa/°];
- $c(\sigma, \delta)$: $C_c = 0.49 \pm 0.06$ [MPa/°].

The mean calibration factor for the SOL3 cell was determined as

$$C = 0.43 \ \text{[MPa/°]},$$

calculated as the arithmetic average of the individual calibration factors C_a, C_b, and C_c obtained for each lattice parameter. The corresponding uncertainty was estimated as the standard deviation of these values, giving

$$u(C) = \pm 0.09 \ \text{[MPa/°]}.$$

The calibration factors C, determined separately for each SOL cell, were then used to convert the screw rotation angles into calibrated uniaxial pressures. The resulting dependencies of the relevant lattice parameters on calibrated pressure are shown in the left panels of Figs. 3.12, 3.13, and 3.15.

The right panels of these figures present the corresponding calibrated datasets for samples B, 1_axas, and C, respectively, superimposed on the reference results obtained for sample A using the calibrated ADMET press.

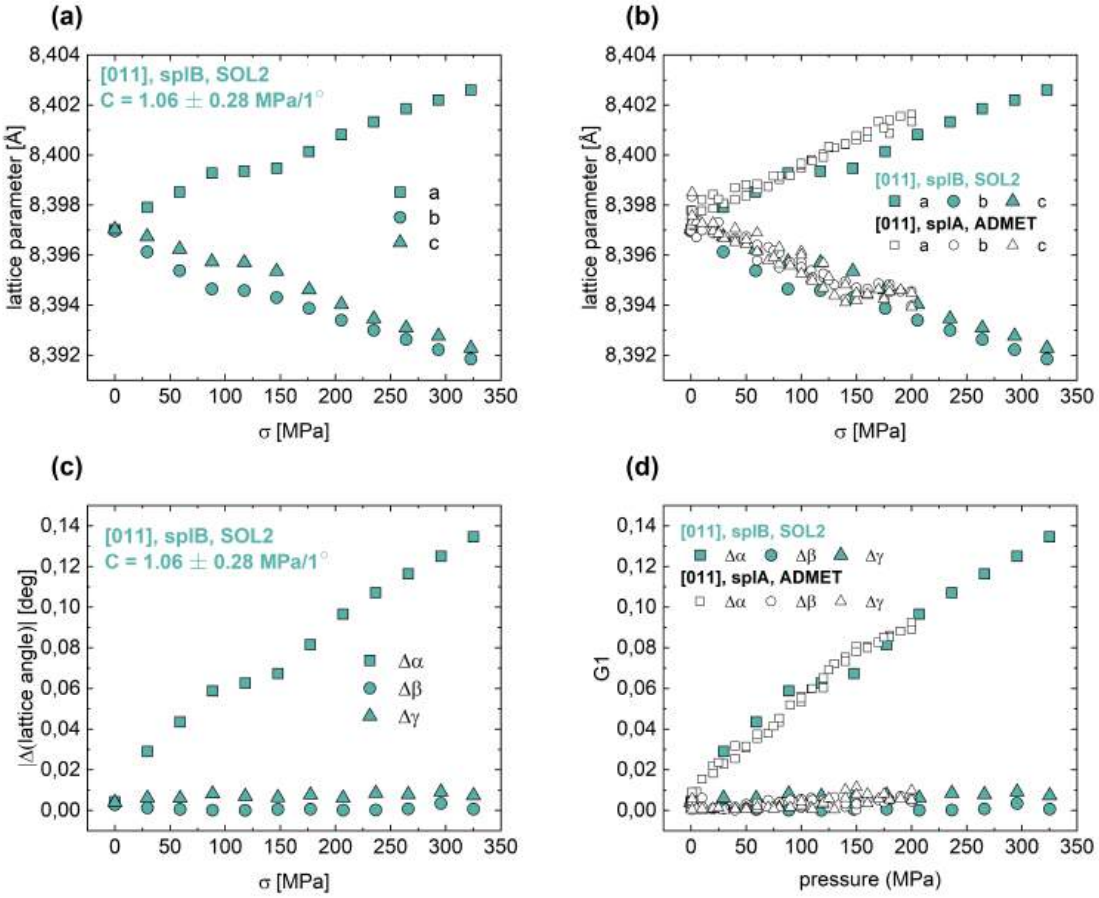

Fig. 3.12. Calibration of the SOL2 cell. The screw rotation angle δ from Figs. 3.7a and 3.7b was converted into uniaxial stress σ using the calibration factor $C = 1.06\,[\mathrm{MPa}/^\circ]$. **(a)** Lattice constants and **(c)** lattice angles of sample B as a function of calibrated stress σ. **(b)** Comparison of lattice constants and **(d)** comparison of lattice angles between sample A (open symbols, ADMET reference) and sample B (filled symbols, SOL2).

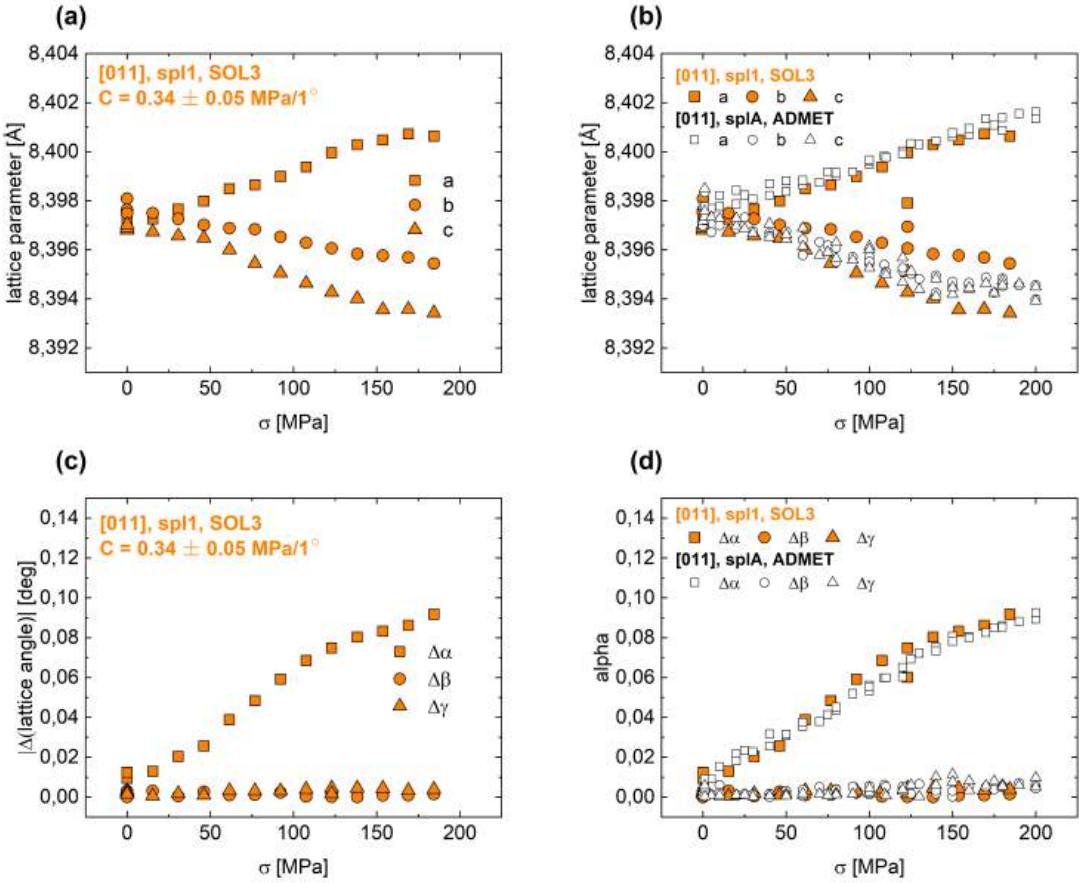

Fig. 3.13. Calibration of the SOL3 cell in the [011] geometry. The screw rotation angle δ from Figs. 3.8a and 3.8b was converted into uniaxial stress σ using the calibration factor $C = 0.34$ [MPa/°]. **(a)** Lattice constants and **(c)** lattice angles of sample 1_axas as a function of calibrated stress σ. **(b)** Comparison of lattice constants and **(d)** comparison of lattice angles between sample A (open symbols, ADMET reference) and sample 1_axas (filled symbols, SOL3).

As explained in the previous Section, the crystal lattice of magnetite deformed in accordance with theoretical predictions for uniaxial compression in the [001] geometry. Since the change in lattice angles did not show any dependence on the applied uniaxial stress, it was assumed that all lattice angles remained equal to 90°. The elongation of lattice parameters a and b combined with the shortening of parameter c prompted an artificial modification of the crystal lattice symmetry from cubic to tetragonal. Thus, the lattice angles were excluded from the analysis performed and sample F could be calibrated against sample G solely on the basis of changes in lattice parameters in the [001] geometry, which is shown in Fig. 3.14.

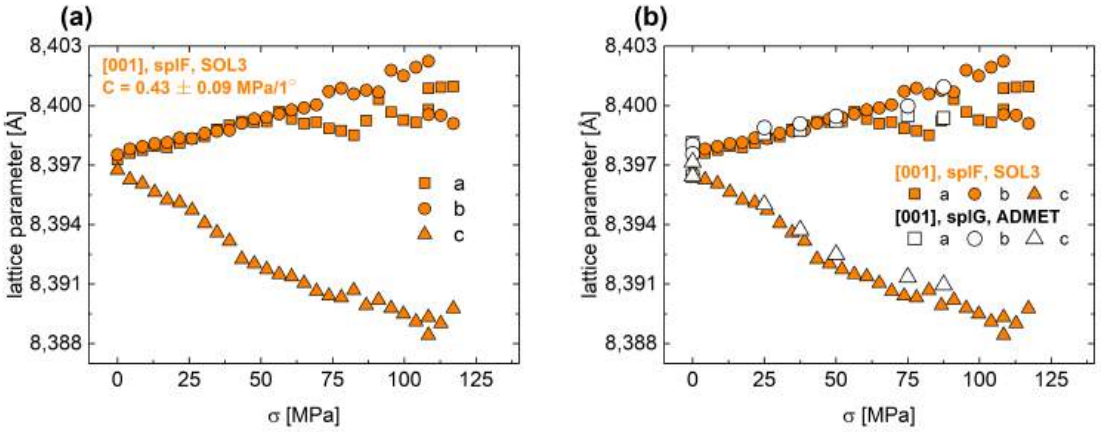

Fig. 3.14. Calibration of the SOL3 cell in [001] geometry. The screw rotation angle δ from Fig. 3.11a was converted into uniaxial stress σ using the calibration factor $C = 0.43$ [MPa/°]. **(a)** Lattice constants of sample F as a function of calibrated stress σ. **(b)** Comparison of lattice constants between sample G (open symbols, ADMET reference) and sample F (filled symbols, SOL3).

For the [011] geometry, the lattice constants and the angle α yielded four calibration factors, C_a, C_b, C_c, and C_α, respectively, for each SOL cell. In the ideal case of a perfectly mounted sample aligned exactly along the [011] crystallographic direction, these factors would be expected to coincide within experimental uncertainty. The largest statistical spread was observed in the data for sample 1_axas measured with the SOL3 cell, as shown in Fig. 3.13. Although the dependence of the α angle on the uniaxial stress σ appeared approximately linear, the divergence between the trends of the b and c lattice constants suggests a slight misalignment of the sample or a non-uniform transmission of force within the SOL3 device. Consequently, the calibration factors obtained for the SOL3 cell carried relative uncertainties exceeding 10%.

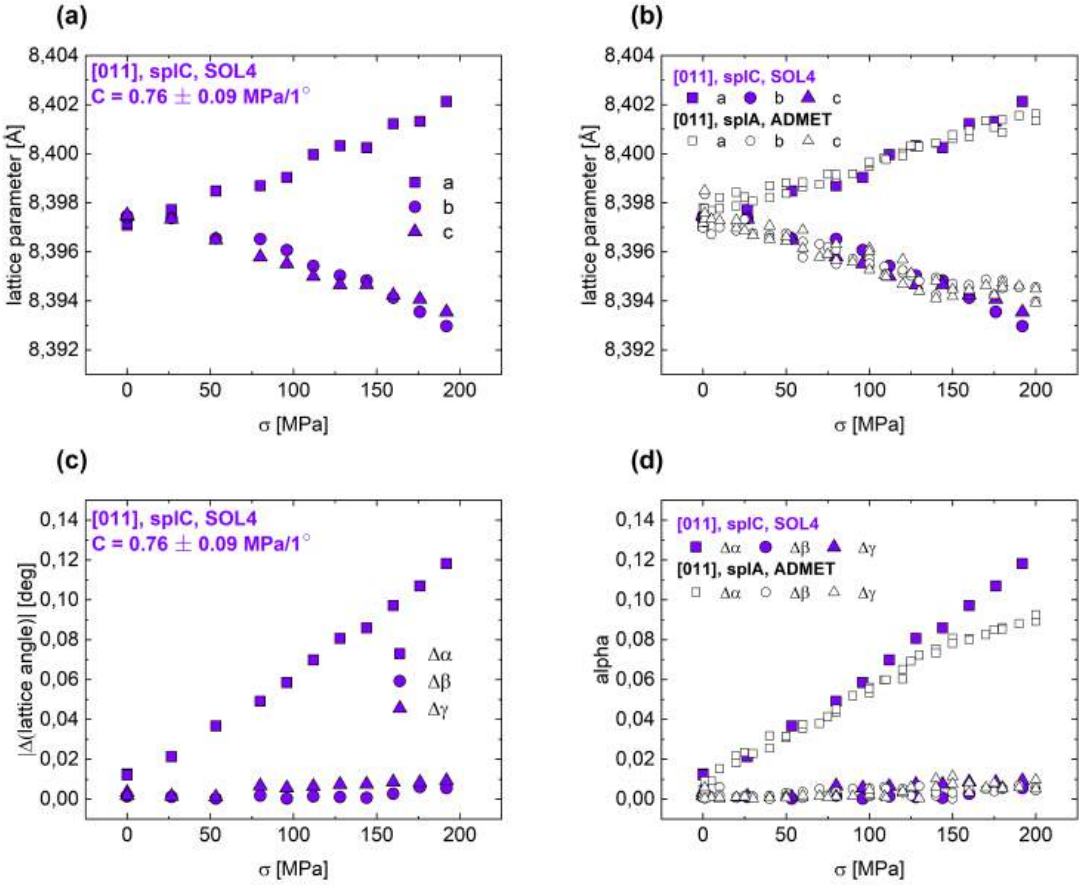

Fig. 3.15. Calibration of the SOL4 cell. The screw rotation angle δ from Figs. 3.9a and 3.9b was converted into uniaxial stress σ using the calibration factor $C = 0.76\,[\mathrm{MPa}/^\circ]$. **(a)** Lattice constants and **(c)** lattice angles of sample C as a function of calibrated stress σ. **(b)** Comparison of lattice constants and **(d)** comparison of lattice angles between sample A (open symbols, ADMET reference) and sample C (filled symbols, SOL4).

The calibrated lattice constants of samples B, 1_axas, and C in the [011] geometry are summarized in Fig. 3.16, which compares their evolution under calibrated uniaxial stress.

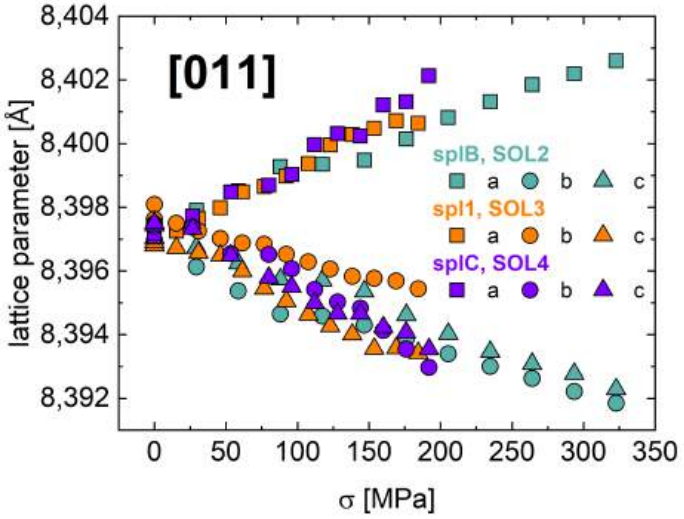

Fig. 3.16. Collective dependence of the lattice constants for samples B, 1_axas, and C under uniaxial compression along the [011] direction, measured with the SOL cells after calibration. The lattice constants of the three samples collapse onto common linear trends, with the exception of the b and c axes of sample 1_axas, which deviate due to misalignment effects.

A complete overview of the calibration factors determined for each SOL cell is provided in Table 3.2.

Instrument	Name	Axis of compression	S [mm^2]	C factor [MPa/1°]	Force [N/1°]
ADMET	**splA**	**[011]**	**1.00**	**reference**	**reference**
SOL2	splB	[011]	0.36	1.10 ± 0.28	0.39
SOL3	spl1_axas	[011]	0.82	0.34 ± 0.06	0.28
SOL4	splC	[011]	0.40	0.77 ± 0.09	0.31
ADMET	**splG**	**[100]**	**0.40**	**reference**	**reference**
SOL3	splF	[100]	0.40	0.43 ± 0.09	0.18

Tab. 3.2. Summary of the performed calibration procedure. S denotes the cross section of the sample. C is the calibration factor, which can be transferred into the compressive force using the sample cross section.

3.6. Evolution of the stress tensor under compression along [100] and [011]

The calibration factors obtained for the respective SOL cells in the previous section were applied to convert the screw rotation angles into calibrated uniaxial stresses σ, which were then used to evaluate the evolution of the stress tensor discussed in this section.

As in the case of the lattice constants and lattice angles, the stress tensor was derived directly from the XRD patterns. The components of the tensor, σ_{ij} with $i,j \in \{x,y,z\}$, were calculated in both the laboratory and sample reference frames using the pyFAI library [7]. The alignment of these coordinate frames, consistent with the cubic symmetry of magnetite, was already illustrated in Fig. 3.5. For the calculations, the following single-crystal elastic constants were adopted from Ref. [8]: $c_{11} = 260.5$ GPa, $c_{12} = 148.3$ GPa, and $c_{44} = 63.3$ GPa. The numerical procedure yielded, at each pressure step, a symmetric stress tensor matrix in the form defined by Eq. 3.6.6.

$$\begin{bmatrix} \sigma_{xx} & \sigma_{yx} & \sigma_{zx} \\ \sigma_{yx} & \sigma_{yy} & \sigma_{zy} \\ \sigma_{zx} & \sigma_{zy} & \sigma_{zz} \end{bmatrix} \tag{3.6.6}$$

The dependence of the stress tensor elements σ_{ij} for sample A on the externally applied uniaxial stress σ is shown in Fig. 3.17. In the laboratory reference frame, only the component σ_{zz} exhibited a significant response to the applied compression, remaining linear up to approximately 150 MPa. This value likely marks the upper limit of the elastic regime. The sample did not display visible damage during the measurements and recovered its original shape after stress release. However, at higher applied stresses, the deviation from linearity suggests the onset of irreversible plastic deformation, consistent with the changes already observed in the lattice constants in Fig. 3.6a.

Rotation of the coordinate system allows the stress tensor to be expressed in the crystallographic reference frame. In this configuration, the strongest evolution was observed in the shear component σ_{zy}, associated with the $\langle 011 \rangle$ family of directions, and in the normal components σ_{yy} and σ_{zz}, corresponding to the $\langle 100 \rangle$ directions. These results demonstrate that the uniaxial compression applied externally along the vertical axis was redistributed within the crystal lattice, giving rise to shear stresses along diagonal directions and normal stresses along the transverse axes of the unit cell.

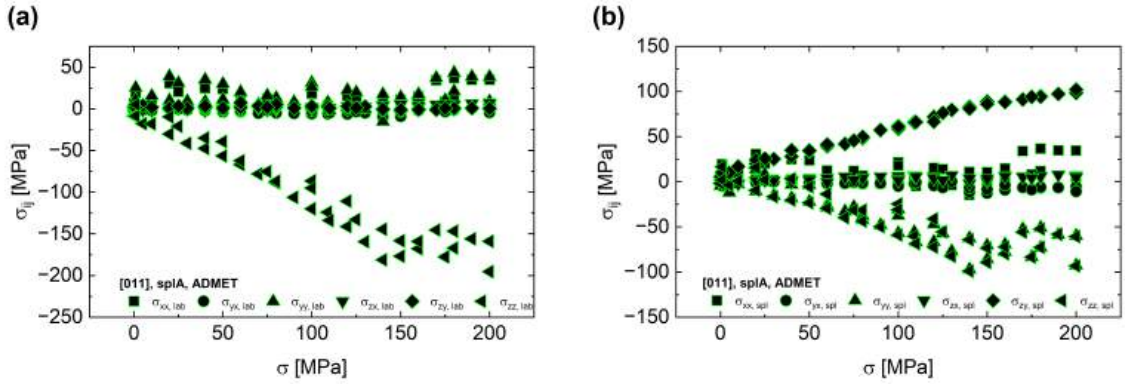

Fig. 3.17. Evolution of the stress tensor components in sample A under uniaxial compression along the [011] direction, measured with the ADMET cell. The elements of the stress tensor σ_{ij} are shown in **(a)** the laboratory reference frame and **(b)** the crystallographic sample reference frame.

The behavior observed for sample A was consistently reproduced in samples B and C. The dependence of the stress tensor elements on the applied uniaxial stress σ for these samples is shown in Figs. 3.18 and 3.19, respectively. In the laboratory reference frame, all stress tensor components except σ_{zz} remained nearly unaffected by the external compression, as expected from the experimental geometry. The evolution of the normal component σ_{zz} was fully consistent with the direction of the applied uniaxial stress. In the crystallographic reference frame, clear linear trends were observed for σ_{zy}, σ_{yy}, and σ_{zz}. The linear dependence of these components on stress in samples B (SOL2) and C (SOL4) demonstrates that both remained within the elastic regime throughout the applied compression.

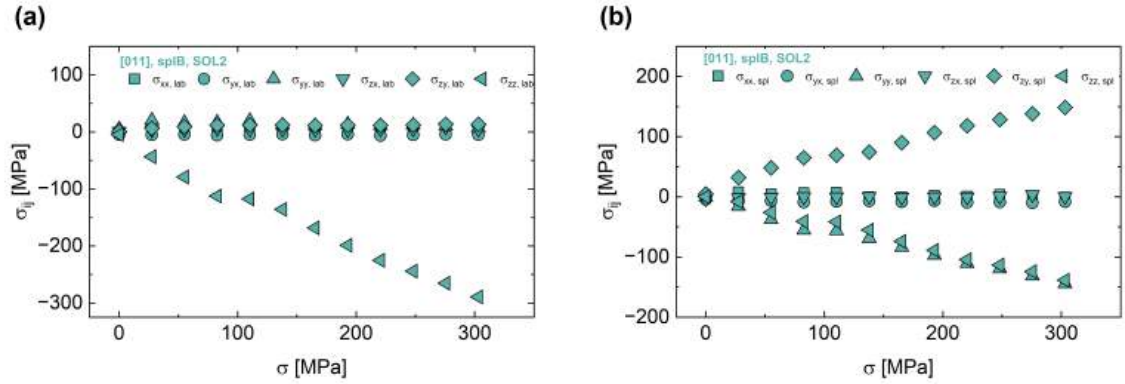

Fig. 3.18. Evolution of the stress tensor components in sample B under uniaxial compression along the [011] direction, measured with the SOL2 cell. The elements of the stress tensor σ_{ij} are shown in **(a)** the laboratory reference frame and **(b)** the crystallographic sample reference frame.

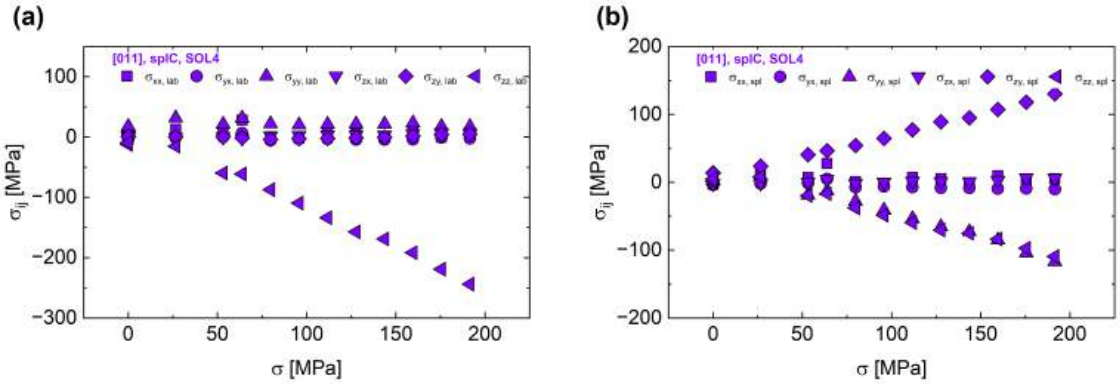

Fig. 3.19. Evolution of the stress tensor components in sample C under uniaxial compression along the [011] direction, measured with the SOL4 cell. The elements of the stress tensor σ_{ij} are shown in **(a)** the laboratory reference frame and **(b)** the crystallographic sample reference frame.

A distinct behavior was observed for sample 1_axas, whose stress tensor components in both the laboratory and crystallographic reference frames are presented in Fig. 3.20. In the laboratory frame, the evolution of the normal component σ_{zz} appeared only quasi-linear and less well-defined than for samples B and C. In the crystallographic frame, an anomalous response was observed in the shear component σ_{zy}. Whereas for samples A, B, and C this element increased systematically with the applied uniaxial stress σ, in the case of sample 1_axas it decreased with increasing stress. This contradictory trend suggests that the sample may have experienced deviations from ideal elastic behavior, likely caused by pre-existing plastic deformation and/or misalignment within the SOL3 cell relative to the compression direction.

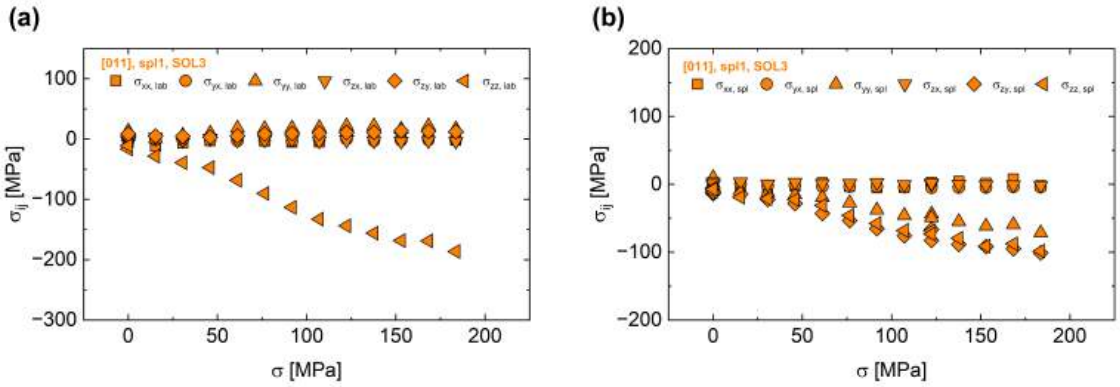

Fig. 3.20. Evolution of the stress tensor components in sample 1_axas under uniaxial compression along the [011] direction, measured with the SOL3 cell. The elements of the stress tensor σ_{ij} are shown in **(a)** the laboratory reference frame and **(b)** the crystallographic sample reference frame.

The stress tensor components for samples B, 1_axas, and C, expressed in both the laboratory and crystallographic reference frames, are summarized in Fig. 3.21. The near-perfect collinearity

of the experimental points in Fig. 3.21b confirms the high precision of the calibration procedure applied to the SOL cells. At the same time, this panel highlights the anomalous response of the shear component σ_{zy} in sample 1_axas, which decreases under compression, in contrast to the tensile evolution observed for samples B and C.

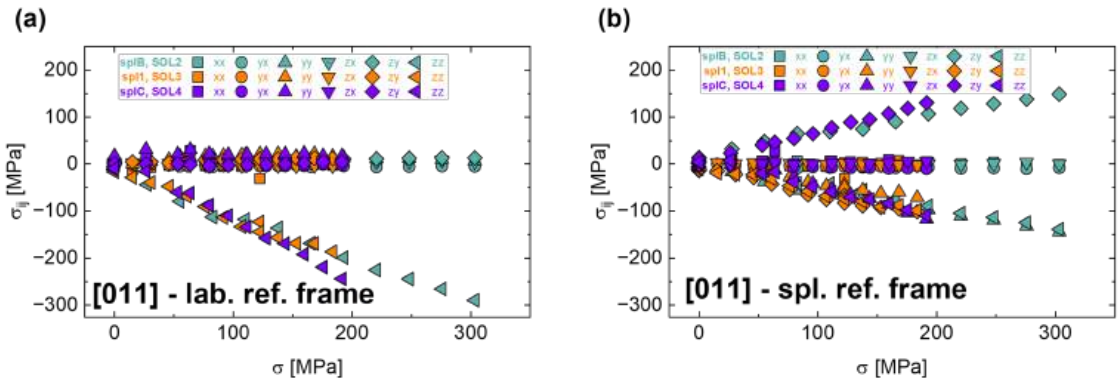

Fig. 3.21. Summary of the stress tensor components for samples B, 1_axas, and C under uniaxial compression along the [011] direction. The elements of the stress tensor σ_{ij} are shown in **(a)** the laboratory reference frame and **(b)** the crystallographic sample reference frame.

The same analysis was carried out for the samples compressed in the [100] geometry. The stress tensor components, expressed in both the laboratory and crystallographic reference frames, are shown for sample G (ADMET reference) and sample F (SOL3) in Figs. 3.22 and 3.23, respectively. In this configuration, the two samples are crystallographically equivalent, enabling a direct comparison of their responses.

For sample G, only the component σ_{zz} exhibited an initial linear response up to approximately 75 MPa, while all other components remained unaffected with the uniaxial stress applied along the [001] direction. Above this value of compression, all stress components took a firm value, which was demonstrated in Fig. 3.22.

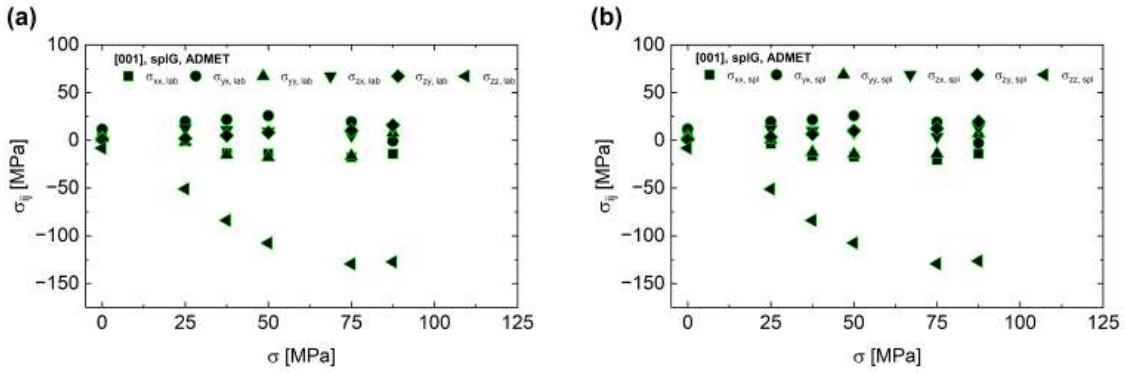

Fig. 3.22. Evolution of the stress tensor components in sample G under uniaxial compression along the [100] direction, measured with the ADMET cell. The elements of the stress tensor σ_{ij} are shown in **(a)** the laboratory reference frame and **(b)** the crystallographic sample reference frame.

For sample F, the evolution of the normal component σ_{zz} was linear up to approximately 80 MPa. Beyond this threshold, all stress tensor components began to deviate from their initial linear trends, indicating a departure from purely elastic behavior. In contrast, for sample G, only a limited number of data points were collected below 100 MPa, which prevented a reliable determination of the elastic limit. Nonetheless, the comparison suggests that while sample G provided only preliminary indications of stress evolution, sample F clearly revealed the onset of non-elastic response at higher applied stresses, cf. 3.23.

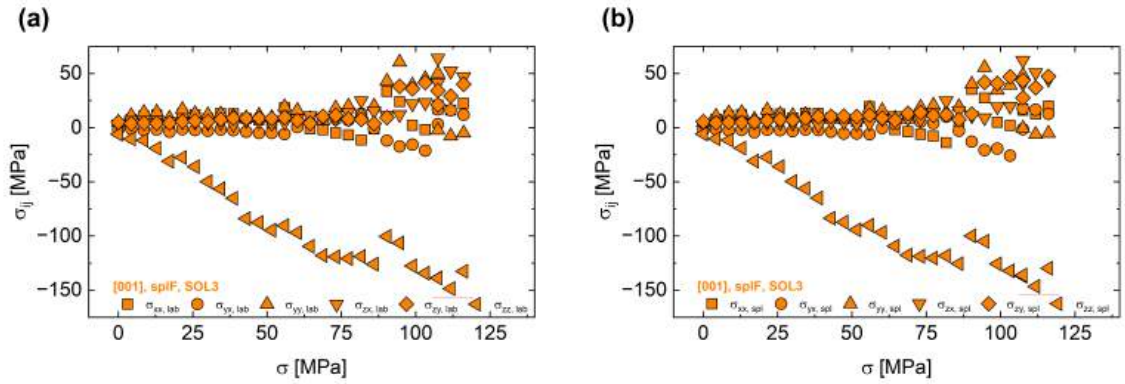

Fig. 3.23. Evolution of the stress tensor components in sample F under uniaxial compression along the [100] direction, measured with the SOL3 cell. The elements of the stress tensor σ_{ij} are shown in **(a)** the laboratory reference frame and **(b)** the crystallographic sample reference frame. The thin red line indicates the boundary between the legend and the last recorded data point.

In the [011] geometry, the stress tensor components in the laboratory reference frame were generally close to zero, with the exception of σ_{zz}, which decreased systematically with increasing uniaxial stress σ. When expressed in the crystallographic reference frame, additional responses were

observed: besides σ_{zz}, the components σ_{yy} and σ_{zy} also evolved with compression, consistent with the monoclinic distortion expected under [011] loading.

In contrast, for the [100] geometry the laboratory and crystallographic reference frames are equivalent. Consequently, the stress tensor components in both frames were indistinguishable within computational precision. In this case, changes under compression were confined exclusively to the σ_{zz} component, consistent with the tetragonal distortion associated with [100] uniaxial stress.

Thus, uniaxial compression along [011] redistributes stress into both shear and transverse directions of the crystal lattice, while compression along [100] preserves the cubic symmetry more closely and confines the stress response to the axial component.

3.7. Conclusions

This chapter has presented the effect of uniaxial compression on the crystal lattice of stoichiometric magnetite, investigated by single-crystal XRD at room temperature.

A series of single-crystalline samples were studied under compression applied along the [100] and [011] crystallographic directions using two types of pressure devices. The ADMET press, equipped with an integrated force sensor, provided an absolute reference for the applied load, while the screw-driven SOL cells introduced in Chapter 2 required calibration. By comparing the evolution of lattice constants and lattice angles obtained with both setups, quantitative calibration factors were derived for the SOL cells. These factors varied slightly among individual devices, reflecting mechanical tolerances, frictional effects, and sample alignment, yet the overall reproducibility between reference and SOL measurements confirmed the reliability of the calibration procedure.

The experiments further enabled the determination of the qualitative and quantitative dependence of the lattice parameters and lattice angles on applied stress. In the [011] geometry, compression reduced the cubic symmetry to monoclinic, leading to equivalent evolution of b and c, accompanied by changes in the shear component σ_{zy}. By contrast, in the [100] geometry the symmetry reduced to tetragonal, where a and b remained equivalent and only σ_{zz} responded significantly to the applied stress. This directional dependence illustrates the strong elastic anisotropy of magnetite, consistent with earlier reports based on ultrasonic velocity and elastic moduli measurements [8, 2].

The stress tensor analysis in both the laboratory and crystallographic reference frames confirmed that the observed lattice distortions are consistent with the applied uniaxial stress. For [011] compression, redistribution into shear and transverse components was evident, while [100] compression confined the stress response to the axial direction. Importantly, the linear evolution of stress tensor components with applied stress demonstrated that the samples generally remained within the elastic regime, with deviations (e.g., in sample 1_axas or sample F) attributed to misalignment or the onset of plastic deformation at higher loads.

The calibration factors established in this study form a quantitative foundation for estimating the applied pressure in all subsequent experiments employing SOL cells. These calibrated values

will be directly utilized in the analysis of electronic transport, magnetic AC susceptibility, and X-ray absorption spectroscopy data presented in Chapters 4 and 5. Their use ensures consistency across different experimental techniques and enables a rigorous, quantitative comparison of uniaxial stress effects in magnetite. This unified calibration framework thus bridges the structural insights obtained from XRD with the functional responses of magnetite, providing a coherent basis for understanding its behavior under uniaxial stress.

Bibliography

[1] M. Documentation. "Stress Tensor". URL: *https://docs.mat3ra.com/properties-directory/non-scalar/stress-tensor/* (visited on 07/03/2025).

[2] D. Chicot et al. "Mechanical properties of magnetite (Fe_3O_4), hematite (α-Fe_2O_3) and goethite (α-FeO·OH) by instrumented indentation and molecular dynamics analysis". *Materials Chemistry and Physics* **129** (2011), pp. 862–870. DOI: 10.1016/j.matchemphys.2011.05.056.

[3] A. Kozłowski et al. "Heat Capacity and Elastic Constants of $Fe_{3-x}Zn_xO_4$ in the Vicinity of the Verwey Transition". *Acta Physica Polonica A* **97** (2000), pp. 883–887. DOI: 10.12693/APhysPolA.97.883.

[4] J. M. Carpenter and C.-K. Loong. "Neutron-scattering instruments: diffractometers and reflectometers". *Elements of Slow-Neutron Scattering, Basics, Techniques, and Applications*. Cambridge University Press, 2015. Chap. 5. DOI: 10.1017/CBO9781139017823.007.

[5] E. L. Bright, C. Giacobbe, and J. P. Wright. "Beam heating from a fourth-generation synchrotron source". *Journal of Synchrotron Radiation* **28** (2021), pp. 1377–1385. DOI: 10.1107/S160057752100669X.

[6] J. H. Hubbell and S. M. S. R. P. D. P. NIST. "NIST: X-Ray Mass Attenuation Coefficients". URL: *https://physics.nist.gov/PhysRefData/XrayMassCoef/tab3.html* (visited on 05/23/2025).

[7] J. P. Wright et al. "Fast Azimuthal Integration using Python". URL: *https://pyfai.readthedocs.io/en/stable/* (visited on 07/14/2025).

[8] H. J. Reichmann and S. D. Jacobsen. "High-Pressure Elasticity of a Natural Magnetite Crystal". *American Mineralogist* **89** (2004), pp. 1061–1066. DOI: 10.2138/am-2004-0718.

Chapter 4.

Intrinsic and induced crystal defect fields probed by diffraction microscopy

This Chapter investigates both intrinsic and stress-induced defects in stoichiometric magnetite single crystals and their influence on the Verwey transition temperature. The structural imperfections were characterized using Dark-Field X-ray Microscopy (DFXM), a synchrotron-based imaging technique enabling three-dimensional mapping of dislocations and strain fields in bulk crystals. Two DFXM experiments were conducted at the ID03 beamline of the ESRF. The fundamentals of this method are outlined in Section 4.1.

Section 4.2 introduces the two main DFXM contrast modes: *mosaicity*, which probes the local angular spread of crystalline domains around the Bragg condition (here, the cubic (004) reflection), and *axial strain*, which detects variations in interplanar spacing d caused by defects or external stress.

In Section 4.3, DFXM measurements at room temperature compare crystals grown by the TSFZ and skull-melter methods (described in Chapter 2). The results show that intrinsic mosaic spread and residual strain depend on the synthesis route, reflecting variations in defect density and lattice homogeneity. Section 4.4 extends the study to crystals subjected to different levels of uniaxial compression. Imaging performed after decompression revealed persistent line-like dislocations aligned with $\{111\}$ slip planes, indicating the formation of stable defect networks. Notably, these extended defects did not alter the Verwey transition temperature, T_V, in contrast to point defects or non-stoichiometry, which strongly suppress or broaden the transition [1, 2].

4.1. Dark-field X-ray Microscopy

Single crystals are often idealized as structures characterized by perfect continuity and periodicity of the atomic lattice up to their external boundaries. In reality, however, crystals, whether of natural or synthetic origin, deviate from this idealized model and invariably contain a variety of imperfections. These defects can be broadly classified according to their spatial extent. The first group consists of extended, long-range defects such as dislocations (edge, screw, or mixed) and slip planes, which may span from tens to thousands of Å. The second group encompasses short-range point defects, including atomic vacancies, interstitials, or substitutional inclusions, which are typically confined to only a few Å. Advances in modern materials characterization techniques have enabled increasingly detailed investigations of how such defects influence macroscopic properties, for example hardness, ductility, or solidification in multi-phase alloys [3]. At the same time, these techniques open new possibilities for exploring the role of crystallographic imperfections in strongly correlated oxides such as magnetite, where their impact on the Verwey transition (VT) remains subject of an ongoing interest.

The internal disorder within solids is most commonly studied using non-destructive X-ray imaging techniques, which typically require synchrotron radiation sources [4]. When interacting with matter, X-rays are partly attenuated and partly scattered, and the different imaging methods can be distinguished according to which fraction of the beam they exploit. Among the most prominent approaches that provide real-space projections are X-ray computed tomography (XCT), which is based on absorption contrast, and diffraction contrast topography (DCT), which exploits diffracted intensity to visualize lattice distortions and defects.

The mathematical foundations of XCT were established in 1917 by the Austrian mathematician Johann Radon, whose integral transform provides the basis for tomographic reconstruction. The first practical tomograph was built by the British engineer Godfrey Hounsfield, who in 1971 performed the first patient scan, an achievement that revolutionized modern medicine and was later recognized with the Nobel Prize in Physiology or Medicine in 1979. XCT reconstructs the internal structure of an object from the spatial distribution of the X-ray attenuation coefficient. Since XCT exploits the radiation transmitted through the sample, often referred to as the "white beam", it is conventionally categorized as a "bright-field" imaging technique. By analogy, methods that instead utilize the diffracted beam, which has lower relative intensity than the transmitted beam, are referred to as "dark-field" imaging [5]. Within this class, diffraction contrast topography (DCT) encompasses a family of hard X-ray techniques, including 3D X-ray diffraction (3DXRD) and Dark-Field X-ray Microscopy (DFXM).

3DXRD, which relies on recording multiple Bragg reflections, enables serial sectioning of samples with dimensions of a few mm^2 and is well suited for imaging numerous structural domains simultaneously, as well as for tracking their evolution over time or under varying temperature conditions [6, 7]. A limitation of this technique is that it employs two detectors in a crossed configuration to ap-

proximate three-dimensional data acquisition, which can limit sensitivity to the deeper-lying grains or substructures. The 3DXRD setup available at the ID11 beamline of the ESRF was briefly described in Section 3.3 of Chapter 3.

DFXM extends the capabilities of 3DXRD by employing a system of focusing X-ray lenses. Unlike 3DXRD, which records multiple Bragg reflections, DFXM operates on a single selected reflection. This enables the technique to probe a specific deeply embedded crystallite and to resolve its size, three-dimensional misorientation, and internal structural properties [7]. In practice, DFXM measures the angular spread of a chosen Bragg reflection within millimeter-sized crystals, providing spatial resolution in the range from a few hundred nanometers down to the micrometer scale [4, 6].

As discussed in Chapter 1, the Verwey transition (VT) in magnetite arises from a subtle interplay between the crystal lattice and the magnetic degrees of freedom, making the compound a model system for studying strong electronic correlations [8, 9]. It is well established, both from thermodynamic considerations [10] and from numerous experimental reports, that the transition temperature T_V decreases under hydrostatic pressure [11, 12, 13, 14], while it increases under uniaxial compression [15, 16]. The lattice strain, which is the central focus of the DFXM studies presented in this chapter, can originate from inhomogeneities in the charge density, manifested as electronic phase separation. In magnetite, such separations have been observed during the symmetry-lowering transition, since the onset temperatures of charge and orbital ordering do not always coincide with the characteristic T_V.

For example, mechanical treatment of magnetite, such as polishing or cutting, affects the long range electronic order by inducing a micrometer-deep and inhomogeneous dead layer, probably of powdered Fe_3O_4 [17]. Thus, VT may be affected by the strain field associated with perturbations in a crystal lattice, since point defects have recently been reported to lower T_V. However, by their nature, the point defects did not result with a long range, stationary lattice deformation [18].

Since strain, whether intrinsic or externally induced, can generate charge inhomogeneities, these electronic inhomogeneities can in turn produce strain fields, leading to charge and structural phase separation that directly impacts the Verwey transition. Together with variations in stoichiometry and the application of external pressure, such crystal strain has therefore emerged as a key factor influencing T_V. It has further been hypothesized that disorder in the form of strain may stabilize the low-temperature phase and hinder the transition. Consequently, a central motivation for the DFXM measurements was to determine the extent and spatial distribution of such crystal strain fields, and to assess their apparent absence in influencing the Verwey transition [2].

Imaging with DFXM requires not only a monochromatic X-ray point source, but also precise alignment of the sample into a specific diffraction reflection. The choice of reflection determines the configuration of the goniometer, the focusing optics, and the detector. Each diffraction reflection is characterized by three Miller indices (hkl), which define the set of crystallographic planes responsible for diffraction and, through their geometry, the corresponding interplanar spacing $d_{(hkl)}$. For magnetite, this spacing can be calculated using Eq. 4.1.1, which simplifies in the case of a cubic crystal with $Fd\bar{3}m$ symmetry to:

$$d_{(hkl)} = \frac{a}{\sqrt{h^2 + k^2 + l^2}}, \tag{4.1.1}$$

Here, $a = 8.3940$ Å denotes the lattice constant of the cubic unit cell at room temperature, which corresponds to the d-spacing of the (001) reflection in cubic notation. In the DFXM sequences performed in this study, the $(004)_{\text{cubic}}$ reflection was selected, corresponding to the four-fold smaller interplanar spacing $d_{(004),\text{cubic}} \equiv d = 2.0985$ Å [19, 20]. The choice of $(004)_{\text{cubic}}$ was motivated by several unique advantages. First, this reflection is present in both the high-temperature cubic and the low-temperature monoclinic phases of magnetite. Second, the temperature evolution of the $(004)_{\text{cubic}}$ reflection directly highlights the onset of charge ordering in the material. Third, this reflection exhibits particularly high intensity compared to others, such as the (003), which is nearly 900 times weaker. The (003) reflection, although sensitive to lattice distortions, is forbidden in the high-temperature cubic phase [17]. Taken together, these factors made the $(004)_{\text{cubic}}$ reflection an excellent candidate for DFXM studies, which were originally designed to also probe the low-temperature monoclinic phase.

The diffraction imaging experiments presented in this Chapter were carried out at the ID03 beamline of the ESRF. This hard X-ray microscopy (HXM) station provides advanced diffraction and imaging capabilities, with a spatial resolution better than 100 nm and a temporal resolution below 1 ms. The beamline is based on an undulator source delivering monochromatic X-rays, tuned by a Si(111) Bragg–Bragg double-crystal monochromator. This configuration allows access to an energy range from 10 to 50 keV with a relative bandwidth of $\Delta E/E = 10^{-4}$. For the present study, the photon energy was set to 17 keV, corresponding to a penetration depth of approximately 0.1 mm, which in turn constrained the maximum thickness of the investigated samples [21]. Vertical focusing of the beam was achieved using a compound refractive lens system composed of 58 one-dimensional Be lenslets, each with a curvature radius of 100 μm.

The HXM bench installed at ID03 is schematically presented in Fig. 4.1. Its active components include the goniometer, the near-field camera, the X-ray optics, and the far-field detector. The goniometer positions and orients the sample into the desired Bragg reflection. The diffraction contrast is first visualized using the near-field camera, while the focused beam is directed by the X-ray optics onto the far-field detector. The operational principles of each of these elements are explained in detail in the following sections.

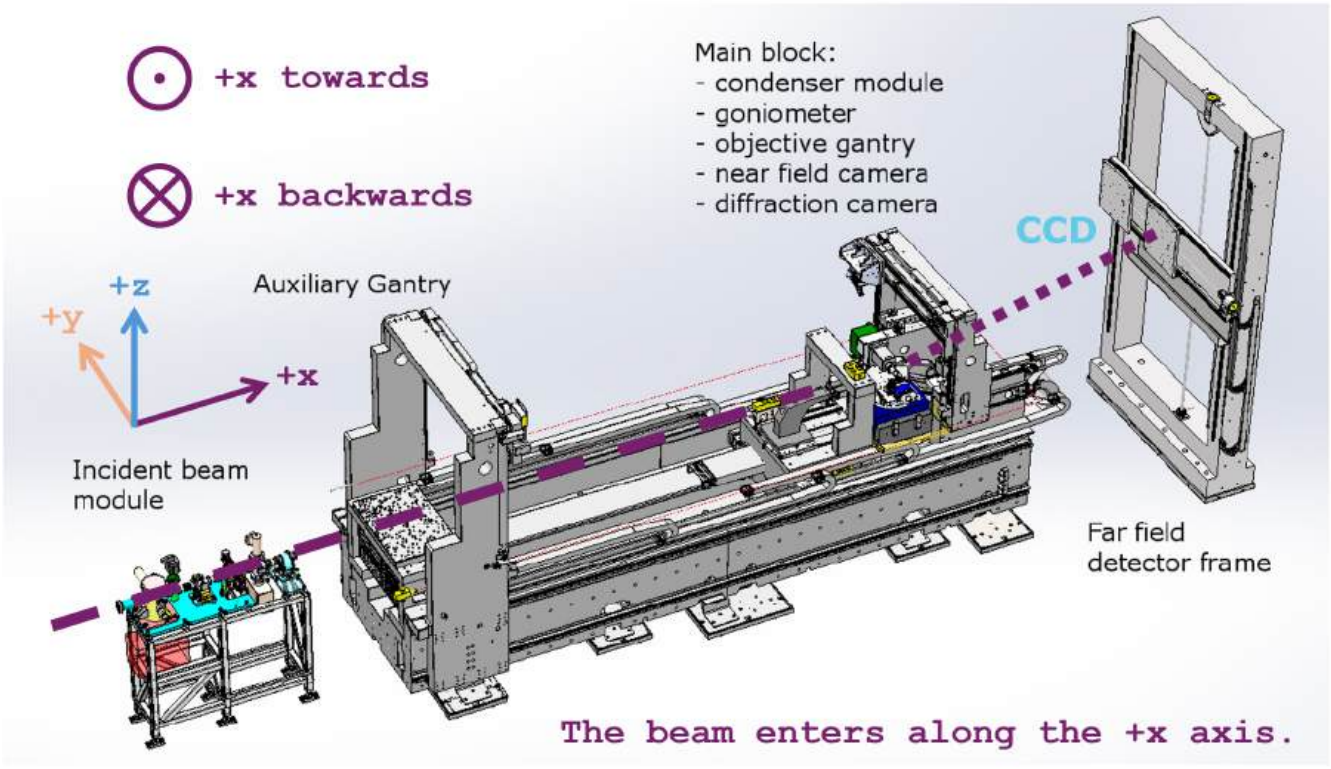

Fig. 4.1. Schematic of the Dark-Field X-ray Microscopy (DFXM) optical bench at ID03. The incident X-rays pass through the beam-conditioning module and are directed onto the sample, which is mounted in the central block and precisely positioned using a goniometer. The diffracted signal can either be observed directly with the near-field camera or transmitted through the X-ray optics to be focused and recorded on the far-field CCD detector. The coordinate system is defined such that the x-axis is aligned with the incident beam direction, the y-axis points horizontally away from the storage ring, and the z-axis is oriented vertically upwards. Adapted from [22].

In the measurements performed in this study, two beam geometries were employed: the box beam and the line beam, as illustrated in Fig. 4.2. The box beam had a profile of approximately 1 mm in width and 0.8 mm in height, whereas the line beam featured a much smaller cross-section of about 100×1 μm^2. Each geometry served a distinct purpose: the box beam provided global information by probing the overall sample volume, while the line beam enabled high-resolution mapping of thin slices, thereby resolving the internal structure of the crystal over micrometer length scales.

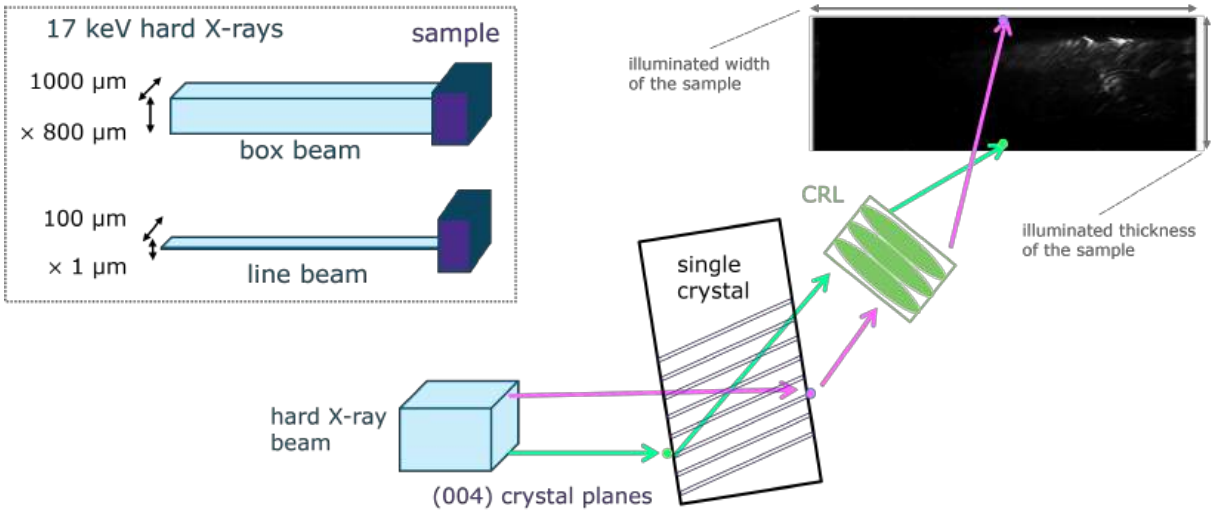

Fig. 4.2. Beam profiles employed at the ID03 beamline. Monochromatic photons of 17 keV produced at ID03 can be shaped by the condenser slits into two distinct geometries. The box beam provides a 1×0.8 mm^2 volumetric projection through the entire sample, whereas the line beam is 100 μm wide and 1 μm thick, enabling the imaging of a thin slice within the specimen. In both cases, the incident X-rays are aligned to satisfy the Bragg condition. The diffracted beam is subsequently magnified by a compound refractive lens (CRL) and recorded by a CCD camera. In this configuration, the horizontal dimension of the CCD image corresponds to the sample width, while the vertical dimension represents the projection of the sample thickness. Since the diffracted beam has much weaker relative intensity compared to the transmitted (attenuated) beam, this technique is referred to as "dark-field" imaging.

The image acquisition sequence was carried out as follows. First, the incident X-ray beam was transmitted through the sample. A near-field alignment camera, positioned 40 mm downstream from the sample, was used to orient the crystal into the Bragg condition. After alignment, the near-field camera was removed and replaced with an X-ray objective, centered in the diffracted beam at a distance of 281 mm from the sample. The objective, a compound refractive lens (CRL), consisted of 88 two-dimensional Be parabolic lenslets, each with a curvature radius of 50 μm. This CRL system provided a horizontal magnification of $M_{\mathrm{CRL},x} = 17.9\times$, projecting the selected region of interest (ROI) in the sample onto the far-field detector.

The far-field detector was located 5010 mm downstream from the sample and consisted of a scintillator crystal coupled to a visible-light microscope and a PCO.edge sCMOS camera (2160 × 2560 pixels). In this configuration, the horizontal dimension of the CCD corresponded to the sample width, while the vertical dimension represented the projection through the sample thickness. An additional $10\times$ magnification was achieved via the visible-light microscope, yielding an effective resolution of 0.75 μm per pixel. Taking into account the combined magnification from both the CRL and the optical microscope, the total magnification of the setup was $M_{\mathrm{total}} = 179\times$.

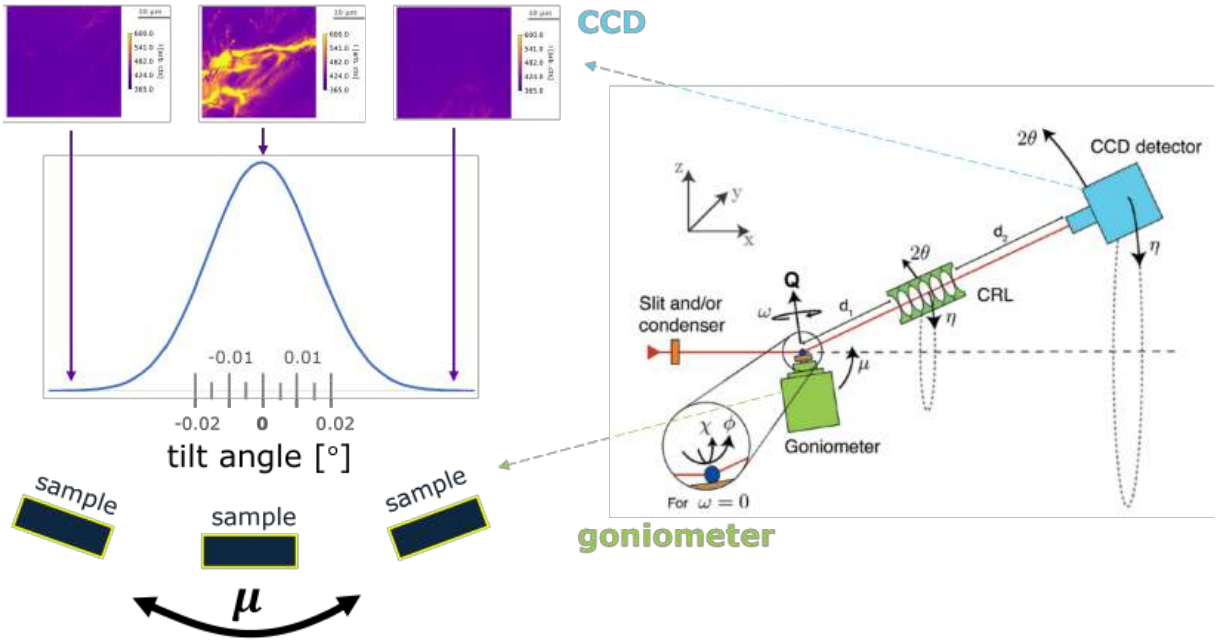

Fig. 4.3. Principle of diffraction-based imaging. The main components of the setup are the goniometer holding the sample, the X-ray optics, and the CCD detector. The incident X-ray beam is diffracted by the sample in accordance with Bragg's law. The diffracted beam is then magnified by the compound refractive lens (CRL) and projected onto the detector. By tilting the sample with one of the goniometer motors (here μ), the angular dependence of the diffraction contrast intensity can be probed. Adapted from [6].

After introducing the ID03 beamline instrumentation, the basics of diffraction-based imaging can now be discussed. Diffraction contrast topography (DCT) is a general term for imaging methods that exploit the contrast of the X-ray beam diffracted by the sample, a category that also includes DFXM. The cross-section of the beam used in topography is typically comparable to the sample size and is on the order of 1–2 mm^2. A topographic projection is obtained by rocking the sample about one of its inclination angles. This principle is illustrated in Fig. 4.3 using the example of the μ rotation. In this procedure, the sample is first positioned in the exact Bragg condition and then incrementally tilted away from equilibrium, while the diffracted intensities are simultaneously recorded on the detector. Because contrast arises only from the crystal regions oriented within the Bragg condition, topography provides direct information on the local defect population and the organization of the diffracting planes. By stacking and processing the series of images acquired during the rocking scan, the overall shape of the diffraction reflection as a function of the tilt angle μ can be reconstructed. The details of the DFXM data treatment are presented in Appendix E.

4.2. Single-crystal uniformity and axial strain in diffraction imaging

Before introducing the operating modes of DFXM, it is necessary to first discuss the topographic technique known as rocking curve imaging (RCI). RCI, as a mode of diffraction contrast topography (DCT), begins by aligning the goniometer holding the sample to the desired Bragg reflection, which in this study was the (004) reflection in cubic notation. The rationale for this choice was thoroughly explained in the previous Section.

The RCI measurement consists of recording a series of diffraction projections while systematically deviating one of the sample's angular degrees of freedom within a range symmetric about the optimal Bragg condition. As the sample is tilted incrementally forward and backward, each pixel of the detector registers the diffracted intensity. For every detector pixel, the set of recorded counts defines a "rocking curve," representing the dependence of the local diffraction intensity on the angular position of the sample. The key parameter extracted from each rocking curve is its center, also referred to as the "Center of Mass" (CoM). A CoM map is constructed by assigning to each detector pixel the midpoint of its rocking curve, thereby providing a spatially resolved representation of the average orientation of the studied reflection across the crystal volume [23]. Understanding the concept of RCI is therefore fundamental to interpreting the imaging modes offered by DFXM.

At ID03, the available DFXM modes are defined by the manipulated angle, as illustrated schematically in Fig. 4.4. Specifically, scanning the scattering angle 2θ probes the axial strain, whereas rotating the sample about μ or χ yields CoM maps corresponding to the local mosaicity.

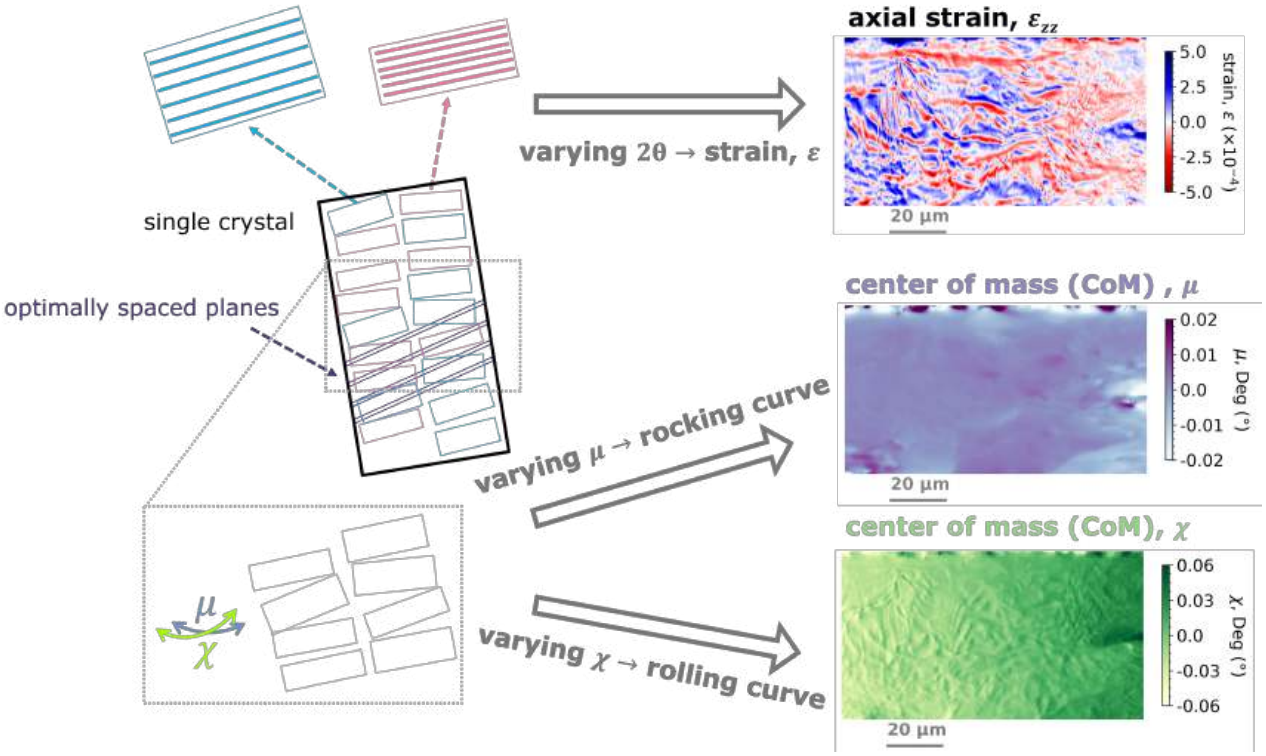

Fig. 4.4. The DFXM imaging modes available at ID03. Variations in the effective scattering angle 2θ are directly related to changes in the interplanar spacing and can be recalculated into the axial strain, ε. Tilting the sample by small increments in either μ or χ reveals regions that are slightly misoriented with respect to the exact Bragg condition. The combined distributions of the μ and χ angles provide a measure of the mosaic spread of the crystal, as further illustrated in Fig. 4.6.

When the diffraction condition is satisfied, the detector is illuminated by X-rays scattered from lattice planes with the nominal interplanar spacing d_0. In real crystals, however, adjacent regions may exhibit locally varying spacings d. Regions where $d < d_0$ correspond to more densely packed planes. These planes cannot relax to the equilibrium spacing and therefore give rise to compressive strain, expressed as $d - d_0 = \Delta d < 0 \Rightarrow \varepsilon_{zz} < 0$. Conversely, regions with $d > d_0$ produce tensile strain, as the expanded planes stretch their surroundings away from d_0, leading to $d - d_0 = \Delta d > 0 \Rightarrow \varepsilon_{zz} > 0$. According to Bragg's law, $2 \cdot d \cdot \sin\theta = n \cdot \lambda$, such local variations in d manifest experimentally as angular shifts in the diffracted beam (2θ). The origin of these two types of axial strain is schematically illustrated in Fig. 4.5 [22].

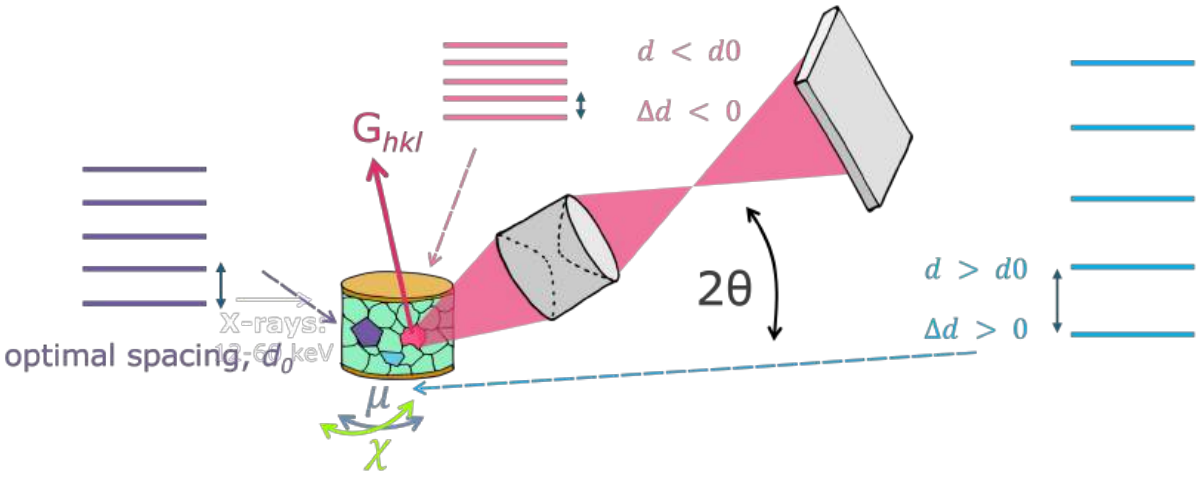

Fig. 4.5. Tilting the X-ray objective around the Bragg angle 2θ modifies the diffraction condition and enables the detection of X-rays scattered from lattice planes with slightly different interplanar spacings. For example, $\mathrm{G_{hkl}}$ denotes the reciprocal lattice vector corresponding to a grain with an interplanar distance d smaller than the reference spacing d_0. By further adjusting the goniometer motors, the diffraction condition can also be satisfied for planes with an increased interplanar distance $d > d_0$. Such angular shifts in 2θ correspond to local compressive ($d < d_0$) or tensile ($d > d_0$) axial strain within the crystal. Adapted from [22].

The strain can be studied indirectly by probing shifts of the diffraction angle 2θ. Starting from Bragg's law, $n \cdot \lambda = 2 \cdot d \cdot \sin\theta$, a small variation in the interplanar distance d around the reference value d_0 results in a corresponding angular shift of the diffraction condition. Repositioning of the initial Bragg condition ($d \equiv d_0$), therefore makes the detector sensitive to crystallographic planes with slightly different d-spacings. The axial strain component ε_{zz} can then be expressed in terms of the spatial distribution of the optimal 2θ (Center of Mass, CoM) as:

$$\varepsilon = \frac{\Delta d}{d_0} = -\frac{1}{2} \cdot \frac{\sin(\Delta 2\theta)}{\tan(\theta)}, \tag{4.2.2}$$

where 2θ is the diffraction angle and d_0 is the unstrained interplanar distance. For the very small angular deviations probed in DFXM ($\Delta 2\theta \ll 1$ rad), the approximation $\sin(\Delta 2\theta) \approx \Delta 2\theta$ holds, and Eq. 4.2.2 simplifies to the commonly used linearized form:

$$\varepsilon = -\frac{\Delta(2\theta)}{2\tan\theta},$$

which is the standard relation adopted in diffraction strain analysis [4, 6, 22].

Mosaicity can be regarded as an extension of rocking curve imaging (RCI). In DFXM, the sample is mounted on the goniometer and aligned in the desired Bragg reflection, after which its orientation can be adjusted with three principal motors that control the rocking angle μ, the rolling angle χ, and the diffraction angle 2θ. Tilting the sample via μ or χ changes only its orientation relative to the incident beam, whereas modifications in 2θ additionally require coordinated adjustments of

the goniometer, the X-ray optics, and the far-field detector to preserve the diffraction condition. In addition to axial strain, another key quantity accessible in DFXM is mosaicity, which characterizes the degree of local crystallographic misorientation within the sample. Mosaicity is determined from the convolution of the simultaneously measured CoM maps obtained by scanning the rocking (μ) and rolling (χ) angles. In this joint angular phase space (μ, χ), each pixel in the detector reflects the local angular spread of crystallographic domains relative to the nominal Bragg condition, and mosaicity maps therefore reveal the magnitude and spatial distribution of misorientation across the illuminated crystal volume. The principle of constructing a mosaicity map is illustrated schematically in Fig. 4.6 [4, 6].

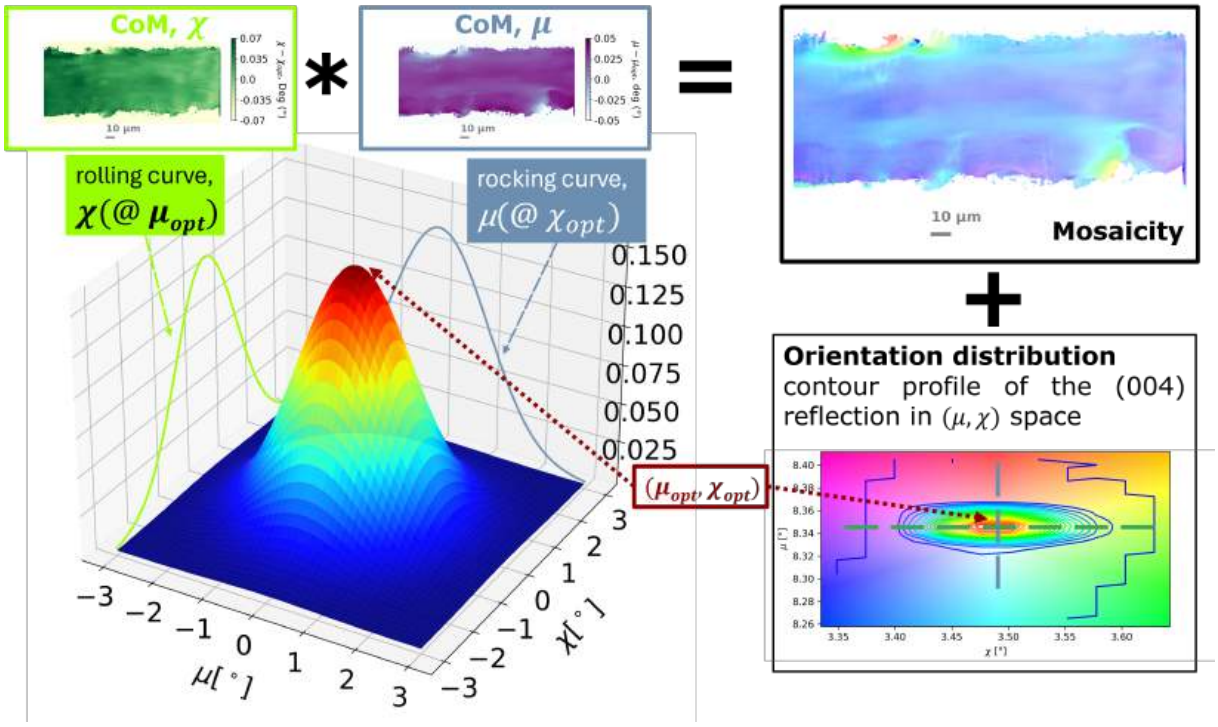

Fig. 4.6. Construction of a mosaicity map in DFXM. The center of mass (CoM) distributions obtained for the rocking angle μ and the rolling angle χ are numerically convolved (denoted by the star operator, $*$) to yield the mosaicity map, which visualizes the local texture of the crystal. The map is represented in a hue-saturation-value (HSV) color scale, where the isolines indicate the orientation distribution of the selected Bragg reflection. The optimal values of the rocking and rolling angles, μ_{opt} and χ_{opt}, respectively, mark the center of the angular spread.

Mosaicity is usually measured in a programmed sequence that divides the sampling ranges of both tilting angles into discrete steps. For a fixed value of the rocking angle μ, all possible values of the rolling angle χ are scanned, after which μ is incremented by one step and the procedure is repeated. In this way, a two-dimensional distribution of the diffracted intensity of the selected Bragg reflection is collected. Mosaicity can therefore be regarded as rocking curve imaging extended to two angular degrees of freedom. The individual CoM maps extracted from the scans of μ or

χ are commonly represented in a one-dimensional grayscale, while the full mosaicity map requires a pole-figure representation of the orientation distribution. This is typically visualized using a two-dimensional color scale combined with isolines, which connect regions of equal frequency of diffracted intensity for successive angle pairs (μ, χ). Broad or irregular distributions in such maps are indicative of local crystallographic misorientations, often linked to dislocations, low-angle grain boundaries, or subgrain structures within the crystal.

4.3. Dependence of the synthesis method on the intrinsic defect fields

This Section presents an experiment aimed at assessing the room-temperature crystalline quality and strain fields in two stoichiometric magnetite single crystals, labeled E_JD3 and SM446. Sample E_JD3 was grown by the Traveling-Solvent Floating Zone (TSFZ) method and provided by Dr. Jose Emilio Lorenzo (Institut Néel CNRS) and Dr. Christophe Marin (Centre d'Études Nucléaires de Grenoble, France). Sample SM446 was synthesized using a skull melter by Professors Andrzej Kozłowski and Zbigniew Kąkol in the laboratory of the late Prof. Jürgen Honig at Purdue University (Indiana, USA).

As discussed in Chapter 2, both methods are well established for producing large single crystals of magnetite, but they differ in their ability to control oxygen stoichiometry. In particular, oxygen stoichiometry can be adjusted with high precision in the skull-melter growth, while it remains less constrained in the TSFZ method. Since deviations in stoichiometry can promote local charge inhomogeneities, this parameter is expected to influence the strain landscape and, consequently, the Verwey transition (VT). Recent work has suggested that such electronic inhomogeneities may manifest as axial strain fields that stabilize the low-temperature phase and modulate the transition temperature [2]. DFXM, with its sensitivity to internal strain and misorientation, thus provides a powerful probe to visualize how synthesis-related defects propagate into the bulk of the crystals.

Both samples were first characterized by AC magnetic susceptibility, which revealed a reproducible difference of approximately 0.6 K in their respective T_V. This difference, shown in Fig. 4.7, was repeatedly confirmed by independent measurements and can plausibly be correlated with the distinct synthesis routes. Consequently, the primary motivation for performing DFXM on these specimens was to assess how the growth method influences crystal quality and defect distributions, thereby providing a structural context for the observed differences in T_V. Importantly, these comparative studies also guided the selection of samples for subsequent electronic transport and magnetic susceptibility experiments under uniaxial pressure. For these investigations, we chose crystals grown by the TSFZ technique, as they exhibited a lower level of mosaicity and dislocation-like defects compared to the skull-melter crystals. Although the TSFZ-grown samples showed a higher average axial strain,

their overall structural uniformity and near absence of extended defects made them more suitable for probing intrinsic uniaxial pressure effects without the complication of growth-induced disorder.

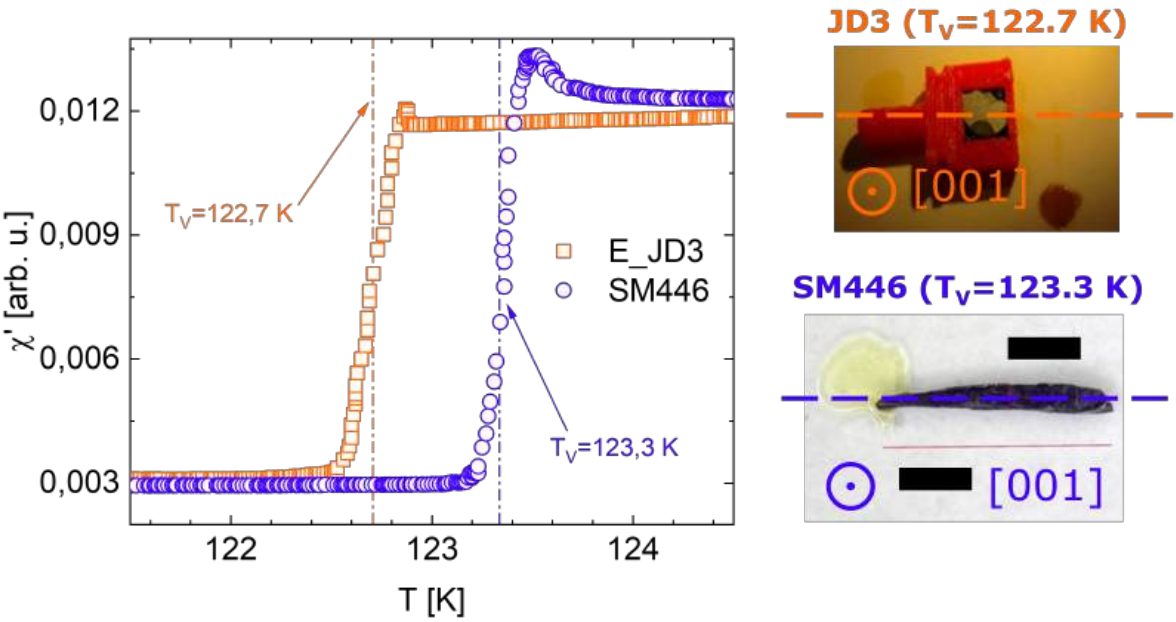

Fig. 4.7. Temperature dependence of the AC magnetic susceptibility in the vicinity of the Verwey transition for two stoichiometric magnetite single crystals synthesized by different methods. Sample E_JD3 was grown using the Traveling-Solvent Floating Zone (TSFZ) technique, while sample SM446 was synthesized in an inductively heated skull melter furnace. The observed difference in T_V between the two crystals exceeded 0.5 K, providing the motivation to investigate their defect concentrations and intrinsic strain states using diffraction-based microscopy. For this purpose, both specimens were oriented with their flat surfaces parallel to the (001) plane and mounted on dedicated 3D-printed DFXM holders.

The samples were mounted with their flat surfaces parallel to the (001) plane. The initial alignment with respect to the incident X-ray beam is shown in Fig. 4.7. Each specimen was first brought into the Bragg condition using the near-field camera to verify the quality of the diffraction contrast. Once aligned, the near-field camera was removed and the diffracted beam was magnified onto the far-field detector using compound refractive lenses (CRL).

The imaging was performed with a line beam of dimensions 100 μm (width) × 1 μm (height). This cross section illuminated approximately 4800 crystallographic planes of type (004). Each sample was scanned vertically in a stack of 10 slices, spanning a total depth of 100 μm with incremental steps of ∼10 μm. The goniometer was programmed to translate the sample along the z-axis through the beam, and for each slice both mosaicity and axial strain maps were collected.

For mosaicity scans, the sequence consisted of 40 steps in the rocking angle μ and 11 steps in the rolling angle χ, corresponding to angular ranges of $\Delta\mu = \pm 0.15°$ and $\Delta\chi = \pm 0.25°$ around

their respective optimal values. For axial strain scans, the rocking angle was again probed with 40 steps within $\Delta\mu = \pm 0.15°$, while the diffraction angle was varied in 7 steps across $\Delta(2\theta) = \pm 0.11°$. Representative slices for each sample, reconstructed from mosaicity and strain imaging, are compared in Fig. 4.8.

For sample E_JD3, the angular spread of the rocking angle was limited to $\Delta\mu \approx 0.03°$, while the rolling angle extended to $\Delta\chi \approx 0.20°$. By contrast, the orientation distribution in sample SM446 exhibited broader misorientations. Here, the rocking angle spread was approximately three times larger, $\Delta\mu \approx 0.10°$, while the rolling angle spread was $\Delta\chi \approx 0.22°$, slightly exceeding that of E_JD3 by about 10%. The quantitative values of the angular spreads determined from the orientation distributions are summarized in Tab. 4.1.

Name	μ_{opt} [°]	$\Delta\mu$ [°]	χ_{opt} [°]	$\Delta\chi$ [°]	**Growth method**
E_JD3	7.89	0.03	2.72	0.20	TSFZ
SM446_Dsmall2	9.54	0.10	3.51	0.22	skull melter

Tab. 4.1. Mosaicity parameters for samples E_JD3 and SM446, which were computed from the maps presented in Fig. 4.8.

A direct comparison of the mosaicity maps revealed contrasting trends. In sample E_JD3, a granular pattern was visible primarily along the crystal edges, which had been polished with lapping paper, suggesting that these features were preparation-induced rather than intrinsic. In contrast, sample SM446 exhibited grains with characteristic sizes on the order of several tens of µm, distributed throughout the bulk volume. The scale and homogeneous distribution of this mosaic defect field strongly suggest that it originated during the final stage of growth, when the boule was rapidly quenched on a copper block in the skull-melter process.

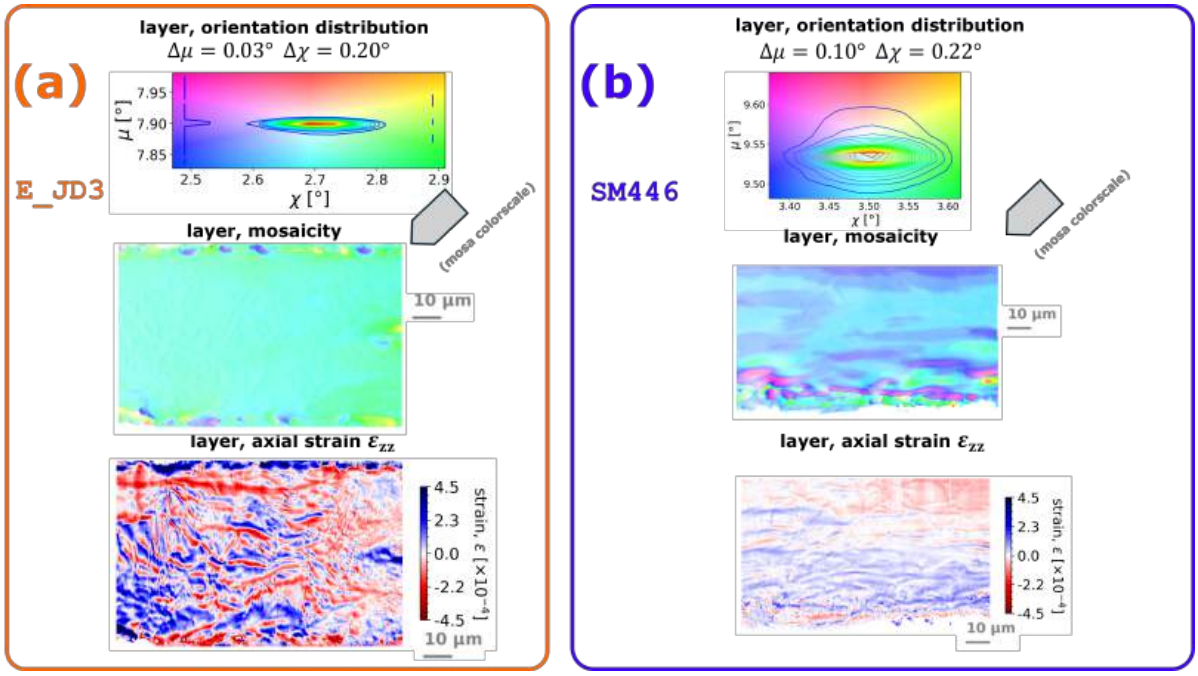

Fig. 4.8. Comparison of mosaicity and axial strain maps collected at room temperature for samples **(a) E_JD3** and **(b) SM446**. Sample E_JD3 displayed nearly defect-free bulk contrast, with only minor features visible near the polished edges, but exhibited an order of magnitude larger average axial strain compared to SM446. In contrast, SM446 showed significantly lower strain but a pronounced mosaic texture, with numerous grains and dislocation-like features, plausibly originating from rapid quenching during skull-melter growth.

The amplitude of the axial strain, ε_{zz}, calculated for sample E_JD3 fluctuated around 3×10^{-4}, but its spatial distribution could not be directly correlated with the granular features observed in the mosaicity map. By contrast, the absolute strain values in sample SM446 were nearly an order of magnitude smaller, not exceeding 0.5×10^{-4}. Interestingly, in SM446 the axial strain maps exhibited a band-like pattern that coincided with the structures visible in the mosaicity maps. This observation appears counterintuitive, since regions of the crystal with stronger mosaic texture were associated with smaller strain.

Ultimately, the lower T_V was measured for sample E_JD3, despite its weaker mosaicity. This outcome is plausibly linked to its higher average axial strain, which may have stabilized the low-temperature monoclinic phase. An alternative explanation is that stoichiometry was not strictly controlled during the TSFZ growth of E_JD3, whereas the skull-melter synthesis of SM446 involved precise regulation of the oxygen partial pressure, thereby reducing non-stoichiometry effects.

4.4. Response of the defect field to external uniaxial stress

Following the in-situ XRD experiments reported in Chapter 3, which characterized the crystallographic response of magnetite under applied uniaxial compression, the present study was designed to determine whether such stresses leave a permanent microstructural imprint that remains detectable after decompression. The primary objective was to investigate how uniaxial stress modifies the defect field in stoichiometric magnetite single crystals and whether these stress-induced features persist in the relaxed state. To this end, three specimens cut from the same TSFZ-grown boule (introduced in Section 2.2.1, Chapter 2) were examined: one pristine, unstressed reference crystal and two others that had previously been subjected to uniaxial compression along a $\langle 110 \rangle$-type direction, reaching medium ($\sim$150 MPa) and above-fracture ($>$300 MPa) stress levels, respectively. Importantly, the DFXM measurements were carried out only after decompression, providing direct insight into the persistence of stress-induced defect structures and their potential influence on the Verwey transition.

An additional aim was to compare the defect population of the pristine crystal at room temperature and below the Verwey transition. However, this part of the study could not be realized due to technical limitations with the cryogenic setup, as discussed later in this Section.

The samples investigated in this experiment are listed below, with their photographs shown in Fig. 4.9. Each sample was marked using a consistent color code to indicate the level of uniaxial stress applied during preparation. Specifically, green indicates the reference sample without applied compression, yellow corresponds to moderate uniaxial compression, and red denotes the sample subjected to compression levels high enough to induce mechanical failure. This color scheme is consistently maintained throughout this Section to facilitate clear identification of each sample and to trace the corresponding experimental results.

- E_JD2 served as the unstressed reference sample. Prior to the DFXM studies, it had never crossed the Verwey transition since its synthesis.
- E_011_ii_spl4 was subjected to a moderate uniaxial compression of approximately 150 MPa applied along the [011] crystallographic direction. This stress magnitude is below the typical fracture threshold for magnetite but sufficient to introduce extended defects [10].
- E_011_spl2_XAS (brokenP) fractured under a uniaxial stress exceeding 300 MPa applied along the [011] direction. The same crystal had previously been investigated in XAS experiments at SOLARIS, National Synchrotron Radiation Centre, Jagiellonian University in Krakow.

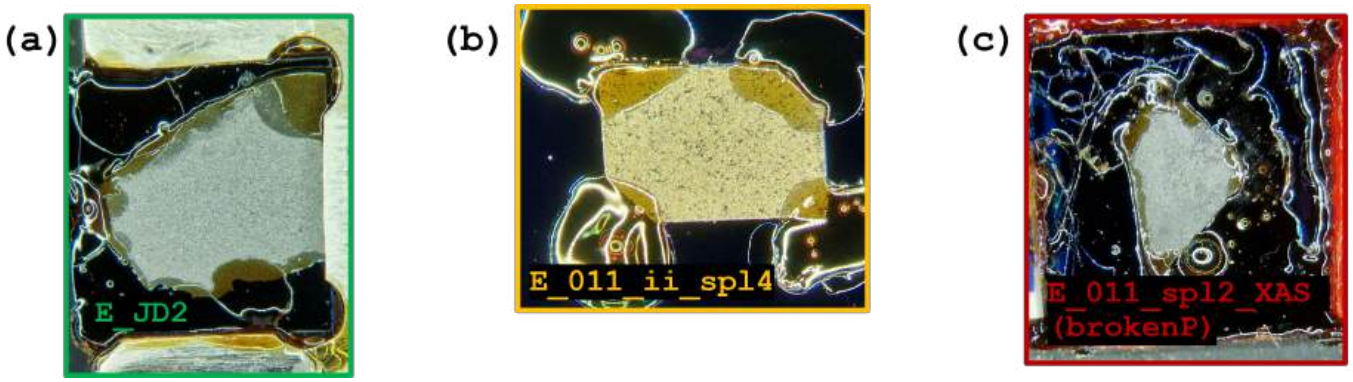

Fig. 4.9. Three samples subjected to different levels of uniaxial stress were mounted on dedicated silicon films with transparent windows (on the bottom side). **(a)** Sample E_JD2 was a pristine reference crystal, not exposed to uniaxial stress. **(b)** Sample E_011_ii_spl4 experienced moderate uniaxial compression of approximately 150 MPa during electrical resistivity measurements; it remained intact and was subsequently thinned for further DFXM studies. **(c)** Sample E_011_spl2_XAS fractured under uniaxial stress exceeding 300 MPa. A fragment from the larger crystal studied with XAS was prepared as described in Fig. 4.12.

The samples investigated in this study had typical dimensions of $1 \times 0.5 \times 0.1$ mm^3. All crystals were mechanically polished to a uniform thickness of 100 μm, a value determined by the penetration depth of 17 keV X-rays used in the DFXM experiments. Each sample presented a flat surface oriented parallel to the (001) crystallographic plane, ensuring consistent geometry for diffraction measurements. The relative alignment of the samples with respect to the incident X-ray beam is illustrated in Fig. 4.10.

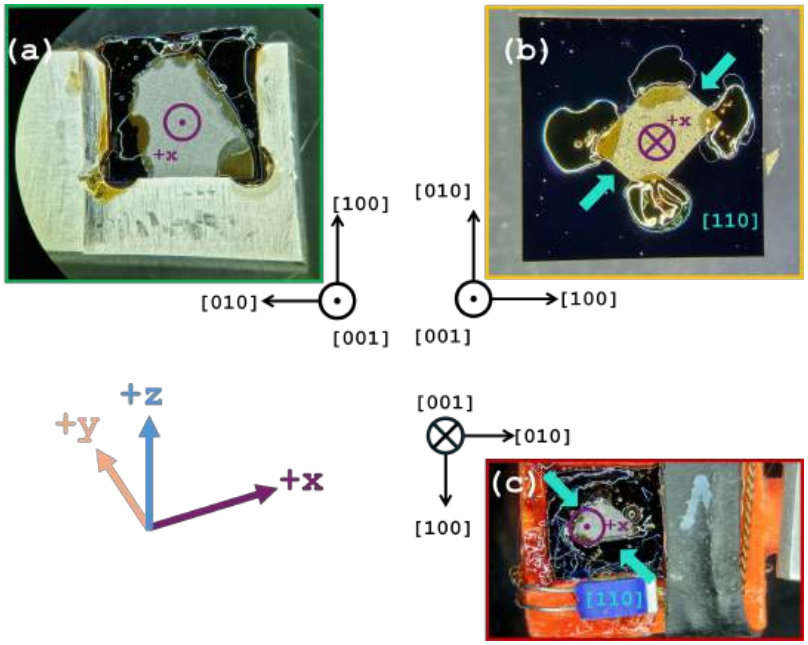

Fig. 4.10. Orientation of the samples **(a)** E_JD2, **(b)** E_011_ii_spl4, and **(c)** E_011_spl2_XAS mounted on the DFXM holders, shown relative to the coordinate system defined at the ID03 beamline in Fig. 4.1. The thick mint-colored arrows in panels (b) and (c) indicate the $< 110 >$ direction along which uniaxial compression was applied.

Each of the tested samples was prepared using a similar protocol, despite differences in their prior experimental history. Sample E_JD2 was mounted on the holder using GE Varnish without prior application of external stress. Since it had never been cooled below room temperature after synthesis, the crystal was regarded as "virgin" with respect to the Verwey transition (VT). It was therefore treated as a reference sample, free from defects associated with uniaxial stress or thermal cycling.

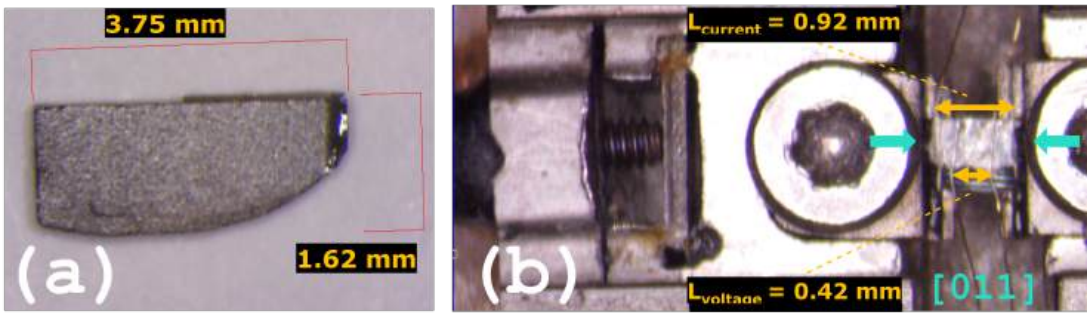

Fig. 4.11. Preparation of the sample E_011_ii_spl4 for resistivity measurements under uniaxial stress. **(a)** Dimensions of the sample prior to cutting and polishing into a bar, shown in panel **(b)**. After polishing to a length of 1 mm, and preparing the electrical contacts, the sample was mounted on the SOL2 cell. L_{current} and L_{voltage} denote the distances between the current and voltage contacts, respectively.

Sample E_011_ii_spl4 underwent a two-step preparation procedure. As illustrated in Fig. 4.11, it was first contacted and mounted on the SOL2 cell to measure the dependence of electrical resistivity under uniaxial stress along the [011] direction. Resistivity was measured up to a compression of approximately 150 MPa. After decompression, the sample was recovered intact, the electrical contacts were removed with acetone, and the crystal was polished to a thickness of 0.1 mm. Results of transport experiments under uniaxial compression are presented and discussed in Chapter 5.

Sample E_011_spl2_XAS was originally oriented, polished, and mounted on the SOL4 cell to investigate the effect of uniaxial compression on the Fe K-edge in stoichiometric magnetite (see Chapter 5, Section 5.3). Among the three crystals later studied with DFXM, this sample was exposed to the highest stress, since the uniaxial compression applied along the [011] direction exceeded 300 MPa, which led to its fracture. A recovered fragment of this sample, referred to as brokenP, was subsequently prepared for DFXM as shown in Fig. 4.12.

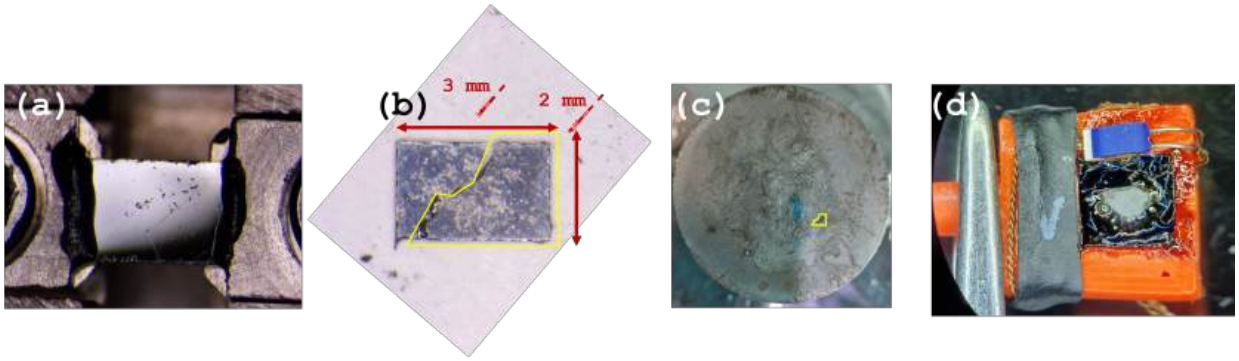

Fig. 4.12. Preparation of the sample E_011_spl2_XAS, which fractured during X-ray absorption spectroscopy measurements. **(a)** After dismounting from the SOL4 cell, the crystal broke into two pieces along the diagonal crack visible in panel **(b)**. **(c)** The recovered fragment was thinned to 100 μm using a manual polisher with P1000/P2000 water sandpapers. **(d)** The sample was then mounted on a 3D-printed holder for DFXM. The blue element is a Pt-100 temperature sensor.

The experimental routine was similar for all samples. After mounting a crystal on the goniometer and aligning it to the Bragg condition, the diffraction contrast was verified with the near-field camera. Once optimal alignment with the maximal reflection intensity was obtained, the motor positions were fixed, the near-field camera was removed, and the CRL was inserted. The far-field camera was then positioned according to the geometry defined by the sample and the X-ray optics. The condenser slits were adjusted to form a rectangular beam of 0.8 mm by 1.0 mm. Each sample was subsequently scanned with this **box-shaped beam, (or box beam)**, first to measure the mosaicity and then the axial strain.

Both scans were automated using a dedicated Python macro. For the mosaicity scan, the rocking angle μ was varied within $\pm 0.05^\circ$ of μ_{opt} in 45 steps, while the rolling angle χ was varied within $\pm 0.14^\circ$ of χ_{opt} in 10 steps. For the strain scan, μ was varied as in the mosaicity scan, while the objective pitch 2θ was stepped 10 times within $\pm 0.06^\circ$ of its optimal value. The resulting mosaicity and strain maps obtained from box-beam scanning are presented in Fig. 4.13.

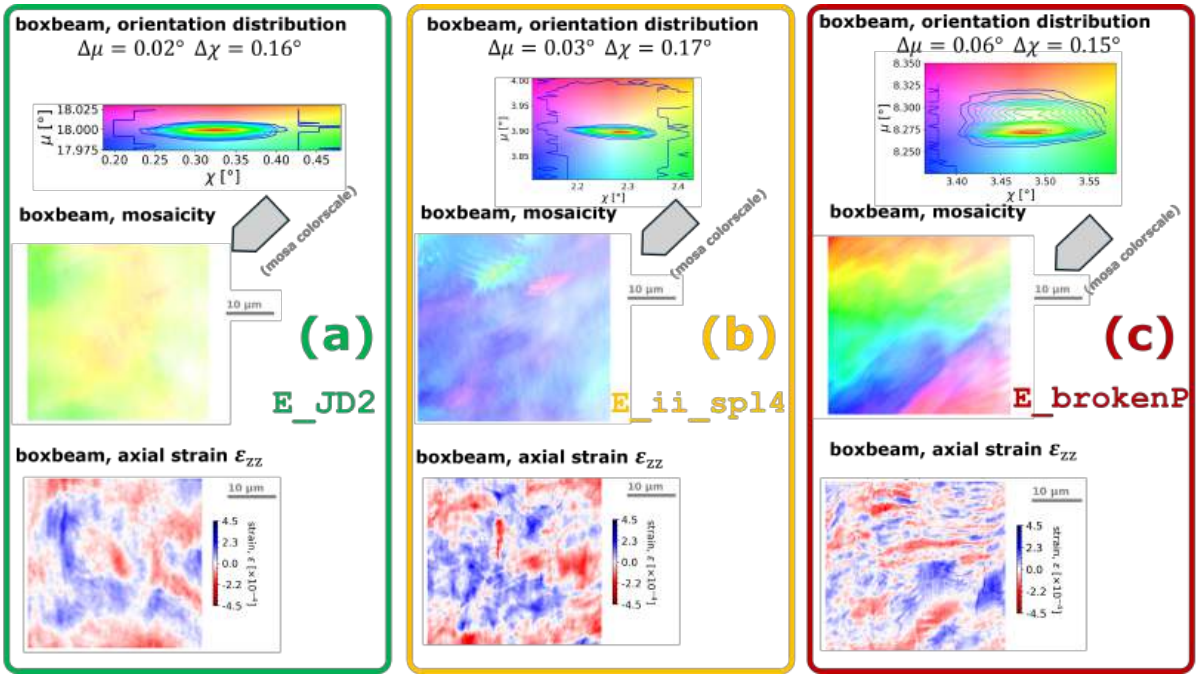

Fig. 4.13. Comparison of mosaicity and axial strain maps obtained with the box beam for samples **(a)** E_JD2, **(b)** E_011_ii_spl4, and **(c)** E_011_spl2_XAS (brokenP). In the mosaicity maps, E_011_ii_spl4 shows a granular dislocation pattern induced by uniaxial stress, while the interior of brokenP exhibits a pronounced folded structure, which is further supported by the splitting observed in the orientation distribution contour plot (panel c, top). The mosaicity map of E_011_ii_spl4 (panel b, middle) also reveals diagonal defect structures as the result of the prior intermediate compression up to 150 MPa. The diagonal lines become more developed in the fractured sample (c). These defects are further reflected in the axial strain maps, where they manifest as localized strain variations along the boundaries of the adjacent crystal regions.

The second stage of the experiment involved recording a layer scan using a thinner **line beam**. The condenser slits were adjusted to produce a beam profile of 100 μm (0.1 mm) in the horizontal direction and 1 μm (0.001 mm) in the vertical direction. Compared to the box beam, this configuration probed a much narrower cross-section of the sample. In this mode, neither the number of motor steps nor their angular ranges in the macro were modified. The sequence was repeated to collect 10 layers of mosaicity and strain, and between each iteration the sample was shifted along the z direction by ± 0.05 mm relative to the central alignment position. For each sample, one representative layer obtained with the line beam was selected for comparison. The layers presented in Fig. 4.13 reveal trends that contrast with those observed in the box-beam images.

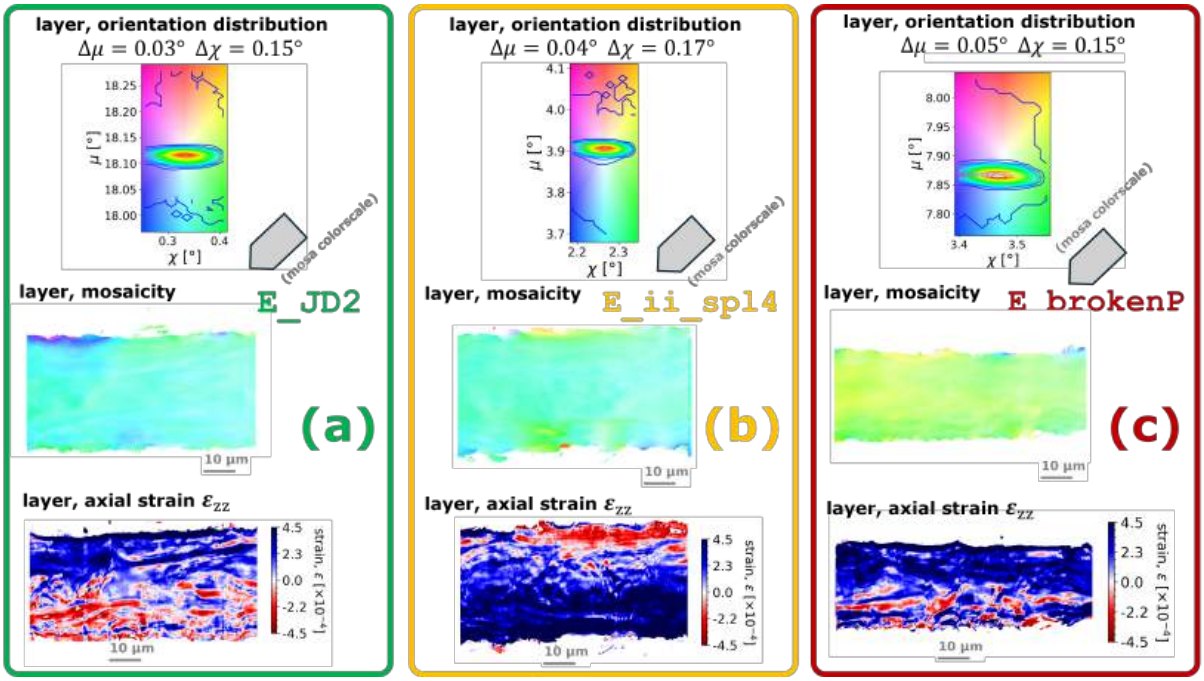

Fig. 4.14. Comparison of mosaicity and axial strain maps obtained with the line beam for samples **(a)** E_JD2, **(b)** E_011_ii_spl4, and **(c)** E_011_spl2_XAS (brokenP). In contrast to the box-beam maps shown in Fig. 4.13, no clear effect of uniaxial stress is visible in panels **(b)** and **(c)**. The interior of all samples appears uniform except for distortions near the polished edges, and the axial strain patterns do not exhibit any systematic features. See text for further explanation.

The following observations were made by comparing the mosaicity maps obtained with the box beam, as presented in Fig. 4.13. The orientation distributions for all samples indicate a relatively broad, but comparable, rolling angle $\Delta\chi$ ranging between 0.15° and 0.17°. In contrast, the distribution in the rocking angle $\Delta\mu$ was an order of magnitude smaller; it increased from 0.02° in the pristine reference E_JD2 sample up to 0.06° for the fractured E_brokenP sample. In this case, the contour plot appears split along $\Delta\mu$, with a secondary maximum emerging. The dislocation fields observed in the corresponding mosaicity maps also differed clearly between E_011_ii_spl4 and E_brokenP, especially in comparison with the unstressed E_JD2. The increase in defect density with applied pressure is most evident in the diagonal line patterns, which are particularly pronounced in the E_brokenP sample.

The mosaicity parameters measured with the line beam were not significantly different from those obtained with the box beam. However, the irreversible structural changes observed on a global scale in samples E_011_ii_spl4 and E_brokenP were not resolved at the micrometer scale in the layer scans. The edges of the crystals consistently appeared more defective than their interiors, which is expected due to standard preparation procedures such as cleaving, cutting, and polishing. The discrepancy between the box-beam and line-beam images arises from the sampling geometry. In the box-beam configuration, the relatively thick beam integrates information across many layers along the depth

of the crystal, effectively projecting structural inhomogeneities from the entire illuminated volume into a two-dimensional map. As a result, defects and strain fields introduced by prior uniaxial stress accumulate in the projection and appear as distinct features in the mosaicity and strain maps. By contrast, the line-beam configuration probes a much thinner cross-section of the crystal, restricting the measurement to a narrow slice. While this improves spatial resolution along the beam direction, it reduces sensitivity to extended or non-uniform fields distributed through the bulk. Consequently, the localized signatures of prior compression are averaged out in the line-beam measurements, leading to the absence of clear stress-related patterns in the corresponding maps.

Name	μ_{opt} [°]	$\Delta\mu$ [°]	χ_{opt} [°]	$\Delta\chi$ [°]	**boundary σ [MPa]**	**Compression**
E_JD2	17.99	0.02	0.33	0.16	0	unstressed
E_011_ii_spl4	3.91	0.03	2.29	0.17	40	SOL2 || [011]
E_011_spl2_XAS (brokenP)	8.28	**0.06**	3.48	0.15	310	SOL4 || [011]

Tab. 4.2. Mosaicity parameters computed from the box-beam maps shown in Fig. 4.14. The spread of the rocking angle $\Delta\mu$ is significantly larger for the E_brokenP sample, which had been exposed to uniaxial compression exceeding 300 MPa.

Table 4.2 summarizes the characteristic parameters extracted from the mosaicity analysis of the studied samples. The amplitude of the computed axial strain was comparable across all samples. Notably, adjacent regions of compressive and tensile strain were aligned with the dislocation boundaries identified in the mosaicity scans along the $\langle 101 \rangle$ directions. These observations indicate that the application of uniaxial stress leaves an irreversible imprint on the crystallographic configuration by generating longitudinal-type dislocations. Such dislocation structures were clearly discernible in the mosaicity and axial strain distributions of stressed samples, whereas no comparable features were observed in the untreated reference crystal.

It was demonstrated that the application of the uniaxial pressure along the [011] direction of the order of 100 MPa leaves a permanent footprint in a form of the defect field. Since this field is persistent after releasing the pressure, it must be resolved whether these defects induced influence the Verwey transition temperature, T_V. The impact of the strain-induced lattice defects in magnetite on T_V was further specifically investigated to address the role of the stress values exceeding 300 MPa and fracturing the samples.

The compression was exerted using a pressure chamber depicted in Fig. 4.15. After careful polishing, each sample was mounted with Stycast epoxy onto ceramic posts to ensure uniform pressure distribution across the crystal. The posts were affixed to a stainless steel frame, providing controlled and directional compressive loading. In this study, samples were compressed along both the $\langle 110 \rangle$ and $\langle 100 \rangle$ crystallographic directions. The applied stress could be increased beyond the fracture threshold of the crystal to probe the effects of severe mechanical deformation on T_V.

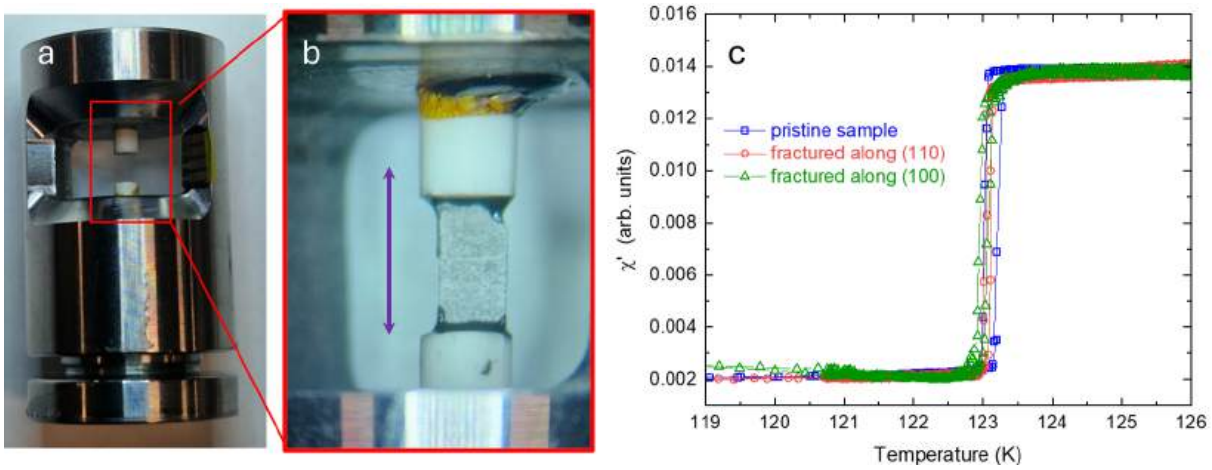

Fig. 4.15. (a) Photograph of the uniaxial compression device, consisting of a cylindrical steel housing and a central piston, used to apply controlled stress to magnetite single crystals. (b) Close-up view of the mounted sample (gray) secured between ceramic posts with Stycast epoxy. The purple arrows indicate the direction of the applied uniaxial compression. (c) Real part of the AC magnetic susceptibility, χ', as a function of temperature for the reference *pristine* sample (blue) and for samples *fractured* by uniaxial compression along the $\langle 110 \rangle$ (red) and $\langle 100 \rangle$ (green) crystallographic directions, respectively. The data demonstrate that the Verwey transition temperature, T_V, remains unchanged after uniaxial compression and fracture along either axis.

The Verwey transition was characterized before and after the application of uniaxial stress by measuring the AC magnetic susceptibility using a custom-built magnetometer described in Chapter 2, Section 2.3.2.

Notably, despite the compression of the samples exceeding the fracture threshold and, thus, leaving structural disorder, magnetic susceptibility measurements reveal that the Verwey transition temperature, T_V, remains effectively unchanged. This observation demonstrates that, whereas doping and stoichiometry variations strongly affect T_V, the extended defect fields, such as those generated by uniaxial compression, do not measurably shift or broaden the transition. This decoupling of lattice disorder from the electronic order parameter underscores the unique robustness of the Verwey state to non-point-like lattice perturbations.

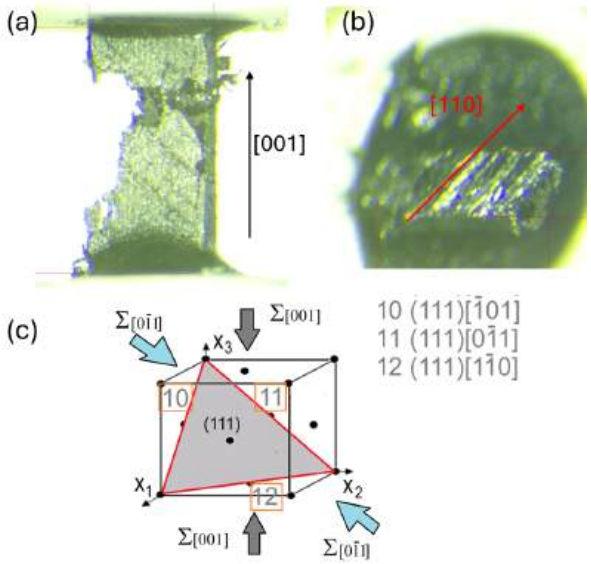

Fig. 4.16. Optical microscopy images and schematic illustration highlighting the fracture morphology and active slip systems in magnetite single crystals compressed along the [100] crystallographic direction. (a) Side view of the fractured sample, showing diagonal damage traces inclined relative to the [100] compression axis. (b) Top view, where the principal fracture lines are aligned approximately along the [110] direction. (c) Schematic representation of the $\{111\}$ slip planes and associated slip directions in the cubic spinel lattice. The consistent orientation of fracture features supports the conclusion that plastic deformation proceeds via slip along $\{111\}$ planes. This mechanism accounts for both the pronounced lattice distortions observed after uniaxial compression and the pronounced brittleness under [100] loading, which promotes simultaneous activation of multiple slip systems and accelerates sample fragmentation.

The optical microscopy images presented in Fig. 4.16 provide additional direct evidence of the preferred slip systems activated in magnetite under uniaxial compression. When the sample was compressed along the [100] crystallographic direction, the fracture surfaces and crack propagation were not random but instead displayed well-defined orientations. In the side view presented in Fig. 4.16a, the damage manifests as diagonal traces inclined relative to the compression axis. The top view from Fig. 4.16b reveals that these features align approximately along the [110] direction.

Such fracture patterns are consistent with slip occurring along the { 111 } planes, which are the most densely packed and energetically favorable slip systems in the cubic spinel lattice of magnetite. The schematic in Fig. 4.16c illustrates how different slip directions within the { 111 } family can be activated under applied stress. This observation reinforces the earlier presented interpretation of the DFXM results, which states that the pronounced line-like defects observed in the strain and misorientation maps originate from dislocation motion and shear along the { 111 } planes.

Furthermore, compression along the [100] direction promotes symmetric activation of multiple slip systems, which likely contributes to rapid accumulation of strain incompatibility and catastrophic brittle fracture. This behavior prevented the preparation of samples suitable for subsequent diffraction experiments. In contrast, compression along the [110] direction favors activation of a more limited subset of slip systems, enabling the crystal to accommodate higher deformation before mechanical failure occurs.

4.5. Conclusions

This Chapter presented the first systematic application of Dark-Field X-ray Microscopy to stoichiometric magnetite single crystals, establishing the technique as a powerful probe of both intrinsic and stress-induced defect fields. Beyond serving as a methodological introduction to DFXM, these experiments provided new insight into the relationship between extended lattice disorder and the Verwey transition.

Two key achievements can be highlighted. First, by comparing crystals grown via the TSFZ and skull-melter methods, there was demonstrated that the synthesis route leaves a distinct structural fingerprint: TSFZ-grown crystals displayed higher average axial strain but fewer extended mosaic defects, while skull-melter crystals exhibited lower strain but pronounced mosaic textures originating from rapid quenching. These findings correlate with measurable differences in T_V between the two growth methods, and are consistent with the idea that strain fields and stoichiometry jointly influence the electronic ordering [2, 4].

Second, by investigating crystals subjected to uniaxial compression along the $\langle 110 \rangle$ and $\langle 100 \rangle$ directions, was established that stresses exceeding 150 MPa generate stable, line-like defect fields aligned with the $\{111\}$ slip planes. In the case of $\langle 110 \rangle$ direction, these extended dislocations persisted even after stress release and were clearly resolved in box-beam DFXM projections, though they were less visible in the line-beam scans due to geometric sampling effects. Optical microscopy of fractured samples confirmed that plastic deformation proceeds via slip along the $\{111\}$ planes, in agreement with established models of dislocation-mediated plasticity in spinel oxides [10, 22].

Remarkably, despite the presence of extended dislocation networks and remanent lattice strain, AC magnetic susceptibility measurements revealed that the Verwey transition temperature T_V remained unchanged, even in samples fractured under compression exceeding 300 MPa. This result contrasts sharply with the well-documented sensitivity of T_V to point defects and stoichiometric deviations,

which strongly suppress or broaden the transition [17, 18]. Therefore, presented findings demonstrate a fundamental distinction that point-like disorder couples strongly to the charge and orbital ordering driving the Verwey transition, while the extended defects such as dislocations do not measurably affect its onset.

This distinction underscores the need to carefully differentiate between types of lattice imperfections when assessing the role of disorder in strongly correlated oxides. The robustness of T_V against remanent dislocation fields highlights a partial decoupling between electronic order and extended lattice strain, which may explain why stoichiometric magnetite maintains sharp first-order transitions even after mechanical deformation. Taken together, these results establish DFXM as a uniquely sensitive technique for visualizing strain and mosaicity in magnetite and provide a structural basis for interpreting the interplay of growth, stress, and electronic order in this prototypical correlated oxide.

Finally, the experiments reported here set the stage for the studies presented in Chapter 5, where the interplay between transport, susceptibility, and strain-induced effects is further investigated under controlled uniaxial compression.

Bibliography

[1] C. Detlefs, C. Yildirim, and J. Wade. "Inauguration and first users for ID03 beamline". URL: *https://www.esrf.fr/home/news/general/content-news/general/inauguration-and-first-users-for-id03-beamline.html* (visited on 08/21/2025).

[2] W. Wang et al. "Verwey transition as evolution from electronic nematicity to trimerons via electron-phonon coupling". *Sci. Adv.* **9** (2023). DOI: 10.1126/sciadv.adf8220.

[3] C. Yildirim et al. "Pink-Beam Dark Field X-ray Microscopy: Expanding 3D/4D Imaging for Complex and Deformed Microstructures". *arXiv preprint arXiv:2503.05921* (2025). DOI: 10.48550/arXiv.2503.05921.

[4] H. Simons et al. "Multiscale 3D characterization with dark-field x-ray microscopy". *Material Science Bulletin* **41** (2016), pp. 454–459. DOI: 10.1557/mrs.2016.114.

[5] H. Simons et al. "Dark-field X-ray microscopy for multiscale structural characterization". *Nat. Commun.* **6** (2015), pp. 6098. DOI: 10.1038/ncomms7098.

[6] H. F. Poulsen et al. "X-ray diffraction microscopy based on refractive optics". *Journal of Applied Crystallography* **50** (2017), pp. 1441–1456. DOI: 10.1107/S1600576717011037.

[7] J. G. Ferrer et al. "darfix – data analysis for dark-field X-ray microscopy". *Journal of Synchrotron Radiation* **30** (2023), pp. 527–537. DOI: 10.1107/S1600577523001674.

[8] K. Renger. "Die anfängliche Suszeptibilität von Eisen und Magnetit in Abhängigkeit von der Temperatur". PhD thesis. Eidgenössische Technische Hochschule Zürich, 1913. DOI: 10.3929/ethz-a-000091771.

[9] P. Piekarz, K. Parlinski, and A. M. Oleś. "Mechanism of the Verwey Transition in Magnetite". *Phys. Rev. Lett.* **97** (2006), pp. 156402. DOI: 10.1103/PhysRevLett.97.156402.

[10] R. S. Coe et al. "The thermodynamic effect of nonhydrostatic stress on the Verwey transition". *Earth and Planetary Science Letters* **319-320** (2012), pp. 207–217. DOI: 10.1016/j.epsl.2011.11.021.

[11] T. Kołodziej et al. "Impact of hydrostatic pressure, nonstoichiometry, and doping on trimeron lattice excitations in magnetite during axis switching". *Phys. Rev. B* **108** (2023), pp. 245148. DOI: 10.1103/PhysRevB.108.245148.

[12] M. P. Pasternak et al. "Pressure-induced coordination crossover in magnetite; the breakdown of the Verwey–Mott localization hypothesis". *J. Magn. Magn. Mater.* **265** (2003), pp. L107–L112. DOI: 10.1016/S0304-8853(03)00549-3.

[13] A. Kuriki et al. "High-Pressure Structural Analysis of Fe_3O_4". *J. Phys. Soc. Jpn.* **71** (2002), pp. 3092–3093. DOI: 10.1143/JPSJ.71.3092.

[14] J. Spałek et al. "Verwey transition in Fe_3O_4 at high pressure: Quantum critical point at the onset of metallization". *Phys. Rev. B* **78** (2008), pp. 100401. DOI: 10.1103/PhysRevB.78.100401.

[15] Y. Nagasawa, R. Hara, T. Seino, et al. "Uniaxial Strain Effect on T_V and Electrical Resistivity in Magnetite (Fe3O4)". *Japanese Journal of Applied Physics* (2006). DOI: 10.1063/1.2355167.

[16] Y. Nagasawa et al. "Effect of uniaxial strain on Verwey transition in magnetite". *J. Phys. Soc. Jpn.* **76** (2007), pp. 110. DOI: 10.1143/JPSJS.76SA.110.

[17] W. Tabis et al. "Effect of surface polishing and oxidization induced strain on electronic order at the Verwey transition in Fe3O4". *J. Phys.: Condens. Matter* **25** (2013), pp. 055603. DOI: 10.1088/0953-8984/25/5/055603.

[18] R. Prozorov et al. "Response of the Verwey transition in magnetite to controlled point-like disorder induced by 2.5 MeV electron irradiation". *Materials Research Bulletin* **167** (2023), pp. 112442. DOI: 10.1016/j.materresbull.2023.112442.

[19] Z. Kąkol et al. "The effect of doping on global lattice properties of magnetite $Fe_{3-x}Me_xO_4$ $(Me = Zn, Ti, Al)$". *J. Solid State Chem.* **192** (2012), pp. 120–126. DOI: 10.1016/j.jssc.2012.04.001.

[20] Z. Kąkol et al. "Charge rearrangement in magnetite: from magnetic field induced easy axis switching to femtoseconds electronic processes". *Philos. Mag.* **95** (2015), pp. 633–648. DOI: 10.1080/14786435.2015.1010625.

[21] C. Yildirim et al. "Extensive 3D mapping of dislocation structures in bulk aluminum". *Scientific Reports* **13** (2023). DOI: 10.1038/s41598-023-30767-w.

[22] M. Kutsal et al. "The ESRF dark-field x-ray microscope at ID06". *IOP Conf. Ser.: Mater. Sci. Eng.* **580** (2019), pp. 012007. DOI: 10.1088/1757-899X/580/1/012007.

[23] T. N. T. Caliste et al. "Rocking Curve Imaging Investigation of the Long-Range Distortion Field between Parallel Dislocations with Opposite Burgers Vectors". *Appl. Sci.* **11** (2021), pp. 9054. DOI: 10.3390/app11199054.

Chapter 5.

Electronic and magnetic responses of magnetite to uniaxial compression

As shown in Chapters 3 and 4, uniaxial compression permanently alters the crystal lattice of magnetite, with stresses as low as 100 MPa producing stable dislocation fields. Importantly, these structural changes do not modify the Verwey transition temperature T_V. Building on these findings, this Chapter examines how uniaxial compression affects charge correlations, magnetic response, and the local coordination of Fe ions near the Verwey transition in stoichiometric magnetite. The Chapter is divided into three sections, each addressing a different experimental probe.

Section 5.1 presents the effect of uniaxial compression on electrical transport near T_V. The resistivity was measured as a function of stress applied along the [100] and [011] axes. The mechanical endurance of the crystals differed depending on the compression direction, reflecting the anisotropy of active slip systems. Section 5.2 describes complementary AC magnetic susceptibility measurements performed after the transport experiments, using a custom-built setup developed in this work. Both resistivity and susceptibility measurements revealed a consistent trend: T_V increased gradually under compression but returned to its initial value after stress release, demonstrating reversibility. The enhancement was more pronounced for stress along [011] than [100], confirming the anisotropic coupling between uniaxial strain and the Verwey transition. Finally, Section 5.3 investigates the effect of uniaxial stress on the local environment of Fe ions magnetite using X-ray absorption spectroscopy (XAS) at the Fe K-edge. Analysis of the absorption and pre-edge regions shows that compression along [100] and [011] induces distortion of the cubic lattice, without breaking the local inversion symmetry of the FeO_6 octahedra. As a result, the pre-edge features remain unchanged, indicating that uniaxial strain modifies the global crystal symmetry, while leaving the local Fe–O bonding geometry essentially intact.

A total of approximately fifteen individual samples were tested in the experiments described in this Chapter, carried out as part of the ongoing development of the measurement procedures. These preliminary trials were essential for optimizing the methodology and ensuring the collection of high-quality data. For clarity and focus, only the most representative results are presented here. Specifically, this Chapter highlights selected examples of electrical resistivity (ρ), AC magnetic susceptibility (χ), and X-ray absorption spectroscopy (XAS) obtained for crystals compressed along both the [100] and [011] directions. The preparation of samples for uniaxial pressure measurements is also outlined shortly. Extended datasets from the remaining tested samples, along with detailed descriptions of the corresponding experimental protocols, are provided in Appendix F.

All samples investigated in this Chapter were labeled according to a consistent naming scheme to ensure unambiguous identification. The prefix "E" denotes that the crystal was grown using the floating-zone method, as described in Chapter 2, Section 2.2.1. The subsequent three-digit code, "_100_" or "_011_", specifies the crystallographic direction along which uniaxial pressure was applied, namely [100] or [011], respectively. The label then ends with the abbreviation "spl" followed by a number $(1, 2, 3, \dots)$, which designates the sample number. For specimens investigated by X-ray absorption spectroscopy, the suffix "XAS" was additionally included in the label. The complete information regarding sample names, dimensions, orientations, and the specific SOL cells used in the electrical resistivity and AC magnetic susceptibility measurements is summarized in Tables 5.1 and 5.2, respectively. Corresponding details for the XAS experiments performed under uniaxial compression are provided in Table 5.3.

Unless otherwise specified, the Verwey transition temperature T_V in the resistivity and susceptibility experiments was determined from the inflection point of the respective curves measured as a function of temperature. In the figures showing the dependence of T_V on applied stress σ, data points marked with warm colors (primarily red and its shades) correspond to measurements performed during heating, while cool colors (various shades of blue) denote measurements performed during cooling. This distinction is necessary because the Verwey transition exhibits a small thermal hysteresis due to the non-ideal thermalization of the uniaxial pressure cell.

5.1. Electrical resistivity under uniaxial compression along the [100] and [011] directions

The preparation of samples for uniaxial pressure measurements, the results of which are presented in this Chapter, was a multi-stage process. Although three different experimental techniques were employed, the initial routine was common to all: each single crystal had to be oriented and cut to match the geometry of the respective pressure cell. For resistivity measurements, electrical contacts were attached to the oriented crystal, which was then mounted onto the clamps of the selected SOL cell using the electrically insulating epoxy resin Stycast_2850FT. Table 5.1 summarizes the

samples studied with electrical resistivity under uniaxial compression. Notably, among the crystals oriented along [100], only sample E_100_spl4 remained intact after removal from the SOL cell clamps, whereas all samples measured along [011] were recovered as complete, undamaged crystals.

Name	Direction	l_{eff} [mm]	S [mm^2]	σ [MPa/1°]	Device
E_100_spl1	[100]	1.200	0.309	1.236	SOL2
E_100_spl3	[100]	1.500	0.353	1.082	SOL2
E_100_spl4	[100]	0.830	0.572	0.668	SOL2
E_011_spl1	[011]	1.100	0.557	0.503	SOL3
E_011_spl2	[011]	0.870	0.343	1.112	SOL2
E_011_spl3	[011]	0.740	0.530	0.721	SOL2
E_011_ii_spl4	[011]	0.420	0.655	0.583	SOL2

Tab. 5.1. Summary of samples measured as a function of uniaxial stress using electrical resistivity. The parameter l_{eff} denotes the effective length of the sample in mm, defined as the distance between the voltage contacts and used for resistivity conversion, while S is the cross-sectional area in mm^2. The coefficient σ represents the calibration factor converting screw rotation of the pressure cell into the corresponding uniaxial stress applied to the crystal in the specified orientation.

Low-temperature electrical resistivity measurements were carried out using a custom-built liquid nitrogen (N_2) system. It consisted of a 50 L Dewar filled with N_2, into which an evacuated stainless-steel cryostat was immersed. The cryostat housed the probe with the mounted SOL cell, wiring, and two calibrated Cernox temperature sensors. The probe was connected to an external electronics rack containing a LakeShore 336 temperature controller (LS 336), a Stanford Research SR860 lock-in amplifier, and a PC workstation running custom Python control scripts. The same system was used for both resistivity and AC magnetic susceptibility measurements. In the case of resistivity, electrical contacts were attached to the sample, while for susceptibility measurements, these contacts were replaced with a set of detection and excitation coils. A photograph of this setup, along with a description of its specific components, is presented in Fig. 5.1.

The SR860 lock-in amplifier served simultaneously as a 1 V AC voltage source and a phase-sensitive nanovoltmeter. The operating frequency was set to $f = 66.0$ Hz for resistivity measurements and $f = 2018.2\ Hz$ for AC susceptibility, deliberately offset from the multiples of the line frequency to suppress harmonic cross-talk. For resistivity, the sample was additionally connected through a 1 kΩ shunt resistor, providing a nominal current of 1 mA in the four-probe configuration. The current leads (or excitation coils in the case of susceptibility) were connected directly to the SR860 output, while the voltage leads (receiving coils) were connected to the SR860 input.

Temperature was regulated by the LS 336 controller equipped with a 50 Ω resistive heater. A Cernox X34550 sensor mounted on the probe and connected to channel B controlled and stabilized

the temperature, while a second sensor (Cernox X161209) placed in close proximity to the sample and connected to channel A provided the experimental readout of the sample temperature.

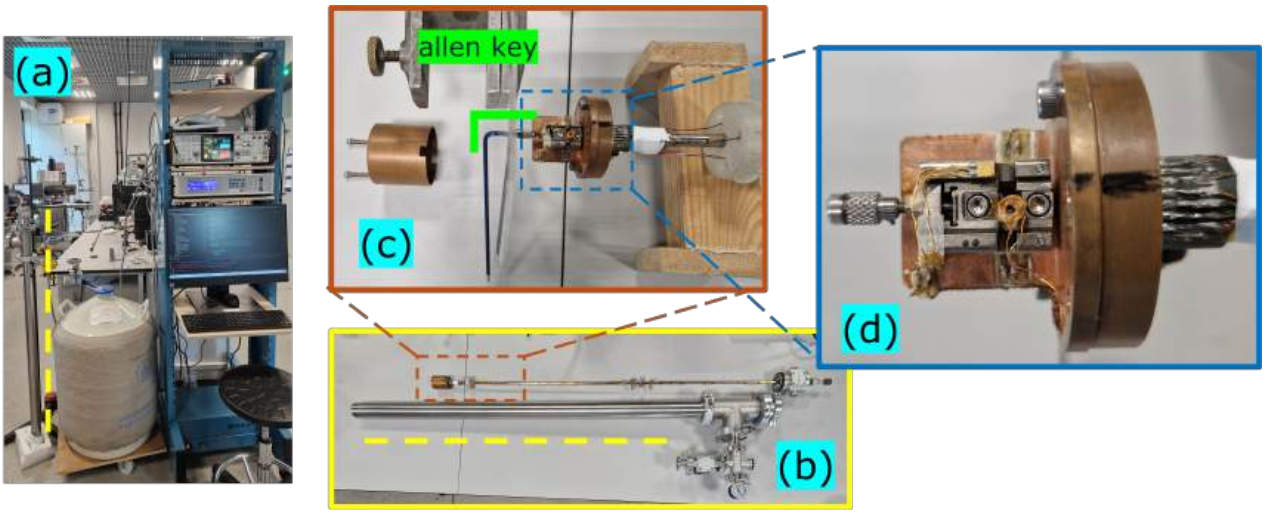

Fig. 5.1. Experimental setup for investigating the properties of magnetite under uniaxial stress, configured for both electrical resistivity and AC magnetic susceptibility measurements. **(a)** Front view of the complete experimental station, including the Dewar vessel and the electronic rack with the control PC and lock-in amplifier. The yellow dashed line indicates the stainless-steel cryostat positioned vertically alongside the Dewar. **(b)** The cryostat assembly with an attached pressure gauge and safety valve, which houses and protects the measuring probe during low-temperature measurements. **(c)** Close-up of the uniaxial pressure cell mounted on the probe, with the copper shielding cylinder visible on the left. The applied pressure was adjusted manually using an Allen key, as marked. **(d)** Magnified view of the SOL2 uniaxial cell showing the susceptometer coils precisely mounted around the magnetite sample.

The general procedure for a single measurement step under uniaxial compression can be illustrated using electrical resistivity as an example. Each step of the experiment began with verifying the electrical contacts with an ohmmeter and inspecting the crystal for mechanical integrity. If no short circuits were detected and the sample showed no visible cracks, data acquisition was initiated. Uniaxial stress was applied by carefully turning the loading screw while continuously monitoring the sample signal. A sudden loss of voltage or a deviation by several orders of magnitude relative to the previous step was considered the first indication of a possible fracture. In such cases, the measurement was immediately stopped, and the sample was examined under an optical microscope. Fracture of the crystals occasionally occurred inside the pressure cell during compression, or alternatively upon removal from the clamps. Such events were relatively frequent, particularly for samples compressed along the [100] direction.

When compression was successfully applied, as indicated by a gradual, reproducible change in resistivity, the probe was sealed with a copper shield and inserted into the cryostat tube. The cryostat was evacuated using a rotary pump for approximately 10 minutes before immersing in a liquid-nitrogen Dewar. Under these conditions, the setup cooled gradually over $\sim$6 hours to 120 K. Once

the target temperature was reached, a Python macro was executed to acquire 2100 data points during continuous heating–cooling cycles between 121 K and 128 K. Data points were recorded only when the LS 336 temperature controller stabilized within ± 0.05 K of the programmed setpoint.

The following two Subsections present the resistivity results for the [100] and [011] crystallographic orientations. The same measurement protocol was applied in the AC susceptibility experiments; however, in this case, potential sample damage could not be directly detected, as electrical continuity, which serves as an immediate diagnostic in resistivity measurements, was not available.

5.1.1. Electronic transport under compression along the [100] direction

The cubic-to-tetragonal distortion induced by uniaxial compression along the [100] direction motivated an investigation of its influence on the electrical resistivity and, in particular, on the Verwey transition. To this end, a series of resistivity measurements was performed, with representative results discussed below. The temperature dependence of resistivity across the transition, recorded for sample E_100_spl4 under uniaxial stresses ranging from 0 to nearly 200 MPa, is presented in Fig. 5.2a.

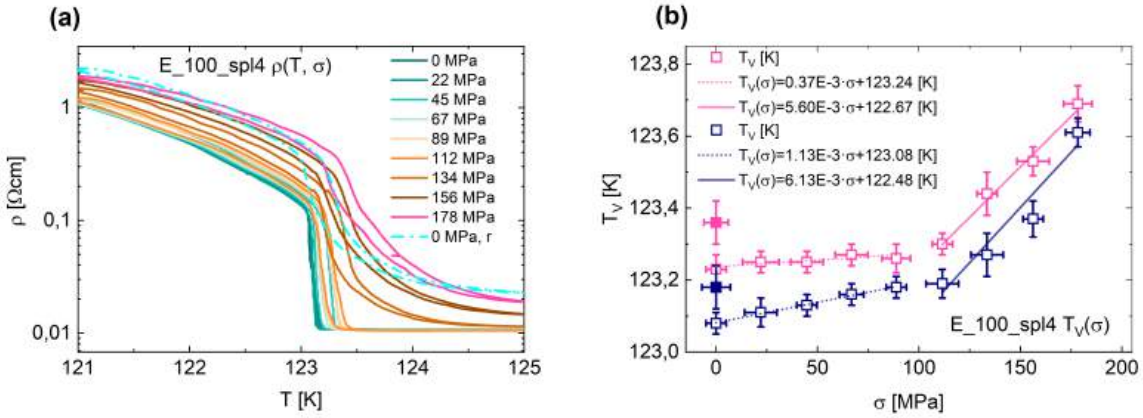

Fig. 5.2. Low-temperature resistivity of sample E_100_spl4 under uniaxial compression applied along the [100] direction. **(a)** Temperature dependence of the resistivity, $\rho_{\mathrm{AC}}(T, \sigma)$, measured for the stress values indicated in the legend (0–178 MPa). The dashed cyan-colored line labeled "0 MPa, r" corresponds to the measurement performed after full decompression, indicating minor changes in the sample during the highest applied stress, but confirming the reversibility of the pressure-induced shift in T_V. The slightly higher absolute resistivity observed after decompression is consistent with the minor sample fracturing. **(b)** Verwey transition temperature T_V as a function of applied stress σ, extracted independently from heating and cooling cycles. Two distinct linear regimes are evident, represented by the dashed and solid linear fits, respectively. The filled symbols denote T_V values obtained after decompression ("0 MPa, r" from panel a).

For the unstressed crystal, the transition temperature was $T_{V,0} = 123.1$ K. Upon increasing compression, T_V shifted gradually upward, reaching a maximum of 123.7 K at 178 MPa. This corresponds to a total increase of only 0.6 K, indicating that the effect of uniaxial stress along [100] on T_V was weak. In addition, the mechanical stability of the samples was limited: fractures typically occurred at stresses near 200 MPa, preventing reliable measurements at higher compression levels.

As summarized in Fig. 5.2b, the dependence of T_V on the applied stress σ exhibited two distinct regimes. In the initial range from 0 to 100 MPa, T_V increased only slightly, whereas at higher stresses (100–178 MPa) the shift became more pronounced. To describe this behavior quantitatively, $T_V(\sigma)$ was fitted with two independent linear functions corresponding to the respective stress intervals. The initial slow increase of T_V is consistent with the susceptibility results obtained under compression along the [100] direction, presented in Section 5.2. The crossover between the two regimes suggests that, once the applied stress exceeded approximately 100 MPa, the sample began to develop microcracks. This interpretation is supported by the broadening of the transition observed in the temperature-dependent resistivity (Fig. 5.2a). Such microstructural damage likely led to a slight overestimation of the apparent variation in T_V at the highest pressures.

Furthermore, Fig. 5.2 shows that the values of T_V determined for a given uniaxial stress exhibit a distinct thermal hysteresis between cooling and heating cycles. This offset, of approximately 0.1 K, arises from imperfect thermal equilibration of the sample near the transition.

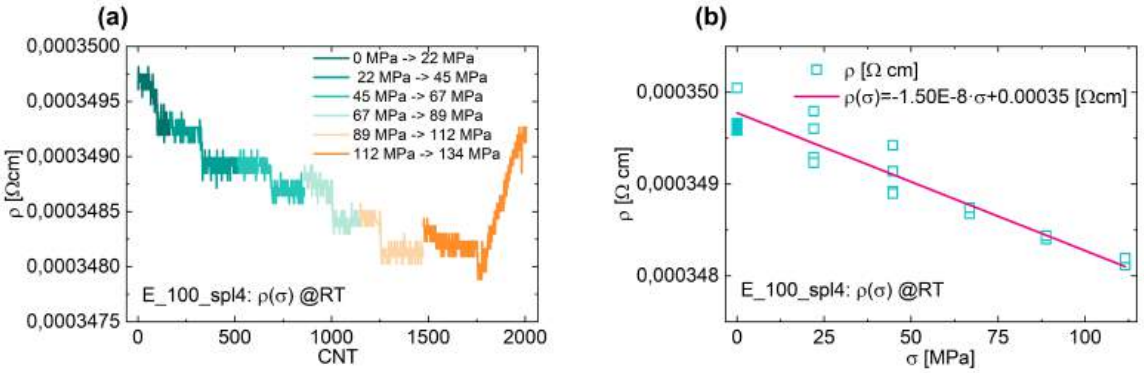

Fig. 5.3. Room-temperature resistivity of sample E_100_spl4 under uniaxial compression applied along the [100] direction. **(a)** Time-dependent resistivity (count number, CNT) recorded during sequential increases of applied stress, with each color segment corresponding to a distinct stress interval indicated in the legend. **(b)** Linear dependence of the resistivity plateau values extracted from panel (a) on the applied stress σ. The filled symbol denotes the resistivity measured after full decompression, confirming the reversibility of the pressure effect within experimental uncertainty.

At each measurement step, the compression applied to the sample was adjusted only after the probe had been warmed to room temperature. Changes in uniaxial stress were monitored through simultaneous resistivity measurements. The variation of the room-temperature resistivity ρ of sample E_100_spl4 under uniaxial compression is shown in Fig. 5.3a. The data display a characteristic step-like evolution, with distinct plateaus corresponding to successive increments of applied stress.

The mean resistivity from each plateau was extracted and plotted as a function of uniaxial stress in Fig. 5.3b. The resulting linear dependence demonstrates that compression along the [100] direction causes a weak but reproducible decrease in ρ. This behavior indicates that the applied stress induces a largely reversible lattice distortion that slightly modifies carrier scattering and, consequently, the electrical resistivity.

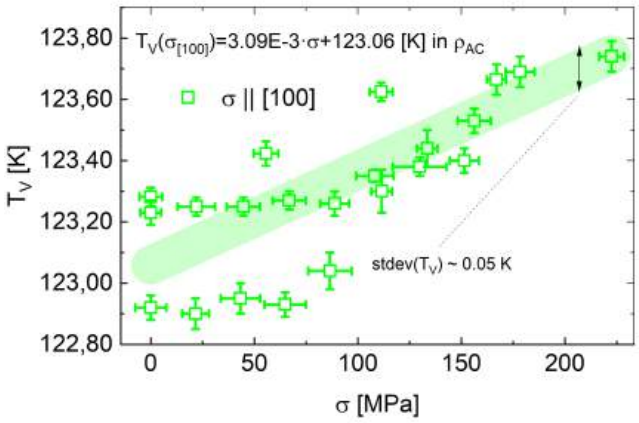

Fig. 5.4. Verwey transition temperature T_V, determined from electrical resistivity measurements during heating, plotted as a function of uniaxial stress applied along the [100] direction. Data from all samples in this orientation, listed in Table 5.1, are included. The results show a clear but weak positive correlation, with a fitted slope of approximately 3 mK/MPa. The shaded region denotes the confidence interval of the linear fit.

To summarize, Figure 5.4 shows the combined dependence of the Verwey transition temperature T_V, determined from electrical resistivity measurements, on uniaxial stress applied along the [100] direction for samples E_100_spl1, E_100_spl3, and E_100_spl4. Despite minor sample-to-sample variations, the data consistently exhibit an upward shift of T_V with increasing compression. A common linear fit to all data points reveals a clear positive correlation between the Verwey transition temperature and uniaxial stress along [100], with an average slope of approximately 3 mK/MPa.

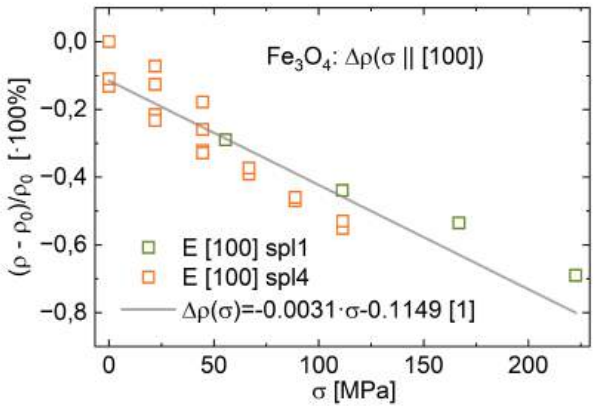

Fig. 5.5. Relative change in room-temperature electrical resistivity as a function of uniaxial stress applied along the [100] direction for samples E_100_spl1 and E_100_spl4. The normalized resistivity, $\Delta\rho = \left(\frac{\rho}{\rho_0} - 1\right) \times 100\%$, decreases linearly with increasing compression, indicating a weak but systematic reduction of resistivity under stress.

Similarly, the summary in Fig. 5.5 presents the relative change in room-temperature electrical resistivity under uniaxial compression along the [100] direction for samples E_100_spl1 and E_100_spl4. In both cases, the resistivity decreases systematically with increasing stress, reaching a reduction of nearly one percent at compressions slightly above 200 MPa. This linear and reproducible behavior indicates that [100]-oriented uniaxial stress induces a modest but consistent decrease in room-temperature resistivity.

5.1.2. Electronic transport under compression along the [011] direction

In contrast to the [100] orientation, uniaxial compression along the [011] direction produces a more complex lattice distortion that couples strongly to the charge and orbital ordering associated with the Verwey transition. As discussed in Chapter 3, X-ray diffraction measurements revealed that while [100] compression primarily induces a simple tetragonal distortion, stress applied along [011] introduces an additional shear component that lowers the cubic symmetry toward an orthorhombic or even monoclinic configuration. This anisotropic deformation is expected to enhance the sensitivity of both the electronic transport properties and the transition temperature to external stress. To investigate these effects, a series of resistivity measurements was performed, and representative results are presented below.

This Subsection illustrates the response of the Verwey transition to uniaxial compression along [011], exemplified by resistivity measurements on sample E_011_spl3. Figure 5.6a shows the evolution of the resistivity across the transition as the applied stress was gradually increased from 0 to 179 MPa. With each compression step, the resistivity curve shifted systematically, demonstrating a clear stress

dependence of the transition. The reproducibility and regularity of this shift confirm that the uniaxial load was transmitted effectively through the SOL2 cell, ensuring precise control of the applied stress.

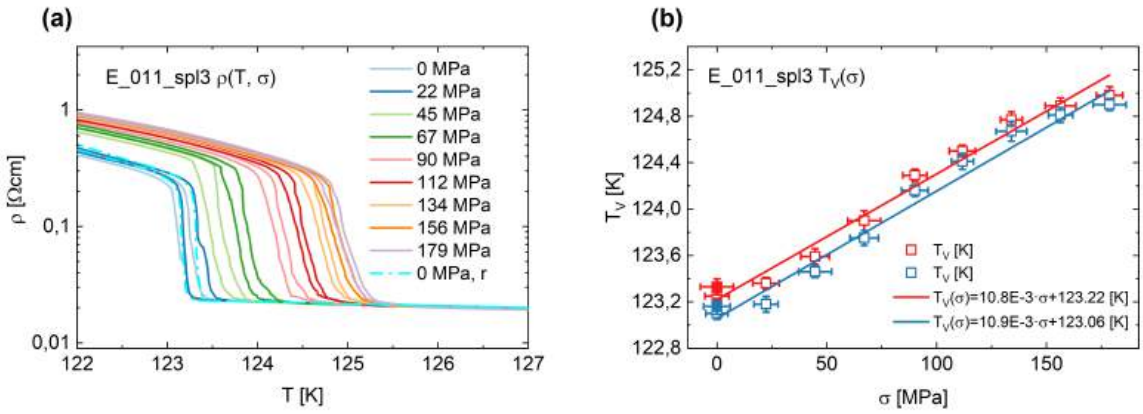

Fig. 5.6. Low-temperature resistivity of sample E_011_spl3 under uniaxial compression applied along the [011] direction. **(a)** Temperature dependence of the resistivity, $\rho_{\mathrm{AC}}(T, \sigma)$, measured for stresses from 0 to 179 MPa. The dashed cyan line labeled "0 MPa, r" corresponds to the resistivity measured after full decompression, confirming the reversibility of the stress effect. **(b)** Transition temperature T_V as a function of applied stress σ. A nearly linear increase of T_V with compression is observed, with filled symbols indicating the decompressed state ("0 MPa, r" from panel a).

For sample E_011_spl3, the initial transition temperature was $T_{V,0} = 123.2$ K and increased systematically with applied stress, reaching a maximum of 124.9 K at 179 MPa. This corresponds to an overall enhancement of nearly 2 K relative to the unstressed state, significantly larger than the shift observed for samples compressed along [100]. The linear fit between T_V and uniaxial stress, shown in Fig. 5.6b, describes the data with a correlation coefficient exceeding 98%, confirming that the stress dependence of T_V along [011] is strongly linear within the studied range. This robust relationship demonstrates the high sensitivity of the Verwey transition to anisotropic strain in this orientation, consistent with the stronger lattice distortion and shear components expected under [011] compression.

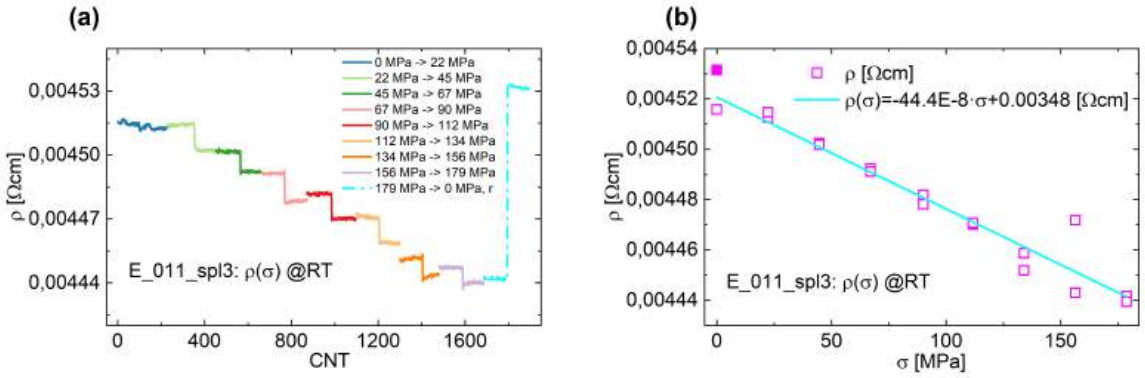

Fig. 5.7. Room-temperature resistivity under uniaxial compression applied along the [011] direction in sample E_011_spl3. **(a)** Evolution of the resistivity, ρ, recorded in real time during successive increments of applied stress, showing step-like plateaus corresponding to stable compression levels.**(b)** Dependence of the plateau resistivity values on applied stress σ, fitted with a linear function. The filled symbol denotes the resistivity measured after full decompression, confirming reversibility of the pressure effect.

Electrical resistivity at room temperature was monitored during the application of uniaxial stress along the [011] direction, following the same procedure described previously for the [100] orientation. As shown in Fig. 5.7a, the resistivity exhibited step-like plateaus that stabilized after each incremental turn of the screw, confirming that the compression was applied reproducibly and that the electrical contacts remained intact throughout the measurement. These plateau values were extracted and plotted as a function of applied stress in Fig. 5.7b. A clear linear trend is observed, with resistivity decreasing systematically over the entire stress range of 0–179 MPa.

The slope of this decrease is approximately one order of magnitude larger than that measured in the [100] orientation, which emphasizes the anisotropic nature of the electronic response of magnetite to uniaxial strain. This stronger suppression of resistivity under [011] compression is consistent with the orthorhombic lattice distortion and shear component revealed in the X-ray diffraction studies of Chapter 3, which apparently couple more strongly to charge and orbital ordering. Taken together, these observations confirm that uniaxial stress along [011] has a more pronounced effect on room-temperature transport than along [100], in line with its stronger influence on T_V.

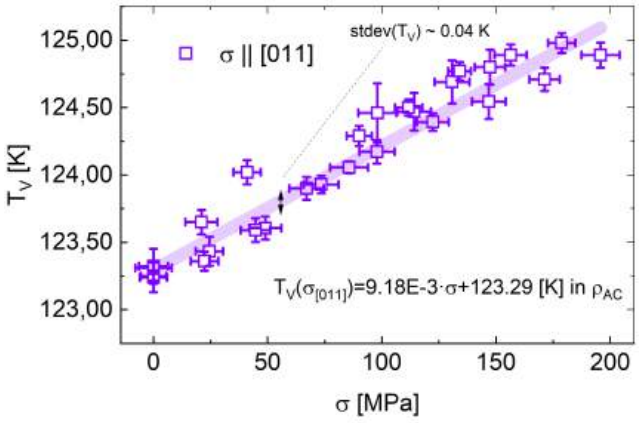

Fig. 5.8. Dependence of the Verwey transition temperature T_V, determined during heating from electrical resistivity measurements, on uniaxial stress applied along the [011] direction. Data from all samples measured in this orientation are included. The transition temperature T_V increases systematically with applied compression, with a fitted slope of ≈ 9.2 mK/MPa. This rate is about three times larger than that observed for compression along the [100] direction (cf. Fig. 5.4), highlighting the anisotropic character of the stress response in magnetite. The shaded band represents the confidence interval of the linear fit.

While Fig. 5.4 summarized the evolution of the Verwey transition temperature T_V, determined from resistivity measurements under uniaxial stress along the [100] direction, Fig. 5.8 presents the corresponding dependence of T_V on stress σ applied along [011]. The results include data from samples E_011_spl1, E_011_spl2, and E_011_spl3, as listed in Table 5.1. The fitted trend line reveals a clear positive correlation between T_V and uniaxial stress along [011]. A comparison of the slopes obtained from Figs. 5.4 and 5.8 shows that the rate of increase in T_V under [011] compression is approximately three times larger than under [100] compression, emphasizing the pronounced anisotropy in the stress response of magnetite.

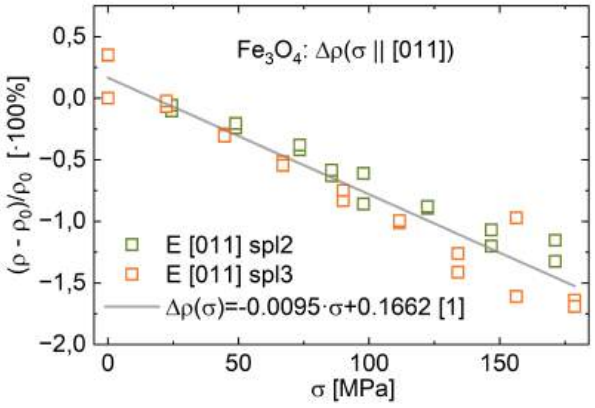

Fig. 5.9. Dependence of the relative resistivity change at room temperature on uniaxial stress applied along the [011] direction for samples E_011_spl2 and E_011_spl3. The relative change in resistivity was calculated as $\Delta\rho = \left(\frac{\rho}{\rho_0} - 1\right) \cdot 100\%$. A systematic decrease is observed with increasing compression, following a linear trend with a slope of $\approx -9.5 \times 10^{-5}$/MPa. Compared to the [100] orientation (cf. Fig. 5.5), the magnitude of the resistivity reduction under [011] compression is about three times larger, underscoring the anisotropic character of electronic transport in magnetite under uniaxial stress.

The dependence of the relative change in electrical resistivity at room temperature under uniaxial stress applied along the [011] direction is presented in Fig. 5.9 for samples E_011_spl2 and E_011_spl3. In both cases, resistivity decreased systematically with increasing compression, reaching a maximum reduction of nearly 2% at ∼180 MPa. The extracted linear slope indicates a stronger stress sensitivity than observed in the [100] orientation (cf. Fig. 5.5), consistent with the enhanced coupling of [011] stress to shear distortions of the cubic lattice. These distortions lower the symmetry towards monoclinic, thereby modifying the electronic bandwidth and carrier scattering more effectively than simple tetragonal distortions along [100].

5.1.3. Comparative response of magnetite to uniaxial compression along the [100] and [011] directions

The resistivity measurements under uniaxial compression along the [100] and [011] orientations were designed to probe the impact of two lattice deformations related to stress applied in different crystallographic directions on the transport properties of magnetite near the Verwey transition. The results presented in the previous Subsections demonstrate that the response of magnetite to uniaxial compression depends strongly on the crystallographic orientation of the applied stress. While compression along [100] primarily induces a tetragonal distortion, stress applied along [011] generates an additional shear component that lowers the cubic symmetry more drastically. This structural anisotropy is directly reflected in the electronic transport properties and, in particular, the evolution

of the Verwey transition temperature T_V. To highlight these differences, this Subsection compares the combined results of resistivity measurements under [100] and [011] compression, emphasizing the stronger sensitivity of both T_V and room-temperature resistivity to stress applied along the [011] direction.

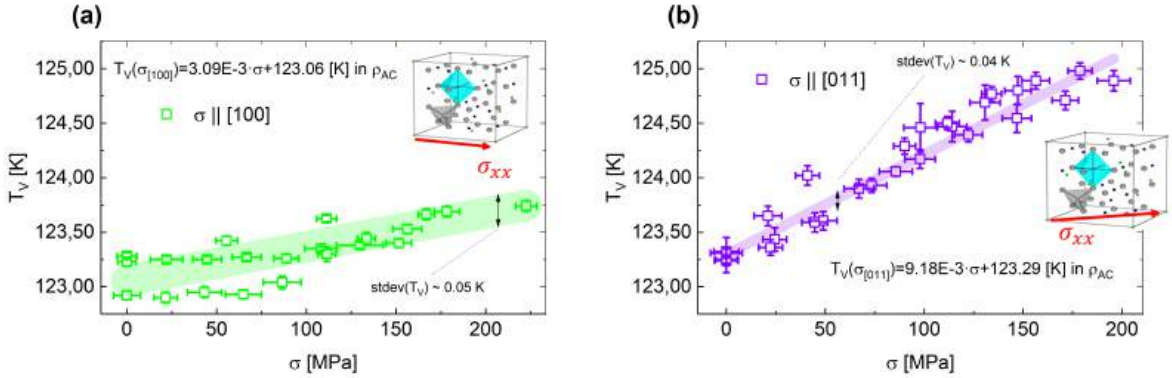

Fig. 5.10. Comparison of the effect of uniaxial compression applied along different crystallographic directions on the Verwey transition temperature T_V, determined from electrical resistivity measurements. **(a)** Dependence of T_V on stress σ applied along the [100] direction (data from Fig. 5.4). **(b)** Dependence of T_V on stress σ applied along the [011] direction (data from Fig. 5.8). In both panels, the shaded region represents the confidence band of the linear fit. The insets show symbolic representations of the magnetite unit cell, with the red arrow indicating the orientation of the applied uniaxial stress, σ_{xx}.

The comparison, summarized in Fig. 5.10, clearly demonstrates that the response is highly anisotropic. In both cases, the application of stress shifts the transition temperature T_V upward, confirming that uniaxial compression stabilizes the low-temperature phase. However, the magnitude of this effect differs strongly with orientation: compression along [011] increases T_V at a rate of nearly 9 mK/MPa, approximately three times larger than the ∼3 mK/MPa slope observed for [100]. This pronounced anisotropy highlights the different lattice distortions induced by stress along these directions and their unequal coupling to the charge and orbital ordering associated with the Verwey transition.

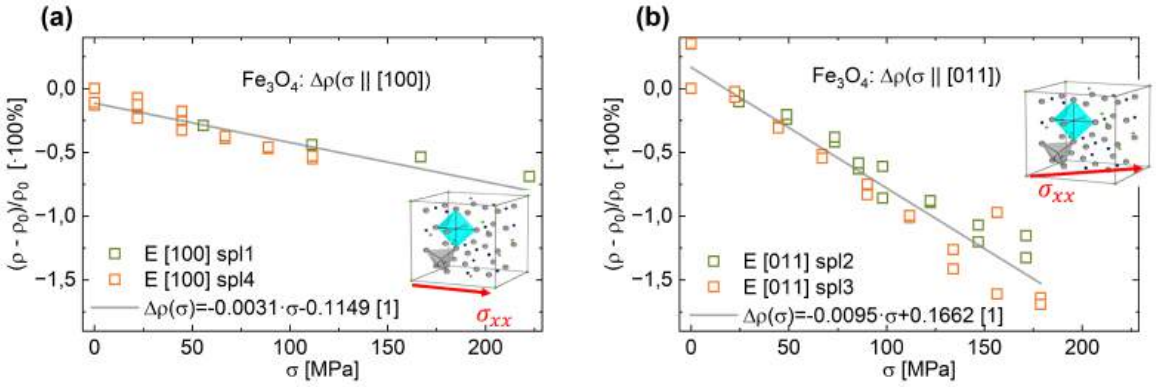

Fig. 5.11. Comparison of the effect of uniaxial compression applied along different crystallographic directions on the relative change in electrical resistivity, $\Delta\rho = \left(\frac{\rho}{\rho_0} - 1\right) \cdot 100\%$, measured at room temperature. **(a)** Dependence of $\Delta\rho$ on stress σ applied along the [100] direction (data from Fig. 5.5). **(b)** Dependence of $\Delta\rho$ on stress σ applied along the [011] direction (data from Fig. 5.9). In both panels, the linear fits illustrate the systematic decrease in resistivity with increasing compression. The insets show symbolic representations of the magnetite unit cell, with the red arrow indicating the orientation of the applied uniaxial stress, σ_{xx}.

The dependence of the relative change in resistivity at room temperature on uniaxial stress for both [100] and [011] orientations is compared in Fig. 5.11. In both cases, compression leads to a systematic decrease of resistivity, reflecting the enhanced carrier mobility induced by strain. However, the magnitude of this effect is strongly orientation dependent. For example, at $\sigma \approx 180$ MPa, the reduction in resistivity reaches only about 0.6% for the [100] orientation, whereas for [011] compression the decrease exceeds 1.5%. This anisotropy is further quantified by the slopes of the linear fits: the stress coefficient extracted for [011] is more than three times larger than that obtained for [100]. These results demonstrate that uniaxial compression along [011] couples much more efficiently to the electronic structure of magnetite, producing a significantly stronger suppression of resistivity. Taken together with the corresponding enhancement of T_V, this comparison provides clear evidence of the pronounced anisotropy in the electronic transport response of magnetite to uniaxial stress.

5.2. Magnetic susceptibility as a probe of the Verwey transition under uniaxial compression

The resistivity measurements under uniaxial compression established a clear link between lattice strain and charge transport in magnetite; however, the experiment itself had certain inherent limitations. Because resistivity measurements rely on electrical contacts, the results can be influenced by the quality of the sample, the contact interface, contact resistance, or partial sample damage during compression. To overcome these limitations, AC magnetic susceptibility was employed as a contactless probe sensitive to changes in magnetic domains and to the structural rearrangements

accompanying the Verwey transition. Susceptibility provides a bulk-sensitive response that is largely unaffected by extrinsic effects at sample surfaces or interfaces. Moreover, susceptibility measurements are particularly effective in detecting subtle variations in the sharpness or width of the transition, offering an independent way to explore the stress dependence of T_V.

Typically, susceptibility was recorded either before or after resistivity on the same crystal, as the sample was already mounted between the compression clamps of the SOL cell. For this purpose, small pickup and drive coils were glued directly onto the top of the sample, and the measurement circuit was reassembled. The shunt resistor used for the four-probe resistivity configuration was removed, and the electrical contacts were replaced with connections to the susceptibility coils. This procedure enabled efficient switching between resistivity and susceptibility modes while maintaining consistent stress conditions on the same sample.

Name	Direction	Mode	S [mm^2]	σ [MPa/1°]	Device
E_001x3_spl1	[100]	pristine	0.607	0.445	SOL2
E_011_spl1	[011]	after ρ	0.557	0.503	SOL3
E_011_spl2	[011]	before ρ	0.343	1.112	SOL2
E_011_spl2	[011]	after ρ	0.343	1.112	SOL2
E_011_spl3	[011]	before ρ	0.530	0.528	SOL3
E_011_spl3	[011]	after ρ (V2, V3)	0.530	0.721	SOL2

Tab. 5.2. Summary of samples studied as a function of uniaxial stress using AC magnetic susceptibility. The column labeled "Mode" specifies the stage of the experimental history at which the measurement was performed (e.g., before or after resistivity, ρ, measurements). The parameter S denotes the sample cross-sectional area in mm^2, while σ represents the conversion factor between screw rotation in the SOL cell and the corresponding uniaxial stress applied in the given crystallographic orientation.

Table 5.2 summarizes the samples and SOL cells used for AC susceptibility measurements under uniaxial compression. In the [100] orientation, only a single sample was studied; however, it fractured upon removal from the pressure cell after the experiment, preventing further reuse. By contrast, all samples tested in the [011] orientation were successfully recovered intact, enabling additional measurements in complementary modes. The following two Subsections present a short discussion of the impact of uniaxial stress applied along the [100] and [011] crystallographic directions on the Verwey transition as probed by AC susceptibility.

5.2.1. Magnetic susceptibility under compression along the [100] direction

The sample E_001x3_spl1 was a rectangular crystal with dimensions $3.00 \times 1.38 \times 0.44$ mm^3, with all faces aligned to $\{100\}$-type planes; hence, the interfix "x3" was included in its label. This crystal was the first to be studied using AC susceptibility under uniaxial stress applied along the [100]

direction. It was also initially intended for imaging with the DFXM technique described in Chapter 4. However, after decompression, the sample disintegrated into fragments during the polishing process required for DFXM measurements, rendering it unusable. In fact, this behavior proved systematic: all crystals previously compressed along the [100] direction tended to fall apart upon polishing, highlighting the inherent fragility of this orientation under uniaxial stress.

The AC susceptibility of sample E_001x3_spl1 was measured under uniaxial compression applied along the [100] direction, with stresses systematically increased from 0 to 189 MPa, as shown in Fig. 5.12a. In agreement with the resistivity results, only a weak increase of T_V with stress was observed. The linearized dependence of T_V, determined separately for heating and cooling cycles, is presented in Fig. 5.12b. The maximum T_V reached under compression was 123.4 K, representing a modest increase of approximately 0.3 K relative to the initial value of $T_{V,0} = 123.1$ K, for the cooling runs.

The experiment was carried out in the SOL2 cell, whose smooth and precise bearings ensured stable load transfer, and no irregularities in the applied stress were detected. Optical inspection of the crystal surface after the final compression step revealed no visible cracks or surface degradation. Nevertheless, the sample disintegrated upon removal from the cell, consistent with the general fragility of magnetite crystals compressed along [100], as also noted in the resistivity measurements.

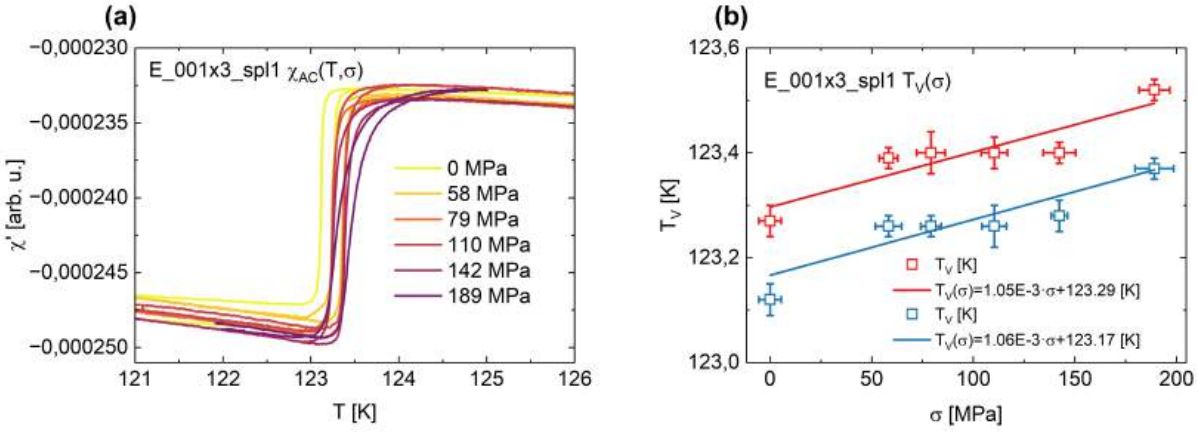

Fig. 5.12. AC susceptibility of sample E_001x3_spl1 under uniaxial compression applied along the [100] direction. **(a)** Temperature dependence of the in-phase susceptibility signal, χ', recorded for applied stresses between 0 and 189 MPa. The transition sharpness was preserved, but the curves exhibit a small shift of the Verwey transition with increasing compression. Although the crystal eventually disintegrated after decompression, no signs of damage were observed during the measurement itself. **(b)** Transition temperature T_V, extracted from the inflection point of $\chi'(T)$, as a function of applied stress σ. A linear increase of T_V with stress is observed, with separate fits shown for heating and cooling.

Figure 5.13 presents the evolution of the Verwey transition temperature T_V, determined from AC susceptibility during heating, as a function of uniaxial stress applied along the [100] direction. The linear fit to the data reveals a weak but systematic increase of T_V with increasing stress, σ,

at a rate of approximately 1 mK/MPa. Within the explored stress range, no clear saturation or deviation from linearity was observed. The reversibility of this effect could not be directly verified in this measurement, since the sample disintegrated upon decompression. Nevertheless, by analogy with resistivity experiments on both [100] and [011] oriented crystals, as well as susceptibility results under [011] compression, it can be reasonably inferred that the pressure-induced shift of T_V is reversible also in the [100] orientation.

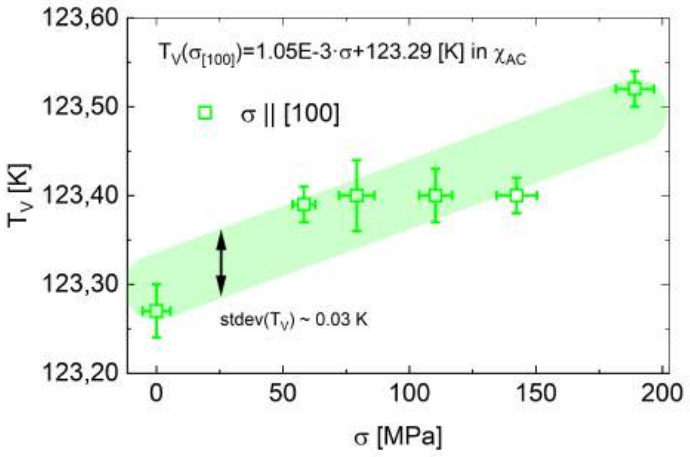

Fig. 5.13. Dependence of the Verwey transition temperature T_V, determined during heating from AC susceptibility measurements, on uniaxial stress applied along the [100] direction for sample E_001x3_spl1. The results reveal a weak but systematic increase of T_V with compression, with a fitted slope of approximately 1 mK/MPa. The shaded band represents the confidence interval of the linear fit.

The AC susceptibility does not provide a direct means of identifying the onset of supercritical plastic deformation, which in practice becomes evident only through irreversible mechanical failure of the crystal. In the case of stoichiometric magnetite compressed along the [100] direction, such brittleness was repeatedly observed, with samples fracturing under stresses on the order of a hundred MPa. This limited mechanical endurance restricted the experimental window in this orientation. By contrast, crystals compressed along the [011] direction exhibited significantly higher mechanical stability in resistivity experiments, which motivated the extension of AC susceptibility studies to this orientation, as discussed in the following Subsection.

5.2.2. Magnetic susceptibility under compression along the [011] direction

The stress thresholds that caused sample failure in the [100] orientation did not apply when uniaxial compression was applied along [011], where crystals exhibited much higher mechanical stability. The results obtained under [011] compression will be illustrated using sample E_011_spl3. For this crystal, AC susceptibility was first measured under compressive strain in the SOL3 cell. Between this initial susceptibility run and a subsequent resistivity measurement, the sample was transferred from

the SOL3 to the SOL2 cell. Both the resistivity experiment and a second series of AC susceptibility measurements as a function of uniaxial stress were then performed in the SOL2 cell. As indicated in Table 5.2, this required applying distinct calibration factors derived from diffraction measurements for each cell. Repeating susceptibility measurements on the same crystal in two independent setups ensured that the observed evolution of T_V reflected the intrinsic response of magnetite under [011] compression, free of effects associated with a specific cell geometry or calibration.

The results of the first series of AC susceptibility measurements under uniaxial compression along the [011] direction for sample E_011_spl3 are summarized in Fig. 5.14. Panel (a) shows the susceptibility curves recorded as a function of temperature for stresses ranging from 0 to 164 MPa. As expected, the transition temperature T_V increased systematically with applied stress. However, an additional effect was observed: the transition broadened significantly with increasing compression. This behavior deviates from the anticipated response of a simple shift in T_V, suggesting the presence of inhomogeneous stress distribution within the crystal. Despite this broadening, the transition profile returned to its original sharp form after decompression, as indicated by the dashed cyan curve in Fig. 5.14, demonstrating that the broadening effect was fully reversible. Furthermore, the thermal hysteresis associated with the transition decreased systematically at higher applied stresses, pointing to a gradual suppression of first-order character under compression.

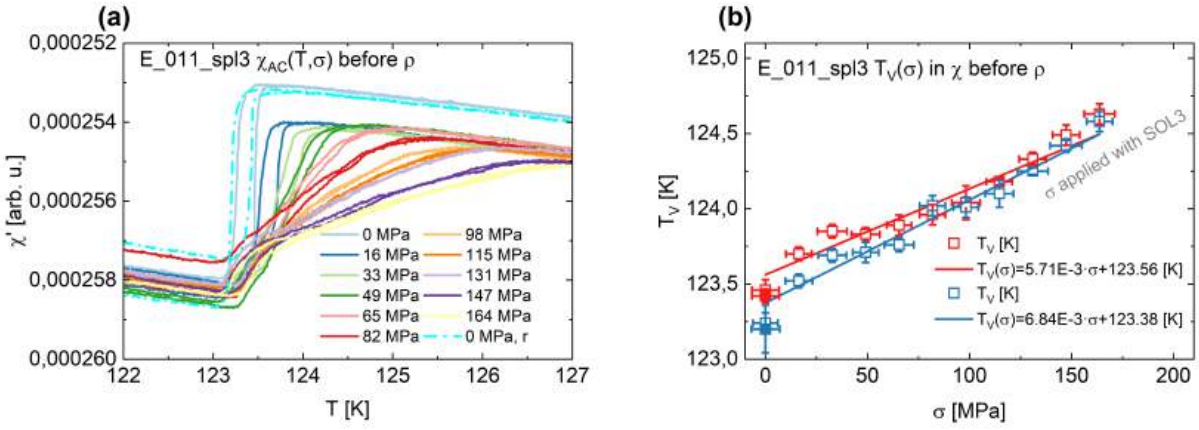

Fig. 5.14. AC susceptibility of sample E_011_spl3 under uniaxial compression applied along the [011] direction, measured prior to the resistivity experiments. **(a)** Temperature dependence of the real part of the susceptibility, χ', recorded for stresses between 0 and 164 MPa. With increasing stress, the Verwey transition systematically shifts to higher temperatures and becomes broadened. The dashed cyan line labeled "0 MPa, r" corresponds to the measurement performed after full decompression, demonstrating the reversibility of the shift and recovery of the sharp transition profile. **(b)** Transition temperature T_V extracted from heating and cooling runs as a function of applied stress σ. The data reveal a clear linear increase of T_V with compression. The filled symbols correspond to the decompression measurement ("0 MPa, r" from panel a).

Figure 5.14b summarizes the evolution of the Verwey transition temperature under uniaxial compression along the [011] direction. The transition temperature T_V increases systematically with applied stress, reaching a maximum value of 124.5 K at 164 MPa, i.e. a net shift of approximately 1.3 K relative to the initial value $T_{V,0} = 123.2$ K. The linear fits to the heating and cooling data demonstrate a good agreement, confirming the robustness of the stress dependence. Taken together with the recovery of the sharp transition upon decompression (Fig. 5.14a), these results establish that the effect of uniaxial stress along [011] on T_V is both strong and reversible.

Following the first AC susceptibility run, electrical resistivity measurements were carried out on the same sample, as already discussed in Fig. 5.6 in Section 5.1. In resistivity, the Verwey transition T_V showed only a systematic upward shift with increasing stress, without any detectable broadening of the transition. To investigate the origin of the broadening observed in the first susceptibility run, a second series of AC susceptibility measurements was performed on the same SOL2 cell that had been used for the resistivity experiment. The results of this second run are presented in Fig. 5.15. Interestingly, although the transition remained somewhat broader than in resistivity, the curves sharpened slightly under compression, and the shift of T_V became more pronounced and systematic compared to the earlier susceptibility run.

In fact, two consecutive susceptibility runs were carried out after the resistivity experiment; the second dataset is included in Appendix A. For clarity, these repeated measurements are labeled "V2" and "V3" both here and in Table 5.2. Despite multiple repetitions, the transition in AC susceptibility never reached the sharpness observed in resistivity. This suggests that the discrepancy cannot be explained solely by pressure inhomogeneity in the setup. Instead, it points to an intrinsic sensitivity of the magnetic susceptibility signal to stress-induced modifications of magnetic domains in the vicinity of the Verwey transition, which tend to broaden the response even when the electronic transport signature remains sharp.

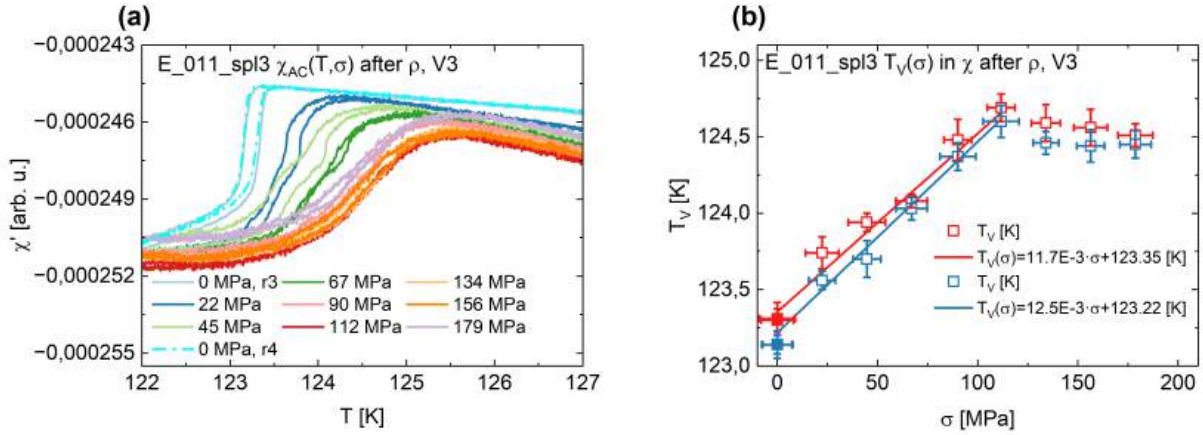

Fig. 5.15. AC susceptibility of sample E_011_spl3 under uniaxial stress applied along the [011] direction, measured after the resistivity run (V3). **(a)** Temperature dependence of the real part of the susceptibility, χ', for applied stresses between 0 and 179 MPa. With increasing compression, the transition systematically shifted to higher temperatures, while the signal amplitude decreased slightly. The dashed cyan line labeled "0 MPa, r4" corresponds to the measurement performed after complete decompression, demonstrating reversibility of the transition temperature. **(b)** Dependence of the Verwey transition temperature T_V on applied stress σ, extracted from the heating and cooling branches. A nearly linear increase of T_V is observed up to ∼120 MPa, with slopes of ∼12 mK/MPa. For higher stresses, the data deviate from linearity and exhibit partial backshift, suggesting the onset of stress saturation or incipient mechanical relaxation. These outlying points were excluded from the linear fits. Filled points denote the post-decompression measurement ("0 MPa, r4" in panel a).

Figure 5.14b shows the variation of the Verwey transition temperature T_V, determined during both heating and cooling, as a function of uniaxial stress applied along the [011] direction. As the stress increased, the transition temperature exhibited a systematic upward shift, consistent with the behavior observed in resistivity. However, beyond approximately 112 MPa, the susceptibility curves began to show signs of saturation, with successive transitions no longer shifting significantly despite further increases in applied stress. The maximum transition temperature, $T_V = 124.6$ K, was recorded at 112 MPa, representing an increase of about 1.2 K compared to the initial unstressed value of $T_{V,0} = 123.4$ K. In the stress regime below 120 MPa, the data followed a well-defined linear trend, and a linear fit was applied to extract the pressure dependence of T_V. In contrast, the points corresponding to higher compressions were excluded from the fit, as they clearly deviated from the linear regime due to the observed saturation.

The apparent saturation of T_V at high stress may partly reflect instrumental limitations, such as the gradual loss of elasticity in the spring of the pressure cell after repeated loading cycles, which reduces the effective force transferred at the highest applied values. This conclusion is supported by the fact that the saturation is not observed in each of the experimental [011] runs.

The Verwey transition temperature determined after decompression, $T_{V,r4} = 123.4$ K, remained essentially unchanged compared to the initial value, $T_{V,0} = 123.3$ K, measured before compression in Fig. 5.14. The difference between $T_{V,r4}$ and $T_{V,0}$ lies well within the uncertainty of the temperature determination, confirming that the observed pressure-induced changes were fully reversible and that no permanent alteration of the transition temperature occurred during the compression cycle shown in Fig. 5.15.

The step in magnetic susceptibility at the Verwey transition is associated with the interplay between structural and magnetic domain walls. In the high-temperature cubic phase above T_V, structural domains are absent, and the magnetic susceptibility reflects the dynamics of magnetic domain walls alone. Upon cooling through the transition into the monoclinic phase, structural domains nucleate and stabilize. These structural domains act as pinning centers for the magnetic domain walls, thereby reducing the overall magnetic susceptibility [1]. The progressive broadening of the susceptibility curves with increasing pressure indicates that the distribution of local transition temperatures within the sample becomes more inhomogeneous.

This broadening can be understood as a universal response to uniaxial stress applied along the [011] direction. The orthorhombic distortion may amplify local strain variations and promote the formation of non-uniform structural domains. These strain-induced variations shift the local T_V differently across the sample, leading to a superposition of slightly displaced transitions and thus to an overall broadening of the susceptibility step. Furthermore, stress enhances domain wall pinning and increases the energy barriers for magnetic domain reconfiguration, which further smears the transition. Hence, the universal broadening of the Verwey transition in AC susceptibility reflects both intrinsic lattice symmetry lowering under [011] stress and extrinsic strain inhomogeneities that arise during compression.

5.2.3. Comparison of the susceptibility response to the uniaxial stress in the [100] and [011] directions

In resistivity measurements, mechanical failure of the crystal was immediately visible as a sudden drop in the measured voltage by several orders of magnitude, providing a clear signature of fracture. By contrast, AC susceptibility does not rely on electrical contacts and is therefore less sensitive to cracking or partial sample damage. Indeed, with the exception of the [100]-oriented sample E_001x3_spl1, which fractured after decompression, all crystals studied in the [011] orientation withstood repeated compression cycles without catastrophic failure. In the following, we summarize and compare the susceptibility results for [100] and [011] compression, highlighting the pronounced anisotropy of the Verwey transition response.

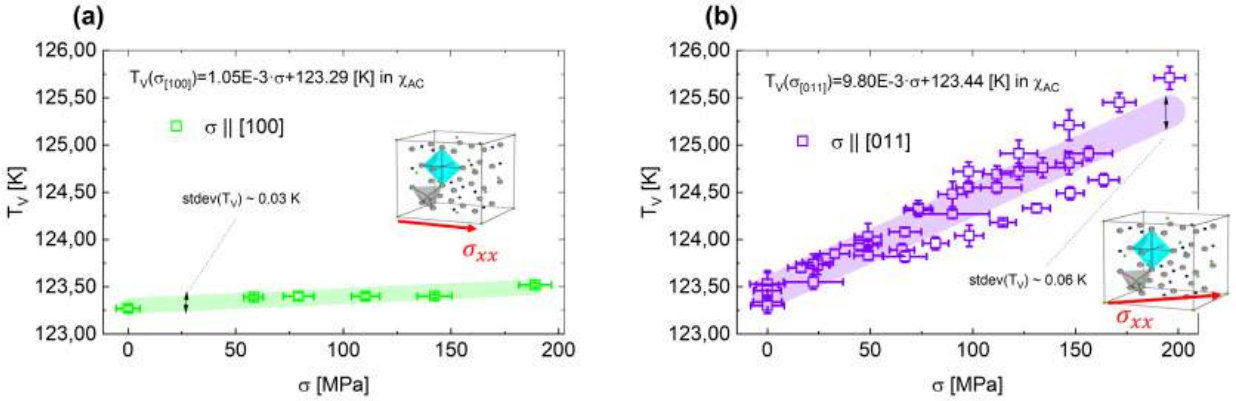

Fig. 5.16. Comparison of the effect of uniaxial pressure direction on the Verwey transition temperature, T_V, determined from AC magnetic susceptibility measurements. **(a)** Dependence of T_V on applied stress σ along the [100] crystallographic direction (data from Fig. 5.13). **(b)** Corresponding dependence for stress applied along the [011] direction for samples E_011_spl1, E_011_spl2, and E_011_spl3. Panels (a) and (b) also show schematic unit cells of magnetite, with the red arrow indicating the direction of applied stress σ_{xx}.

Figure 5.16 brings together the results of AC susceptibility under uniaxial stress along [100] and [011], plotted on the same vertical scale for T_V. This comparison strengthens the findings from the resistivity measurements presented in the previous Sections: while compression in both directions shifts the transition temperature upward, the slope of $T_V(\sigma)$ is significantly larger for [011] than for [100]. This confirms that the orthorhombic distortion induced by [011] compression couples much more strongly to the charge–orbital ordering at the Verwey transition than the simpler tetragonal distortion generated along [100].

When the resistivity data presented in Figs. 5.4 and 5.8 are compared with the susceptibility results, the overall trends are consistent: in both techniques, T_V increases under uniaxial stress, with a significantly stronger effect observed for the [011] orientation. Quantitatively, the resistivity measurements yielded slopes of approximately 3 mK/MPa for [100] and 9 mK/MPa for [011], whereas the susceptibility measurements gave smaller slopes of about 1 mK/MPa for [100] and a comparable 10 mK/MPa for [011]. The discrepancy between the two methods for the [100] orientation most likely arises from the greater susceptibility of this configuration to microcracking and contact degradation under stress. When only the low-pressure portion of the resistivity data is considered (Fig. 5.2), the extracted slope of $\sim$1 mK/MPa agrees well with the susceptibility result. Furthermore, the high level of consistency between resistivity and susceptibility for the [011] orientation, confirmed across several intact samples, demonstrates that these values are robust. It is therefore reasonable to regard the slope obtained at low pressure values as the most representative estimate of the uniaxial stress response along [100].

Taken together, both techniques confirm a pronounced anisotropy in the stress dependence of the Verwey transition: uniaxial compression along [011] enhances T_V by approximately an order of magnitude compared to compression along [100]. This difference reflects the underlying lattice response: while stress along [100] primarily induces a simple tetragonal distortion, compression along [011] generates a shear-driven orthorhombic distortion that couples more strongly to the charge and orbital ordering central to the Verwey transition.

5.3. Influence of uniaxial stress on local environment of Fe ions

The impact of lattice deformation induced by uniaxial stress along the [100] and [011] directions on the local symmetry of the Fe ions was investigated using X-ray absorption near-edge structure (XANES) measurements at the Fe K-edge. The experiment was conducted at the ASTRA end-station of the SOLARIS synchrotron in Krakow. The primary objective was to determine whether the lattice distortion caused by uniaxial compression is manifested in the lifting of inversion symmetry at the Fe sites, particularly those occupying octahedral positions.

In XANES spectra, the pre-edge feature arises from electric quadrupole transitions ($1s \rightarrow 3d$) and reflects deviations from centrosymmetry at the absorbing atom. For Fe in tetrahedral coordination, where inversion symmetry is intrinsically absent, this pre-edge peak is clearly visible. In contrast, Fe ions in centrosymmetric octahedral sites do not contribute to the pre-edge under ideal cubic conditions. The key question motivating this study was, therefore, whether compression along either the [100] or [011] direction can partially lift the inversion symmetry of the octahedral Fe sites, as evidenced by an enhancement of the pre-edge intensity.

A further goal was to examine how the induced lattice distortion influences the local electronic structure of magnetite, including potential modifications in the coordination environment of Fe atoms. In particular, this analysis was aimed to probe how symmetry breaking within the surrounding O $2p$ orbitals affects the hybridization with Fe $3d$ states in the tetrahedral and octahedral sublattices. As demonstrated in the preceding sections, the interatomic shifts induced by uniaxial compression are directly linked to changes in charge transport and magnetic properties. The present experiment, therefore, aimed to establish a direct correlation between the crystal lattice response to external stress and the resulting modifications of the local electronic structure in magnetite.

X-ray absorption spectra at the Fe K-edge were collected as a function of progressively applied uniaxial compression using the SOL3 and SOL4 pressure cells. The measurements were performed at room temperature over the photon energy range 7000–7300 eV, allowing observation of the spectral features in the pre-edge region of the Fe K-edge under. Data were obtained for one sample oriented along the [100] direction and two samples oriented along the [110] direction.

Table 5.3 summarizes all samples studied in this experiment, including their dimensions, the cell employed, and the corresponding stress conversion coefficients. Although the crystal subjected to uniaxial compression along the [100] direction is discussed in this Section, the two samples compressed

Name	Direction	S [mm^2]	σ [MPa/1°]	Device
E_100_spl2_XAS	[100]	0.630	0.341	SOL4
E_011_spl2_XAS (brokenP)	[011]	0.800	0.380	SOL4
E_011_spl1_XAS	[011]	0.820	0.342	SOL3

Tab. 5.3. Summary of samples measured as a function of uniaxial stress using X-ray absorption spectroscopy (XAS). S denotes the cross-sectional area, expressed in mm^2, while σ represents the conversion coefficient between the screw rotation and the uniaxial stress applied in each crystallographic orientation.

along the [011] direction are described in detail in Appendix F. During the XAS experiments, samples E_100_spl2_XAS and E_011_spl2_XAS fractured under load, whereas E_011_spl1_XAS remained intact and was subsequently used for the uniaxial pressure diffraction measurements presented in Chapter 3. A fragment of the fractured sample E_011_spl2_XAS was later utilized for the diffraction imaging experiments discussed in Chapter 4.

The measurements were performed on single crystals of magnetite grown by the zone-melting method. Each crystal was oriented using back-reflection Laue diffraction and subsequently cut along the desired crystallographic direction. The exposed surfaces were mirror-polished using lapping films to ensure high optical quality and minimize surface irregularities before the X-ray measurements.

A reference sample was prepared from a portion of the crystal that was ground to a fine powder in an agate mortar and pestle. The powdered material was mixed with boron nitride (BN) and pressed into a pellet. The Fe K-edge spectrum obtained from this reference sample was recorded first and used throughout the experiment for energy calibration and normalization of the XAS data.

The main experimental challenge in these measurements was the strong self-absorption of fluorescence photons within the bulk of the material. The thickness of each studied sample was approximately 0.4 mm, which resulted in significant attenuation of the emitted X-rays. As a consequence, the extended X-ray absorption fine structure (EXAFS) region could not be reliably analyzed, and the total fluorescence yield (TFY) data were limited to the pre-edge and the initial part of the main absorption edge.

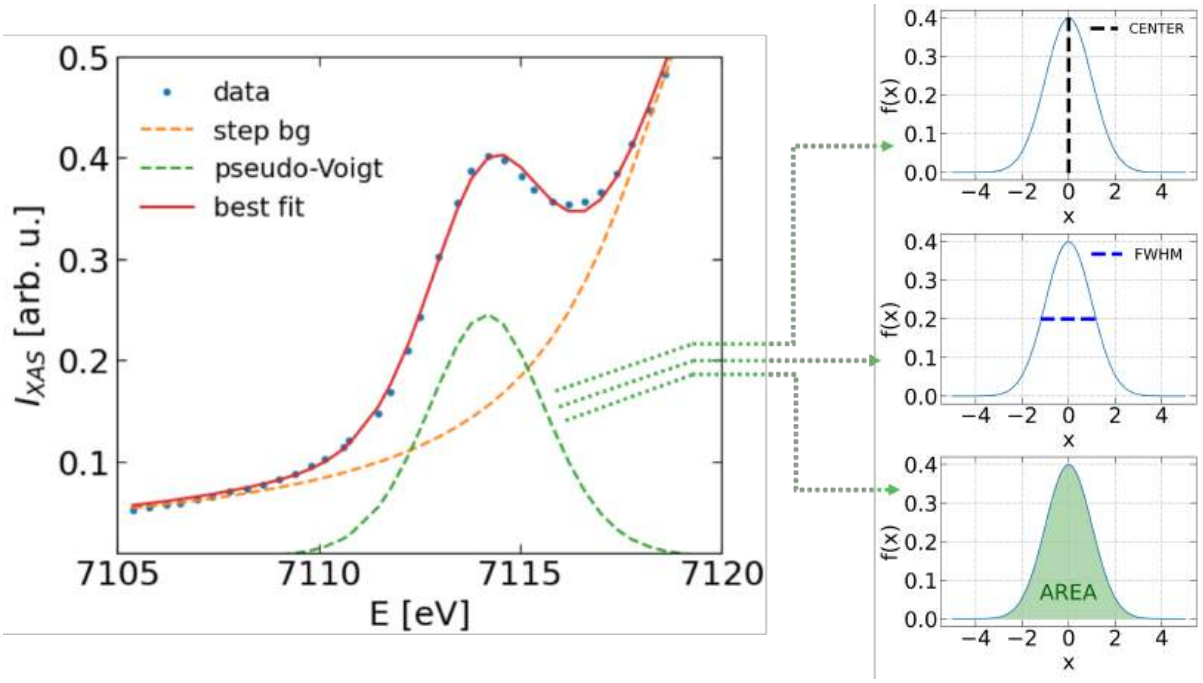

Fig. 5.17. Illustration of the fitting procedure applied to the pre-edge region of the Fe K-edge. A step-like background ("step bg") was subtracted from the raw XAS data in the energy range 7105–7120 eV. The residual spectrum was then fitted using a pseudo-Voigt profile to model the pre-edge feature. Characteristic parameters of this fitted peak, its center position, full width at half maximum (FWHM), and integrated area, were subsequently analyzed as a function of the applied uniaxial stress. The red curve labeled "best fit" represents the sum of the step background and pseudo-Voigt components.

A series of Fe K-edge XAS spectra was collected as a function of uniaxial pressure. The raw scans were pre-processed using the *Athena* software package [2], which included filtering, deglitching, and subtraction of the white-line background. In the following step, all spectra were energy-calibrated and normalized to the Fe K-edge position of the reference pellet. Subsequently, the pre-edge region of each spectrum was fitted with a pseudo-Voigt function using a non-linear least-squares routine implemented in the `lmfit` Python library [3]. From each fitted profile, the peak center, full width at half maximum (FWHM), and integrated area were extracted. The fitting procedure is illustrated schematically in Fig. 5.17.

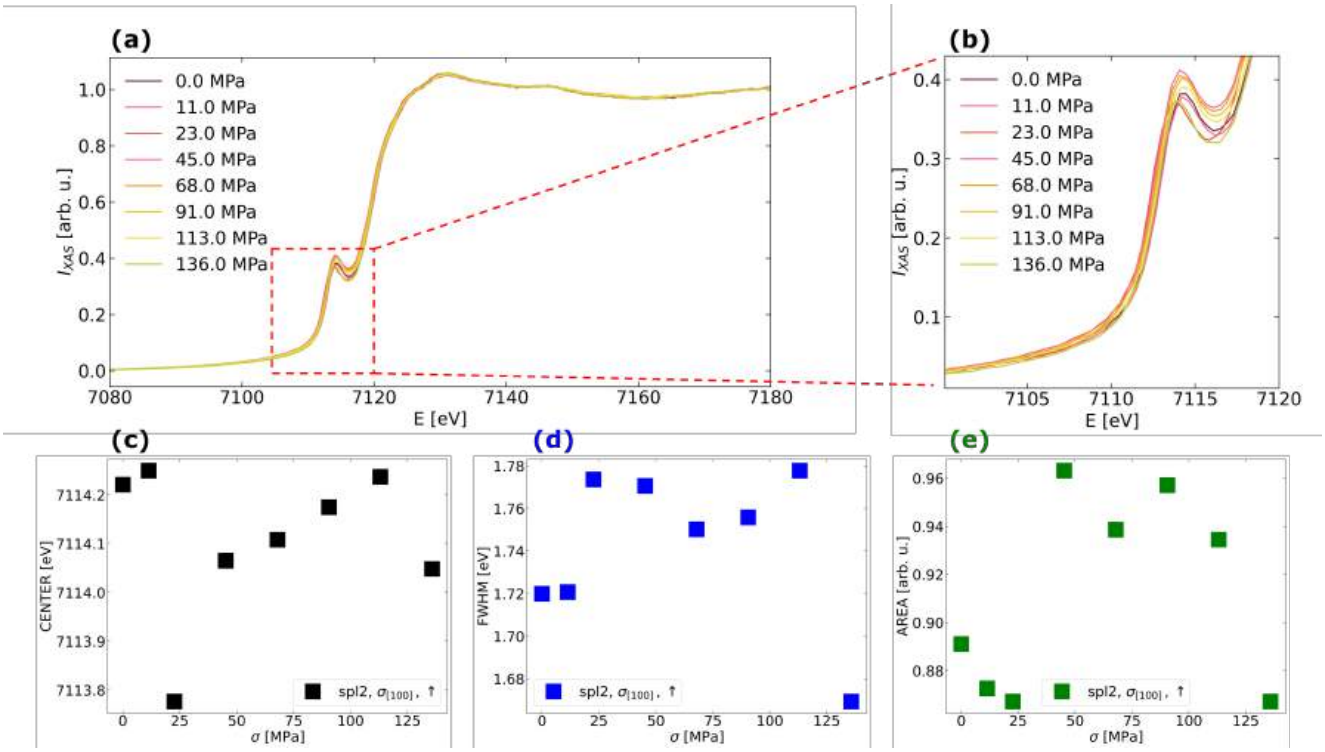

Fig. 5.18. The absorption data at the Fe K-edge collected as a function of uniaxial stress applied along the [100] direction for sample E_100_spl2_XAS measured using the SOL4 cell. **(a)** Full Fe K-edge spectra recorded in the energy range 7080–7180 eV under successive compression steps. **(b)** Magnified view of the pre-edge region (7105–7120 eV), where the fitting procedure described in Fig. 5.17 was applied. Dependence of the **(c)** pre-edge peak center, **(d)** **full width at half maximum (FWHM)**, and **(e)** **integrated peak area** on the applied uniaxial stress σ.

For sample E_100_spl2_XAS, uniaxial compression was applied along the [100] direction in the range from 0 to 136 MPa. The evolution of the Fe K-edge pre-edge features under these conditions is presented in Fig. 5.18. The parameters extracted from the fitted pre-edge region did not show a clear monotonic dependence on the applied stress up to the point of fracture, which occurred at stresses above approximately 130 MPa (Fig. 5.19).

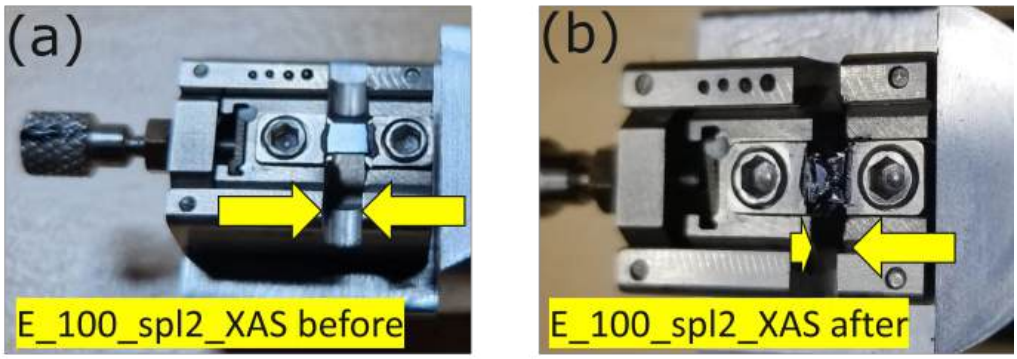

Fig. 5.19. Photographs of sample E_100_spl2_XAS mounted in the SOL4 cell **(a)** before and **(b)** after the XAS experiment under uniaxial compression. Although the outer edges of the sample remained clamped, the central region fractured into multiple pieces, forming randomly oriented flakes.

Figure 5.20 compares the pre-edge parameters obtained for the [100] and [011] orientations as a function of uniaxial stress. Additional data for samples E_011_spl1_XAS and E_011_spl2_XAS are provided in Figs. F.17 and F.18 in Appendix F, respectively.

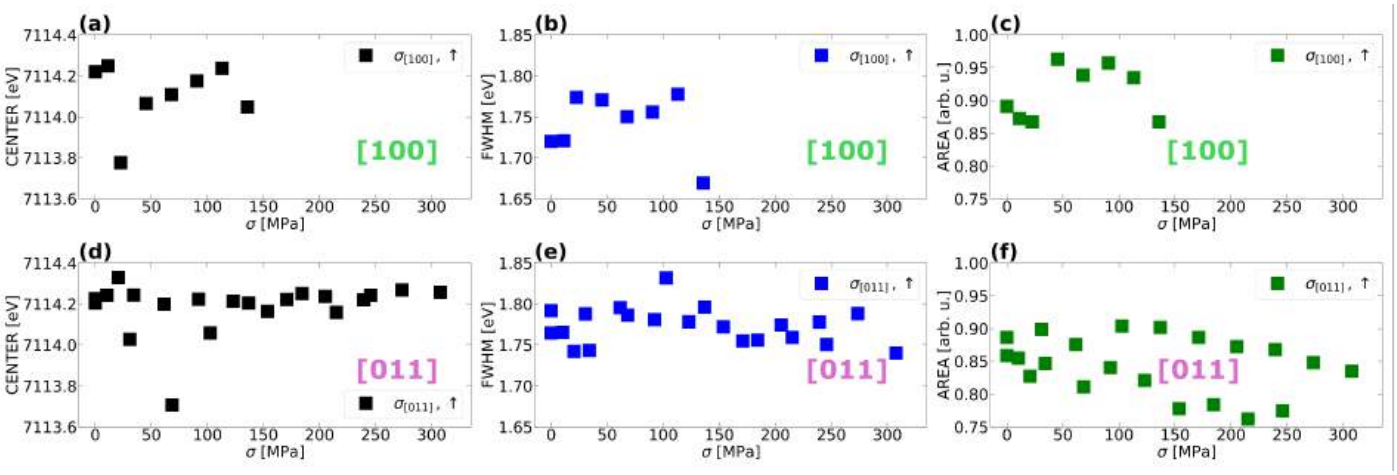

Fig. 5.20. Evolution of the pre-edge peak parameters as a function of uniaxial stress applied along the [100] {panels **(a)**–**(c)**} and [011] {panels **(d)**–**(f)**} crystallographic directions. Panels **(a)** and **(d)** show the dependence of the **peak center**, panels **(b)** and **(e)** present the **full width at half maximum (FWHM)**, while panels **(c)** and **(f)** display the **integrated peak area** as a function of the applied uniaxial stress, σ.

In summary, uniaxial compression along neither of the studied crystallographic directions produced measurable changes in the position, width (FWHM), or integrated area of the pre-edge peak at the Fe K-edge. Within the applied stress range, these parameters remained essentially constant, indicating that the local electronic and structural environment of the Fe ions is largely preserved under moderate uniaxial deformation.

The most plausible explanation for this behavior lies in the nature of the lattice distortion itself. Both diffraction and transport measurements presented earlier in this Dissertation demonstrate that uniaxial compression along [100] and [011] primarily induces a tetragonal or orthorhombic strain that does not lift the inversion symmetry of the FeO_6 octahedra. The applied stress causes small angular rotations and bond-length anisotropies within the octahedra, particularly between apical and distal oxygen atoms, but the overall centrosymmetric arrangement around the Fe site is retained. Consequently, the dipole-forbidden $1s \rightarrow 3d$ transitions responsible for the pre-edge feature remain inactive, and no significant variation in intensity or energy position is expected. The hybridization between Fe $3d$ and O $2p$ orbitals is altered only marginally by such small distortions, and these changes are insufficient to generate a detectable pre-edge modulation.

A secondary contributing factor may stem from the limited experimental sensitivity of the present fluorescence-yield XAS configuration. The combination of strong self-absorption within the $\sim$0.4 mm-thick samples and the restricted pre-edge signal-to-noise ratio likely masked any minute intensity variations that could accompany subtle symmetry perturbations.

The absence of a detectable pre-edge response is therefore consistent with a distortion mode that modifies the long-range lattice symmetry, as reflected in the anisotropic shift of the Verwey transition temperature, without significantly altering the local coordination environment of the Fe ions. The mechanical failure of samples at stresses above $\sim$130 MPa further illustrates the technical limitations of maintaining homogeneous elastic strain, restricting access to regimes where stronger local distortions might occur.

Despite these constraints, the present study demonstrates the feasibility of performing *in situ* near-edge absorption spectroscopy under uniaxial compression. To the best of our knowledge, this constitutes the first systematic investigation of the Fe K-edge fine structure in magnetite under controlled mechanical stress. The methodology developed here provides a foundation for future high-precision synchrotron experiments employing thinner samples, transmission geometries, and polarization-dependent detection, which will be essential to probe stress-induced symmetry breaking and local electronic anisotropy in correlated oxides.

5.4. Conclusions

The purpose of this Chapter was to present a comprehensive investigation of the response of stoichiometric magnetite to uniaxial compression applied along the [100] and [011] crystallographic directions, focusing on its electrical resistivity, AC magnetic susceptibility, and X-ray absorption spectroscopy at the Fe K-edge.

Electrical resistivity and AC susceptibility measurements were performed near the Verwey transition to probe the coupling between lattice strain and charge-orbital ordering. In both techniques, a positive correlation was observed between the transition temperature T_V and the applied uniaxial stress, indicating that compression stabilizes the low-temperature phase. The magnitude of this

effect was strongly anisotropic: the enhancement of T_V under [011] compression was approximately an order of magnitude larger than that under [100] compression. This pronounced anisotropy reflects the distinct lattice distortions induced along the two directions: while [100] stress mainly generates a simple tetragonal distortion, [011] compression introduces a shear-driven orthorhombic component that couples more strongly to the electronic ordering underlying the Verwey transition.

The observed experimental behavior is in close quantitative agreement with the thermodynamic framework developed by Coe *et al.* [4], which predicts that the response of T_V to external stress depends sensitively on crystallographic orientation. Within this model, the rate of change $\partial T_V/\partial\sigma_{\langle hkl\rangle}$ is proportional to the projection of the transformation strain tensor along the stress direction. Using experimentally determined parameters, Coe *et al.* calculated a hydrostatic coefficient of $dT_V/dP = -3.7$ K/GPa, confirming that isotropic compression suppresses the transition, while uniaxial stress produces a directional response characterized by $M_1 = -23.3$ K/GPa for compression along $\langle 111\rangle$ and $M_2 = +8.8$ K/GPa and $M_3 = +10.8$ K/GPa along $\langle 110\rangle$-type directions. In the present study, uniaxial compression was applied exclusively along the cubic [100] and [011] axes; two of the orientations predicted to yield a positive $\partial T_V/\partial\sigma$. The experimentally determined slopes of approximately $+3$ K/GPa for [100] and $+9$ K/GPa for [011] confirm that the Verwey transition temperature increases under uniaxial stress, in excellent agreement with theoretical predictions. The stronger enhancement observed for [011] compression is attributed to its more efficient coupling to the shear component of the transformation strain, whereas the weaker [100] response likely reflects the predominance of a simple tetragonal distortion and partial strain relaxation at higher loads. These findings provide the first quantitative experimental verification of the anisotropic stress dependence predicted by Coe *et al.*, demonstrating that uniaxial compression modifies the Verwey transition in magnetite through symmetry-selective coupling between lattice strain and electronic order.

In addition to the temperature-dependent studies, room-temperature resistivity was monitored as a function of applied uniaxial stress. In both orientations, ρ decreased linearly with increasing compression, consistent with strain-enhanced carrier mobility. The relative changes in resistivity, $\Delta\rho\,[\%]$, were again orientation-dependent: compression along [011] produced approximately three times greater reduction in resistivity than along [100], further emphasizing the anisotropic nature of the strain-transport coupling in magnetite.

Complementary XAS measurements at the Fe K-edge were conducted to probe possible stress-induced modifications of the local electronic and structural environment. Because of strong self-absorption of fluorescence photons within the ∼0.4 mm-thick samples, the analysis was restricted to the pre-edge region (7105–7120 eV), which is particularly sensitive to inversion-symmetry breaking and to the degree of $3d$–$2p$ orbital hybridization at the Fe sites. Each pre-edge feature was fitted using a pseudo-Voigt profile to extract the peak position, full width at half maximum (FWHM), and integrated area. Within the accessible stress range, none of these parameters exhibited a systematic or monotonic dependence on uniaxial compression, indicating that the local coordination symmetry around the Fe ions remains essentially preserved up to nearly 200 MPa.

This invariance of the pre-edge parameters reflects the intrinsic character of the strain field in magnetite. As revealed by diffraction measurements in Chapter 3, uniaxial stress applied along $\langle 100 \rangle$ and $\langle 110 \rangle$ primarily induces tetragonal and orthorhombic distortions of the cubic lattice, respectively. These distortions correspond to small angular rotations and bond-length anisotropies of the FeO_6 octahedra that do not lift their local inversion symmetry. As a result, the dipole-forbidden $1s \rightarrow 3d$ transitions, which define the pre-edge intensity, remain largely inactive, and no measurable variation of peak intensity, width, or energy position is expected. The observed structural anisotropy thus affects mainly the long-range crystal symmetry and macroscopic properties, such as the Verwey transition temperature, rather than the local Fe–O bonding geometry.

Taken together, the results of this Chapter establish a consistent picture of the influence of uniaxial stress on magnetite. Moderate compression modifies transport and magnetic susceptibility through anisotropic but symmetry-preserving lattice distortions, leading to orientation-dependent shifts in the Verwey transition temperature without significant alteration of the local electronic configuration. The combination of resistivity, AC susceptibility, and synchrotron-based XAS measurements provides a comprehensive and mutually consistent experimental framework that captures both the macroscopic and microscopic aspects of stress-structure coupling in magnetite.

Bibliography

[1] M. Bałanda et al. "Magnetic AC susceptibility of stoichiometric and low zinc doped magnetite single crystals". *Eur. Phys. J. B* **43** (2005), pp. 201–212. DOI: 10.1140/epjb/e2005-00043-5.

[2] B. Ravel. "ATHENA: XAS Data Processing". URL: *https://bruceravel.github.io/demeter/documents/Athena/index.html* (visited on 09/13/2025).

[3] M. Newville, T. Stensitzki, R. Otten, et al. "LMFIT: Non-Linear Least-Squares Minimization and Curve-Fitting for Python". URL: *https://lmfit.github.io/lmfit-py/* (visited on 09/14/2025).

[4] R. S. Coe et al. "The thermodynamic effect of nonhydrostatic stress on the Verwey transition". *Earth and Planetary Science Letters* **319–320** (2012), pp. 207–217. DOI: 10.1016/j.epsl.2011.11.021.

Chapter 6.

Summary and conclusions

The main scientific objective of this Dissertation was to systematically investigate how uniaxial stress modifies the structural, magnetic, and electronic properties of stoichiometric magnetite, with particular emphasis on the coupling between lattice symmetry and correlated electronic states both near the Verwey transition and at room temperature. The study combined synchrotron X-ray diffraction, dark-field X-ray microscopy, X-ray absorption spectroscopy, as well as in-house electrical resistivity and AC magnetic susceptibility measurements with the development of a dedicated uniaxial pressure platform.

A major technical achievement was the design, construction, and calibration of compact, screw-driven SOL uniaxial pressure cells compatible with synchrotron diffraction and cryogenic transport measurements. Their calibration, performed both analytically and experimentally using a reference ADMET press at the ESRF, enabled quantitative determination of applied compression up to several hundred megapascals. This development provided a robust and versatile experimental platform for exploring strain-correlation coupling in magnetite and other strongly correlated materials.

Single-crystal X-ray diffraction experiments at the ESRF demonstrated that uniaxial compression induces anisotropic lattice distortions whose symmetry depends on the loading direction. Compression along $\langle 100 \rangle$ produces a tetragonal distortion, while along $\langle 110 \rangle$ it generates an orthorhombic shear component. These distortions were reversible within the elastic regime up to approximately 200 MPa. Magnetite was found to be mechanically more robust under $\langle 110 \rangle$ loading due to the reduced number of active slip systems compared to $\langle 100 \rangle$.

The influence of crystal growth method on the intrinsic defect structure of magnetite was examined using dark-field X-ray microscopy. Crystals grown by the traveling-solvent floating-zone method exhibited low defect densities and homogeneous strain fields, whereas skull-melter-grown crystals displayed significant mosaicity originating from rapid quenching. TSFZ-grown samples were therefore selected for all subsequent uniaxial compression studies. DFXM imaging of decompressed samples revealed that stresses above approximately 150 MPa generate stable, line-like dislocation networks

oriented along $\{111\}$ planes. Despite these extended defects, the Verwey temperature T_V remained unchanged, indicating that dislocation fields do not perturb the cooperative charge-orbital ordering.

The macroscopic response of magnetite to uniaxial stress was probed by temperature-dependent electrical resistivity and AC magnetic susceptibility measurements near the Verwey transition. Both techniques revealed a linear increase of the transition temperature T_V with applied compression, demonstrating that uniaxial stress stabilizes the low-temperature monoclinic phase. The magnitude of this effect was strongly anisotropic: the slope $dT_V/d\sigma$ for $\langle 110\rangle$ loading was roughly an order of magnitude larger than for $\langle 100\rangle$. This anisotropy originates from the different strain symmetries: orthorhombic for $\langle 110\rangle$ and tetragonal for $\langle 100\rangle$. It reflects the stronger coupling between shear-induced distortions and the underlying ordering. In contrast, hydrostatic compression leads to a suppression of T_V, emphasizing that anisotropic, symmetry-breaking strain enhances the cooperative electronic order, while isotropic pressure suppresses it.

Complementary Fe K-edge X-ray absorption spectroscopy confirmed that uniaxial compression up to 200 MPa does not alter the local Fe-O coordination observed via the pre-edge fine structure. This invariance indicates that the observed macroscopic changes in transport and magnetic properties originate from symmetry-preserving lattice distortions rather than local electronic rearrangements.

In summary, the results presented in this Dissertation establish a coherent picture of the interplay between lattice strain, electronic correlations, and phase stability in magnetite. Moderate uniaxial compression modifies the global crystal symmetry and tunes the charge and orbital ordering without perturbing the local electronic environment. The Verwey transition is thereby stabilized through a strain-driven enhancement of the cooperative coupling between lattice and electronic degrees of freedom.

Beyond magnetite, the developed methodology provides a quantitative framework for investigating uniaxial stress effects in a broad range of strongly correlated materials, such as high-T_c superconductors, charge-density-wave compounds, and Mott insulators, where controlled symmetry breaking can serve as a powerful route for engineering emergent quantum states.

Information on the scientific achievements

Publications

(1) H. Elnaggar, S. Graas, S. Lafuerza, B. Detlefs, W. Tabiś, **M. A. Gala** , A. Ismail, A. van der Eerden, M. Sikora, J. M. Honig, P. Glatzel, F. de Groot, *Temperature-driven self-doping in magnetite*, Phys. Rev. Lett. 127, 186402 (2021). https://doi.org/10.1103/PhysRevLett.127.186402

(2) P. Popčević, Y. Utsumi, I. Biało, W. Tabiś, **M. A. Gala** , M. Rosmus, J. J. Kołodziej, N. Tomaszewska, M. Garb, H. Berger, I. Batistić, N. Barišić, L. Forró, E. Tutiš, *Role of intercalated cobalt in the electronic structure of* $Co_{1/3}NbS_2$, Phys. Rev. B 105, 155114 (2022). https://doi.org/10.1103/PhysRevB.105.155114

(3) B. Klebel-Knobloch, W. Tabiś, **M. A. Gala** , O. S. Barišić, D. K. Sunko, N. Barišić, *Transport properties and doping evolution of the Fermi surface in cuprates*, Sci. Rep. 13, 13562 (2023). https://doi.org/10.1038/s41598-023-39813-z

(4) T. Kołodziej, J. Piętosa, R. Puźniak, A. Wiśniewski, G. Król, Z. Kąkol, I. Biało, Z. Tarnawski, M. Ślęzak, K. Podgórska, J. Niewolski, **M. A. Gala** , A. Kozłowski, J. M. Honig, W. Tabiś, *Impact of hydrostatic pressure, nonstoichiometry, and doping on trimeron lattice excitations in magnetite during axis switching*, Phys. Rev. B 108, 245148 (2023). https://doi.org/10.1103/PhysRevB.108.245148

(5) Y. Utsumi Boucher, I. Biało, **M. A. Gala** , W. Tabiś, M. Rosmus, N. Olszowska, J. J. Kołodziej, B. Gudac, M. Novak, N. K. Chogondahalli Muniraju, I. Batistić, N. Barišić, P. Popčević, E. Tutiš, *Intercalation-induced states at the Fermi level and the coupling of intercalated magnetic ions to conducting layers in* $Ni_{1/3}NbS_2$, Phys. Rev. B 109, 085135 (2024). https://doi.org/10.1103/PhysRevB.109.085135

(6) K. Podgórska, **M. A. Gala** , K. Komędera, N. K. Chogondahalli Muniraju, S. Nasrallah, Z. Kąkol, J. Sabol, C. Marin, A. Włodek, A. Kozłowski, J. E. Lorenzo, N. Barišić, D. Rybicki, W. Tabiś, *Correlation between magnetism and the Verwey transition in magnetite*, Phys. Rev. B 111, 245161 (2025). https://doi.org/10.1103/yn1s-3hv3

Conference contributions

Oral presentations

(I) *Influence of uniaxial pressure on electronic properties of a simple cuprate superconductor*, Multiscale Phenomena in Condensed Matter – YOUNG MULTIS 2021, Institute of Nuclear Physics PAS, Krakow, (Jul 5-7, 2021)

(II) *The interplay between lattice distortion and superconductivity in cuprate superconductors*, XX National Conference on Superconductivity, Lublin, (May 22–26, 2022)

(III) *Search for dependency between Verwey and Curie temperatures in magnetite monocrystals doped with Mn, Zn, Al and Ti*, MULTIS 2022, Institute of Nuclear Physics PAS, Krakow, (Jun 27–30, 2022)

(IV) *Uniaxial strains as a tool to modify lattice symmetry and influence superconductivity in cuprates*, Kraków–Zagreb Condensed Matter Workshop, Krakow, (Feb 15–16, 2023)

(V) *Role of intrinsic and external strain on the Verwey phase transition in magnetite*, Zakopane School of Physics – Breaking frontiers: submicron structures in physics and biology, IFJ PAN, Zakopane, (May 23–27, 2023)

(VI) *Evolution of the Verwey transition in magnetite observed through electronic transport studies under uniaxial stress*, Young Multis 2023 – Multiscale phenomena in condensed matter, Institute of Nuclear Physics PAS, Krakow, (Jul 3–5, 2023)

(VII) *Rola dystorsji sieciowych na własności elektronowe i przemianę Verweya w magnetycie*, Środowiskowe Seminarium Fizyki Ciała Stałego, AGH University, Kraków, (Jan 3, 2024)

(VIII) *Impact of the uniaxial compression on the stress tensor and lattice parameters in magnetite*, 49th Congress of Polish Physicists, University of Silesia, Katowice, (Sep 5–11, 2025)

(IX) *The role of focus and empiricism in blended learning at the intersection of school and university*, 49th Congress of Polish Physicists, University of Silesia, Katowice, (Sep 5–11, 2025)

Posters

(i) *The importance of in-situ and ex-situ strain in the dynamics of the Verwey transition in magnetite*, 48th Congress of Polish Physicists, Gdańsk University of Technology, Gdańsk, (Sep 1–7, 2023)

(ii) *Impact of stress on the Verwey transition in magnetite*, Hercules European School, Univ. Grenoble Alpes, Grenoble, (Mar 17, 2023)

Supervised students

1. **Agnieszka Domalewska**, "*Uniaxial compression on the critical temperature through the resistance of $Nd_{2-x}Ce_xCuO_{4-y}$ (NCCO) superconductor*", AGH Physics and Applied Computer Science Summer School, (2021)

2. **Eryk Matecki**, "*PyMeasure and PyQt libraries in computerization of resistance and AC susceptibility measurements*", AGH Physics and Applied Computer Science Summer School, (2022)

3. **Jakub Banach**, "*Development of a window-based application for controlling a set of meters and visualizing data in high-temperature electrical resistance measurements*", Developmental tutoring, (Mar 17 – Oct 20, 2022)

4. **Karolina Podgórska**, "*Electrical resistance of $Fe_{3-x}M_xO_4$ (M = Zn, Ti, Al, Mn) single crystals at temperatures up to 1000 K*" [„Badanie oporu elektrycznego monokryształów Fe3-xMxO4 (M = Zn, Ti, Al i Mn) w temperaturach do 1000 K"], Master of Science thesis (Technical Physics), Faculty of Physics and Applied Computer Science, AGH, (defended Jul 22, 2022)

5. **Edyta Oleś**, "*Effect of uniaxial pressure on the Verwey transition in magnetite*" [„Wpływ ciśnienia jednoosiowego na przemianę Verweya w magnetycie"], Bachelor of engineering diploma project (Technical Physics), Faculty of Physics and Applied Computer Science, AGH, (defended Jan 29, 2023)

6. **Maja Iveljić**, "*Influence of lattice deformation on the Verwey transition in magnetite*", Bachelor of science thesis (Studienrichtung: Technische Physik), TU Wien, (defended Dec 5, 2023)

Teaching experience

– Academic year 2021/2022, Winter semester, remedial classes in Physics 1, 15 h, field of study: Computational Engineering, WIMiIP

– Academic year 2021/2022, completion of the tutoring course for academic teachers "Szkoła Tutorów Akademickich (STA)", within the Ministerial Programme "Excellence Initiative: Research University for AGH University (IDUB)" (Nov 13 – Dec 12, 2021)

- Academic year 2024/2025, Winter semester, course: Physics Laboratory, 30 h, field of study: Micro- and Nanotechnologies in Biophysics, WFiIS
- Academic year 2024/2025, Winter semester, course: Physics Laboratory, 15 h, field of study: Computer Science and Intelligent Systems, WEAIiIB
- Academic year 2024/2025, Summer semester, course: Physics Laboratory 2, 45 h, field of study: Microelectronics in Technology and Medicine, WEAIiIB
- Academic year 2025/2026, Winter semester, laboratory classes: Physics Laboratory 2 (15 h) and Elements of Modern Physics (15 h), field of study: Computer Science and Intelligent Systems, WEAIiIB
- Academic year 2025/2026, Winter semester, auditory classes: Mechanics and statistical physics (60 h), field of study: Medical Physics, WFiIS
- Preparatory courses for the second and third grade of the secondary school as part of the "AGH Zero Year" program in the 2024/2025 (30 hours) and 2025/2026 (30 hours) school years, respectively

Experimental campaigns at large scale facilities

The experiments of particular relevance to the Dissertation were highlighted in mulberry. The experiment in which the author of the Dissertation was the main proposer, has been highlighted in **bold**.

The experiments carried out at the National Synchrotron Radiation Facility SOLARIS, Jagiellonian University in Krakow, were marked with the diamond symbol [♢], while the experiments performed at the ESRF were denoted with the spade symbol [♠].

♢ "Uniaxial pressure as a tool to tune the carrier distribution within CuO2 planes in cuprates", Main proposer: Wojciech Tabiś, Beamline: XAS, (Oct 12-17, 2020), SOLARIS, Krakow

♢ "*Role of the 3d transition metal intercalates in the electronic structure of* $Ni_{1/3}NbS_2$", Main proposer: Yuki Utsumi Boucher, Beamline: UARPES, (Apr 6-10, 2021), SOLARIS, Krakow

♢ "*Role of the 3d transition metal intercalates in the electronic structure of* $Ni_{1/3}NbS_2$", Main proposer: Yuki Utsumi Boucher, Beamline: UARPES, (May 17-22, 2022), SOLARIS, Krakow

♢ "*Role of the chalcogen substitution on the band structure of murunskite*", Main proposer: Davor Tolj, Beamline: UARPES, (Sep 12-17, 2022), SOLARIS, Krakow

– "*Feasibility experiment of resonant photoelectron spectroscopy on Mn_2P*", Main proposer: Yuki Utsumi, Beamline: not specified, (Apr 25-29, 2023), SOLARIS, Krakow

♢ "*Band dispersion and Fermi surface along k_z direction in $Ni_{1/3}NbS_2$*", Main proposer: Petar Popčević, Beamline: PHELIX, (Sep 18-23, 2023), SOLARIS, Krakow

♢ "*Role of the metal and chalcogen substitution on the electronic structure and oxidation states of murunskite*", Main proposer: Davor Tolj, Beamline: PHELIX, (Oct 17-21, 2023), SOLARIS, Krakow

♢ "*Modification of the electronic structure by application of uniaxial pressure in magnetite*", Main proposer: Wojciech Tabiś, Beamline: ASTRA, (Nov 14-17, 2023), SOLARIS, Krakow

♢ "*Tuning of unconventional superconductivity through application of uniaxial pressure*", Main proposer: Wojciech Tabiś, Beamline: PIRX, (Dec 5-9, 2023), SOLARIS, Krakow

♠ "*Influence of strains in the occurrence and on the dynamics of the Verwey phase transition in magnetite*", Main proposer: Jose Emilio Lorenzo, Beamline: ID06, (Nov 16-23, 2021), ESRF, Grenoble

♠ **"*Tracking the low temperature lattice ordering and strain distribution during Verwey phase transition in magnetite*", Main proposer: Mateusz Gala, Beamline: ID03, (Jun 4-10, 2024), ESRF, Grenoble**

♠ "*Effect of the uniaxial compression on the short-range charge order in magnetite observed with diffuse X-ray scattering*", Main proposer: Wojciech Tabiś, Beamline: not specified, (Nov 26 - Dec 2, 2024), ESRF, Grenoble

Schools & Workshops

- VI School on Vacuum Techniques, organized by the Polish Vacuum Society as a satellite event of the VIII Congress of the Polish Vacuum Society at the Faculty of Physics, Astronomy and Applied Computer Science, (Jul 4–5, 2022), Jagiellonian University, Krakow
- Krakow–Zagreb Condensed Matter Workshops, organized by the Faculty of Physics and Applied Computer Science, (Feb 15–16, 2023), AGH University of Krakow, Krakow
- HERCULES European School on Synchrotron and Neutron Science, organized by Université Grenoble Alpes, ESRF, and ILL, (Feb 26 – Apr 1, 2023), Grenoble, France

- Zakopane School of Physics “Breaking Frontiers: Submicron Structures in Physics and Biology”, organized by the Institute of Nuclear Physics, Polish Academy of Sciences, (May 23–27, 2023), Zakopane, Poland

Research Internships

⊗ Research internship within the D4 IDUB minigrant, host: Prof. Dr. Neven Barišić, (May 1 – Jul 1, 2022), TU Wien, Vienna, Austria

⊗ NAWA PROM internship, research tasks related to the doctoral dissertation, host: Prof. Dr. Neven Barišić, (Feb 3–11, 2023), TU Wien, Vienna, Austria

⊗ Research internship: preparation of Fe_3O_4 single crystals for resistance measurements under uniaxial pressure, host: Prof. Dr. Neven Barišić, (Jul 21 – Aug 7, 2023), TU Wien, Vienna, Austria

Research projects

♣ National Agency for Academic Exchange (NAWA), Polish Returns 2019, project no. PPN/PPO/2019/1/00014, period 2019–2023, **PI: Wojciech Tabiś**, role: investigator

♣ National Science Center (NCN), OPUS-21, project no. 2021/41/B/ST3/03454, period 2021–2025, project title: *An attempt to understand the high-temperature superconductivity through its damping* **PI: Wojciech Tabiś**, role: holder of a scholarship for PhD students

♣ AGH University of Krakow, Excellence Initiative – Research University (IDUB), Action D4: University grant system for research projects carried out by the doctoral students, proposal no. 2773, period 2021–2022, project title: *Influence of lattice symmetry breaking on high-temperature superconductivity in copper–oxide compounds*, **PI: Mateusz Gala**

♣ AGH University of Krakow, Excellence Initiative – Research University (IDUB), Action D4: University grant system for research projects carried out with the participation of doctoral students, proposal no. 6387, period 2023–2025, project title: *Development of technologies and devices for studies of the influence of uniaxial pressure on structural and transport properties of strongly correlated electron systems*, **PI: Wojciech Tabiś**, role: PhD student

Rewards and other experience

- ✓ IDUB AGH Excellence Initiative: Research University, Action D5. Quality-related scholarship for the best doctoral students, granted for the academic year 2023/2024
- ✓ Increased scholarship from the ministerial subsidy for the best doctoral students at AGH, granted for the academic year 2022/2023
- ✓ Increased scholarship from the ministerial subsidy for the best doctoral students at AGH, granted for the academic year 2023/2024
- ✓ Member of the AGH University Senate, (Jan 2023 – Oct 2025)
- ✓ President of the AGH University PhD Candidates' Council [Uczelniana Rada Samorządu Doktorantów - URSD AGH], (Jan 1, 2023 – Dec 31, 2024), responsible for managing a budget of approx. PLN 50,000/year and coordinating an organization of 30–40 members
- ✓ Member of the Physical Sciences Discipline Council, AGH University, (Jan 2024 – Dec 2025)
- ✓ Physics teacher, A. Mickiewicz VI High School, Krakow, (school years 2024/2025 and 2025/2026)

Appendices

Appendix A.

Details of sample preparation for electrical resistivity measurements

Gold wires of 0.05 mm diameter were used as electrical contacts and attached to the top surface of the sample using 6838 HT silver conducting paint. This paint, composed of a suspension of fine silver particles, required thermal curing to achieve sufficient electrical conductivity. The initial curing was performed under ambient conditions on a hot plate at 150°C for 10 minutes. In the subsequent step, the temperature was increased to 300°C, and the contacts were cured for an additional 15 minutes. At this stage, the contact resistance was on the order of several hundred Ω, indicating limited interfacial conductivity. Final curing was carried out in a tube furnace preheated to 500°C. The sample was placed in a U-shaped ceramic crucible and enclosed within a glass tube that was repeatedly evacuated and purged with 99.9999% Ar to ensure an oxygen-free atmosphere. The final curing, lasting 10 minutes under continuous argon flow, prevented oxidation of the magnetite surface. After cooling, the contact resistance was reduced to below 3 Ω. The prepared sample was then mounted on the uniaxial pressure cell using the non-conductive epoxy resin LOCTITE® STYCAST 2850 FT, as shown in Fig. A.1.

Resistivity measurements were performed using phase-sensitive detection with a Stanford Research SR 860 lock-in amplifier, which served simultaneously as the AC voltage source and voltmeter. The measurement circuit consisted of the lock-in amplifier connected in series with a precision shunt resistor of $R_{\mathrm{sh}} = 1\ \mathrm{k\Omega}$ and the sample of resistance R. The lock-in supplied an input voltage of $U_{\mathrm{in}} = 1\ \mathrm{V_{rms}}$ at a frequency of $f = 2018.2\ \mathrm{Hz}$, deliberately chosen to avoid interference with the 50 Hz line frequency and its harmonics. This configuration produced a nearly constant current of $I \approx 1\ \mathrm{mA}$ through the circuit. Since the shunt resistance was several orders of magnitude larger than the sample resistance ($R_{\mathrm{sh}} \gg R$), variations in the sample resistivity near the Verwey transition did not significantly affect the circuit stability. The sample voltage U was in phase with the source signal and could be determined using the voltage divider relation:

$$U = U_{in} \cdot \frac{R}{R + R_{sh}} \Rightarrow U_{in} \cdot \frac{R}{R_{sh}}. \tag{A.0.1}$$

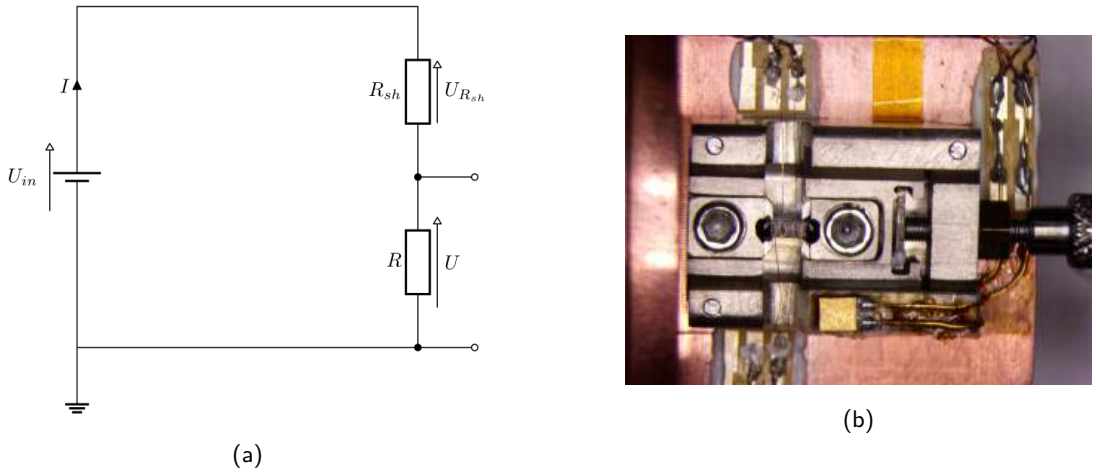

(a) (b)

Fig. A.1. Electrical resistivity measurement protocol under uniaxial compression using a lock-in amplifier. **(a)** Schematic of the voltage-divider configuration used for phase-sensitive signal detection. According to Kirchhoff's second law, the supply voltage U_{in} is divided between the shunt resistor R_{sh} and the sample resistance R ($R \ll R_{\mathrm{sh}}$). The measured output voltage U remains in phase and at the same frequency as the source signal. **(b)** Stoichiometric magnetite sample prepared for electronic transport measurements. The crystal, oriented along the [110] direction, was mounted in the SOL2 uniaxial pressure cell using non-conductive epoxy resin. Pairs of current and voltage leads were connected to the gold contact pads. The square golden component at the bottom of the image is the CX-161209 temperature sensor.

The sample resistance was calculated as $R = \dfrac{U}{I}$, and the corresponding resistivity was determined from

$$\rho = R \cdot \frac{w \cdot t}{l_{\mathrm{eff}}},$$

where l_{eff}, w, and t denote the effective length, width, and thickness of the sample, respectively. Considering the geometric measurement uncertainty of approximately 0.1 mm for each dimension, the estimated uncertainty in ρ is on the order of 5 m$\Omega \cdot$cm.

Appendix B.

Preparation of the miniaturized AC susceptibility measuring system

The procedure for preparing the experimental setup for AC magnetic susceptibility measurements under uniaxial compression is described below. For this purpose, a series of custom excitation and pickup coils was designed, manufactured, and tested.

Each coil was wound manually using 1 m of insulated copper wire, which was divided into two parallel strands. The winding was performed anticlockwise around a 0.7 mm steel needle serving as the temporary core, with the number of turns carefully counted. After reaching the target number of loops for the signal coils, the winding direction of one strand was reversed to ensure symmetry of the magnetic field. Upon completion, the coils were impregnated with GE Varnish and left to dry at room temperature. After removal from the steel carcass, the coils were reinforced with a fast-setting epoxy adhesive (DISTAL® Rapid) to improve mechanical stability.

The free ends of the wires were twisted into pairs to minimize inductive pickup and external electromagnetic interference. The tips were then stripped of insulation and pre-tinned with solder to facilitate later connections. The final step involved measuring the electrical resistance of both the emitter and receiver coils. Only assemblies exhibiting a resistance below 2 Ω were accepted for further testing using the calibration box shown in Fig. B.1.

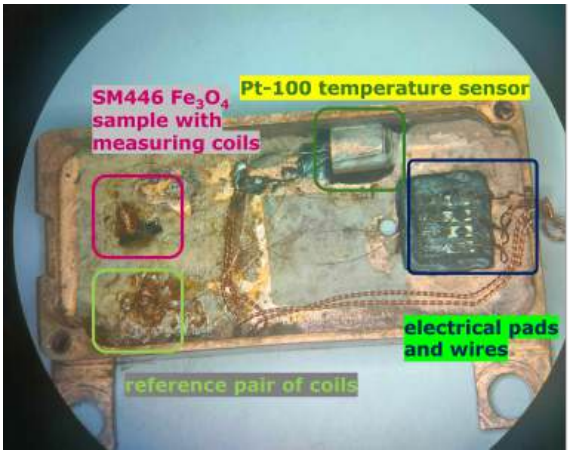

Fig. B.1. Experimental setup used for testing the manufactured detection coils. One pair of coils was attached to a reference sample, which was then fixed to the bottom of the copper box using an insulating paper layer. Electrical connections between the coils and the lock-in amplifier were made through dedicated contact pads. The temperature was monitored using a platinum resistance thermometer, thermally shielded with a copper foil. The box itself was machined from a solid copper bar and sealed by screwing a cap onto its top. The closed and thermally isolated assembly, containing the sample with mounted coils, was placed inside a cryogenic refrigerator operating in a closed helium gas cycle, allowing temperature control in the range from 300 K down to 10 K.

The results of the coil testing are summarized in Table B.1. The temperature dependence of the real component of the AC magnetic susceptibility, $\chi'(T)$, was measured for the reference magnetite sample SM446 using four excitation frequencies: **188.88**, **509.70**, **1007.4**, and **2018.2** Hz, each supplied by the lock-in amplifier SR830.

Measurements were performed sequentially for each of the manufactured coil sets. The first pair of coils was wound with identical helicity of both primary (emitter) and secondary (receiver) windings, denoted as $[\uparrow,\uparrow]$, whereas the second pair exhibited opposite winding directions, marked as $[\uparrow,\downarrow]$.

This configuration allowed for evaluating the influence of the number of windings, the primary coil current, and the frequency on the detected susceptibility signal and on the overall sensitivity of the measurement setup.

No.	ϕ [mm]	$[\uparrow,\uparrow]$ loops	$[\uparrow,\downarrow]$ loops	R_{shunt} [Ω]	Date	$\chi'[T]$ plot
1.	0.10	25, 25	25, 25	1000	12.11.2023	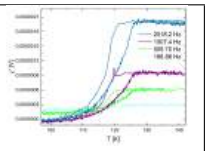
2.	0.05	50, 50	50, 50	1000	29.11.2023	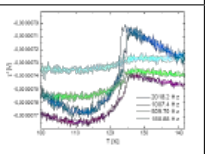
3.	0.10	50, 50	25, 25	1000	30.11.2023	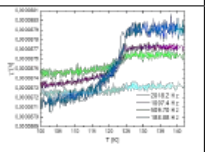
4.	0.10	50, 25	50, 25	1000	01.12.2023	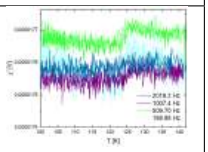
5.	0.10	50, 25	50, 25	1000	01.12.2023	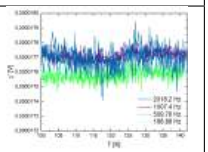
6.	0.05	25, 25	25, 25	1000	05.01.2024	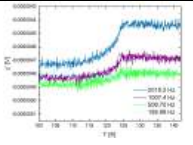
7.	0.10	50, 50	50, 50	500	09.01.2024	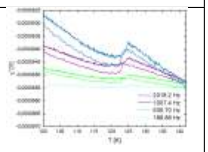
8.	0.10	50, 50	50, 50	1000	09.01.2024	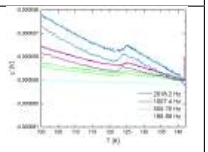
9.	0.05	50, 50	25, 25	500	12.01.2024	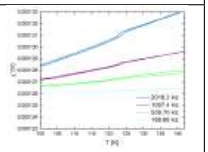
10.	0.05	50, 50	25, 25	1000	12.01.2024	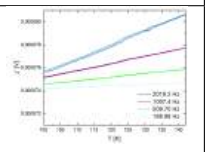

Tab. B.1. Summary of the design parameters and testing results for the miniaturized AC susceptibility coils. The column *No.* refers to the coil configuration number, while ϕ denotes the diameter of the copper wire used for winding. In configurations 4 and 5, the input and output circuits were intentionally interchanged to assess the effect of reversed electrical connections on the susceptibility signal.

Appendix C.

ABAQUS simulation environment and principle of Finite Element Method

C.1. The ABAQUS software

The Complete Abaqus Environment (ABAQUS/CAE) is a commercially available computer-aided engineering (CAE) software package used for the design and numerical analysis of complex engineering problems, including stress and strain distribution, thermal conduction, and heat dissipation in heterogeneous or composite materials.

Abaqus is based on the Finite Element Method (FEM), which provides an efficient numerical framework for solving large systems of coupled partial differential equations (PDEs). The software employs either the *Standard* (implicit) or *Explicit* (dynamic) computational engines to integrate the Newtonian equations of motion and determine the displacement, stress, and strain fields at discrete nodal points within the modeled geometry.

It should be noted that Abaqus does not enforce a predefined system of physical units. The user is therefore responsible for maintaining consistency among all quantities entered in the model. In this study, the simulations were performed using the following unit convention: stress in megapascals (MPa), length in millimeters (mm), force in newtons (N), and angles in degrees.

The Graphical User Interface (GUI) of Abaqus/CAE is composed of several functional modules that guide the modeling workflow. The most relevant for this work include the *Sketcher* module for defining the sample geometry, the *Material* module for assigning constitutive properties, and the *Mesh* module, which discretizes the geometry into finite elements such as hexahedra, tetrahedra, or octahedra.

The output of a completed FEM simulation, referred to as a *Job*, is stored in a Model Output Database file (.odb), which contains all computed field variables. The post-processing environment allows visualization and quantitative analysis of results such as total and component stress, engineering and logarithmic strain, nodal displacements and rotations, reaction forces, and overall model deformation.

The standard analysis procedure consists of the following steps, listed in the Tab. C.1.

No. module	**Name**	**Function**
1	Part	geometry definition of a model component
2	Property	definition of the material parameters
3	Section	assignment of materials to parts
4	Mesh	selection of grid type elements and meshing
5	Assembly	integration of the meshed parts
6	Step	definition of stages in the analysis
7	Boundary Conditions (BCs)	imposition of loads and contacts
8	Job	submission for the FEM engine solver
9	Visualization	plotting and post-processing of the results

Tab. C.1. List of modules in Abaqus CAE along with their functionalities explained.

In the modeling stage, an input file for the simulation is generated, job.inp. The simulation is then evaluated and run. The solver returns four result files: job.odb, job.dat, job.msg, and job.log. These outputs contain the job database and the job details, the messages sent during the completion of calculations, and the system logs, respectively. The files with the name "job" serve for post-processing and visualization. The generalized schematic of this workflow is presented in Fig. C.1.

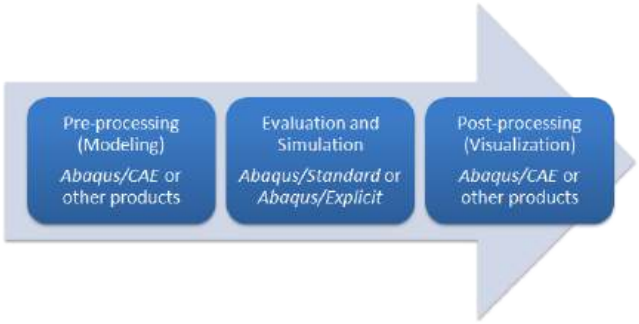

Fig. C.1. Workflow for solving a task using ABAQUS/CAE environment [1].

C.2. Example of solving a 1D problem with the FEM approach

The principle of FEM will be demonstrated, after [2], on a simple differential equation:

$$\frac{\partial^2 u}{\partial x^2} = 2, \tag{C.2.1}$$

defined in the one-dimensional segment $[0,1]$. The unique solution of Eq. C.2.1 is constrained by declaring the boundary conditions (BCs):

- the Dirichlet condition, $u(x=0)=0$,
- and the Neuman condition, $\dfrac{\partial u}{\partial x} = 2$ for $x = 1$.

The exact solution is $u(x) = x^2$. To solve Eq. (C.2.1) with the FEM, in the $[0,1]$ domain the finite elements e_1 and e_2 are defined with the nodes w_1, w_2, and w_3, which were marked in Fig. C.2(A).

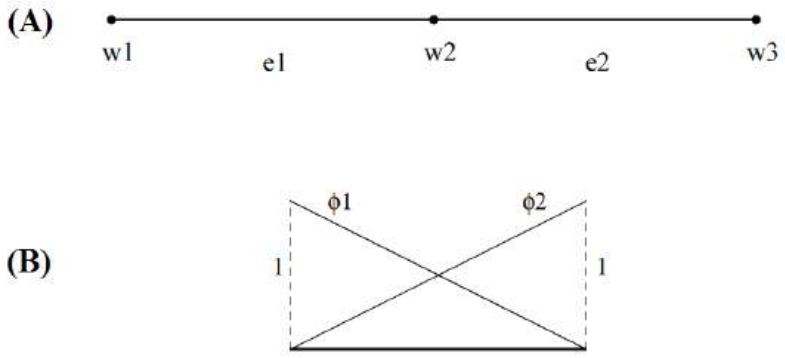

Fig. C.2. Definition of the element nodes (w) and the shape function. **(A)** Segmentation of the equation domain into finite elements (e). **(B)** Linear shape functions, ϕ_i, $i = \{1,2\}$ taking values between 0 and 1 in the 1-D element.

In the next step, shape functions are proposed. Here, they are simply assumed for each element as the linear functions ϕ_1 and ϕ_2, see Fig. C.2(B). From these shape functions, the basis functions ψ are built for each node of the domain.

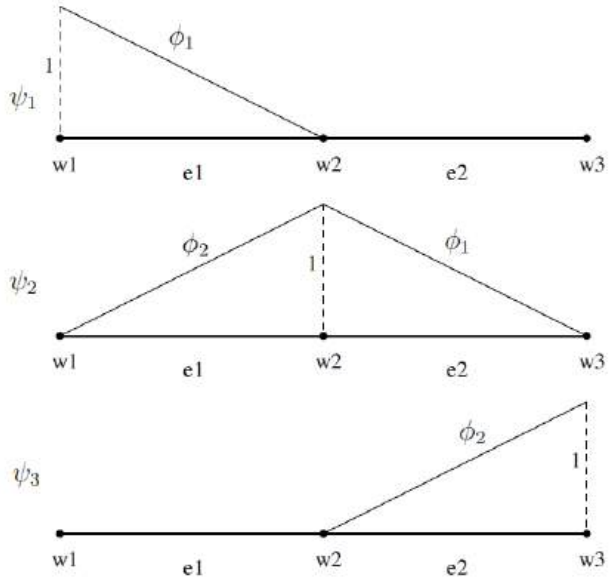

Fig. C.3. Explicit form of the basis functions in the FEM domain.

Each basis function ψ_i is attached to node w_i, where it takes the value of 1 and 0 in the other nodes. Those three basis functions ψ_1, ψ_2, and ψ_3 are drawn in Fig. C.3. The approximate solution of Eq. C.2.1 will be proposed as a certain linear combination of the basis functions,

$$u^h(x) = U_1^h \cdot \psi_1(x) + U_2^h \cdot \psi_2(x) + U_3^h \cdot \psi_3(x), \tag{C.2.2}$$

which can be interpreted as a vector in a 3-dimensional space, $u^h(x) \in V^h = \{U_1^h, U_2^h, U_3^h\}$. Note that U_i^h are values of u^h at the position of the node, w_i.

The partial differential equation (PDE) C.2.1 will now be transformed into an approximated integral form:

$$-\int_0^1 dx \left(\frac{\partial u^h}{\partial x} \cdot \frac{\partial w}{\partial x} \right) = \int_0^1 dx \, (2 \cdot w(x)) - 2 \cdot w(1). \tag{C.2.3}$$

The problem is thus reformulated to fulfill the requirement of finding the unknown function $u^h(x)$ in the form given by Eq. C.2.2. Currently, the boundary condition $u^h(0) = 0$ is satisfied and $u^h(x)$ satisfies for any test function belonging to the same vector space $w(x) \in V^h$ that $w(x) = \sum_{l=1}^{3} W_l \cdot \psi_l(x)$ and $w(0) = 0$.

Both BCs taken previously are incorporated into the integral equation C.2.3, since the Dirichlet condition is included in the requirement $u^h(0) = 0$. The Neumann condition is forced by the form of the right hand side of Eq. C.2.3, because $\dfrac{\partial u}{\partial x}(x = 1) = 2$.

Since the unknown function $u^h(x)$ and the test functions $w(x)$ can be written as the linear combination of the basis functions,

$$u^h(x) = \sum_{k=1}^{3} U_k^h \cdot \psi_k(x), \qquad w(x) = \sum_{l=1}^{3} W_l \cdot \psi_l(x), \tag{C.2.4}$$

after substituting them into Eq. C.2.3 there arises a set of algebraic linear equations. In the case considered, these equations have the following form:

$$\sum_{k=1}^{3} A_{lk} \cdot U_k^h = F_l + B_l, \quad l = \{1,2,3\}, \tag{C.2.5}$$

where A_{lk} represents the matrix with two pointers:

$$A_{lk} = -\int_0^1 dx \left(\frac{\partial \psi_k}{\partial x} \cdot \frac{\partial \psi_l}{\partial x} \right), \quad k,l = \{1,2,3\}. \tag{C.2.6}$$

In this case, the vector F_l is equal to:

$$F_l = \int_0^1 dx \, (2 \cdot \psi_l(x)), \quad l = \{1,2,3\}, \tag{C.2.7}$$

while the complementary vector, B_l, carries the BCs and reads $B_l = [0, 0, -2]$. The solution to the FEM problem, the vector $[U_1^h \quad U_2^h \quad U_3^h]$ may be written as:

$$\begin{bmatrix} A_{11} & A_{12} & A_{13} \\ A_{21} & A_{22} & A_{23} \\ A_{31} & A_{32} & A_{33} \end{bmatrix} \cdot \begin{bmatrix} U_1^h \\ U_2^h \\ U_3^h \end{bmatrix} = \begin{bmatrix} F_1 \\ F_2 \\ F_3 \end{bmatrix} + \begin{bmatrix} B_1 \\ B_2 \\ B_3 \end{bmatrix}. \tag{C.2.8}$$

The general solution obtained can be implemented into a dedicated software such as ABAQUS/-CAE. The specific set of coefficients:

$$u^h(x) = 0.0 \cdot \psi_1(x) + 0.25 \cdot \psi_2(x) + 1.0 \cdot \psi_3(x) \tag{C.2.9}$$

is one of the accurate solutions to Eq. C.2.8. This approximate solution is illustrated in Fig. C.4 together with the explicit solution of Eq. C.2.1, $u(x) = x^2$.

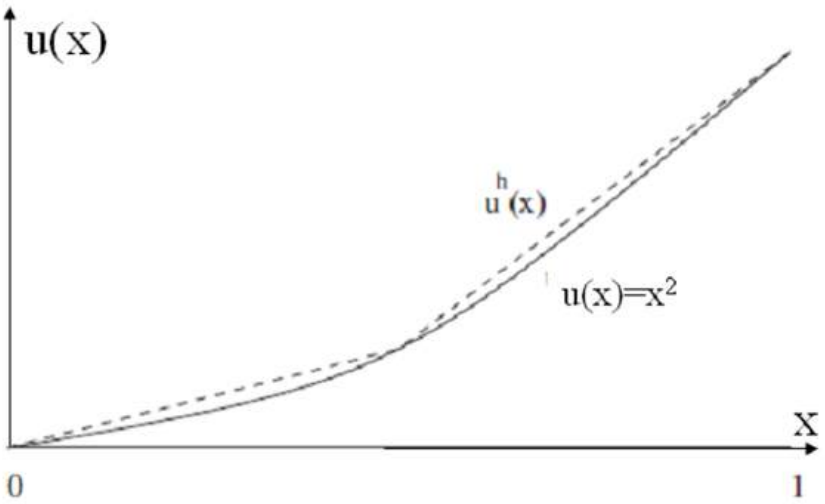

Fig. C.4. The accurate, $u(x)$ and the approximate, $u^h(x)$ solutions of the discussed FEM problem.

Appendix D.

Selected elements from theory of elasticity

This Section presents the general forms of the stress tensors corresponding to the most common types of mechanical loading, including hydrostatic compression, uniaxial compression, uniaxial tension, and simple shear. In addition, a detailed derivation of the Euler–Bernoulli beam equation is provided to describe the bending of a one-dimensional elastic beam under an external load.

D.1. General formulation of the stress and strain tensors

Figure D.1 illustrates the general geometry of a specimen used in a uniaxial tensile test. During such an experiment, it is assumed that the applied load acts exclusively along a single axis, resulting in a one-dimensional stress state without any shear components, lateral glides, or rotational deformation of the sample.

Fig. D.1. A metallic sample with characteristic neck used for tensile test. The mounting screws of the tensing machine are placed into the holes.

The description of material properties in more than one spatial dimension requires the use of tensor calculus. Zeroth-order tensors correspond to scalar quantities, whereas first-order tensors represent vector quantities. Second-order tensors, on the other hand, are used to describe properties of materials

in three-dimensional space. These tensors are mathematical objects invariant under coordinate system rotations and are typically represented as 3×3 matrices. An example of such a representation is given in Eq. D.1.1, where the coordinate indices correspond to $\{x \to x_1\,(1), y \to x_2\,(2), z \to x_3\,(3)\}$.

$$\hat{\sigma}_{ij} = \begin{bmatrix} \sigma_{11} & \sigma_{12} & \sigma_{13} \\ \sigma_{21} & \sigma_{22} & \sigma_{23} \\ \sigma_{31} & \sigma_{32} & \sigma_{33} \end{bmatrix} \tag{D.1.1}$$

When all principal components of the stress tensor are equal and the off-diagonal shear components vanish, the stress state corresponds to a hydrostatic (or isotropic) pressure, as illustrated in Fig. D.2.

$$\sigma_{ij} = \sigma \cdot \begin{bmatrix} 1 & 0 & 0 \\ 0 & 1 & 0 \\ 0 & 0 & 1 \end{bmatrix}$$

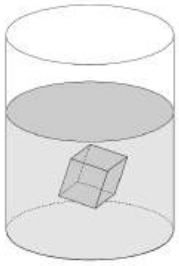

Fig. D.2. The principal tensor components are non-zero and the scalar, $\sigma = \sigma_{11} = \sigma_{22} = \sigma_{33}$ denotes the hydrostatic pressure.

Fig. D.3 contains the tensor that describes the uniaxial compressive stress. All the results reported in this dissertation were collected with this type of stress.

$$\sigma_{ij} = \sigma \cdot \begin{bmatrix} 0 & 0 & 0 \\ 0 & 0 & 0 \\ 0 & 0 & -1 \end{bmatrix}$$

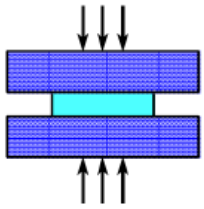

Fig. D.3. Stress tensor for compression of a sample along the axis marked as $z = x_3$.

The other two typical cases of stress, which are uniaxial tension and simple shear, are characterized in Figs. D.4 and D.5, respectively.

$$\sigma_{ij} = \sigma \cdot \begin{bmatrix} 0 & 0 & 0 \\ 0 & 0 & 0 \\ 0 & 0 & 1 \end{bmatrix}$$

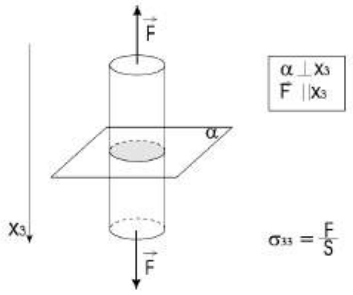

Fig. D.4. Uniaxial tension along the $z = x_3$ axis. S denotes the cross-sectional area of the sample.

When a material is elongated along one direction, characterized by the longitudinal strain ε_3, it undergoes simultaneous transverse contractions ε_1 and ε_2 in the perpendicular directions. The ratio between the transverse strain and the longitudinal strain defines the Poisson's ratio, ν, given by

$$\nu = -\frac{\varepsilon}{\varepsilon_3}, \qquad (|\varepsilon_1| = |\varepsilon_2| \equiv \varepsilon),$$

where the negative sign reflects that elongation in one direction is accompanied by contraction in the others. The Poisson's ratio typically lies within the range $-1 < \nu < 0.5$. For most isotropic materials, ν ranges from 0.2 to 0.4, while negative values correspond to *auxetic* materials, such as certain polymeric foams, which expand laterally when stretched.

$$\sigma_{ij} = \sigma \cdot \begin{bmatrix} 0 & 1 & 0 \\ 1 & 0 & 0 \\ 0 & 0 & 0 \end{bmatrix}$$

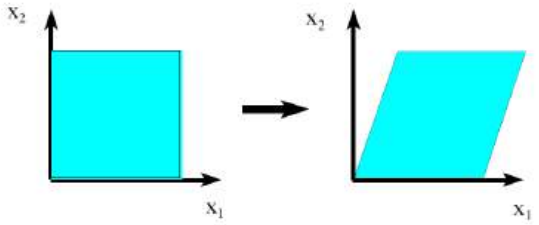

Fig. D.5. The sample in the form of a square is fixed in the origin. Shearing causes a unit cube to deform into a parallelogram.

In a general case, the stress and strain components acting in all directions must be considered. This leads to formulating the stiffness, $\hat{C}_{sutw}$ and compliance, $\hat{S}_{sutw}$ tensors. They are both 4^{th} order tensors since each of their matrix elements possess 4 pointers:

$$\sigma_{su} = \hat{C}_{sutw} \cdot \varepsilon_{tw} \tag{D.1.2}$$

$$\varepsilon_{su} = \hat{S}_{sutw} \cdot \sigma_{tw} \tag{D.1.3}$$

The compliance and stiffness tensors are not mutually reversible $\hat{S}_{sutw} \neq \dfrac{1}{\hat{C}_{sutw}}$, since they are defined with respect to different experiments. The stiffness tensor, $\hat{C}_{sutw}$ refers to the situation where

the stimulus of origin is strain, ε_{tw} and the material responds with the stress, σ_{su}. The compliance tensor, $\hat{S}_{sutw}$ describes the experiment, where the applied stress, σ_{tw} invokes strain, ε_{su}. This short summary of the most important definitions in the field of material science was prepared based on the scripts of Prof. K. Wierzbanowski LINK .

D.2. Derivation of the deforming force in a flat rectangular tile

Knowing the distribution of the forces moments along the beam, the form of the shape function $w(x)$ and the extremum value at its center $w(x) \to w\left(\frac{L_b}{2}\right) \equiv w_{max}$ can be calculated. The Bernoulli-Euler theory of bending a one-dimensional beam was applied with the following assumptions:

1. The decimated length of the beam is greater than or similar to the thickness and width of the beam, $\frac{L_b}{10} \gtrsim T_b \approx B_b$.

2. The force $\underline{\mathbf{F}}$ is concentrated and constant and the cross section of the beam, $B_b \cdot T_b$ is invariant due to that force.

3. The beam is uniformly dense and its surface density reads $\Sigma = \frac{dm}{dy \cdot dz}$.

The boundary conditions for the position coordinates of the points A, B, and C of Fig. 2.7 are:

$$A: \quad x = 0 \tag{D.2.4}$$

$$B: \quad x = x_F \tag{D.2.5}$$

$$C: \quad x = L_b \tag{D.2.6}$$

Taking $\varepsilon := \frac{x_F}{L_b}$ as the dimensionless length and defining $\varepsilon \in (0,1)$, the reactions at points A and C read, respectively:

$$F_A = F \cdot \frac{L_b - x_F}{L_b} = F \cdot (1 - \varepsilon) \tag{D.2.7}$$

$$F_C = F \cdot \frac{x_F}{L_b} = F \cdot \varepsilon. \tag{D.2.8}$$

They contribute to the moments of forces written in the following form:

$$M_{AB}(x) = F_A \cdot x = F \cdot (1 - \varepsilon) \cdot x \tag{D.2.9}$$

$$M_{BC}(x) = F_C \cdot (L_b - x) = F \cdot \varepsilon \cdot (L_b - x). \tag{D.2.10}$$

I_y is the geometric moment of inertia [m^4] with respect to the y axis, which belongs to the beam plane. The surface element, dA is defined in this cross section as the product of the steps on the axes y and z, so $dA = dy \cdot dz$.

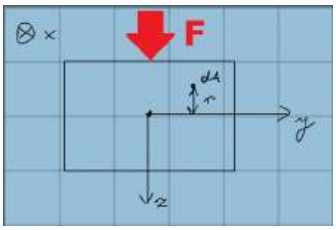

The radius of rotation along the y axis is equal to the absolute value of $|z| = r$ and is always perpendicular to it, $r \perp y$. The integration $I = \iint dAr^2$ is executed using the theorem of integrating an even polynomial over a symmetric range, which is equal to a doubled integral from 0 to the absolute end of that range.

$$I_y = \int_{-B_b/2}^{B_b/2} dy \int_{-t_b/2}^{t_b/2} dz\ z^2 = [y]_{-B_b/2}^{B_b/2} \cdot \left[\frac{z^3}{3}\right]_{-t_b/2}^{t_b/2} = B_b \cdot 2 \cdot \left[\frac{z^3}{3}\right]_0^{t_b/2} = B_b \cdot 2 \cdot \frac{t_b^3}{3 \cdot 8} = \frac{B_b t_b^3}{12}.$$

If $w(x)$ is the shape function that describes the bending of a beam at point x, the curvature of that bending, $\rho(x)$ can be written as:

$$\frac{M(x)}{E \cdot I_y} = \frac{1}{\rho(x)} = \frac{|w"(x)|}{[1 + (w'(x))^2]^{\frac{3}{2}}} \to |w''(x)|. \tag{D.2.11}$$

Putting $w'(x) \cong 0$ in Eq. D.2.11 enforces that the moment of force dependent on the position is positive:

$$-\frac{M(x)}{E \cdot I_y} = w''(x) \tag{D.2.12}$$

$$-E \cdot I_y \cdot w''(x) = M(x). \tag{D.2.13}$$

This condition is applied to the dependencies given by Eq. D.2.10, and the boundary conditions (BCs) for the equilibrium of the beam are formulated. Since the expression for the second derivative is the polynomial of positive and integer order, the integration is explicit. $D_1, D_2, D_3, D_4 \in \mathbb{R}$ are real integration constants, respectively. This has for segment AB the following form:

$$\begin{cases} -E \cdot I_y \cdot w''_{AB}(x) & = F \cdot (1 - \varepsilon) \cdot x = M_{AB}(x) \\ -E \cdot I_y \cdot w'_{AB}(x) & = F \cdot (1 - \varepsilon) \cdot \dfrac{x^2}{2} + D_1 \\ -E \cdot I_y \cdot w_{AB}(x) & = F \cdot (1 - \varepsilon) \cdot \dfrac{x^3}{6} + D_1 \cdot x + D_2, \end{cases} \tag{D.2.14}$$

and for the segment BC:

$$\begin{cases} -E \cdot I_y \cdot w''_{BC}(x) & = F \cdot \varepsilon \cdot (L_b - x) = M_{BC}(x) \\ -E \cdot I_y \cdot w'_{BC}(x) & = F \cdot \varepsilon \cdot \left(-\dfrac{(L_b - x)^2}{2} \right) + D_3 \\ -E \cdot I_y \cdot w_{BC}(x) & = F \cdot \varepsilon \cdot \dfrac{(L_b - x)^3}{6} + D_3 \cdot x + D_4. \end{cases} \tag{D.2.15}$$

The shape function takes 0 at the ends of the beam, so the following BCs must be satisfied:

$$w_{AB}(0) = 0 \quad \longrightarrow \quad D_2 = 0 \quad \Rightarrow \quad -E \cdot I_y \cdot w_{AB}(x) = F \cdot (1 - \varepsilon) \cdot \frac{x^3}{6} + D_1 \cdot x$$

$$w_{BC}(L_b) = 0 \quad \longrightarrow \quad D_3 \cdot L_b + D_4 = 0 \quad \Rightarrow \quad -E \cdot I_y \cdot w_{BC}(x) = F \cdot \varepsilon \cdot \frac{(L_b - x)^3}{6} - D_3 \cdot (L_b - x)$$

For uniform deformation, the shape function must have the same values in the center, since the beam as a continuous medium is supported, so the calculated BCs lead to the following sewing constraint:

$$\begin{aligned} (1)\ w_{AB}(\varepsilon L_b) = w_{BC}(\varepsilon L_b) \Longrightarrow \cancel{F \cdot (1-\varepsilon) \cdot \varepsilon L_b} \left(\frac{\varepsilon^2 L_b^2}{6} + D_1 \right) &= \cancel{F \cdot \varepsilon \cdot (L_b - \varepsilon L_b)} \left(\frac{(L_b - \varepsilon L_b)^2}{6} - D_3 \right) \quad \Big| \cdot 6 \\ \varepsilon^2 L_b^2 + 6 \cdot D_1 &= L_b^2 \cdot (1-\varepsilon)^2 - 6 \cdot D_3 \\ 6 \cdot (D_1 + D_3) &= L_b^2 \cdot \left[(1-\varepsilon)^2 - \varepsilon^2 \right] \\ D_1 + D_3 &= \frac{L_b^2}{6} \cdot (1 - 2\varepsilon). \end{aligned}$$

Beyond that, the first derivatives of the shape functions that express the deformation gradients must agree at the point of equilibrium:

$$\begin{aligned} (2)\ w'_{AB}(\varepsilon L_b) = w'_{BC}(\varepsilon L_b) \Longrightarrow F \cdot (1-\varepsilon) \cdot \frac{\varepsilon^2 L_b^2}{2} + D_1 &= -F \cdot \varepsilon \cdot \frac{L_b^2 \cdot (1-\varepsilon)^2}{2} + D_3 \\ D_1 - D_3 &= -F \cdot \varepsilon \cdot (1-\varepsilon) \cdot \frac{L_b^2}{2} \cdot [1 - \varepsilon + \varepsilon] \\ D_1 - D_3 &= -F \cdot \varepsilon \cdot (1-\varepsilon) \cdot \frac{L_b^2}{2}. \end{aligned}$$

If x_F denotes the point of the interacting force, from the supporting conditions this force is compensated by the reactions at points A and C, $F_A = F_C = \dfrac{1}{2} \cdot F$, respectively. This determines that point B lies symmetrically on the AC segment and is parameterized as follows:

$$\begin{cases} D_1 + D_3 = \dfrac{L_b^2}{6} \cdot (1 - 2\varepsilon) \\ D_1 - D_3 = -F \cdot \varepsilon \cdot (1-\varepsilon) \cdot \dfrac{L_b^2}{2} \end{cases} \quad \Longrightarrow \varepsilon \equiv \frac{1}{2} \rightarrow \quad \begin{cases} D_1 = -\dfrac{L_b^2}{16} \cdot F \\ D_2 = 0 \\ D_3 = \dfrac{L_b^2}{16} \cdot F \\ D_4 = -L_b \cdot D_3 = -\dfrac{L_b^3}{16} \cdot F \end{cases} \tag{D.2.16}$$

Thus, the shape function was optimized:

$$w_{max} = w_{AB}\left(\frac{L_b}{2}\right) = w_{BC}\left(\frac{L_b}{2}\right) = \frac{F \cdot \left(1 - \frac{1}{2}\right) \cdot \frac{L_b^3}{6 \cdot 8} - F \cdot \frac{L_b^2 \cdot L_b}{16 \cdot 2}}{-E \cdot I_y} =$$
$$= \frac{F \cdot L_b^3}{E \cdot I_y} \cdot \left(\frac{1 \cdot 3}{32 \cdot 3} - \frac{1}{96}\right) = \frac{F \cdot L_b^3}{E \cdot I_y} \cdot \left(\frac{2}{96}\right) = \frac{F \cdot L_b^3}{48 \cdot E \cdot I_y}.$$

After substituting I_y, the maximal deformation reads $w_{max} = \frac{F \cdot L_b^3}{48 \cdot E \cdot I_y} = \frac{F \cdot L_b^3}{48 \cdot E} \cdot \frac{12}{B_b \cdot t_b^3} = \frac{F \cdot L_b^3}{4 \cdot E \cdot B_b \cdot t_b^3}$. However, w_{max} depended on the pitch of the screw, P and the rotation angle of the screw, α through the relationship, $w_{max} = P \cdot \alpha$. Eventually, the central force bending the material can be expressed as

$$F = \frac{4 \cdot E \cdot B_b \cdot t_b^3 \cdot w_{max}}{L_b^3} = \frac{4 \cdot E \cdot B_b \cdot t_b^3 \cdot P \cdot \alpha}{L_b^3}. \tag{D.2.17}$$

quod erat demonstrandum (q.e.d.)

Appendix E.

Details of processing the DFXM results and the Orange3 "darfix" add-on

The DFXM imaging with the currently available resolution generates huge amounts of data. The acquisition and storage of these data require tremendous memory resources, while computational power is required to process them, such as that achieved by GPUs with tens of GB of RAM. In this experiment, the number of steps for any varying motor ranged between 10 and 45. Thus, one set of data for a consisted of some 450 scans and each scan composed of 2160 x 2560 individual intensities in all pixels, giving 11 MB size per scan.

The collected DFXM images were processed and analyzed using the Orange3 software dedicated to data science and machine learning. One of the ESRF groups developed an Orange3 add-on called "darfix", dedicated specifically to handle DFXM data [3]. Darfix is a Python package that involves the import, the pre-processing, and calculation of the grain plots, such as mosaicity or the statistical distributions, i.e. center-of-mass (CoM), full width at half maximum (FWHM), skewness, and kurtosis. The abbreviated schematic for processing the DFXM data with darfix is presented in Fig. E.1. The live link to the project is available HERE .

In the import stage, the data path is chosen and the output directory is defined to save the metadata obtained during the consecutive stages of calculations. Then, all the acquired scans are imported into the workflow. Their number is equal to the product between the number of steps for the varying motors, which were χ and μ for the mosaicity maps or μ and 2θ for the strain scans. These parameters can be extracted in a partially automated way, but to avoid malfunctioning of the software in the next stages of operation, it is strongly advised to cross-check these values in this

widget.

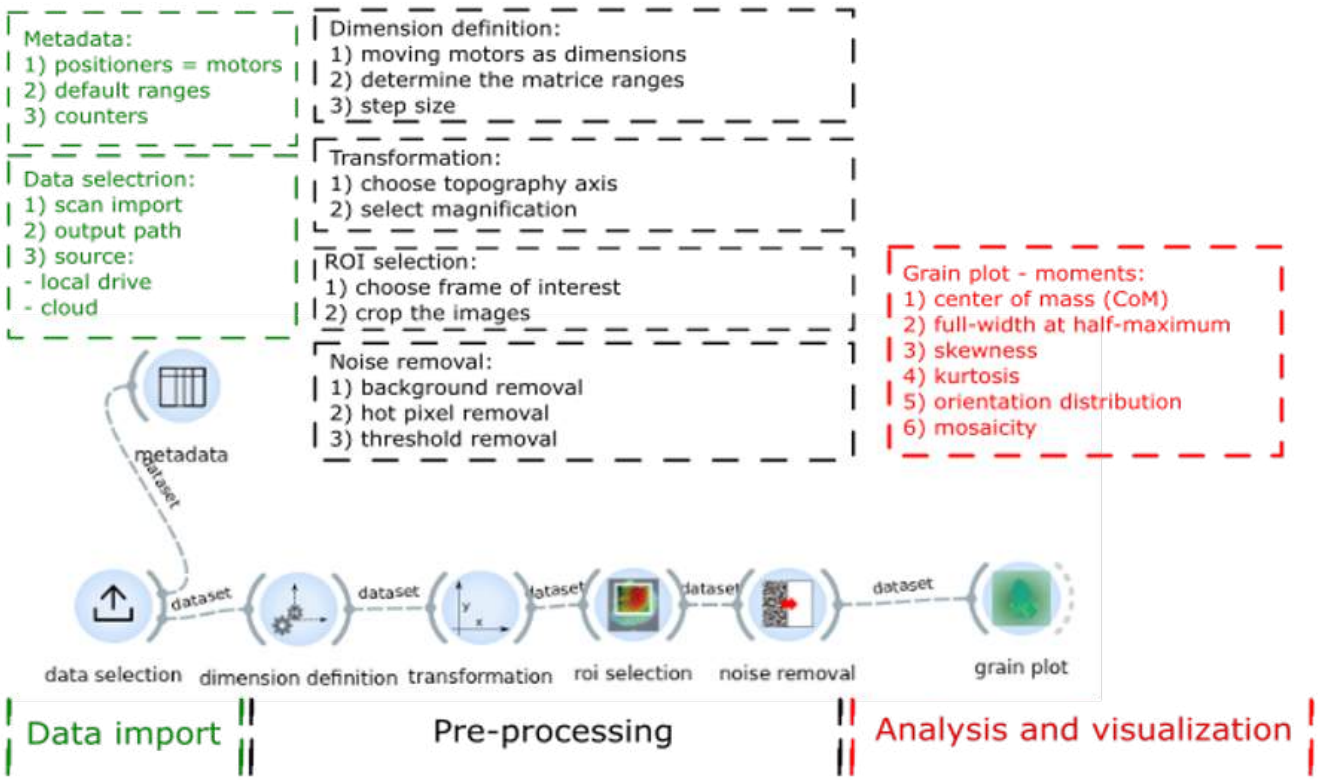

Fig. E.1. The workflow built with the darfix add-on in the Orange3 data analysis software. The analysis of the dataset starts with importing the raw data and checking the ranges of the varying motors in the metadata widget. Next, in the preprocessing stage, the dimensions and the magnification for the data are defined. Subsequently, cropping of the images to the selected Region of Interest ("roi selection" widget) and denoising ("noise removal" widget) are performed. Finally, the corresponding statistics are determined from the preprocessed images. Here, only the center-of-mass and mosaicity with the orientation distribution were computed. The results of these calculations can be further exported into most commonly utilized numeric or graphical formats, such as .csv, .py, .dat, .png, or .tiff. Adapted from [3].

In preprocessing, the horizontal topography (imaging axis in the y-direction) was defined along with choosing the magnification of the objective, where $M_x = 10\times$ was used. In the next step, the analyzed region of interest (ROI) was chosen and the data was cropped to the selected ROI. This reduced memory usage and saved computation time by excluding pixels that were out of the sample range and remained dark in every scan. The final step of the preprocessing involved applying the median filter, subtracting the background, removing the hot pixels that were artifacts that appeared due to instrumental errors outside of the sample area, and eventually determining the optimal

threshold for extracting features.

The "grain plot" widget ran the calculation of moments. During that, an individual rocking curve was fitted to every detector pixel for each pair of moving motors (μ, χ). Thus, the grain plots demonstrated the spatial distribution of the characteristic Gaussian magnitudes, such as the center of the rocking curve (CoM).

Mosaicity is a texture map that represents the respective misorientation of the adjacent parts of the crystal. It is obtained by numerical convolution of the CoM maps for the rocking angle μ and the rolling angle χ and must be decoded with the key hue saturation value (HSV) color scale reflecting the deviation from the optimal Bragg condition (μ_{opt}, χ_{opt}) in the 2D phase space (μ, χ). The most frequent intensities are integrated as isolines in the contour plot of the orientation distribution.

The determination of the axial strain component, ε_{zz} required the export of CoM maps for the objective pitch angle (2θ) into the .h5 numeric format. The linear intensity gradient was then found and subtracted from the image. Subsequently, the values of 2θ were recalculated into the values of the varying interplanar distance, d corresponding to the axial strain component, $\varepsilon_{33} = \frac{\Delta d}{d_0} = -\frac{1}{2} \cdot \frac{\Delta(2\theta)}{\tan(\theta)}$. If after this procedure artificial strain values still appeared outside the sample region, they were excluded from the image with an arbitrarily selected threshold.

The plots of CoM and mosaicity and the post-processing of CoM-2θ into the axial strain ε_{zz} were completed with self-developed Python scripts. An example script in the form of a Jupyter notebook is presented below.

gh8tbbvuz

August 13, 2025

1 importing libraries and directory paths

input: path to maps.h5 file

[1]:
```
import h5py
import numpy as np
import pandas as pd
import matplotlib as mpl
import matplotlib.pyplot as plt
import matplotlib.patches as patches
from scipy import stats
from matplotlib.ticker import StrMethodFormatter
from matplotlib.gridspec import GridSpec
from mpl_toolkits.axes_grid1.inset_locator import inset_axes, mark_inset

i = 25
layer_dict = {0: "00", 1: "01", 2: "02", 3: "03", 4: "04", 5: "05", 6: "06", 7:␣
↪"07", 8: "08", 9: "09", 10: "10",
              11: "11", 12: "12", 13: "13", 14: "14", 15: "15", 16: "16", 17:␣
↪"17", 18: "18", 19: "19", 20: "20",
              21: "21", 22: "22", 23: "23", 24: "24", 25: "25"}
print(layer_dict[i])

smz_dict = {0: "-0.1767 mm", 1: "-0.1687 mm", 2: "-0.1607 mm", 3: "-0.1527 mm",␣
↪4: "-0.1447 mm", 5: "-0.1367 mm", 6: "-0.1287 mm",
            7: "-0.1207 mm", 8: "-0.1127 mm", 9: "-0.1047 mm", 10: "-0.0967␣
↪mm", 11: "-0.0887 mm", 12: "-0.0807 mm", 13: "-0.0727 mm",
            14: "-0.0647 mm", 15: "-0.0567 mm", 16: "-0.0487 mm", 17: "-0.0407␣
↪mm", 18: "-0.0327 mm", 19: "-0.0247 mm", 20: "-0.0167 mm",
            21: "-0.0087 mm", 22: "-0.0007 mm", 23: "+0.0073 mm", 24: "+0.0153␣
↪mm", 25: "+0.0233 mm"}
print(smz_dict[i])

mosa_path = ("./_RT_layer_" + layer_dict[i] + "/mosa/maps.h5")
strain_path = ("./_RT_layer_" + layer_dict[i] + "/strain/maps.h5")
output_path = ("D:/Downloads/mat_met-images/DFXM/brokenP/")
```



```
mu_boundary = 0.05
chi_boundary = 0.07
str_boundary = 4.5e-04
threshold = -str_boundary

leg_bar = [1.15, 0.35]
```

25
+0.0233 mm

1.1 CoM for diffry (mu)

[2]:
```
with h5py.File(mosa_path, "r") as h5file:
    data = np.array(h5file.get(str('entry/diffry/Center of mass/Center of␣
↪mass')))
    h5file.close()

    print('Pixels in the image along width: %d, height: %d' % (data.shape[1],␣
↪data.shape[0]))
    leg_pos = (int(leg_bar[1] * data.shape[1]), int(leg_bar[0] * data.shape[0]))

    com_min_mu = np.nanmin(data)
    com_cen_mu = np.nanmean(data)
    com_max_mu = np.nanmax(data)
    df_mu = pd.DataFrame([{'min_mu': com_min_mu, 'cen_mu': com_cen_mu, 'max_mu':
↪ com_max_mu}])
    print(df_mu)

    # standard colormaps diffry - BuPu, chi - YlGn, phi - BrBG
    im  = plt.imshow(data, cmap=plt.cm.BuPu, vmin=com_cen_mu - mu_boundary,␣
↪vmax=com_cen_mu + mu_boundary)
    plt.title('RT_bknP_rm_cs_' + layer_dict[i] + ', difftz=' + smz_dict[i] +␣
↪r', CoM $\mu$')
    plt.axis('off')
    plt.text(leg_pos[0], 0.95 * leg_pos[1], r'10 $\bf{\mu}$m', color='gray',␣
↪fontsize=16, fontweight='semibold')
    rect = patches.Rectangle(leg_pos, 276, 15, linewidth=1, edgecolor='gray',␣
↪facecolor='gray', clip_on=False)
    im.axes.add_patch(rect)

    cbar = plt.colorbar(im, orientation='vertical', format='%.3f', shrink=0.50,␣
↪label=r'$\mu - \mu_{opt}$ [$\degree$]')
    cbar.ax.yaxis.label.set_rotation(-90)
    cbar.ax.yaxis.label.set_fontsize(16)
    cbar.ax.minorticks_on()
```



```
    cbar.set_ticks(np.linspace(com_cen_mu - mu_boundary, com_cen_mu +␣
↪mu_boundary, 5, endpoint=True))
    ticks = np.round(np.linspace(-mu_boundary, mu_boundary, 5, endpoint=True),␣
↪3)
    cbar.set_ticklabels([f"{val}{' ' * 4}" for val in ticks])
    cbar.ax.tick_params(labelsize=16)

    plt.savefig(output_path + 'com_diffry_layer.png', bbox_inches='tight',␣
↪dpi=300)
    plt.show()
```

```
C:\Users\mateusz1996a\AppData\Local\Temp\ipykernel_13472\1880076973.py:2:
DeprecationWarning: `product` is deprecated as of NumPy 1.25.0, and will be
removed in NumPy 2.0. Please use `prod` instead.
  data = np.array(h5file.get(str('entry/diffry/Center of mass/Center of mass')))
```

```
Pixels in the image along width: 2000, height: 1300
   min_mu   cen_mu  max_mu
0  7.8111  7.83941  8.0111
```

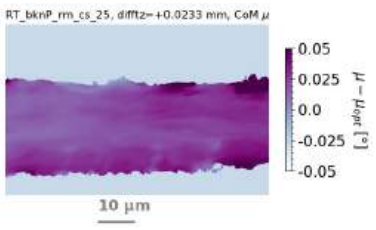

1.2 CoM for chi

[3]:
```
with h5py.File(mosa_path, "r") as h5file:
    data = np.array(h5file.get(str('entry/chi/Center of mass/Center of mass')))
    h5file.close()
```



```
    print('Pixels in the image along width: %d, height: %d' % (data.shape[1],␣
↪data.shape[0]))
    leg_pos = (int(leg_bar[1] * data.shape[1]), int(leg_bar[0] * data.shape[0]))

    com_min_chi = np.nanmin(data)
    com_cen_chi = np.nanmean(data)
    com_max_chi = np.nanmax(data)
    df_chi = pd.DataFrame([{'min_chi': com_min_chi, 'cen_chi': com_cen_chi,␣
↪'max_chi': com_max_chi}])
    print(df_chi)

    # standard colormaps diffry - BuPu, chi - YlGn, phi - BrBG
    im  = plt.imshow(data, cmap=plt.cm.YlGn, vmin=com_cen_chi - chi_boundary,␣
↪vmax=com_cen_chi + chi_boundary)
    plt.title('RT_bknP_rm_cs_' + layer_dict[i] + ', difftz=' + smz_dict[i] +␣
↪r', CoM $\chi$')
    plt.axis('off')
    plt.text(leg_pos[0], 0.95 * leg_pos[1], r'10 $\bf{\mu}$m', color='gray',␣
↪fontsize=16, fontweight='semibold')
    rect = patches.Rectangle(leg_pos, 276, 15, linewidth=1, edgecolor='gray',␣
↪facecolor='gray', clip_on=False)
    im.axes.add_patch(rect)

    cbar = plt.colorbar(im, orientation='vertical', format='%.3f', shrink=0.50,␣
↪label=r'$\chi - \chi_{opt}$ [$\degree$]')
    cbar.ax.yaxis.label.set_rotation(-90)
    cbar.ax.yaxis.label.set_fontsize(16)
    cbar.ax.minorticks_on()
    cbar.set_ticks(np.linspace(com_cen_chi - chi_boundary, com_cen_chi +␣
↪chi_boundary, 5, endpoint=True))
    ticks = np.round(np.linspace(-chi_boundary, chi_boundary, 5,␣
↪endpoint=True), 3)
    cbar.set_ticklabels([f"{val}{' ' * 4}" for val in ticks])
    cbar.ax.tick_params(labelsize=16)

    plt.savefig(output_path + 'com_chi_layer.png', bbox_inches='tight', dpi=300)
    plt.show()
```

```
C:\Users\mateusz1996a\AppData\Local\Temp\ipykernel_13472\3038616545.py:2:
DeprecationWarning: `product` is deprecated as of NumPy 1.25.0, and will be
removed in NumPy 2.0. Please use `prod` instead.
  data = np.array(h5file.get(str('entry/chi/Center of mass/Center of mass')))
```

```
Pixels in the image along width: 2000, height: 1300
   min_chi   cen_chi   max_chi
0  3.394987  3.430945  3.544987
```

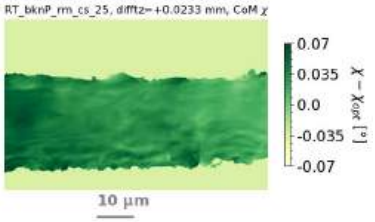

2 Orientation distribution

[4]:
```
# IMPORTANT METHODS of NumPy: rot90, flipud, fliphr
# Orientation distribution --> ori_dist
# list_curves = h5file.get(str('entry/Orientation distribution/curves')).keys()

with h5py.File(mosa_path, "r") as h5file:

    ori_dist_key = h5file.get(str('entry/Orientation distribution/key'))
    ori_dist_ogn = h5file.get(str('entry/Orientation distribution/
↪key'))["origin"][:]
    ori_dist_cvs = []
    for cur in h5file.get(str('entry/Orientation distribution/curves')):
        ori_dist_cvs.append(str(cur))
    image = np.flipud(np.array(ori_dist_key["image"]))

    plt.title('RT_bknP_rm_cs_' + layer_dict[i] + ', difftz=' + smz_dict[i] +␣
↪r', orientation distribution')
    plt.tick_params(axis='both', which='major', labelsize=18)
    plt.box('False')
    plt.xlabel(r'$\chi$ [$\degree$]', fontsize=24)
    plt.ylabel(r'$\mu$ [$\degree$]', fontsize=24)

    for cur in ori_dist_cvs:
```



```
        pts = h5file.get(str('entry/Orientation distribution/curves/' +␣
↪cur))["points"][:]
        cls = h5file.get(str('entry/Orientation distribution/curves/' +␣
↪cur))["color"][:]
        plt.plot(pts[0][:], pts[1][:], color=mpl.colors.rgb2hex(cls/255))

    xmin, xmax = plt.xlim()
    ymin, ymax = plt.ylim()
    im = plt.imshow(image, extent=[xmin, xmax, ymin, ymax])

    h5file.close()

    plt.savefig(output_path + 'ori_dist_layer.png', bbox_inches='tight',␣
↪dpi=300)
    plt.show()
```

```
C:\Users\mateusz1996a\AppData\Local\Temp\ipykernel_13472\1260563502.py:12:
DeprecationWarning: `product` is deprecated as of NumPy 1.25.0, and will be
removed in NumPy 2.0. Please use `prod` instead.
  image = np.flipud(np.array(ori_dist_key["image"]))
```

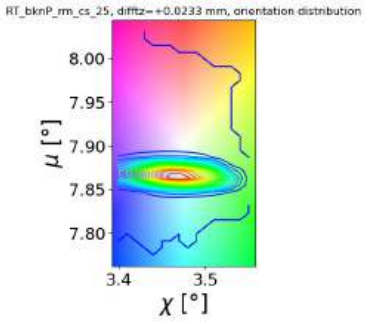

2.1 Mosaicity map

[5]:
```
with h5py.File(mosa_path, "r") as h5file:
    data = np.array(h5file.get(str('entry/Mosaicity/Mosaicity')))
    h5file.close()

    print('Pixels in the image along width: %d, height: %d' % (data.shape[1],␣
↪data.shape[0]))
    leg_pos = (int(leg_bar[1] + data.shape[1]), int(leg_bar[0] + data.shape[0]))

    plt.title('RT_bknP_rm_cs_' + layer_dict[i] + ', smz=' + smz_dict[i] + r',␣
↪Mosaicity', fontsize=16)

    im = plt.imshow(data)
    plt.axis('off')
    plt.text(leg_pos[0], 0.95 * leg_pos[1], r'10 $\bf{\mu}$m', color='gray',␣
↪fontsize=16, fontweight='semibold')
    rect = patches.Rectangle(leg_pos, 276, 15, linewidth=1, edgecolor='gray',␣
↪facecolor='gray', clip_on=False)
    im.axes.add_patch(rect)

    plt.tight_layout()
    plt.savefig(output_path + 'mosaicity_layer.png', bbox_inches='tight',␣
↪dpi=300)
    plt.show()
```

```
C:\Users\mateusz1996a\AppData\Local\Temp\ipykernel_13472\3202385374.py:2:
DeprecationWarning: `product` is deprecated as of NumPy 1.25.0, and will be
removed in NumPy 2.0. Please use `prod` instead.
  data = np.array(h5file.get(str('entry/Mosaicity/Mosaicity')))
```

```
Pixels in the image along width: 2000, height: 1300
```


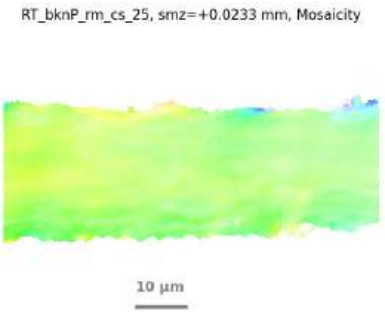

2.2 CoM for 2theta (obpitch) and strain map corrected wrt. the linear background

[6]:
```
with h5py.File(strain_path, "r") as h5file:
    data = np.array(h5file.get(str('entry/obpitch/Center of mass/Center of␣
↪mass')))
    data = data[850:1650][:]
    h5file.close()

    print('Pixels in the image along width: %d, height: %d' % (data.shape[1],␣
↪data.shape[0]))
    leg_pos = (int(leg_bar[1] + data.shape[1]), int(leg_bar[0] + data.shape[0]))

    data_2th_mean = np.nanmean(data)
    print(data_2th_mean)

    corrected_data = np.zeros(data.shape)
    corrected_data[:,:] = np.NaN
```

```
    # Looking for a linear gradient over the image
    ind_y = np.asarray(range(0, data.shape[1], 1))
    for j in ind_y:
        ind_x = np.asarray(range(- data.shape[0] // 2, data.shape[0] // 2, 1))
        data_y = data[:, j]
        n_NaN_indices = ~np.isnan(data_y)
        if any(idx != False for idx in n_NaN_indices):
            slope, intercept, r_val, p_val, std_err = stats.
↪linregress(ind_x[n_NaN_indices], data_y[n_NaN_indices])
            corrected_data[:, j] = data_y - (slope * ind_x)

    corr_mean = np.nanmean(corrected_data)
    print(corr_mean)

    strain_data = - (1 / 2) * (np.sin(np.deg2rad(data_2th_mean - data))) / (np.
↪tan(np.deg2rad(data_2th_mean / 2)))
    corrected_strain_data = - (1 / 2) * (np.sin(np.deg2rad(corr_mean -␣
↪corrected_data))) / (np.tan(np.deg2rad(corr_mean / 2)))

    # Now, set values to NaN where the threshold signal is too intense
    corrected_strain_data[corrected_strain_data < threshold] = np.NaN

    str_min_eps = np.nanmin(corrected_strain_data)
    str_cen_eps = np.nanmean(corrected_strain_data)
    str_max_eps = np.nanmax(corrected_strain_data)
    df_eps = pd.DataFrame([{'min_eps': str_min_eps, 'cen_eps': str_cen_eps,
                            'max_eps': str_max_eps, 'avg_2th': data_2th_mean}])

    print(df_eps)

    im = plt.imshow(corrected_strain_data, cmap=plt.cm.seismic_r,␣
↪vmin=-str_boundary, vmax=str_boundary)
    plt.title('RT_bknP_rm_cs_' + layer_dict[i] + ', smz=' + smz_dict[i] + r',␣
↪$\varepsilon$')
    plt.axis('off')
    plt.text(leg_pos[0], 0.95 * leg_pos[1], r'10 $\bf{\mu}$m', color='gray',␣
↪fontsize=16, fontweight='semibold')
    rect = patches.Rectangle(leg_pos, 276, 15, linewidth=1, edgecolor='gray',␣
↪facecolor='gray', clip_on=False)
    im.axes.add_patch(rect)

    cbar = plt.colorbar(im, orientation='vertical', format='%.3f', shrink=0.50,␣
↪label=r'strain, $\varepsilon$ [$\times 10^{-4}$]')
    cbar.ax.yaxis.label.set_rotation(-90)
    cbar.ax.yaxis.label.set_fontsize(16)
```



```
    cbar.ax.minorticks_on()
    ticks = np.linspace(-str_boundary, str_boundary, 5, endpoint=True)
    cbar.set_ticks(ticks)
    ticks = np.round(1e4 * ticks, 1)
    cbar.set_ticklabels([f"{val}{' ' * 4}" for val in ticks])
    cbar.ax.tick_params(labelsize=16)

    plt.savefig(output_path + 'str_2th_layer.png', bbox_inches='tight', dpi=300)
    plt.show()
```

```
C:\Users\mateusz1996a\AppData\Local\Temp\ipykernel_13472\3066531969.py:2:
DeprecationWarning: `product` is deprecated as of NumPy 1.25.0, and will be
removed in NumPy 2.0. Please use `prod` instead.
  data = np.array(h5file.get(str('entry/obpitch/Center of mass/Center of
mass')))

Pixels in the image along width: 2000, height: 800
20.034370792302486
20.03437554357262
   min_eps   cen_eps   max_eps    avg_2th
0 -0.00045  0.000238  0.001562  20.034371
```

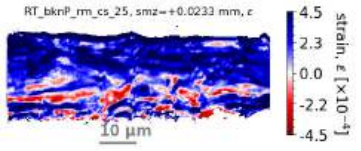


```
[ ]:
```

Appendix F.

Supplementary results of resistivity, magnetic susceptibility and XAS under uniaxial pressure

This Appendix presents supplementary results from the uniaxial compression experiments conducted on various samples of stoichiometric magnetite, as discussed in Chapter 5. The influence of uniaxial stress on electrical resistivity (ρ_{AC}), magnetic susceptibility (χ_{AC}), and X-ray absorption spectroscopy (XAS) was analyzed in Sections 5.1, 5.2, and 5.3 of Chapter 5, respectively. In the present Appendix, the results are organized according to the individual samples examined and the crystallographic direction along which uniaxial compression was applied.

Similarly to Chapter 5, the samples analyzed in this Appendix were labeled according to a consistent convention. The capital letter "E" denotes that the sample originated from the batch grown by the traveling-solvent floating-zone (TSFZ) method, described in Chapter 2, Section 2.2.1. The following three-digit binary code "_iii_", where $i = (0 \vee 1)$, specifies the crystallographic direction along which the uniaxial compressive stress was applied, either [100] or [011]. The label is completed by an ordinal identifier of the specimen measured under the given orientation, for example, `spl1`, `spl2`, etc.

For each sample presented in this Appendix, the Verwey transition temperature, T_V, was determined as the inflection point of the experimental curves $\rho(T)$ or $\chi_{\mathrm{AC}}(T)$. Both the resistivity and magnetic susceptibility measurements exhibited a pronounced thermal hysteresis, originating from the relatively high specific heat of magnetite. Owing to this hysteresis, T_V was determined independently from the data recorded during heating and cooling cycles. In the plots showing the dependence of the transition temperature on the applied uniaxial pressure σ, the T_V values obtained

upon heating are indicated by warm colors, while those determined during cooling are represented by cold colors.

F.1. Impact of uniaxial pressure applied along [100] direction on resistivity and magnetic susceptibility

F.1.1. Sample E_100_spl1

Sample E_100_spl1 was measured in resistivity as a function of uniaxial compression from 0 to 223 MPa. The determined T_V depended linearly on the applied uniaxial stress, σ. The shape of the resistivity curves was smooth, except for a slight kink that systematically occurred near the VT region. This suggested that the mounted sample could be compressed incompletely. However, T_V recovered its initial value after the compression was released at the end of the experiment.

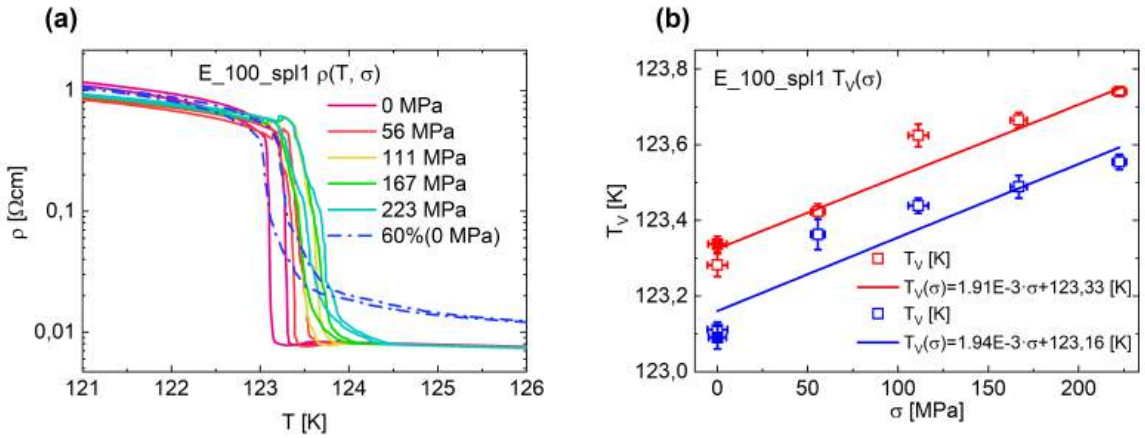

Fig. F.1. Low-temperature electrical resistivity as a function of uniaxial pressure σ applied along the [100] crystallographic direction in sample E_100_spl1. **(a)** Temperature dependence of resistivity $\rho(T)$ measured under uniaxial compression from 0 to 223 MPa. The dashed line corresponds to the resistivity curve recorded after complete stress release. **(b)** Linear dependence of the Verwey transition temperature T_V on the applied uniaxial stress σ. Filled symbols denote the data acquired after unloading.

Between consecutive measurements presented in Fig. F.1, the probe was removed from the liquid nitrogen bath and subsequently brought back to room temperature under inert conditions. Uniaxial compression was applied by incrementally rotating the screw of the SOL pressure cell, while the sample voltage was continuously recorded at a rate of three measurements per second. The resulting voltage exhibited a step-like dependence corresponding to discrete increments of applied pressure.

The plateau regions between successive pressure steps were extracted and linearized as a function of the applied uniaxial stress, as shown in Fig. F.2.

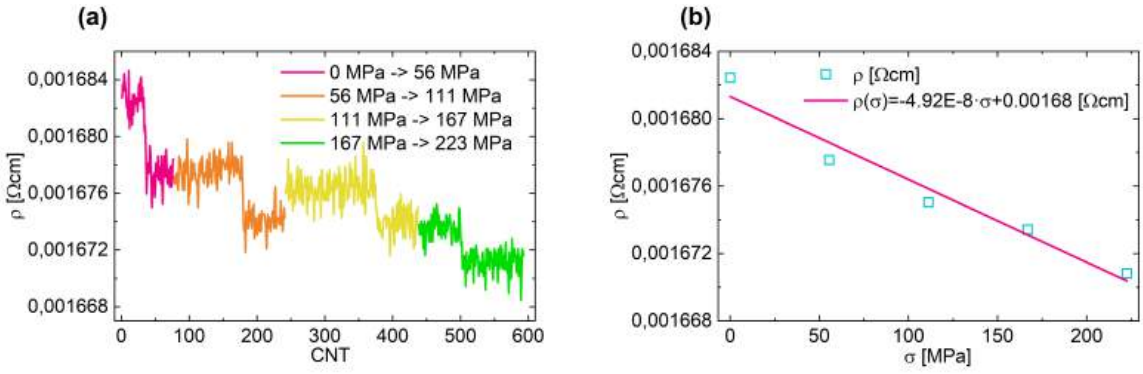

Fig. F.2. Room-temperature electrical resistivity during the application of uniaxial compression σ along the [100] crystallographic direction in sample E_100_spl1. **(a)** Temporal evolution of the sample resistivity $\rho(t)$ recorded during incremental screw rotation in the SOL pressure cell. **(b)** Dependence of the resistivity plateau values extracted from panel (a) on the applied uniaxial stress σ. The filled symbol represents the resistivity measured after complete stress release, confirming the reversibility of the deformation process.

F.1.2. Sample E_100_spl3

The incomplete recovery of resistivity after stress release observed in sample E_100_spl1 motivated a repeatability test of the uniaxial compression procedure using the SOL pressure cells. Consequently, a second specimen (E_100_spl2) was prepared for resistivity measurements. However, this sample fractured spontaneously into multiple pieces during mounting in the SOL cell. A properly prepared and successfully mounted specimen (E_100_spl3) was subsequently subjected to ten successive compression–release cycles. The maximum applied stress in each cycle exceeded that of the previous one, allowing for a systematic assessment of the material's elastic and plastic response. For each loading step, a corresponding unloading measurement was recorded. The resistivity data collected during compression are shown in Fig. F.3, where two distinct regimes of the Verwey transition response to applied stress can be identified. In the final compression stage, corresponding to a maximum stress of 216 MPa, the sample underwent plastic deformation. This is evidenced by the last "zero-load" curve (0 MPa, X) recorded after decompression, which deviates significantly from the previous stress-released resistivity traces, as illustrated in Fig. F.4.

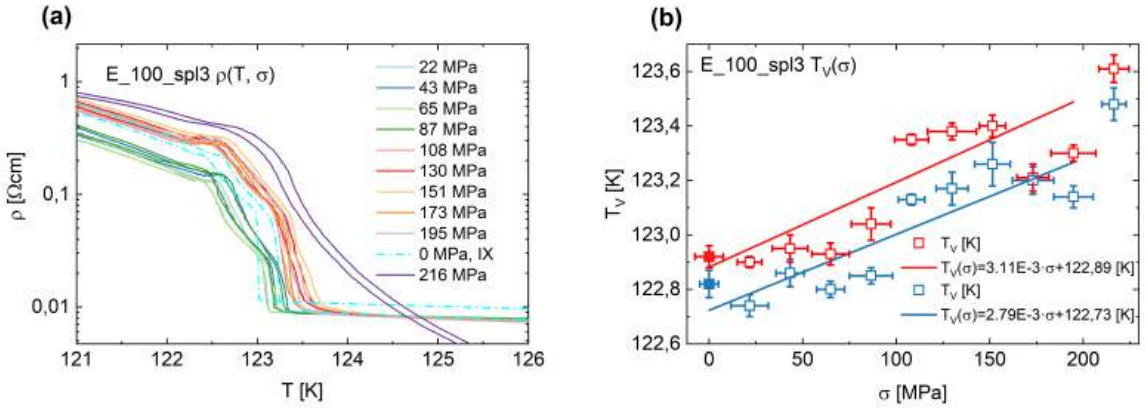

Fig. F.3. Low-temperature electrical resistivity as a function of uniaxial stress σ applied along the [100] crystallographic direction in sample E_100_spl3. **(a)** Temperature dependence of resistivity $\rho_{AC}(T, \sigma)$ measured under progressively increasing uniaxial compression. The cyan trace ("0 MPa, IX") corresponds to the resistivity curve recorded at zero applied stress between the intermediate and final loading steps. **(b)** Linear dependence of the Verwey transition temperature T_V on the applied uniaxial stress σ. The filled symbols denote the data points associated with the "0 MPa, IX" measurement shown in panel (a).

For this sample, the measurements of electrical resistivity performed under uniaxial compression at room temperature yielded inconclusive results. As shown in Fig. F.4, the resistivity plateau levels exhibited irregular and non-reproducible shifts between successive screw rotations and releases. Owing to this instability, no quantitative analysis of the room-temperature resistivity was carried out for sample E_100_spl3.

The curve labeled "0 MPa, X" in Fig. 5.7a, which differs in both shape and transition temperature T_V from the other resistivity curves recorded under zero applied stress, was multiplied by a factor of ten for clarity. This anomalous behavior was the first indication that the sample might have been structurally damaged. Indeed, sample E_100_spl3 disintegrated upon removal from the SOL2 pressure cell.

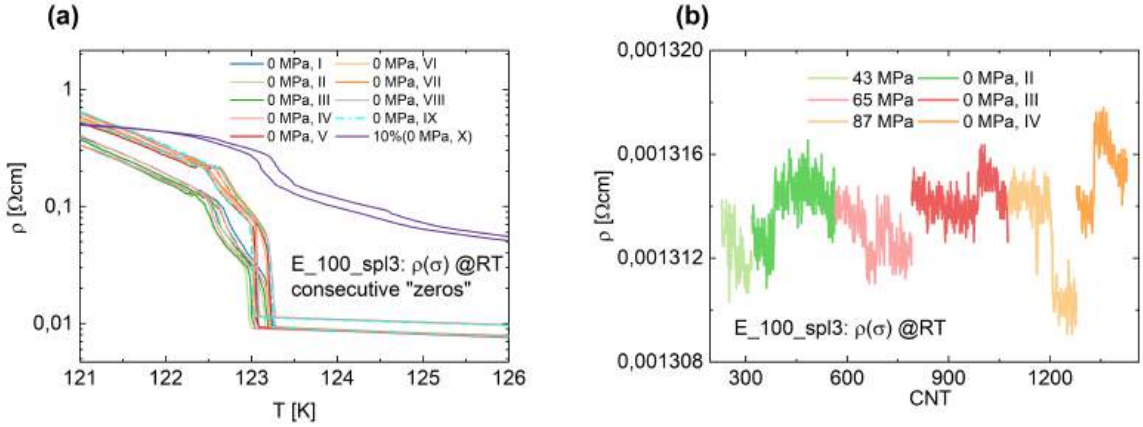

Fig. F.4. (a) Control sequence of electrical resistivity measurements through the Verwey transition in sample E_100_spl3, recorded for the relaxed crystal between consecutive uniaxial compression steps shown in Fig. F.3. **(b)** Dependence of the room-temperature resistivity on the applied uniaxial stress σ, corresponding to the second (43 MPa), third (65 MPa), and fourth (87 MPa) compression steps in Fig. F.3a, and the respective post-release states labeled "0 MPa, II", "0 MPa, III", and "0 MPa, IV" in panel (a).

F.1.3. Sample E_100_spl4

Sample E_100_spl4 exhibited a systematic variation of electrical resistivity in response to uniaxial compression σ applied along the [100] direction, both at room temperature and in the vicinity of the Verwey transition, as discussed in Section 5.1. Quantitatively, the resistivity changes in this sample were determined with higher precision than in the other crystals oriented along the $\langle 100 \rangle$ direction.

Nevertheless, the qualitative trend, a monotonic increase of the transition temperature T_V with applied uniaxial stress, was consistent with the behavior observed for samples E_100_spl1 and E_100_spl3. Sample E_100_spl4 was recovered intact, without visible signs of cracking or plastic deformation after the experiment. The dependencies of T_V on σ derived from the resistivity curves of these three samples were combined and are shown together in Fig. F.5.

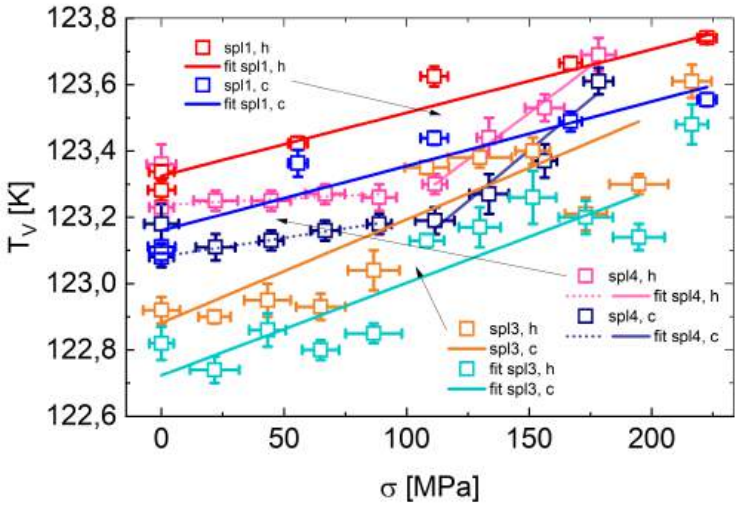

Fig. F.5. Dependence of the Verwey transition temperature T_V on uniaxial compression applied along the [100] direction, as determined from resistivity measurements. The results obtained for sample E_100_spl4 are superimposed on those from samples E_100_spl1 (Fig. F.1) and E_100_spl3 (Fig. F.3). Data points plotted in warm colors correspond to T_V values determined during heating (h), while those plotted in cool colors represent T_V determined during cooling (c).

F.2. Impact of uniaxial pressure applied along [011] direction on resistivity and magnetic susceptibility

The observed mechanical instability of magnetite under uniaxial compression along the $\langle 100 \rangle$ direction, combined with the concurrent increase in the Verwey transition temperature T_V, motivated the investigation of single-crystalline magnetite subjected to compression along the $\langle 110 \rangle$ direction. To this end, four samples were examined: E_011_spl1, E_011_spl2, E_011_spl3, and E_011_ii_spl4.

The investigation of samples oriented along the [011] direction commenced concurrently with the implementation of the AC magnetic susceptibility setup compatible with the uniaxial pressure system. The AC susceptibility module operated jointly with the resistivity probe, allowing consecutive measurements of both quantities without remounting the sample.

All samples oriented along the [011] direction were therefore examined through an interlaced sequence of resistivity and susceptibility measurements. The results presented in this Appendix

follow the chronological order of their acquisition for each sample.

The AC susceptibility in samples E_011_spl1, E_011_spl2, and E_011_spl3 was measured as a function of the quantitatively applied uniaxial stress using miniature detection coils directly glued to the crystal surface. The fabrication and calibration of these coils were described in Appendix B. The first *in-situ* verification of their performance was carried out on sample E_011_spl1, immediately after completing two full resistivity measurements under uniaxial stress.

For sample E_011_spl2, the susceptibility coils were attached to the specimen with the electrical contacts already in place. The measurement sequence consisted of three consecutive stages: first, the AC susceptibility was recorded as a function of applied stress; second, the electrical resistivity was measured over the same pressure range; and finally, the susceptibility sequence was repeated. Between each experimental cycle, the applied pressure was fully released to ensure complete elastic relaxation of the sample.

The experimental protocol applied to sample E_011_spl3 followed the same scheme. Four successive compression cycles were performed, with complete stress release after each. The first and third cycles corresponded to AC susceptibility measurements, and the second cycle to electrical resistivity. Due to low signal quality in the third sequence (V2 - susceptibility), the entire susceptibility measurement was repeated (V3). Consequently, Chapter 5 includes two post-resistivity susceptibility datasets labeled V2 and V3, respectively.

F.2.1. Sample E_011_spl1

Uniaxial compression was applied to sample E_011_spl1 along the [011] direction in three successive cycles. The first two sequences consisted of electrical resistivity measurements, while the third sequence was dedicated to AC magnetic susceptibility.

In both resistivity measurements, a shift in the Verwey transition temperature, T_V, was detected only over a portion of the resistivity curve. This partial response indicates that uniaxial stress was not homogeneously transmitted across the entire crystal volume.

The first resistivity run, performed under uniaxial compression increasing from 0 to 147 MPa along the [011] direction, is shown in Fig. F.6. The maximum transition temperature determined from this sequence reached $T_V = 124.8$ K at 147 MPa. The dashed cyan line labeled "0 MPa, r" represents the resistivity curve recorded after complete decompression of the sample.

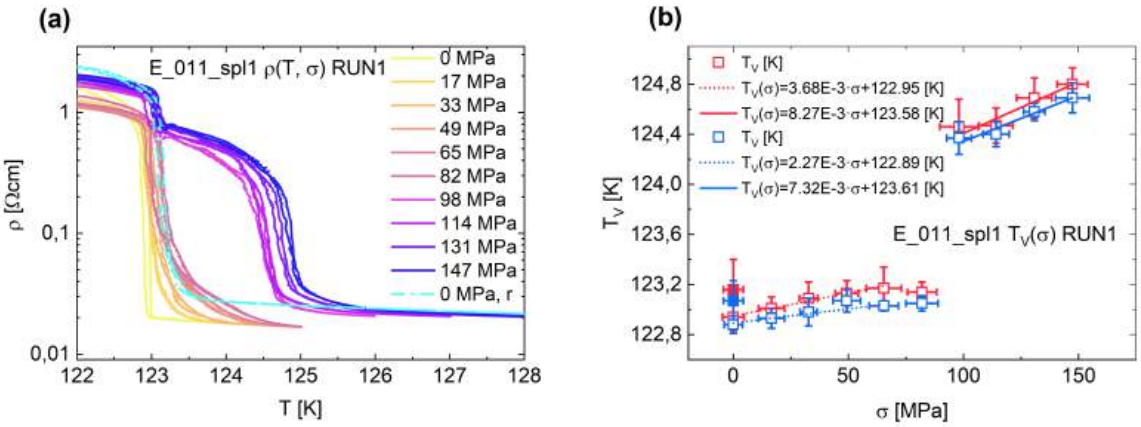

Fig. F.6. Low-temperature resistivity as a function of uniaxial stress, σ applied along the [011] direction in sample E_011_spl1. **(a)** Resistivity studied as a function of uniaxial compression, $\rho_{AC}(T, \sigma)$ from 0 to 147 MPa. The resistivity responded to uniaxial compression in two distinguished ranges. **(b)** A linear relation was fitted in each of these ranges between the transition temperature T_V and the applied stress σ. The filled points refer to the measurement collected after the stress was released, marked as "0 MPa, r" in panel (a).

In Fig. F.6a, two distinct regions of the sample response to uniaxial compression can be identified. These regimes are separated near 82 MPa and 98 MPa, where a change in the slope of the resistivity curve is observed. The origin of this behavior is attributed to partial mechanical blockage of the sample by an excess of STYCAST adhesive within the cell, which initially prevented uniform stress transmission. Only after exceeding approximately 98 MPa did the cell begin to transmit the pressure evenly, resulting in a second linear regime of T_V shift with stress. Independent linear fits were therefore applied to the 0–82 MPa and 98–147 MPa data ranges, respectively.

The second resistivity run, shown in Fig. F.7, demonstrated smooth and reproducible pressure application, confirming proper operation of the cell. The transition temperature reached a maximum of $T_V = 125.2$ K at 98 MPa, about 0.4 K higher than in the first run, and remained constant for higher stress values. The dashed forest-green line labeled "98 MPa, r2" and the dashed cyan line

labeled "0 MPa, r2" correspond to the resistivity curves collected during compression and after full decompression, respectively.

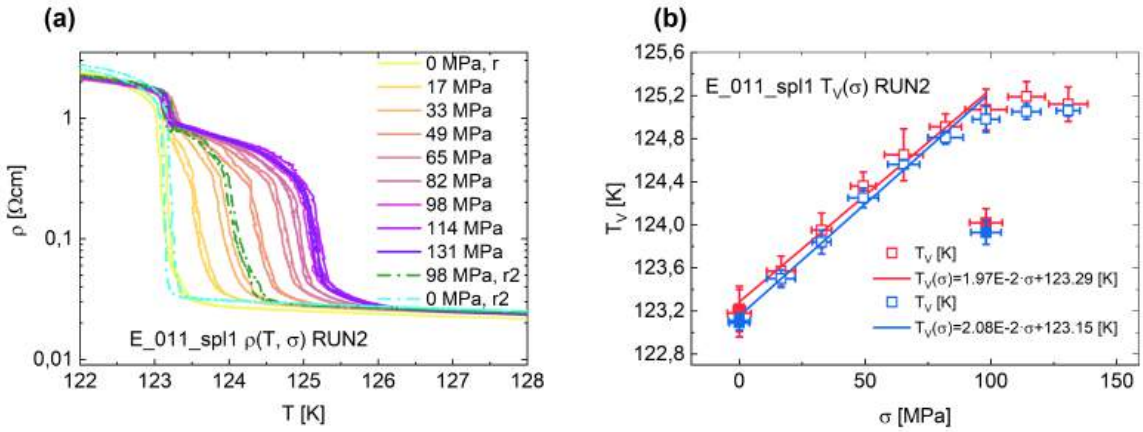

Fig. F.7. Low-temperature resistivity as a function of uniaxial stress, σ, applied along the [011] direction in sample E_011_spl1. **(a)** Resistivity, $\rho_{AC}(T, \sigma)$, measured under uniaxial compression up to 131 MPa. For lower pressures, only part of the sample responded due to partial mechanical blockage by excess STYCAST adhesive, while above 98 MPa uniform pressure transmission was restored. Dashed curves correspond to measurements collected during decompression. **(b)** Dependence of the Verwey transition temperature, T_V, on applied stress. A linear fit was applied to data for $\sigma \leq 98$ MPa, above which T_V became pressure-independent. Filled symbols correspond to the decompression steps labeled "98 MPa, r2" and "0 MPa, r2" in panel (a).

In the second run, the response of sample E_011_spl1 to uniaxial compression was improved compared to the first experiment; however, the applied stress still did not act homogeneously across the entire crystal. This was evidenced by the low-temperature part of each resistivity curve, which remained nearly unchanged despite the increasing compression. Furthermore, the dependence of the transition temperature T_V on the applied uniaxial stress along the [011] direction saturated for $\sigma > 98$ MPa. Consequently, the data points corresponding to 114 and 131 MPa were excluded from the linear fit presented in Fig. F.7b.

Figure F.8 shows the room-temperature resistivity for each compression sequence measured near the Verwey transition and presented in Figs. F.6 and F.7. In panel F.8a, the distinct plateau levels of ρ correlate with the anomalous transition splitting observed between the two resistivity regimes in Fig. F.6a, confirming the nonuniform pressure distribution during the first measurement cycle.

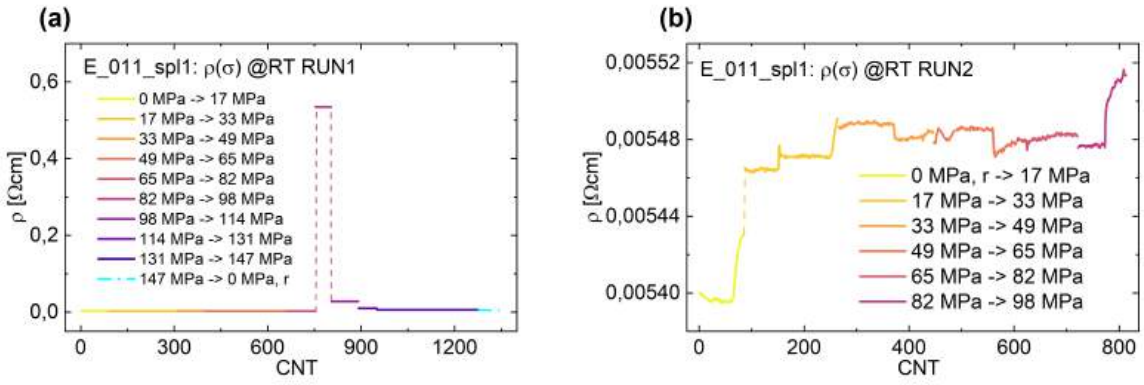

Fig. F.8. Room-temperature resistivity during the application of uniaxial stress, σ, along the [011] direction in sample E_011_spl1 for the two resistivity runs presented in Figs. F.6 and F.7. **(a)** In the first run, resistivity exhibited irregular plateau levels, reflecting incomplete stress transmission through the sample. The abrupt change observed between 82 and 98 MPa corresponds to the transition between the two response regimes identified in Fig. F.6a. **(b)** In the second run, the resistivity displayed step-like variations with increasing stress.

In the second sequence shown in Fig. F.8b, the room-temperature resistivity exhibited a step-like variation with applied uniaxial stress. The data did not follow a monotonic or analytically predictable trend, suggesting that the pressure transmission across the sample was nonuniform.

In contrast to all other crystals studied under compression along both [100] and [011] directions, where the room-temperature resistivity systematically decreased with increasing uniaxial stress, sample E_011_spl1 displayed an anomalous increase in ρ_{AC} with compression in both runs (Figs. F.8a and F.8b). This behavior likely resulted from irregular strain distribution caused by partial mechanical decoupling of the sample from the clamps during compression.

After completing the two resistivity measurement series under uniaxial stress, the self-fabricated AC susceptibility coils were tested on sample E_011_spl1. The results, representing the first successful magnetic susceptibility measurements performed under uniaxial compression from 0 to 147 MPa along the [011] direction, are summarized in Fig. F.9.

The AC susceptibility signal exhibited a systematic decrease in baseline amplitude and an increasingly pronounced sigmoidal shape with rising compression, indicating enhanced magnetic anisotropy near the Verwey transition. The dashed cyan line "0 MPa, r3" corresponds to the susceptibility curve measured after full decompression, which recovered its original form, confirming elastic sample behavior. The dependence of the transition temperature T_V on applied stress

showed an approximately linear trend, though with significant data scatter, yielding a coefficient of determination $R^2 \approx 0.65$.

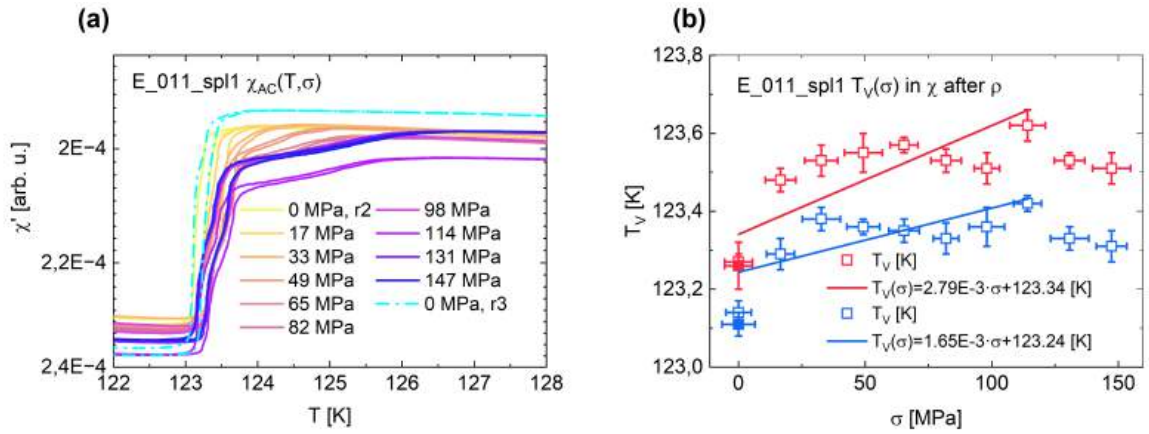

Fig. F.9. AC magnetic susceptibility as a function of uniaxial compression, σ, applied along the [011] direction in sample E_011_spl1. **(a)** Real component of the susceptibility, χ', measured for compressive stresses from 0 to 147 MPa. The amplitude of χ' systematically decreased and the transition became more sigmoidal with increasing σ. The dashed cyan line "0 MPa, r3" denotes the curve recorded after full decompression, which recovered the original signal shape. **(b)** Dependence of the Verwey transition temperature, T_V, determined from panel (a), on the applied uniaxial stress. The trend is approximately linear, with the filled symbols corresponding to the decompressed state ("0 MPa, r3").

F.2.2. Sample E_011_spl2

For sample E_011_spl2, the AC magnetic susceptibility was first measured as a function of uniaxial compression applied along the [011] direction. As shown in Fig. F.10, the applied stress was systematically increased from 0 to 196 MPa. The susceptibility signal exhibited a gradual widening of the VT. The dashed cyan line "0 MPa, r" denotes the susceptibility curve recorded after full decompression, which recovered the initial shape, confirming the elastic reversibility of the sample response.

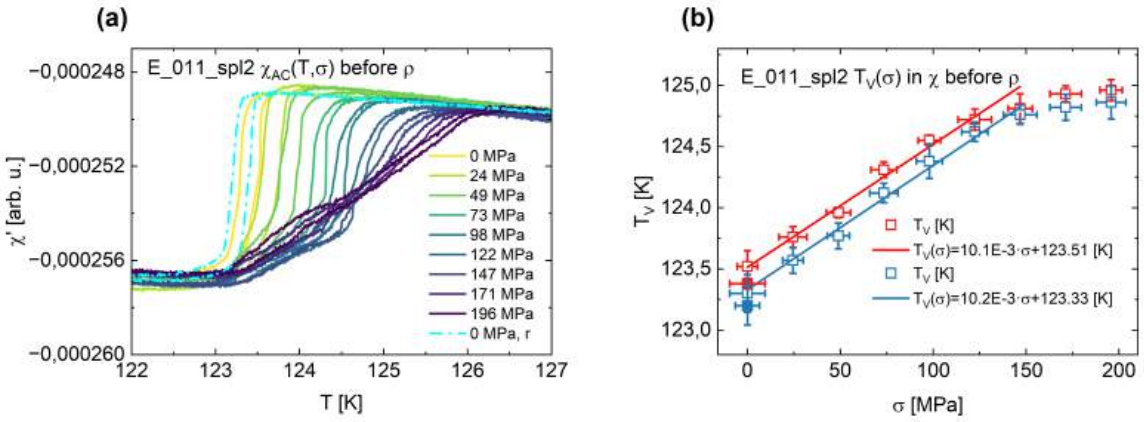

Fig. F.10. AC magnetic susceptibility as a function of uniaxial stress, σ, applied along [011] direction in sample E_011_spl2, measured on SOL2, prior to the resistivity experiment. **(a)** Real component of the susceptibility, χ', measured for compressive stresses from 0 to 196 MPa. The signal progressively decreased in amplitude and exhibited a shape distortion up to about 147 MPa. The dashed cyan line "0 MPa, r" denotes the curve recorded after full decompression, which recovered the initial response. **(b)** Dependence of the Verwey transition temperature, T_V, on the applied uniaxial stress, σ. The filled symbols correspond to the decompressed state ("0 MPa, r"). Since T_V saturated above 147 MPa, the terminal points at 171 and 196 MPa were excluded from the linear fit.

Unlike in the case of sample E_011_spl1, the Verwey transition temperature, T_V, in sample E_011_spl2 exhibited a systematic linear increase with applied uniaxial compression. The last two data points, corresponding to stresses of 171 MPa and 196 MPa, were excluded from the linear fit due to the onset of saturation in the stress response.

Subsequently, the electrical resistivity of sample E_011_spl2 was measured as a function of uniaxial compression applied along the [011] direction. Figure F.11a presents the evolution of the resistivity signal with increasing applied stress, ranging from 0 to 196 MPa.

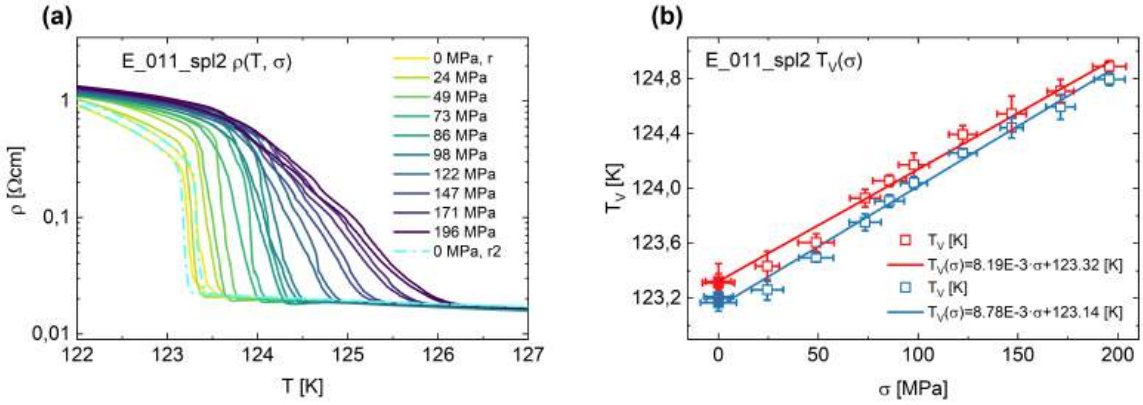

Fig. F.11. Low-temperature resistivity as a function of uniaxial stress, σ applied along the [011] direction in sample E_011_spl2. **(a)** Resistivity studied as a function of uniaxial compression. The dashed cyan line marked as "0 MPa, r2" denotes the resistivity curve measured after decompression. **(b)** Dependence of the transition temperature, T_V, on the applied stress, σ. The filled points refer to the measurement on the decompressed sample marked as "0 MPa, r2" in panel (a). A linear increase of T_V with σ was observed up to about 150 MPa, followed by saturation at higher pressures.

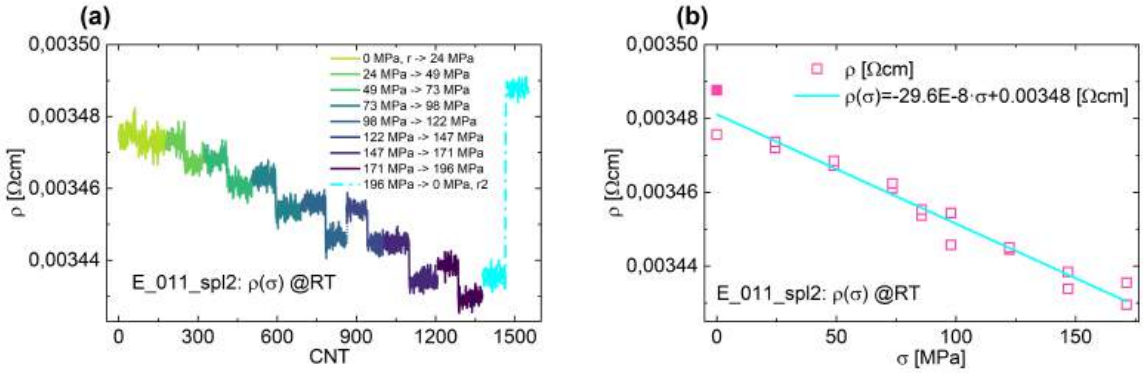

Fig. F.12. Room-temperature resistivity during application of uniaxial stress, σ, along the [011] direction in sample E_011_spl2. **(a)** Sample resistivity recorded over time as the screw was turned. The cyan line denotes the release of uniaxial stress from 196 MPa to 0 MPa, performed for the second time in the sample history (marked as "r2"). **(b)** Linearized dependence of the specific resistivity plateau levels from panel (a) on the applied stress, σ. The filled point marks the resistivity plateau after decompression, indicated as "0 MPa, r2" in panel (a).

In addition to the low-temperature measurements, resistivity variations at room temperature were recorded during the application of uniaxial compression. As shown in Fig. F.12a, distinct resistivity plateaus appeared after each screw rotation, indicating stabilization of the mechanical load. These plateau values, linearized as a function of applied stress, exhibited a systematic decrease in specific resistivity, as presented in Fig. F.12b.

Figure F.13 shows the AC susceptibility measured in the stress range from 0 MPa to 196 MPa, repeated after the resistivity sequence. The dashed cyan line marked as "0 MPa, r3" denotes the susceptibility curve measured after decompression. The purpose of this experiment was to confirm the reproducibility of pressure transmission in the SOL2 cell.

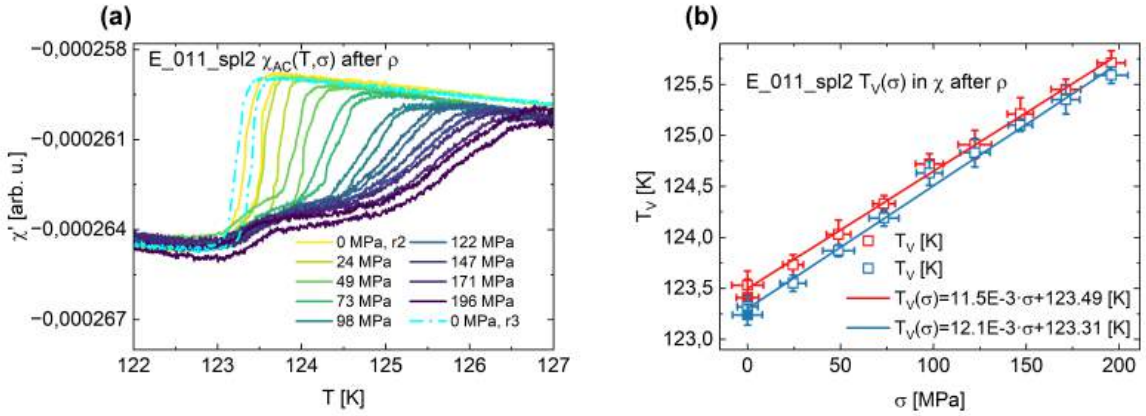

Fig. F.13. Dependence of the AC susceptibility on uniaxial stress, σ, applied along the [011] direction in sample E_011_spl2 after the resistivity measurement. **(a)** The susceptibility signal χ' progressively shifted and decreased in amplitude with increasing uniaxial stress from 0 to 196 MPa. The dashed cyan line marked as "0 MPa, r3" denotes the susceptibility curve measured after decompression. **(b)** Linear dependence of the transition temperature T_V, determined from AC susceptibility, on the applied uniaxial stress σ. The filled points correspond to the measurement performed after stress release, marked as "0 MPa, r3" in panel (a).

F.2.3. Sample E_011_spl3

For sample E_011_spl3, the AC susceptibility measured prior to the resistivity sequence (Fig. 5.14), the resistivity studied at both room (Fig. 5.7) and low temperatures (Fig. 5.6), as well as the final susceptibility series acquired after the resistivity measurement and labeled "V3" (Fig. 5.15), were already presented in Chapter 5, Section 5.1, as functions of uniaxial compression.

Figure F.14 compares the resistivity response of sample E_011_spl3 with those obtained for samples E_011_spl1 (Fig. F.7) and E_011_spl2 (Fig. F.11), showing all results superimposed to highlight the common dependence of T_V on the applied uniaxial stress along the [011] direction.

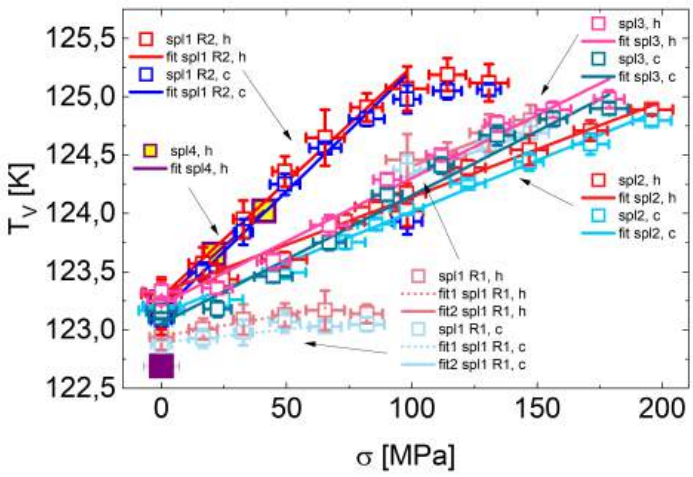

Fig. F.14. Dependence of the Verwey transition temperature determined from resistivity measurements on uniaxial compression applied along the [011] direction. The results obtained for sample E_011_spl3 are superimposed on those for RUN2 of sample E_011_spl1 (Fig. F.7) and sample E_011_spl2 (Fig. F.11). The points shown in warm colors correspond to T_V values determined during heating (h), whereas those in cool colors represent T_V obtained during cooling (c).

The dependence of the Verwey transition temperature, T_V, on uniaxial compression was determined from AC susceptibility measurements in sample E_011_spl3, performed immediately after the resistivity cycle in the stress range from 0 to 223 MPa. The results are presented as series "V2" in Fig. F.15. The dashed cyan line labeled "0 MPa, r3" denotes the susceptibility curve that recovered its initial form after decompression. A noticeable deviation of the data at the highest compression values (201 MPa and 223 MPa) from the general trend led to their exclusion from the linear fit describing the dependence of T_V on the applied uniaxial stress.

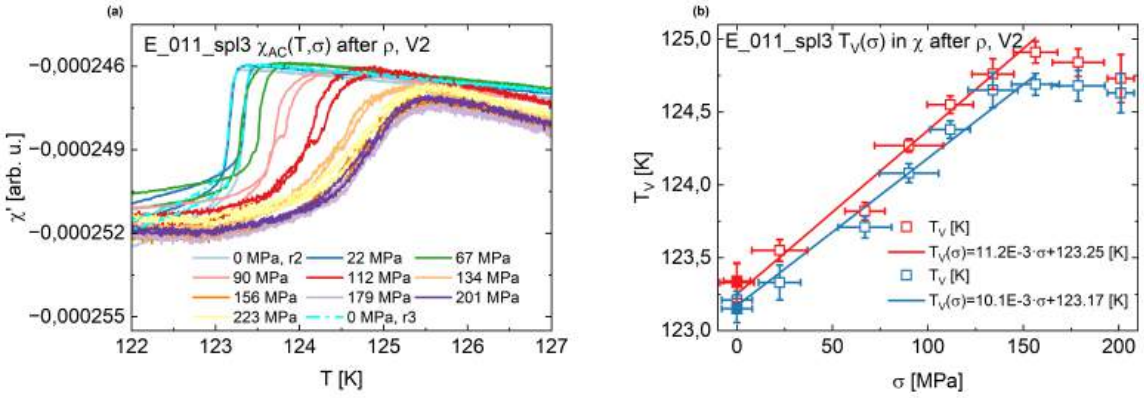

Fig. F.15. Dependence of the Verwey transition temperature, T_V, determined from AC susceptibility on uniaxial stress, σ, applied along the [011] direction in sample E_011_spl3, measured immediately after the resistivity cycle (V2). **(a)** The real component of the susceptibility, χ', systematically shifted with increasing uniaxial stress in the range 0–223 MPa. The dashed cyan line labeled "0 MPa, r3" denotes the susceptibility curve recorded after decompression. **(b)** Linear dependence of T_V on the applied stress, σ. The data points corresponding to 201 MPa and 223 MPa deviated from the general trend and were excluded from the linear fit. The filled symbols correspond to the decompressed state, marked as "0 MPa, r3" in panel (a).

Due to the relatively low signal-to-noise ratio and the modest shift of the Verwey transition temperature, T_V, with uniaxial stress applied along the [011] direction, the AC susceptibility measurements were repeated as the series labeled "V3", shown in Fig. 5.15 and discussed in Section 5.2. The relative changes in electrical resistivity at room temperature under uniaxial stress were presented in Section 5.1 in two separate panels of Fig. 5.11 for the [100] and [011] orientations, respectively.

Figure F.16 combines these results to compare the relative resistivity variation, $\Delta\rho = \left(\frac{\rho}{\rho_0}\right)\cdot 100\%$, at room temperature as a function of uniaxial compression applied along the [100] and [011] crystallographic directions on a single plot.

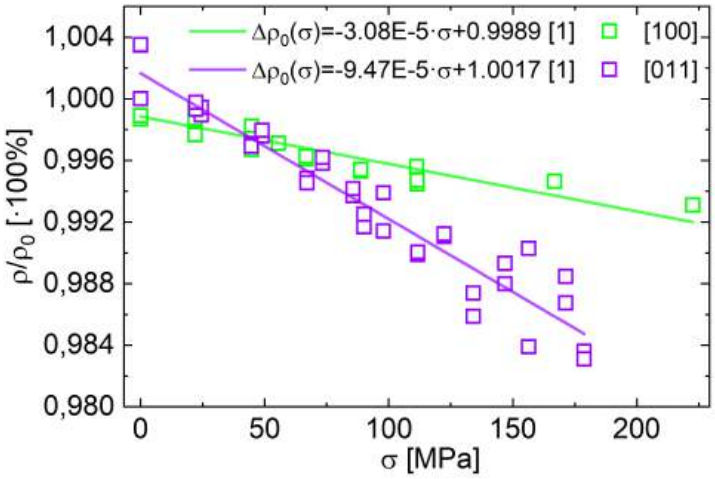

Fig. F.16. Comparison of the effect of uniaxial stress on the relative change in electrical resistivity of stoichiometric magnetite at room temperature for two crystallographic orientations. Light green dots correspond to measurements performed under compression along the [100] direction, with line of the same color indicating the corresponding linear trend. Purple dots and the associated line represent the results obtained for compression along the [011] direction.

By comparing the slope coefficients of the fitted linear relations, it is evident that the resistivity of magnetite responds approximately three times more strongly to uniaxial stress applied along the [011] direction than along the [100] direction. This enhanced sensitivity reflects the anisotropic nature of the strain–transport coupling in the crystal lattice. The graph in Fig. F.16 illustrates this difference by visually emphasizing the contrast between the respective slope gradients.

F.2.4. Sample E_011_ii_spl4

The preparation and results of the resistivity measurements under uniaxial compression in sample E_011_ii_spl4 were discussed in detail in Section 4.4. Following these measurements, the sample was mechanically thinned to a thickness of approximately 0.1 mm. Its mosaic structure and internal strain distribution were subsequently examined using DFXM at the ID03 beamline of the ESRF. The methodology and results of this experiment are presented in Chapter 4.

F.3. Fe K-edge XAS under uniaxial pressure applied along [011] direction

The results of XAS measurements for sample E_100_spl2_XAS subjected to uniaxial compression along the [100] direction were discussed in Chapter 5, Section 5.3. Similarly, due to the strong self-absorption of fluorescence photons in the Fe K-edge region, the analysis for samples oriented along the [011] direction was limited to examining the evolution of the pre-edge features under applied uniaxial stress.

This part of the Appendix complements the XAS data presented in Chapter 5 by including the pre-edge region of the Fe K-edge recorded under uniaxial compression for sample E_011_spl1_XAS, measured using the SOL3 cell, and for sample E_011_spl2_XAS, measured using the SOL4 cell.

Sample E_011_spl1_XAS was cut and polished to dimensions of $3 \times 2 \times 0.41$ mm^3. The XAS spectra of the Fe K-edge pre-edge region collected as a function of uniaxial compression from 0 MPa to 246 MPa are shown in Fig. F.17. The sample remained intact after the experiment and was subsequently labeled "1_axas". This sample was later used for the calibration of the SOL setups during X-ray diffraction (XRD) measurements conducted at the ID11 beamline of the ESRF, as described in Chapter 3.

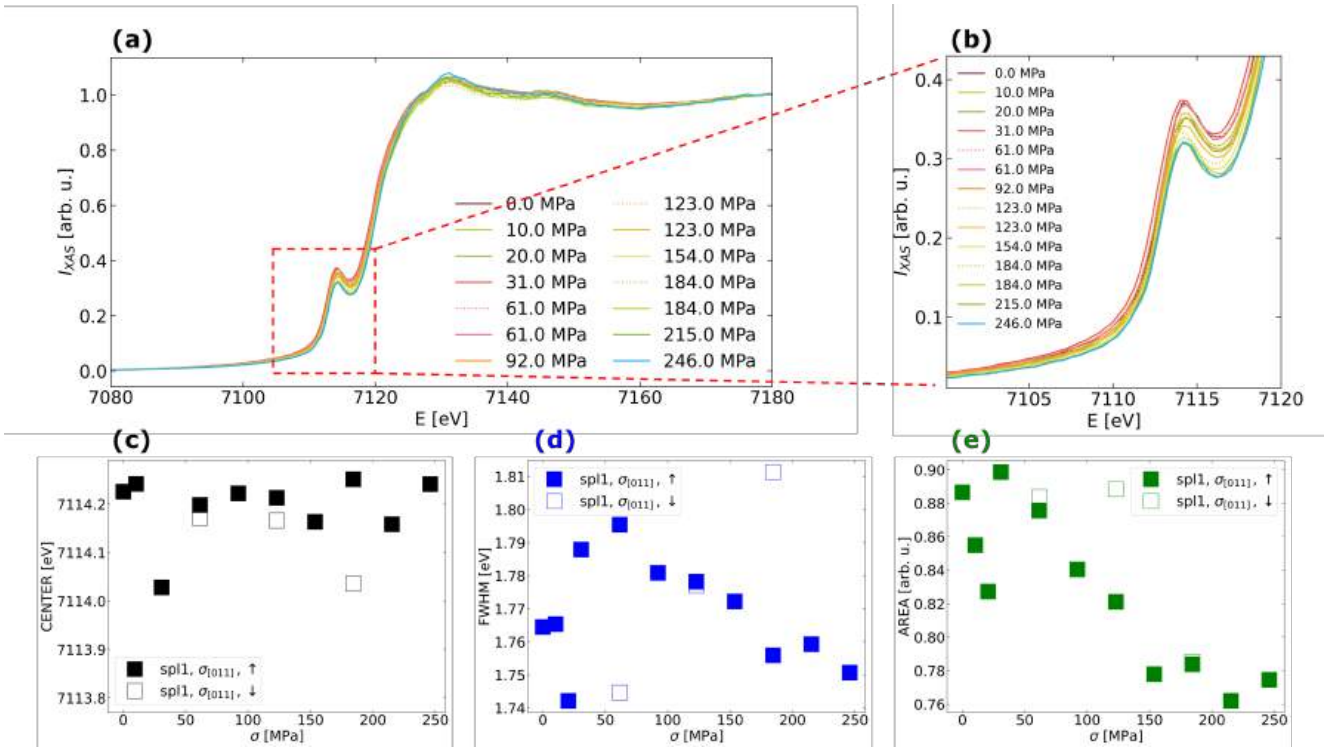

Fig. F.17. X-ray absorption spectra (XAS) at the Fe K-edge collected as a function of uniaxial stress applied along the [011] direction for sample E_011_spl1_XAS using the SOL3 cell. **(a)** Full Fe K-edge spectra recorded for increasing uniaxial stress in the 7080–7180 eV range; dotted lines denote spectra collected during gradual pressure release. **(b)** Enlarged view of the pre-edge region (7105–7120 eV), used for quantitative fitting. Evolution of **(c)** peak position, **(d)** **full width at half maximum (FWHM)**, and **(e)** **integrated peak area** as a function of applied uniaxial stress, σ. Empty symbols correspond to measurements during gradual stress release.

The sample E_011_spl2_XAS, prepared using the same procedure, had final dimensions of $3 \times 2 \times 0.40$ mm^3. The XAS spectra collected in the pre-edge region of the Fe K-edge as a function of uniaxial compression in the range from 0 MPa to 308 MPa are presented in Fig. F.18. The crystal fractured when the applied uniaxial stress along the [011] direction exceeded approximately 300 MPa. A well-oriented fragment of this sample was subsequently polished to a thickness of 0.1 mm, labeled "brokenP", and characterized by dark-field X-ray diffraction microscopy, as described in Chapter 4.

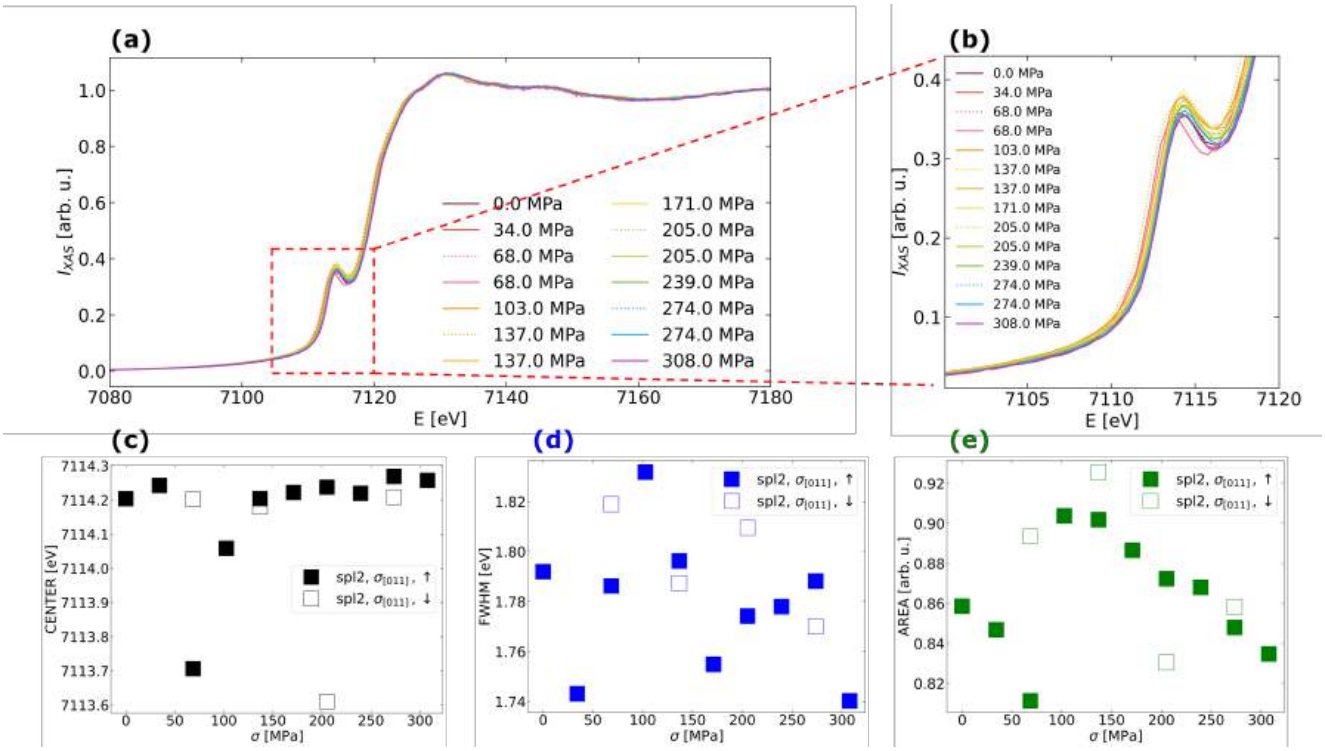

Fig. F.18. XAS at the Fe K-edge collected as a function of uniaxial stress applied along the [011] direction for sample E_011_spl2_XAS using the SOL4 cell. **(a)** Full Fe K-edge spectra recorded for increasing uniaxial stress in the 7080–7180 eV range; dotted lines denote spectra collected during gradual pressure release. **(b)** Enlarged view of the pre-edge region (7105–7120 eV) used for quantitative fitting. Evolution of **(c)** peak position, **(d)** **full width at half maximum (FWHM)**, and **(e)** **integrated peak area** as a function of applied uniaxial stress, σ. Empty symbols correspond to measurements performed during gradual stress release.

In both Figures F.17 and F.18, no systematic dependence on the uniaxial stress applied along the [011] direction was observed for either the peak position or the full width at half maximum (FWHM) of the fitted pre-edge feature. In contrast, the integrated peak area showed an apparent reduction with increasing compression for both samples. However, this effect was not reproducible upon decompression, indicating that the observed variation is likely within the experimental uncertainty rather than a genuine pressure-induced change.

Bibliography

[1] V. Saeed. "Schemat symulacji w środowisku ABAQUS". URL: *https://en.wikipedia.org/wiki/File:Abaqus_software_FEA_process.png* (visited on 01/14/2025).

[2] K. Banaś. "Wprowadzenie do MES". URL: *http://ww1.metal.agh.edu.pl/~banas/wprowadzenie%5C_do%5C_MES.pdf* (visited on 06/14/2025).

[3] J. G. Ferrer et al. "darfix – data analysis for dark-field X-ray microscopy". *Journal of Synchrotron Radiation* **30** (2023), pp. 527–537. DOI: 10.1107/S1600577523001674.